©Copyright 2025
Fargol Rezayaraghi

Leveraging substructural brain mechanics to understand brain pathophysiology and develop intervention systems

Fargol Rezayaraghi

A dissertationsubmitted in partial fulfillment of the
requirements for the degree of

Doctor of Philosophy

University of Washington

2025

Reading Committee:

Mehmet Kurt, Chair

Samuel Browd

Per Reinhall

Azadeh Yazdan

Program Authorized to Offer Degree:
UW Mechanical Engineering

University of Washington

Abstract

Leveraging substructural brain mechanics to understand brain pathophysiology and develop intervention systems

Fargol Rezayaraghi

Chair of the Supervisory Committee:
Mehmet Kurt
Department of Mechanical Engineering

Neurodegenerative diseases and traumatic brain injuries (TBIs) represent significant public health challenges globally, particularly in the United States, where they are projected to impact 88 million individuals by 2050. These conditions, often linked to sports that involve repetitive head impacts, can lead to conditions like chronic traumatic encephalopathy (CTE) and are associated with considerable disability and mortality. Despite decades of research, there remains a critical need for advancements in detection, diagnosis, prevention, and treatment strategies.

This thesis explores the missing mechanical factors that influence neurodegenerative diseases, focusing on how mechanical forces and brain substructure dynamics can be utilized to enhance understanding and management of these diseases. Specifically, it investigates the biomechanics of brain injuries from the perspective of substructural mechanics and the effects of morphological changes within the brain, providing a comprehensive view of how such dynamics relate to disease processes.

The research begins with an evaluation of the biomechanical performance of current sports helmets, particularly bicycle helmets that incorporate various impact mitigation strategies. Findings indicate that helmets equipped with rotation damping systems and other novel technologies outperform traditional helmets in managing kinematics at low impact velocities and angular momentum. This uncovers the necessity for re-considering helmet designs

to better prevent cycling-related TBIs, advocating for more inclusive impact testing that considers a range of motion and impact scenarios.

Further, the study utilizes dynamic amplified MRI (aMRI) to assess *in vivo* displacement of brain substructures in patients with Normal Pressure Hydrocephalus (NPH), examining how these movements are altered by surgical interventions such as shunt placement. The research demonstrates that aMRI can effectively indicate shunt functionality, offering a non-invasive method to monitor and evaluate surgical outcomes.

Additionally, leveraging data from the DIAGNOSE CTE project, the thesis applies machine learning algorithms to predict neurocognitive and neuropsychiatric outcomes based on blood and cerebrospinal fluid (CSF) biomarkers, alongside magnetic resonance imaging (MRI) morphometrics. This innovative approach highlights the potential of integrating computational methods with clinical data to better understand and manage TBIs and neurodegenerative diseases.

Overall, this thesis investigates a multidisciplinary approach that integrates mechanical assessments, advanced imaging techniques, and machine learning to provide new insights into the prevention, diagnosis, and management of neurodegenerative diseases and TBIs. The findings contribute to the broader field of neurology by suggesting that mechanical factors are crucial for understanding the complex dynamics of brain diseases and by offering promising new directions for enhancing patient care and treatment strategies.

TABLE OF CONTENTS

LIST OF FIGURES

LIST OF TABLES

ACKNOWLEDGMENTS

Firstly, I'd like to hugely thank my advisor, Prof. *Mehmet Kurt*, for his support throughout my PhD journey. From my acceptance into the program to the visa approval process, and our lab's cross-country move, he has encouraged my growth in various projects I'm passionate about and supported my ambition to start a startup. His passion for novelty in science is amazing and has made the lab more vibrant.

I would also like to thank my PhD committee members, Prof. *Samuel Browd*, who is an incredible professor, wonderful human being, and a very dedicated neurosurgeon who is also an inspiration for students like me and makes this path more promising for us to put more effort. I would like to thank Prof. *Per Reinhall* for his support during my PhD journey and for the great feedback that he provided. I would also like to thank Prof. *Azadeh Yazdan* for her support, kindness, and great mentorship. Thanks for all her feedback and guidance and her willingness to help students.

In addition, I would like to thank *Wanwisa Kisalang*, the Mechanical Engineering Graduate Student Advisor, for her kind support and being so patient with my endless questions.

I would like to thank all members at KurtLab. PhD is a long journey, and having wonderful colleagues like these makes it easier. I would like to thank *Javid* for his continuous support, guidance, and mentorship. I was so lucky to have such a knowledgeable and humble colleague and friend. I also would like to thank *Efe*, who was a great friend and a colleague to work with, always willing to help and make the path easier. I thank *Gloria* for being a wonderful and encouraging mentor, *Ya-Chen* for her kindness, who taught me resilience. Thanks to *Em* for patiently answering all my questions and providing support. I

thank *Caitlin* for bringing such a positive vibe and energy to the lab. I'm grateful to *Agam, Juampablo*, and *Tyson* for their hard work and positivity. I would like to thank *Tianyi* for being a good colleague and for our long, insightful conversations about different aspects of the project.

I am grateful to the University of Washington for providing diverse resources for students and embracing humanity across campus. I deeply appreciate the financial support from UW-Incubator, CoMotion, which has been crucial since I started exploring the entrepreneurial journey. This support enabled me to work at CoMotion, expanding our project to improve patient care without financial constraints. My experience as a Summer Commercialization Fellow, supported by the Washington Research Foundation/Institute of Translational Health Sciences (WRF/ITHS), was particularly enlightening. I thank *Jessica Roberto*'s support and guidance. Over the past one and a half years, I've been part of the Technology Entrepreneurship Certificate (CTE) Program, which was incredibly enriching, thanks to the insightful professors involved. Additionally, our team at the UW Foster School of Business won both the local and regional Venture Capital Investment Competitions (VCIC) at UW and Silicon Valley, respectively. We are now excitedly preparing for the international competition and are committed to making UW proud.

I want to thank my parents, *Sima Morvarid* and *Abbas Rezayaraghi*, for their endless love and support. Having my sister, Dr. *Farnoosh Rezayaraghi*, by my side has been a huge blessing and I couldn't feel luckier. I am also deeply grateful to my grandparents, whose kindness and patience added so much to the love I received from my parents. Additionally, I extend my heartfelt thanks to my friends all around the world, whose support has made me stronger, happier, and more loved. It's a privilege to have such a supportive network, and I hope to give back the kindness and blessings I've received by improving the lives of others.

DEDICATION

To my incredible parents, Sima and Abbas,
my lovely sister, Farnoosh,
and my cherished grandparents

Chapter 1

INTRODUCTION

1.1 Background and Motivation

Neurodegenerative diseases are major causes of disability, death, and mortality worldwide, including in the US, where they are predicted to affect 88 million Americans by 2050 [2]. It has been shown that neurodegenerative disease mortality risks are linked to sports associated with repetitive head impacts, which may increase the risk of repetitive mild TBI and other neurodegenerative diseases [3, 4]. These diseases have been the focus of various types of studies over the past decades; however, there is still a need for more research to improve diagnostic, detection, prevention, prediction, and treatment strategies. One important aspect that is sometimes underestimated is the role of mechanical factors in these studies, and how they can play a role in identifying factors correlated with detection, diagnosis, prevention, prediction, and even treatment of these diseases. More specifically, understanding the mechanical perspective of specific regions and the effects of morphological changes and behavior in certain diseases can be super informative. In the following paragraphs, I'll elaborate more on this aspect, providing some examples of diseases and how a mechanical perspective can aid in studying these diseases.

TBI is a major cause of disability and mortality worldwide affecting approximately 2.8 million people in the US [5] with mild TBI (mTBI) accounting for 80 % of all cases. To improve diagnosis techniques and develop prevention strategies, there is a need to understand the underlying injury mechanism, especially from a biomechanical perspective. Head kinematic parameters are often used to assess brain injury risk, although recent focus has shifted towards using brain-level mechanical markers such as tissue deformation (i.e., strain) obtained through computer simulations. [6–10]. For instance, analyzing TBI risk based on regional-dependent brain strain criteria has shown a correlation between concussion diagnosis and maximum principal strain [11, 12], emphasizing the importance of brain substructural me-

chanics [13, 14]. Finite element (FE) model simulations of head impacts have revealed that brain substructures exhibit frequency-dependent and nonlinear behavior during impacts, with strain concentration occurring in the corpus callosum [15] and deep white matter, and localized vibration modes [16, 17]. Although it has been demonstrated that brain substructures play a significant role in brain injury mechanisms [7, 18–22], helmet designs have historically focused solely on mitigating linear head kinematics [23–26]. While rotational head kinematics have been addressed in recent improvements to helmet design, consideration of brain substructural mechanics remains lacking. Also, the critical role of localized phenomena in brain injuries [16, 17], necessitates the need to examine the impact of various helmet types on the dynamics of brain substructures. Given substructral nonlinearity, regional vulnerability, and existence of multimodal behavior [16] in the brain, there is a need to address missing dynamical factors in helmets design.

Brain motion is another mechanical factor that plays a crucial role in assessing certain diseases. While the human brain is not typically considered mechanically active, its soft material properties and complex boundary conditions—including vasculature, CSF, and dural folds—result in continuous motion and deformation within the skull [17, 27]. As the heart beats, variations in blood pressure cause the blood vessels and surrounding tissue to deform [28]. Recent research suggests that these dynamics may be altered in certain brain pathologies, which has sparked increased interest in understanding the interactions among brain tissue, CSF, and blood flow. For example, in Chiari I malformation (CM-I), impaired CSF drainage into the spinal canal is believed to increase intracranial pressure, subsequently altering brain motion [28]. Similarly, conditions like hydrocephalus and syringomyelia are thought to impact CSF drainage and consequently affect brain movement. These interactions have been studied using various computational and imaging methods. For instance, Pahlavian et al. developed a patient-specific computational fluid dynamics (CFD) model with moving boundaries at the cervical-medullary junction to explore CNS tissue motion and its effects on CSF dynamics [29]. Moireau et al. treated the interface between blood vessel walls and surrounding tissues as a viscoelastic support, proposing a framework to study the influence of blood flow on artery deformation and brain tissue movement [30]. Additionally, advanced imaging techniques such as Phase-contrast MRI,

4D Flow MRI, DENSE MRI, Magnetic Resonance Elastography (MRE), tagged MRI, Cine Balanced Steady-state Free Precession (bSSFP) MRI, and aMRI have been employed to capture these subtle motions. In particular, exploring brain behavior with these modalities, and specifically the motion of the brain via aMRI, has showed promising results [1]. This approach enhances our understanding of how specific types or directions of motion within brain substructures correlate with various diseases or the effectiveness of surgical interventions. For example, in Chiari Malformation I (CMI), this method allows us to study how the brain and its substructures move [31, 32]. By analyzing the differences in brain motion before and after surgery, we can gauge the success of surgical treatments. In conditions like NPH, where excessive fluid restricts natural movement of brain regions, placing a shunt is a common treatment approach. Monitoring changes in the brain and the displacement of its substructures post-surgery helps in assessing the effectiveness of the treatment. Successful outcomes not only validate this approach but also suggest its potential applicability to other conditions in the future.

Nowadays, modern technologies like AI are becoming increasingly useful in exploring the complex factors underlying neurodegenerative diseases. Given the multifaceted nature of these diseases and the myriad factors that may influence them, AI and ML tools are invaluable [33]. They help us identify which morphometric factors or mechanical properties in specific brain regions play critical roles in the development of neurodegenerative diseases linked to contact sports and mild TBI such as CTE. By analyzing these variables, AI can pinpoint changes or patterns in certain areas that could serve as indicators or predictors of these impact-related neurodegenerative conditions.

In this work, it was proposed to demonstrate how studying the substructural mechanics of the human brain could contribute to understanding and preventing mTBI. Specifically, the impact performance of current sports helmets, particularly bicycle helmets, that employed different impact mitigation strategies was first investigated (Aim 1). Then, the effects of various impact mitigation technologies in sports helmets on the underlying brain substructure mechanics during helmeted impacts were examined (Aim 2). To understand the role of brain substructural motion in the biomechanics of neurodegenerative diseases such as NPH, the in vivo displacement of human brain substructures using dynamic amplified MRI mea-

surements was investigated (Aim 3). Finally, utilizing retrospective multimodal datasets from the DIAGNOSE CTE project, along with machine learning (ML) algorithms, it was evaluated whether blood and CSF biomarkers, as well as morphometric parameters from brain substructures, could successfully predict neurocognitive scores and neuropsychiatric metric assessments (Aim 4).

1.2 Aims

1.2.1 Aim 1: To Investigate the current state of bicycle helmets and test the efficacy of rotation-dominated impacts on bicycle helmets with rotation-damping systems

To advance our understanding of mTBI for diagnostic and preventative purposes, it was essential to expand our knowledge of brain substructural mechanics. To investigate the biomechanics of these substructures, head kinematic parameters were commonly used to evaluate injury risk and reflect the inertial response of the brain. To evaluate the effectiveness of current prevention strategies, such as helmets, in reducing impact energy and head kinematics, it was essential to investigate their impact on injury-related parameters. In this aim, we conducted a literature review to analyze drop test datasets of bicycle helmets with various impact mitigation systems, assessing their ability to mitigate head kinematics. Using an impact pendulum device, we proposed to experimentally test multiple bicycle helmets with different mitigation systems, assessing their performance through impacts at two velocities and four impact locations.

1.2.2 Aim 2: To investigate the effect of sports helmets on dynamical behavior of the brain substructures in helmeted impacts

The design of helmets used in contact sports previously focused on mitigating head kinematics by absorbing impact energy, without considering the role of brain substructure mechanics in injury mechanisms. It was imperative to investigate the effect of various mitigation systems in different helmet types on the dynamic behavior of brain substructures. In this aim, we investigated the effect of brain substructural mechanics on helmet design and performance. We examined different sports helmets to determine the dynamic behavior of brain substructures. We performed impact pendulum tests on helmeted dummies and simulated impact scenarios to extract nodal coordinates of both the brain substructures and the skull to calculate their relative displacements. Using the dynamic mode decomposition

(DMD) technique, we analyzed the modal behavior of the brain substructures.

1.2.3 Aim 3: To investigate In Vivo brain substructure displacement as indicators of ventriculoperitoneal shunt outcomes in NPH using aMRI

To better understand the effectiveness of shunt surgery in patients with NPH, it was essential to incorporate additional mechanical factors derived from image processing analysis. NPH is a particularly intriguing condition; despite the presence of excessive fluid, which typically suggests high pressure, these patients exhibit normal intracranial pressure. Thus, examining the success of surgery involved exploring additional factors beyond standard clinical assessments. The displacement and motion of brain substructures were seen as promising indicators. Our initial hypothesis indicated that successful surgery might result in increased displacement within specific brain regions. By comparing brain motion before and after surgery, we aimed to assess the impact of the shunt and its efficacy in treating NPH. Such analyses not only helped in understanding the direct outcomes of surgical interventions but also enhanced our broader comprehension of this disease. The findings could potentially inform treatment approaches for similar conditions in the future.

1.2.4 Aim 4: To identify key biomarkers and substructural MRI morphometric features for predicting neuropsychological outcomes in CTE using machine learning

TBIs and their resultant condition, CTE, can lead to severe long-term effects, significantly impacting patients' lives and ability to work. CTE, in particular, presents a unique diagnostic challenge as it remains impossible to definitively diagnose during a patient's lifetime. This limitation limits effective management and treatment strategies, underscoring the need for innovative approaches to uncover hidden patterns and contributing factors. To address this, this aim leveraged ML algorithms to analyze data from the DIAGNOSE CTE project. By utilizing a diverse range of features—including two sets of blood biomarkers, three sets of CSF biomarkers, and MRI morphometric features—this study aims to predict neurocognitive and neuropsychiatric metrics. These efforts not only strive to advance the understanding of CTE but also aim to provide critical insights into the relationships between biomarkers, brain morphometrics, and patient outcomes, potentially paving the way for improved diagnostic and therapeutic strategies.

Chapter 2

BACKGROUND

2.1 mild Traumatic Brain Injury (mTBI)

TBI, is one of the main causes of deaths and disabilities worldwide [5, 10] and it occurs when a sudden impact causes a damage to the brain [34]. The common causes of TBI are falls, motor vehicle crashes, traffic accidents, sports injuries and blast injuries [35]. Centers for Disease Control and Prevention (CDC) reported approximately 2.8 million TBI-related emergencies, hospitalizations, and deaths in the United States [5]. TBI is classified into three categories according to the severity and symptoms: Moderate-Severe TBI, Mild TBI (mTBI) and Symptomatic TBI [36]. Mild Traumatic Brain Injury (mTBI) is caused by head trauma from contact or acceleration/deceleration. mTBI is a prevalent neurological disorder, ranking third after migraines and herpes zoster in terms of incidence and second after migraines in terms of prevalence. Although most mTBI patients recover within a few weeks to months without any targeted treatment, around 15% of patients continue to experience debilitating symptoms even a year after the injury [37]. The patient is briefly unconscious or disoriented, but typically for only seconds to minutes, and may have amnesia for a short period of time [36, 37]. A Glasgow Coma Scale (GCS) score of 13-15 is required for diagnosis, with a score of 15 indicating true mild TBI [37, 38]. Patients may experience symptoms such as paleness, sweating, nausea, and difficulty with coordination [37].

2.2 mTBI Mechanism from Biomechanical Perspective

Elucidating the mechanisms of brain injury is a critical area of research that can significantly advance the development of techniques for predicting mTBI, improving protection devices, refining diagnostic tools, and identifying potential patterns in medical images or physiological tests. The study of mTBI mechanisms can improve our understanding of how and why brain injuries occur, leading to the creation of better prevention strategies and protective equipment. Moreover, accurate identification and diagnosis of mTBI can improve patient outcomes, and understanding the biomechanics of mTBI can aid in developing ef-

fective treatments. Additionally, investigating mTBI mechanisms can facilitate the design and evaluation of helmets and protective gear for athletes, military personnel, and other individuals at risk of mTBI.

To enhance our comprehension of the physical mechanisms of mTBI, experts have examined the mechanics and deformation of the brain during impacts. This has been accomplished through collecting human head impact data [39–43] or utilizing in-depth computational models of the brain-skull system to simulate impact scenarios [39–48]. Studies that have assessed the severity of brain injuries by simulating head impact kinematics in a computational model have demonstrated that the peak principal strain represents the severity of the injury in various contact sports [43, 49]. As a result, besides conventional helmet testing and evaluation methods that examine the rotational and linear kinematics of the head [24, 50–60], experts have proposed examining the mechanical behavior of the brain, which is closely associated with the rotational kinematics of the head during impacts. This approach can offer valuable insights into helmet effectiveness and improve our understanding of how helmets can reduce head injuries in different types of impacts [21, 60–62].

Apart from analyzing the brain deformation as a brain injury metric, spatial and temporal variations in brain deformation characteristics have been hypothesized to have injury-related implications [63–67]. This has involved analyzing the mechanical behavior of human brain tissue through imaging techniques [15], computational simulations [16, 68, 69], and mechanical impacts to the brain [16, 39]. These studies have shown that certain regions, particularly periventricular regions such as the corpus callosum (CC), experience strain concentrations [15], localized vibration modes [16], and higher strains [39, 68, 69] during impacts. It is believed that when a force impulse is applied to the head, shear waves inside the brain propagate and attenuate differently in various regions [16, 70], making certain regions such as the white matter and CC more vulnerable to injury [71]. The pattern of these shear waves is hypothesized to be affected by rigid structures such as stiff ventricular or membranous structures in the brain [15, 72]. Furthermore, it has been observed that the brain's finite element (FE) model shows nonlinear behavior during impacts, particularly around the deep white matter [17]. Investigating the biomechanics of the substructures of the brain FE model during impacts has revealed crucial frequency-dependent and local-

ized phenomena that have been associated with injury outcomes [16, 17]. By conducting tagged MRI during mild head acceleration and analyzing 3D strain fields using dynamic mode decomposition (DMD), researchers have been able to identify the natural modes and frequencies of 3D deformation of the human brain in vivo [73]. These studies have revealed fundamental oscillatory modes of deformation at damped frequencies near 7 Hz in neck rotation and 11 Hz in neck extension, and strain concentrations in deep regions of the white matter and distinct modal frequencies in the CC using DMD technique with FE simulations [16, 17, 73]. Additionally, investigating the frequency response of the brain model's substructures during an impact has shown that the CC experiences higher deformation at certain frequencies, potentially leading to mTBI [16].

Given the vulnerability of certain brain substructures such as the corpus callosum (*e.g.* CC) to strain concentration caused by localized, multimodal behavior, it is important to investigate the impact of helmet design on the frequency response of brain structures. While studies on helmet performance have mainly focused on head motion and kinematics [23, 24] rather than substructural brain mechanics, this may be due to the computational complexity of large-scale models for helmet optimization. Although attempts have been made to analyze helmet efficacy by examining brain strain levels during impact, no design optimization has been proposed. However, analyzing brain tissue strain levels alone is not sufficient for a comprehensive understanding of the helmet's role in the brain injury mechanism [11, 12]. Regional-dependent strain criteria have shown a correlation between concussion diagnosis and maximum principal strain, emphasizing the need to consider substructural mechanics of the brain in concussion studies, particularly with regard to vulnerable brain regions[13, 14].

2.3 Sport-related mTBI; Protective Strategies and Missing Factors

mTBI, and more specifically sport-related mTBI, risks the health of hundreds of thousands of athletes every year [74, 75], leading to, in certain cases, long term disability and neurocognitive deficits [36]. Helmets have been used in several contact sports as a protection strategy to prevent or reduce the severity of mTBI. Although helmets have been shown to significantly reduce the risks of severe head injuries in football [76], bicycling [50, 77], skiing [78], and other sports, their effectiveness in mitigating the risks of milder forms of TBI is still being investigated [79–81].

Sports helmets vary in shape, mechanical properties, and testing criteria depending on the specific contact sport [82–85]. Football and hockey helmets typically have hard shells and thicker but softer liners made of polyurethane (PU) and vinyl nitrate (VN) foams [76, 82, 83, 86]. Bicycle and ski helmet liners, on the other hand, typically consist of Expanded Polystyrene (EPS) foam [84, 85]. Safety performance is evaluated by studying the head's kinematics using laboratory impact setups. Hockey and football helmets are tested with rotational kinematics setups, such as an impact pendulum device and a horizontal impactor, while ski and bicycle helmets undergo vertical drop-test setups for linear kinematics. Different standards, such as those set by the Consumer Product Safety Commission (CPSC) [23, 87] for bicycle helmets and the National Operating Committee on Standards for Athletic Equipment (NOCSAE) [88] for football helmets, determine the criteria helmets must pass during testing. Traditional helmet designs focus on reducing linear kinematics during impacts. However, due to evidence suggesting the role of rotational head kinematics in head injuries and concussion mechanisms, new helmet designs have been proposed to mitigate head rotation. Incorporating rotational kinematics into helmet testing standards and evaluating different helmet types has been encouraged [7, 9, 18–22, 89, 90]. Experimental studies and computational simulations have shown that these mitigation systems can reduce rotational kinematics and brain strain [50]. Despite these advancements, mild traumatic brain injury (mTBI) remains prevalent in contact sports [89, 91], highlighting the need for improved helmet designs, testing criteria, and design frameworks. Understanding the mechanisms of brain injury is crucial for developing more effective helmets.

MRI Application in Studying Brain Mechanics and the contribution of amplified MRI

MRI has emerged as a valuable tool for studying brain mechanics, offering non-invasive imaging capabilities that allow researchers to investigate the structural and functional properties of the brain. By using MRI techniques, such as diffusion tensor imaging (DTI) [92], researchers can assess the microstructural integrity of white matter fibers and investigate how they contribute to brain mechanics. This provides insights into the connectivity and organization of brain networks, helping to understand the underlying mechanisms of brain function and dysfunction [92].

Another application of MRI in studying brain mechanics is the assessment of cerebral

blood flow and perfusion. By employing techniques like arterial spin labeling (ASL) [93], researchers can measure regional blood flow and quantify perfusion parameters in different brain regions. These measurements enable the study of hemodynamic changes associated with brain activity and provide insights into how blood flow dynamics influence brain mechanics and function.

MRI is also utilized to investigate brain deformation and biomechanical properties during various physiological processes and pathological conditions. Through techniques like MRE, researchers can assess the mechanical properties of brain tissues, such as stiffness and elasticity, by measuring their response to mechanical waves [94–98]. This allows the characterization of brain tissue properties and helps in understanding the impact of external forces on brain mechanics, such as in traumatic brain injury or neurodegenerative diseases. These studies contribute to the advancement of our knowledge about brain mechanics and pave the way for potential clinical applications in the future.

MRI plays a crucial role in studying brain mechanics by enabling the assessment of brain deformation and motion during various mechanical processes. Techniques like cine MRI [99, 100] allow researchers to observe brain dynamics in response to external stimuli or internal processes, providing valuable insights into the mechanical behavior of the brain. Cine Balanced Steady-state Free Precession (bSSFP) MRI, or cine MRI, is a valuable imaging technique for visualizing intrinsic brain motion [101, 102]. It provides enhanced image contrast to highlight anatomical details, useful especially in observing significant movements in lower brain areas like the cerebellar tonsil and hindbrain [31, 102]. Cine MRI captures time-resolved data synchronized with the patient's cardiac cycle using an electrocardiogram or pulse oximeter, populating the k-space which holds spatial frequency information. Each frame corresponds to a specific cardiac phase, allowing for the creation of video sequences of brain movement during one heartbeat [31, 103, 104]. Although cine MRI is an advanced imaging method capable of capturing brain motion, its limitations in spatial noise and resolution restrict the analysis of intrinsic brain motion to the lower regions of the brain, rendering comprehensive motion characterization across the entire brain unfeasible [102, 104]. By analyzing the displacement and deformation of brain structures, researchers can investigate how mechanical forces and interactions affect brain function and connectivity. These

studies contribute to our understanding of brain biomechanics and have implications for the diagnosis and treatment of neurological disorders related to mechanical abnormalities.

2.4 Deep Learning Frameworks in Predicting Injury Pattern

With recent advancements in ML algorithms, there is growing interest in leveraging these techniques to enhance the analysis of medical images [105] and improve the assessment of neurodegenrative conditions [105–107]. Deep learning algorithms, a subset of machine learning, have revolutionized various fields by automatically learning complex patterns and features from large datasets [105]. These algorithms provide an objective and quantitative approach [108] to evaluate medical images and by analyzing a wide range of MRI features, these algorithms can generate quantitative metrics that correlate with injury, enabling more accurate and consistent assessments [105]. In the context of MRI analysis for mTBI, deep learning algorithms can be trained to extract meaningful information from MRI scans and aid in the identification of injury-related patterns. These algorithms can learn to analyze image features, such as regions of abnormal shape or texture, structural abnormalities, and biomarkers that are associated with mTBI.

Prior research has examined mTBI, focusing on its associated structural alterations, injury patterns within brain structures, and their impact on various neurological parameters [109–113]. To investigate these aspects, advanced imaging techniques, including fractional anisotropy (FA) [109], MRI [110], computed tomography (CT) [111], diffusion tensor imaging (DTI) [112], and diffusion-weighted MRI (dMRI) [112], have been employed. In conjunction with these imaging modalities, ML algorithms, such as convolutional neural networks (CNN) [113], have been utilized to analyze and interpret the acquired data. These studies have shed light on the complex relationship between TBI and the alterations observed in brain structure, facilitating a deeper understanding of the underlying mechanisms and potential diagnostic and prognostic applications.

The use of machine learning algorithms for the detection of mTBI using MRI has gained significant attention. Researchers have explored various features derived from MRI scans to differentiate between normal brains and those affected by mTBI. These features include volumetric measurements of brain structures [114], texture analysis to capture variations in

tissue texture [115, 116], diffusion parameters to assess white matter integrity [117], functional connectivity analysis to examine brain network disruptions, and the utilization of deep learning models to automatically extract relevant features. By combining these features with machine learning algorithms, researchers aim to develop accurate models for the detection and classification of mTBI using MRI. Ongoing research is focused on refining these approaches to enhance their accuracy and clinical utility, with the goal of improving mTBI diagnosis and patient management.

Chapter 3

TO INVESTIGATE THE CURRENT STATE OF BICYCLE HELMETS AND TEST THE EFFICACY OF ROTATION-DOMINATED IMPACTS ON BICYCLE HELMETS WITH ROTATION-DAMPING SYSTEMS

3.1 Introduction

TBI is a major cause of death and disability, affecting millions of people every year in the U.S. [5]. Sport-related TBIs which annually affects about 300,000 to 3.8 million people in the U.S. makes up a large portion of these TBI cases [5, 118]. Cycling has been associated with a significant number of sports-related head injuries [60, 119], and its growing popularity has resulted in an increase in both bicycle-related injuries and fatalities [120, 121]. According to the American Association of Neurological Surgeons, cycling injuries estimated 85,389 of the 446,788 sports-related head injuries reported in the emergency rooms in 2009 [122, 123]. To mitigate the risk of severe head and brain injuries, bicycle helmets are currently the best protective strategy [53, 124–126], and extensive attention has been given to their design due to evidence of their effectiveness in reducing fatality rates [127]. As a result, there has been substantial focus on the development of protective equipment for cyclists [128, 129].

Over the years, bicycle helmet designs have employed similar approaches to combating TBIs and have consistently utilized similar, if not the same, materials. These helmets are usually made up of a hard rigid polycarbonate shell to prevent skull fracture and contain a softer liner to absorb energy upon impact and ultimately mitigate mild TBI (mTBI) [130]. Traditional expanded polystyrene (EPS) liners are primarily designed and manufactured to dampen the impacts and reduce the head impact force [54]. Conventional bicycle helmets have been shown to mitigate linear acceleration which is a requirement by bicycle helmet different safety standards [52, 131, 132]. In these tests, helmets are placed on a sensor-instrumented headform and dropped onto a steel anvil coated with adhesive-backed 80-grit paper [23, 131–133], and the head kinematics then measured. As outlined in these mandatory safety standards, the linear acceleration of the headform should not exceed a

certain limitation (*e.g.* 300g and 250g for CPSC and AS/NZS 2063, respectively [134, 135]). However, cyclists often fall off their bicycles and impact their heads at angles that are not always direct and usually varies between 30°- 60°[136, 137]. These impacts not only can cause linear acceleration but can also result in rotational acceleration due to the tangential forces to the head [132, 138] which has been shown as an important contributor in causing large shear strains in the brain tissue, which could potentially result in mTBI [139–143].

Recent technologies have been introduced to mitigate the head's rotational kinematics through rotation-damping systems. These systems include spherical slip interfaces [23], collapsible and expandable structures [52, 54, 56] in the liner structure. Multi-directional Impact Protection System (MIPS) is a relatively new concept that introduces a slip liner inside the helmet to mitigate rotational impact forces by allowing the helmet and head to slide during impact [144]. Other technologies, such as WaveCel and Koroyd, utilize a collapsible cellular structure that absorbs the force of impact and minimizes the energy transferred to the head [23, 52]. Although these advancements are opening the door to the future of cycling safety and TBI prevention, an overview of the effectiveness of these novel helmets in mitigating impacts as compared to the conventional helmets is lacking.

The goal of this chapter is to investigate the effectiveness of various impact mitigation systems in reducing head kinematics during bicycle accidents. A comprehensive literature review was be conducted to analyze drop test datasets of bicycle helmets and to investigate the kinematic-based injury metrics including PLA, PRA, and GAMBIT between these helmet types to analyze their effectiveness in TBI prevention. Additionally, experimental tests were conducted using an impact pendulum device to evaluate the performance of multiple bicycle helmets with different mitigation systems. The impact tests were be conducted at four different locations and two different velocities.

3.2 Current State of Bicycle Helmets

To investigate the current state of bicycle helmets, we reviewed articles that met our selection criteria and included essential factors. The relevant articles were collected from the electronic databases PubMed and SCOPUS, based on criteria that included the application of helmet drop tests on either side impacts, as well as the inclusion of kinematic parameters

such as peak linear acceleration (PLA), peak rotational acceleration (PRA), peak rotational velocity (PRV), and impact velocity. The inclusion criteria and data extraction of the papers were cross-checked by three independent reviewers. Having identified all the relevant articles in the two databases, we retrieved the following information for each of the helmet tests from each paper: (1) Type of mitigation technology in the bicycle helmet, (2) PLA, PRA, and PRV, (3) Drop test impact velocity, (4) Anvil angle, (5) Headform model, (6) Presence or absence of the neck surrogate in the headform, (7) Impact location.

3.2.1 Types of Impact Mitigation Technologies in Bicycle Helmets

The helmets collected and analyzed in this paper were mainly organized into two different categories: (1) Conventional helmets, which only use one layer of EPS or Expanded Polypropylene (EPP) as a liner. (2) Helmets with a mitigation system that use one of the following materials or technologies in the liner or the overall design: *MIPS*, *Shear Pad Inside (SPIN)*, *Omni-Directional Suspension (ODS)*, *WaveCel*, *Angular Impact Mitigation (AIM)*, *Koroyd* and *Hövding* [50].

Conventional bicycle helmets are typically composed of an ABS plastic outer shell, an EPS or EPP foam liner, and an inner layer of soft foam padding. However, various technologies have been developed to enhance helmet safety. MIPS (Multi-directional Impact Protection System) reduces rotational kinematics of the head during an impact by allowing sliding between the helmet and head [23, 57, 144]. SPIN (Shearing Pad INside) replaces comfort padding with specially developed silicone pads that can shear in any direction to produce the same effect as a moving slip liner [23, 57, 144]. ODS (Omni-Directional Suspension) utilizes two EPS liners connected by an array of elastomeric dampers to isolate impact energy from the brain and deflect angular impacts [144]. AIM (Advanced Impact Mitigation) is a cellular structure technology that uses an elastically suspended aluminum honeycomb liner to absorb linear and angular acceleration through in-plane deformation [23, 52]. Collapsible structure mitigation systems that were considered include WaveCel, made from a cellular copolymer material that flexes and glides to absorb and redirect impact energy while providing rotational suspension, and Koroyd, which utilizes thousands of co-polymer extruded tubes that create a crumple zone for minimal energy transfer to the head [23, 57, 145]. Additionally, Hövding, is an expandable helmet that employs air

pressure as a means of protection and uses high-rate micro-electrical-mechanical sensors to detect a collision and expand to protect the rider's head before impact [56].

3.2.2 Post Processing of the Extracted Data

To be able to compare all the extracted headform kinematics whose drop tests were performed at anvil angles ranging from 0° to 60° , an impact velocity normalization step was performed so that the velocity vector would be perpendicular to the anvil:

$$V_N = V cos\theta \tag{3.1}$$

where V_N is the impact velocity perpendicular to the anvil plate with angle θ.

Next, the K-means algorithm from Python's machine learning library Scikit-learn [146] was used to separate the data into two clusters based on V_N. The two clusters centers were selected for low and high V_N and the impact tests with V_N within ±10% of the cluster centers were retained for each group.

The kinematic-based injury metrics including PLA, PRA, and GAMBIT were then compared between the helmets within each group of low and high V_N. Here, we used GAMBIT since it can be directly calculated from the available kinematics data, and can be used as injury criteria investigating the combined effect of linear and rotational impulses [147–149]. The GAMBIT value in its general form can be written as:

$$G = max([(\frac{a(t)}{a_c})^n + (\frac{\alpha(t)}{\alpha_c})^m]^{1/s}) \tag{3.2}$$

where $a(t)$ and $\alpha(t)$ are translational and rotational accelerations at time t, respectively. n, m, and s are empirically derived constant parameters that were fitted to experimental data [148]. a_c and α_c are thresholds derived for a pure translational and rotational acceleration, respectively. Here, we selected n = m = s = 2, a_c = 250 g, and α_c = 25000 rad/s^2 as was suggested by [148]. It should be noted that when analyzing GAMBIT, $G = 1$ correspond to a 50% probability of Abbreviated Injury Scale (AIS)>3 [148].

3.2.3 Statistical Analysis

In the next step, we investigated the collected drop test results for the following parameters: (1) Presence or absence of the mitigation system, (2) Effect of mitigation type, and (3) Presence or absence of the neck surrogate. To analyze the effect of the presence of the

mitigation system, PLA, PRA, and GAMBIT at low and high V_N were compared between the conventional helmets and helmets that used a mitigation system. We then restricted our data to tests that had either included or excluded the neck surrogate in their experiments and performed the same analysis.

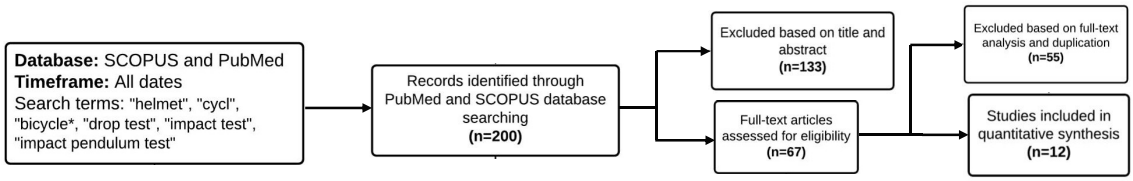

Figure 3.1: Flowchart outlining the selection of relevant studies.

3.3 Impact of Mitigation Technologies on Injury Criteria: Key Findings and Implications from Literature Review

A flowchart is used to show the procedure of the literature review and the articles that were excluded and included (Fig. 3.1). The PubMed database search resulted in 53 articles pertaining to bicycle helmet testing and the SCOPUS search resulted in 147 articles. Each resulting article was screened and excluded if the title and abstract were not deemed relevant, which resulted in the removal of 133 studies from the data pool. The remaining 67 articles were screened for the necessary inclusion criteria, such as PLA, PRV, PRA. In the end, 12 articles were eligible for inclusion in this chapter. A total of 148 bicycle helmet drop tests were collected from the selected papers. 88 of these drop tests were performed on the conventional helmets which only used one layer of EPS or EPP as a liner in their design (Fig. 3.2). The remaining 60 of the drop tests were performed on MIPS, SPIN, ODS, WaveCel, AIM, and Koroyd helmets and Hövding protective gear (Fig. 3.2). The impact velocities of the tests varied between 3.4 m/s and 7.7 m/s. After applying the k-mean clustering algorithm [146], we found $V_N = 4.2$ m/s and $V_N = 5.9$ m/s to be the cluster centers of low and high impact velocities, respectively (Fig. 3.2). Impact tests outside the 10% of the cluster centers were removed, resulting in 75 conventional and 51 mitigation type helmet drop tests. Among the studied literature, four different types of neck-headform attachments were observed: **1-** No neckform was attached to the head (N in Fig. 3.2), **2-** The headform was attached to a ball-arm neck (Ball arm in Fig. 3.2), **3-** The headform was

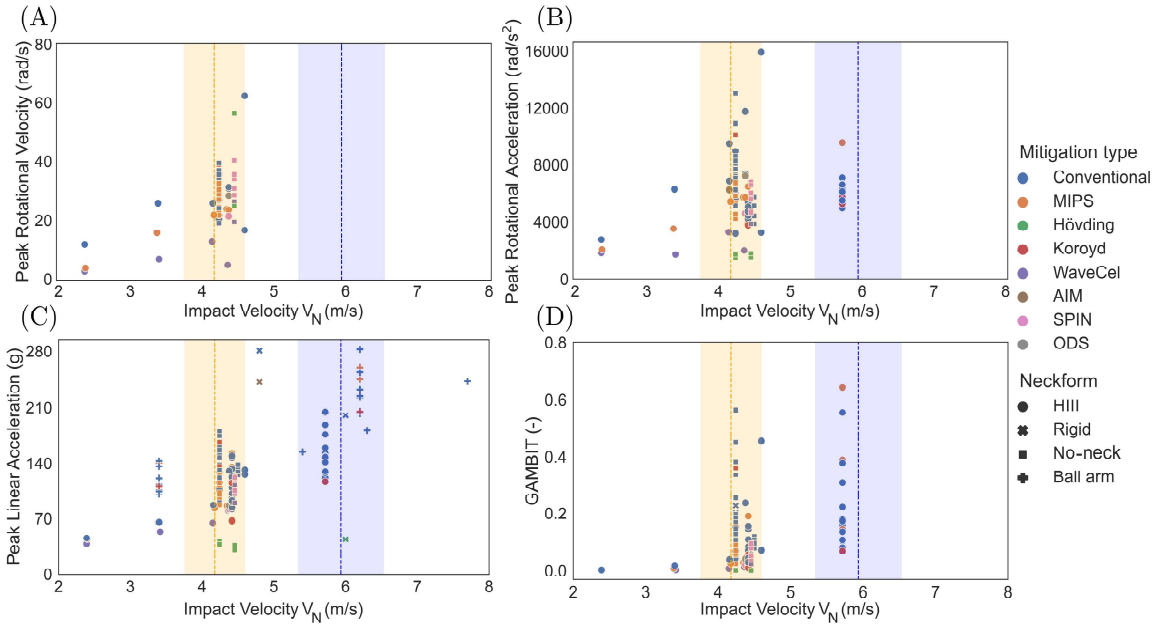

Figure 3.2: Head kinematics and GAMBIT value at low and high clustered impact velocity (V_N) for all bicycle helmets. (A) Peak rotational velocity, (B) peak rotational acceleration, (C) peak linear acceleration, (D) and GAMBIT in bicycle helmets with different mitigation systems which were tested on headforms with or without a neck surrogate. Dashed lines indicate the cluster centers of low and high V_N and the shaded areas show those impact tests in which the velocities are within 10% of the cluster centers. No data were available in the high V_N range for peak rotational velocity.

attached to a rigid neck (Rigid in Fig. 3.2), and **4-** The headform was attached to a Hybrid III 50th-percentile male neck (HIII neckform, Fig. 3.2).

We first analyzed the effect of the presence or absence of the impact mitigation systems on the resultant kinematics and the associated injury metrics during drop tests (Fig. 3.3). We observed that at low V_N (4.2 ± 0.8 m/s) drop tests, the bicycle helmets with a mitigation system, on average, had significantly lower PLA, PRA, and GAMBIT values compared to conventional helmets (approximately 20.2%, 21.8%, and 52.6% lower respectively, Fig. 3.3(A-C), $p < 0.01$). Here, the low V_N (4.2 ± 0.4 m/s) drop test experiments of the bicycle helmets with a mitigation system resulted in average PLA, PRA, and GAMBIT of 100.1 ± 30.4 m/s, 5043.6 ± 1740.8 rad/s^2, and 0.062 ± 0.066, respectively. The conventional bicycle helmets, on the other hand, experienced an average PLA, PRA and GAMBIT of 125.5 ± 26.9 m/s, 6448.8 ± 1985.6 rad/s^2, and 0.131 ± 0.111, respectively. In the drop

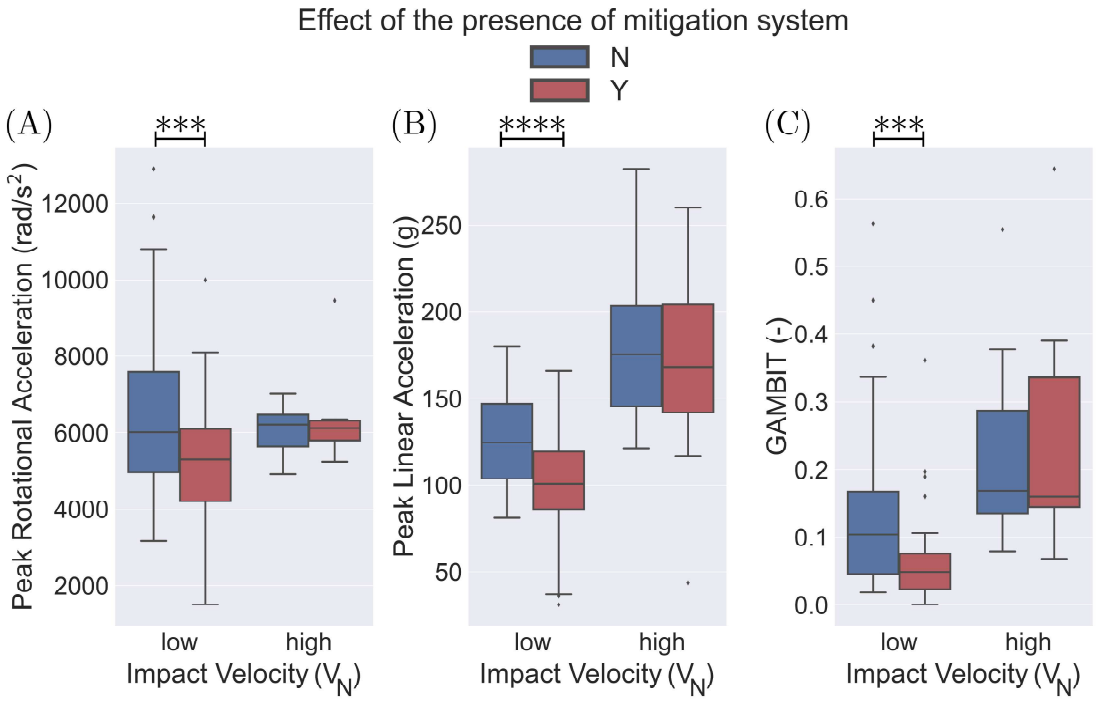

Figure 3.3: Effect of the presence or absence of the mitigation system on bicycle helmet performance in impact tests. Helmets using a mitigation technology had a significantly lower (A) PRA, (B) PLA, and (C) GAMBIT at low V_N (4.2 ± 0.4 m/s) as compared to the conventional helmets ($p < 0.001$). No statistical significance was observed in high V_N (5.9 ± 0.6 m/s) drop tests between the two different helmet types. ♦ shows the outlier data.

tests at high V_N (5.9 ± 0.6 m/s), we did not observe any statistically significant differences between the kinematics of the bicycle helmets with and without the mitigation systems (Fig. 3.3(A-C)). The value of PLA, PRA, and GAMBIT for conventional helmets were in average 179.6 ± 41.6 m/s, 6075.7 ± 548.9 rad/s^2, and 0.215 ± 0.126, respectively.

One crucial difference in the different drop tests we considered for this paper was the presence or absence of the neck surrogate. We found that 65 experiments were performed on headforms with an attached neck surrogate and the remaining 52 were tested on headforms without a neck component. 8 helmets were tested with a rigid neck attached to the headform and 23 were tested while being attached to a ball arm. In our analysis, we considered the headforms attached to a ball arm in the no-neck group since in both of these groups the headform could rotate without resistance at the time of the impact. Our first finding was that in almost all of the categories, tests without a neck component experienced a higher

PLA, PRA, and GAMBIT on average as compared to the group with an attached neck component (Fig. 3.4 and Fig. 3.5). Here, in the low V_N (4.2 ± 0.4 m/s) drop tests, PLA, PRA, and GAMBIT, on average, were approximately 10.3%, 7.3%, and 59.3% higher in the no-neck group, respectively. At high V_N (5.9 ± 0.6 m/s) drop tests, PLA was on average 51.0% higher in the no-neck group. It should be noted that no PRA values were available at high V_N (5.9 ± 0.6 m/s) drop tests for the no-neck group. Next, we analyzed the effect of the presence of an impact mitigation system in each of the neck and no-neck groups. We observed that for the low V_N (4.2 ± 0.4 m/s) tests, in the no-neck group the bicycle helmets with a mitigation system had a significantly lower PLA (24.7%), PRA (27.5%), and GAMBIT (59.7%) as compared to the conventional bicycle helmets (Fig. 3.4, $p < 0.001$). Whereas, in the neck-included group, only PLA (13%) and GAMBIT (36.2%) were significantly lower in the helmets with a mitigation system (Fig. 3.5, $p < 0.05$). Additionally, we did not observe any statistically significant differences of PLA between the helmet models at high V_N (5.9 ± 0.6 m/s) drop tests. No data points were available for PRA and GAMBIT in the no-neck group at high V_N (Fig. 3.4(A-C)).

In the next step, we investigated the efficacy of the different mitigation technologies by comparing PRA, PLA, and GAMBIT of each specific mitigation technology with conventional bicycle helmets (Fig. 3.6). Here, we only considered helmet types with at least 4 data points for the comparison. We found that among the helmets that used rotation-damping based technologies, only MIPS had approximately 16.8% and 49.3% lower PRA and GAMBIT at low V_N (4.2 ± 0.4 m/s) as compared to the conventional helmets, respectively (Fig. 3.6(A,C), $p < 0.05$). While SPIN helmets had on average lower PLA, PRA, and GAMBIT of about 14.5%, 11.9%, and 53.8%, respectively, we did not find any statistically significant differences in these helmets as compared to the conventional ones.

Next, we analyzed the performance of helmets with collapsible liner structures. Helmets based on the WaveCel technology had a significantly lower PLA, PRA, and GAMBIT of approximately 31.0%, 46.6%, and 81.1% at low V_N (4.2 ± 0.4 m/s) as compared to the conventional helmets, respectively (Fig. 3.6(A-C), $p < 0.05$). Whereas, Koroyd did not show any statistical differences compared to the conventional ones (Fig. 3.6(A-C), $p < 0.05$). Compared to the investigated helmets in the literature, the Hövding protective gear had the best

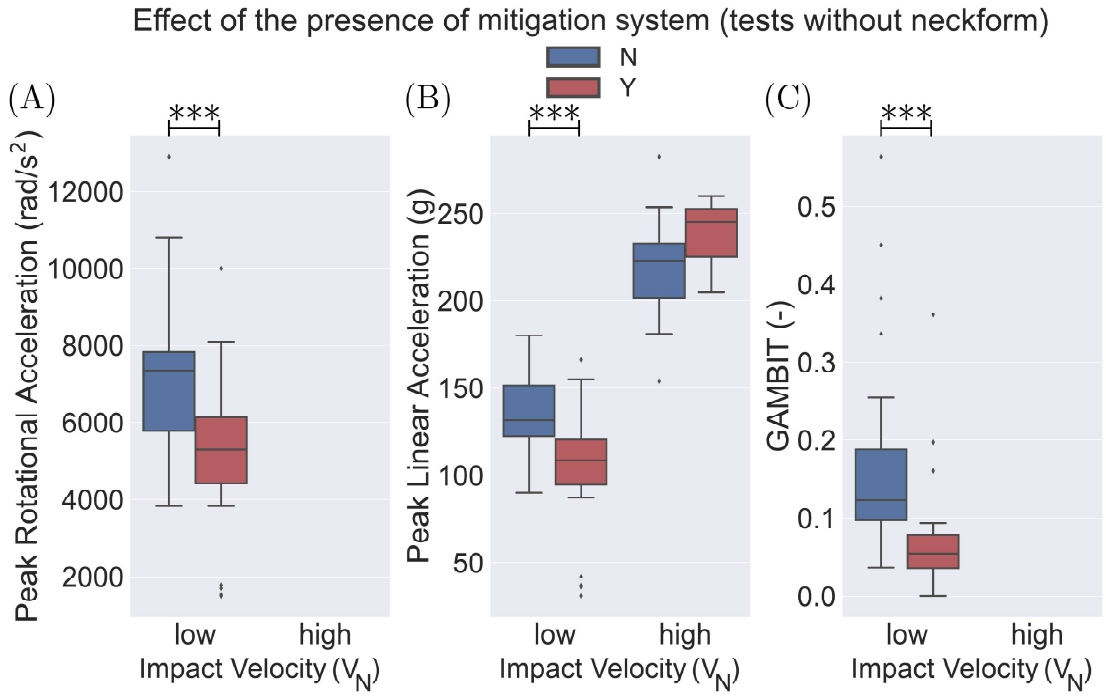

Figure 3.4: Effect of the presence of the mitigation system on bicycle helmets that were tested on headforms without a neck surrogate. Helmets with a mitigation technology had a significantly lower (A) PRA ($p < 0.001$), (B) PLA ($p < 0.001$), and (C) GAMBIT ($p < 0.001$) in drop tests at low V_N (4.2 ± 0.4 m/s). No statistical significance was observed in PLA at high V_N (5.9 ± 0.6 m/s). In high V_N, no data were available for PRA and GAMBIT. ♦ depicts the outlier data.

performance in the analyzed kinematic based injury metrics with PLA, PRA, and GAMBIT of about 70.9%, 74.8%, and 99.5% lower than the conventional helmets ($p < 0.0001$). At high V_N (5.9 ± 0.6 m/s), no statistical significance observed when we compared PRA, PLA, and GAMBIT between the conventional and each of the other helmet types (Fig. 3.6(A-C)). It should also be noted that, for high V_N (5.9 ± 0.6 m/s) we did not have data points for PRA, and GAMBIT values of SPIN, WaveCel, and Hövding protective gears.

To investigate the effect of headform orientation at the time of impact, as well as the presence or absence of the neckform, we clustered the data according to the impact angular momentum (H_{Impact}) and checked the rotational acceleration of the helmets (Fig. 3.7). After removing the outlier data, we found $H_{Impact} = 3.0 \pm 0.5$ kgm^2/s to be the cluster center. This narrowed the data from the literature to 79 tested helmets within the range of $H_{Impact} = 3.0 \pm 0.5$ kgm^2/s (Fig. 3.7(A)). Then, we analyzed the effect of the mitigation

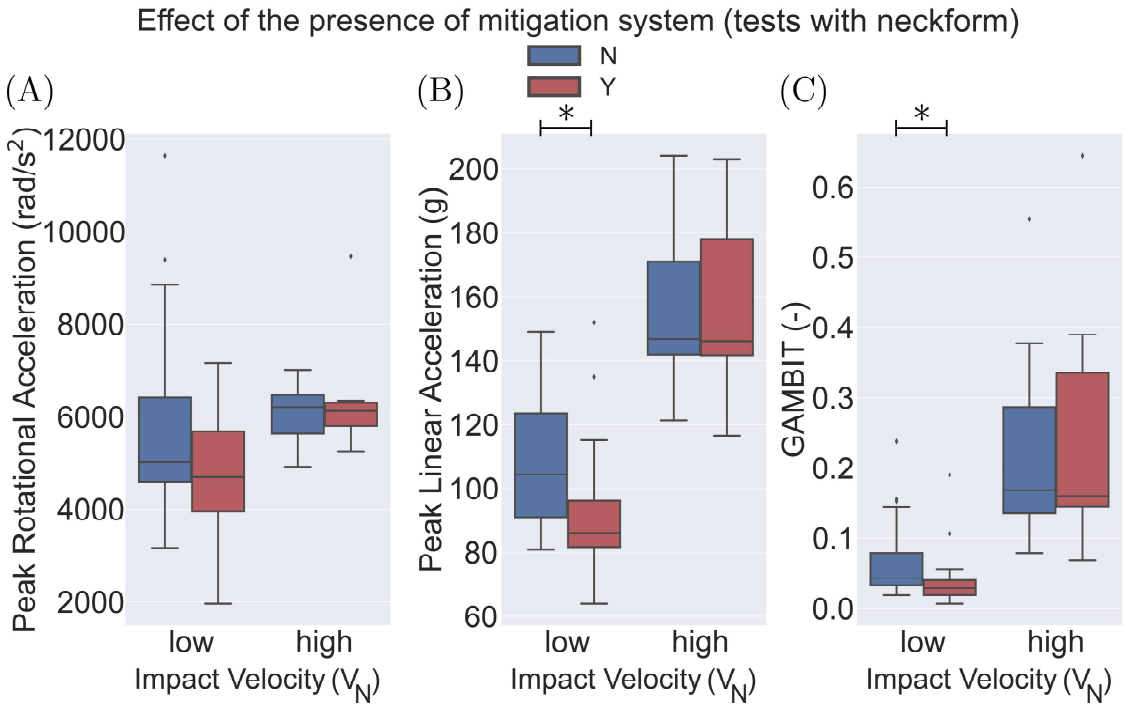

Figure 3.5: Effect of the presence of the mitigation system on bicycle helmets that were tested on headforms with a neck surrogate. (A) No statistical significance was observed in PRA between the two groups at both low and high V_N (5.9 $\pm$ 0.6 m/s) drop tests of neck included groups. Helmets with a mitigation system had a significantly lower (B) PLA and (C) GAMBIT at low V_N as compared to the conventional helmets ($p < 0.05$). No statistical significance was observed for PLA and GAMBIT at high V_N (5.9 $\pm$ 0.6 m/s). ♦ depicts the outlier data.

system on PRA . We observed that within $H_{Impact} = 3.0 \pm 0.5$ kgm^2/s, the PRA of the helmets that used a mitigation system was approximately 31% lower compared the conventional helmets ($p < 0.0001$; Fig. 3.7(B)). Next, we separately analyzed the PRA of the groups with and without the neckform. We observed in both groups that the PRA of the helmets with a mitigation system was significantly lower compared to the conventional ones ($p < 0.01$; Fig. 3.7(B)). Finally, within the range of $H_{Impact} = 3.0 \pm 0.5$ kgm^2/s, we analyzed the performance of each of these mitigation technologies against the conventional helmets. We observed that within this H_{Impact} range, Hövding protective gear had the best performance, with a lower PRA of approximately 78% in comparison to the conventional helmets ($p < 0.0001$; Fig. 3.7(C)). WaveCel with a lower PRA of about 58% as compared to the conventional helmets was the next best performing technology in PRA that followed Hövding

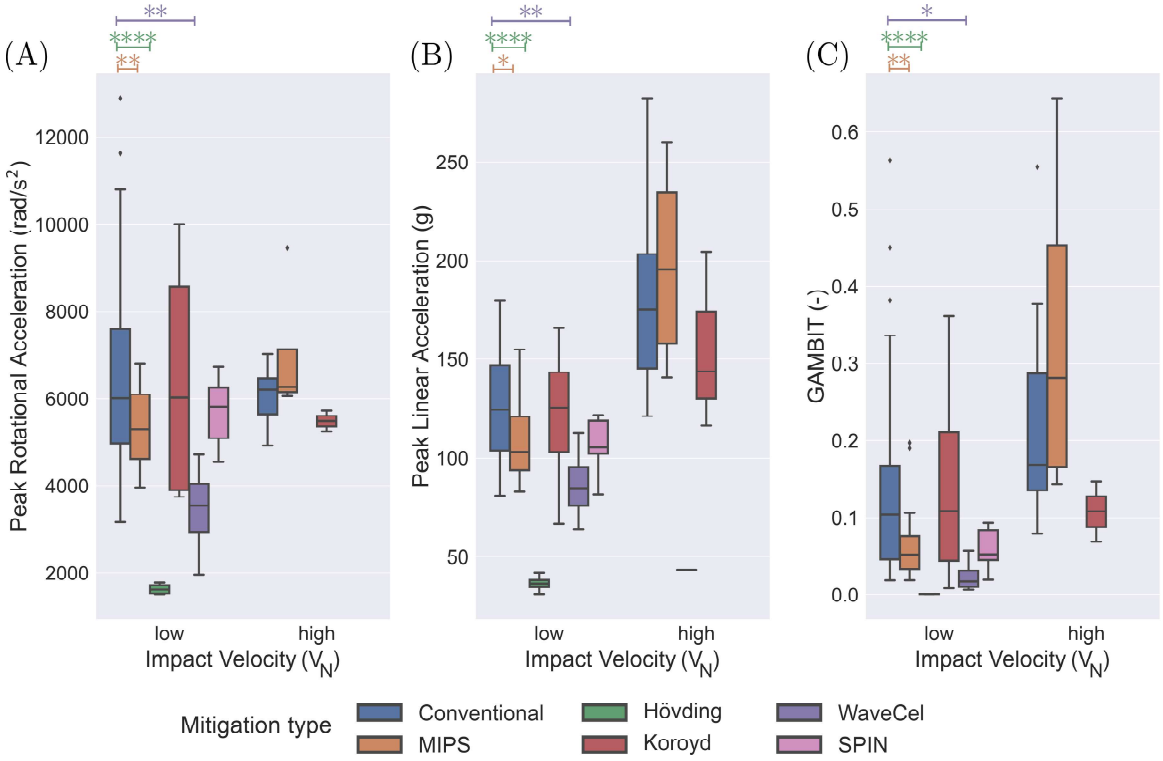

Figure 3.6: Effect of different mitigation systems in drop tests at low (4.2 ± 0.4 m/s) and high (5.9 ± 0.6 m/s) V_Ns. (A) Compared to the conventional bicycle helmets, PRA was significantly less in WaveCel ($p < 0.0001$), SPIN ($p < 0.05$), Hövding ($p < 0.001$) and MIPS ($p < 0.05$) at low V_N drop tests. (B) Compared to the conventional bicycle helmets, PLA was significantly less in Hövding ($p < 0.0001$) and WaveCel ($p < 0.05$) in drop tests at low V_N. (C) GAMBIT was significantly less in Hövding ($p < 0.001$), WaveCel ($p < 0.05$) and SPIN ($p < 0.05$) compared to the conventional ones in low V_N drop tests. No statistically significant differences were observed at high V_N drop tests between the conventional helmets and other technologies. ♦ depicts the outlier data.

($p < 0.001$; Fig. 3.7(C)). Helmets with a dedicated rotation-damping technologies including MIPS and SPIN also had a significantly lower PRA of approximately 27% ($p < 0.001$) and 22% ($p < 0.05$) as compared to the conventional helmets, respectively (Fig. 3.7(C)).

3.4 Key Takeaways from Literature and Contributions

Overall, we found that new protective gear technologies, including MIPS, WaveCel, and Hövding, significantly reduced headform impact metrics at low velocities. The MIPS helmets had significantly lower PRA, PLA, and GAMBIT values compared to conventional helmets due to their dedicated rotation-damping systems. In these helmets, the rotational damping mechanism works by adding slip liners underneath the main EPS liner, which

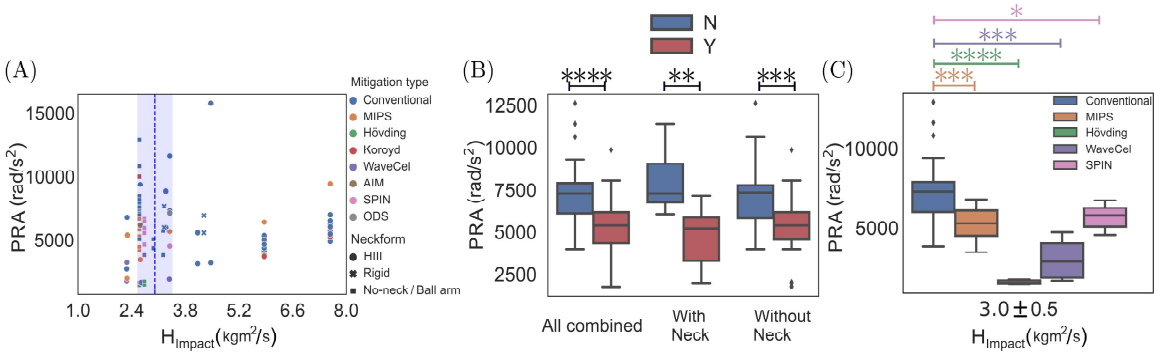

Figure 3.7: Effect of the presence of mitigation systems on the bicycle helmets after normalization with respect to the angular momentum H_{Impact}. (A) Peak rotational acceleration of the helmets with different mitigation technologies clustered with respect to H_{Impact}. (B) Presence of the mitigation system on bicycle helmets that were tested on headforms with and without a neck surrogate showed significantly less PRA as compared to the conventional helmets ($p < 0.001$). (C) Compared to the conventional bicycle helmets, PRA was significantly less in WaveCel ($p < 0.001$), SPIN ($p < 0.05$), Hövding ($p < 0.0001$) and MIPS ($p < 0.001$).

allows sliding between the head and the helmet during the impact [24, 144, 150]. It was also found that WaveCel helmets performed consistently better than all others except for Hövding, which had lower PLA, PRA, and GAMBIT values due to its large size and low stiffness. The significant mitigation of PRA by these helmets could be due to the folding properties of its cellular structure [23]. However, further tests are necessary to determine the potential neck injuries associated with Hövding helmets before their widespread use. Overall, the study highlights the potential benefits of including rotation damping technologies in helmets to reduce TBI risks during cycling accidents.

We examined the effect of mitigation systems on the safety of bicycle helmets. The data was clustered based on the normal impact velocity (V_N) and impact angular momentum H_{Impact}. The results showed that helmets with mitigation technologies have significantly lower PLA, PRA, and GAMBIT values than conventional helmets. The presence or absence of the neckform during the drop test experiment also affected the recorded kinematics. The findings highlight the importance of standardized testing and analysis of drop tests, but the study has some limitations such as lack of enough data points for some categories and different experimental procedures.

3.5 Efficacy of Bicycle Helmets in Response to Multi-Directional Rotational Forces

The number of bicycle-related accidents and fatalities is increasing globally despite the rising popularity of cycling [121, 151]. Head injuries are the most common among victims of bicycle accidents who sustain severe injuries [152, 153]. TBIs are often associated with high hospitalization rates and negative outcomes, leading to lifelong disability and mortality [53, 154–157]. Wearing a bicycle helmet has been found to effectively reduce the severity of head injuries, and many countries have specific standard tests that helmets must pass to be commercialized [132, 158, 159]. However, the current regulations only consider peak linear acceleration (PLA) and do not account for rotational kinematics [39, 160], which is widely acknowledged to be correlated with damage to brain tissue. In relation to bicycle helmets, the most commonly used injury criteria that are based on kinematic-injury criteria include PLA [50, 51, 56, 57, 60, 161, 162], peak rotational velocity (PRV) [23, 54, 136, 144], peak rotational acceleration (PRA) [50–52, 54, 161], head injury criterion (HIC) [52, 53, 56, 163], and brain injury criterion (BrIC) [23, 143, 144]. To gain insights into the mechanisms behind TBIs, computational finite element (FE) models of the human head are used as a powerful tool to investigate the response of the intracranial region to head trauma [44, 164–169]. FE models have also been employed to compute brain strain and strain rate to evaluate the effectiveness of sport helmets in preventing tissue-level injuries associated with TBI [170–174]. There is ongoing work to update the bicycle helmet standards and include rotational impacts. However, the new standards are not yet in force, and the lack of a universally recommended finite element head model to estimate tissue-level metric values has hindered the comparison of different bicycle helmets with both kinematics-based and finite element-based injury metrics. Furthermore, the importance of considering tissue-level FE-derived injury metrics to evaluate helmet performance during impact tests has been acknowledged [138, 172]; however, no standard has officially adopted this assessment approach and only a few studies compared different bicycle helmets with both kinematics-based and FE-based injury metrics, possibly due to the lack of a universally recommended FE head model to estimate the tissue-level metric values [57, 143, 173].

Here, we used a pendulum test device to experimentally recreate an impact scenario

with amplified head rotational kinematics. The study aimed at assessing the effect of multi-directional rotational impacts on the performance of helmets with and without head rotation mitigation technologies. The evaluation was based on both global head kinematics and tissue-level TBI metrics.

3.6 Testing Setup and Impact Conditions

Three types of commercially available bicycle helmets were tested: those with friction-reducing slip layers (MIPS) and collapsible cell structures (WaveCel), and a third type with no additional head rotational kinematics mitigation system (Conventional). All helmets had certification from both the US Consumer Product Safety Commission and the European Commission. The Specialized S-Works Prevail II Vent (MIPS) and Bontrager Specter (WaveCel) helmets were selected for their high ratings [60, 175] and recommendation by Folksam Insurance Group [173], while the conventional helmets were chosen as the best-selling option on Amazon US despite their lower rating. The helmets were tested on a medium-sized headform with a circumference of 57.6 cm. Prices ranged from $25 to $250.

The helmets were tested using a custom-made pendulum impact device [176] that dropped a weighted hammer onto the helmet. The device included a pendulum arm with a steel hammer attached to it. The pendulum arm weighs 11.8 kg, and its length from the center of the pivot point to the center of its impacting mass is 1.91 m. A steel hammer head, weighting 19.7 kg, was fixed to the lower end of the pendulum arm. The total moment of inertia of the swinging arm-hammer system is 87.6 kg m2. The impacting pendulum was lifted using an electric winch that was connected to the pendulum arm with an electromagnet. An inclinometer attached to the main arm of the pendulum was used to verify the desired drop angle. The dummy head used was a NOCSAE headform, mounted on a male HIII neckform [177] and placed on a slide table that mimicked the mass of the torso. To simulate road friction conditions, sandpaper was used on the impacting surface of the hammer. The dummy head was instrumented with one ACC3 120 PRO tri-axial accelerometer and three ARS PRO uniaxial angular rate sensors (DTS, Seal Beach, CA, USA), which were placed at the CoG of the headform. The data from the sensors were collected at a sampling rate of 20 kHz using SLICEWare software (DTS, Seal Beach, CA, USA), and the linear acceleration and angular velocity data were filtered in accordance with SAE J211.

All helmet types were tested at two impact velocities 4.1 m/s and 5.4 m/s (which correspond to pendulum arm angles of 55° and 73°), and four impact locations: frontal rim, temporal, frontotemporal, and occipital sides (Fig. 3.8) to evaluate helmet performance over a range of commonly impacted areas [53, 136, 137]. The two velocities match with common ranges of values used to tests bicycle helmets, as reported in the review article by Abderezaei et al. [50]. The testing parameters were chosen to ensure repeatability and comply with safety standards. Each helmet type underwent three tests per velocity-location condition and four tests per location for a fixed velocity level. The helmet fit was checked and readjusted as needed before each impact.

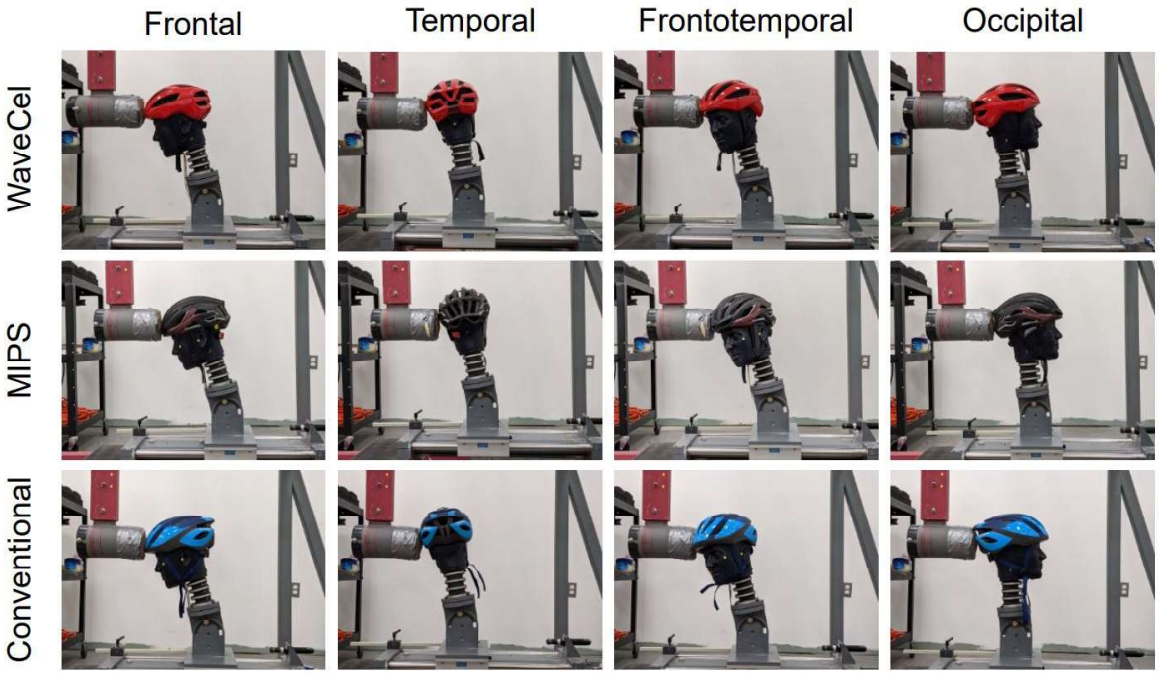

Figure 3.8: Relative Impact Locations for Tested Helmets. Before fitting the helmet, the dummy head was positioned according to the desired direction

3.7 Kinematics- and FE-based TBI Metrics

To evaluate helmet protection against TBI, we analyzed both overall head movement and tissue-level damage criteria using FE simulations. Overall head movement criteria included PLA, PRV, PRA, HIC, and BrIC. PLA, PRV, and PRA indicate the highest value of linear acceleration, rotational velocity, and rotational acceleration, respectively, at the CoG of the

helmeted dummy head during impact. HIC is defined as: Eq. 3.3 [178]:

$$HIC = max\left\{(t_2 - t_1)(\frac{1}{(t_2 - t_1)}\int_{t_1}^{t_2} a(t)dt)^{2.5}\right\} \tag{3.3}$$

with t_1 and t_2 any two time points during any interval in the impact, and $a(t)$ the resultant of the linear acceleration of the CoG of the head. BrIC is calculated as Eq. 3.4 [6]:

$$BrIC = \sqrt{(\frac{\omega_x}{\omega_{x,cr}})^2 + (\frac{\omega_y}{\omega_{y,cr}})^2 + (\frac{\omega_z}{\omega_{z,cr}})^2} \tag{3.4}$$

with ω the rotational velocity vector (x = anterior-posterior direction, y = medial-lateral direction, z = proximal-distal direction), and ω_{cr} the critical rotational velocity vector:

$$\omega_{cr} = \{\omega_{x,cr}, \omega_{y,cr}, \omega_{z,cr}\} = \{66.2, 59.1, 44.2\}(rad/s^2). \tag{3.5}$$

The three components of the linear acceleration and rotational velocity that were measured over time at the CoG of the helmeted headform, were used as boundary conditions of the FE model to simulate the impact tests. We used the KTH FE model developed by Kleiven et al. [166], that consists of the skull, bridging veins, CSF, cerebrum, cerebellum, brainstem, spinal cord, and neck bone. Three linear accelerations and three angular velocities were applied to the CoG of the model, which was modeled as a rigid body. We simulated the first 60 ms of the impacts with the non-linear explicit solver LS-DYNA R6.0.0 (LSTC, Livermore, CA, USA). We extracted maximum principal Green-Lagrange strain (MPS) and maximum principal Green-Lagrange strain rate (MPSR) of the brain elements. These deformation-based injury metrics evaluate the risk of specific types of TBI at tissue level which have high incidence among bicycle accidents including cerebral contusion, concussion, DAI, and ASDH. We calculated the 95th percentile of the peak MPS and MPSR values of the elements in the regions of interest (ROIs) including cerebral cortex, corona radiata, thalamus, brainstem, CC, cerebellum, and the whole brain.

3.8 Statistical Analysis

We investigated the effect of rotational motion-inducing impacts on three different helmet technologies. The brain protection performance was assessed with both kinematics-based and FE-based injury criteria. For each combination of impact velocity, impact location, and kinematics-based injury metric, we performed two-sample Student's t-test to compare

helmets with head rotational kinematics mitigation systems, i.e., MIPS and WaveCel, versus Conventional helmets, considered as control. We performed the same type of statistical test with respect to FE-based injury metrics, as well. We limited the analysis to MPS and MPSR evaluated across the elements of the whole brain. The effect of the impact location on the injury metrics was investigated by grouping the data by impact location and impact velocity. Then, we performed two-sample t-tests to compare location-specific groups (sample size N=9) with each other, for each impact velocity.

3.9 Results

We assessed the effectiveness of the bicycle helmets that were tested, by analyzing global head kinematics and tissue-level injury metrics.

3.9.1 Kinematics-based TBI metrics

Fig. 3.9 shows the results of evaluating helmet performance using injury metrics based on kinematics. When calculating PRA and FE-based metrics for frontal impacts, the time history before the peak rotational velocity was used to exclude the deceleration peak after nose contact, which didn't occur in other directions. MIPS helmets showed significantly lower PLA and HIC than conventional helmets, at both low and high impact velocities in frontal (Fig. 3.9 a), temporal (Fig. 3.9 b), and frontotemporal (Fig. 3.9 c) impacts, for all five criteria. In these cases (pvalue ¡ 0.05), the PLA reduced from 8% to 33% and HIC reduced from 11% to 40%. This mitigation system also significantly reduced PRA in low velocity frontal impacts (-16%), and in both low and high velocity temporal impacts (-46% and -33%, respectively) compared to conventional helmets. MIPS helmets also have significantly lower BrIC values in temporal impacts at low velocity and in frontotemporal impacts at high velocity. When comparing PRV values, MIPS helmets significantly outperformed Conventional helmets only in case of low velocity temporal impacts. In contrast, for occipital impacts, MIPS helmets had the highest mean values for all five global head injury metrics (Fig. 3.9 d). Notably, PRV and BrIC were significantly higher in MIPS helmets when compared to conventional ones. WaveCel helmets showed better performance than conventional helmets in impacts directed to the temporal side of the headform in terms of kinematics-based injury metrics (Fig. 3.9 b), with a reduction of up to 18% and 11% for PRV and BrIC, respectively. The PLA and HIC values were also lower for WaveCel helmets

compared to Conventional helmets at both velocities. In frontotemporal impacts, WaveCel helmets performed significantly better than Conventional helmets in terms of PLA and HIC at low velocity, while higher PRV and BrIC values were observed for WaveCel helmets during high-velocity impacts (Fig. 3.9 c). There were no significant differences between WaveCel and Conventional helmets during frontal impacts, except for HIC at low velocity (Fig. 3.9 a). In occipital impacts, WaveCel helmets generally recorded higher mean values for all five TBI metrics, with statistically significant differences for HIC at low impact velocity, and for PRV and BrIC at both impact velocities (Fig. 3.9 d).

Fig. 3.10 shows how the location of impact affects kinematics-based injury metrics.

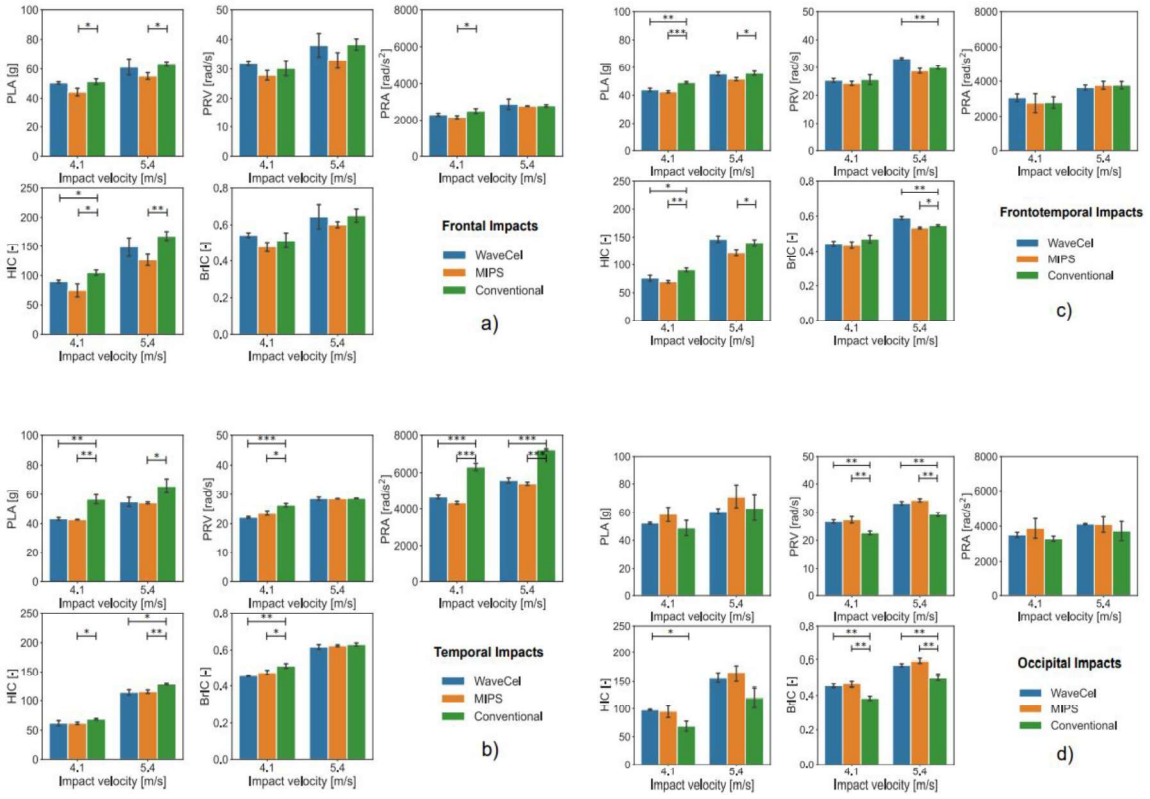

Figure 3.9: Helmet performance evaluation using global head kinematics and TBI metrics. The impact tests are grouped into: a) frontal, b) temporal, c) frontotemporal, and d) occipital impacts. * denote significance levels compared to conventional group: * $p < 0.05$, ** $p < 0.01$, *** $p < 0.001$.

Mean PLA values varied between 45 and 53 g for low-velocity tests and between 54 and 65 g for high-velocity tests. Frontotemporal impacts resulted in the lowest PLA values, while

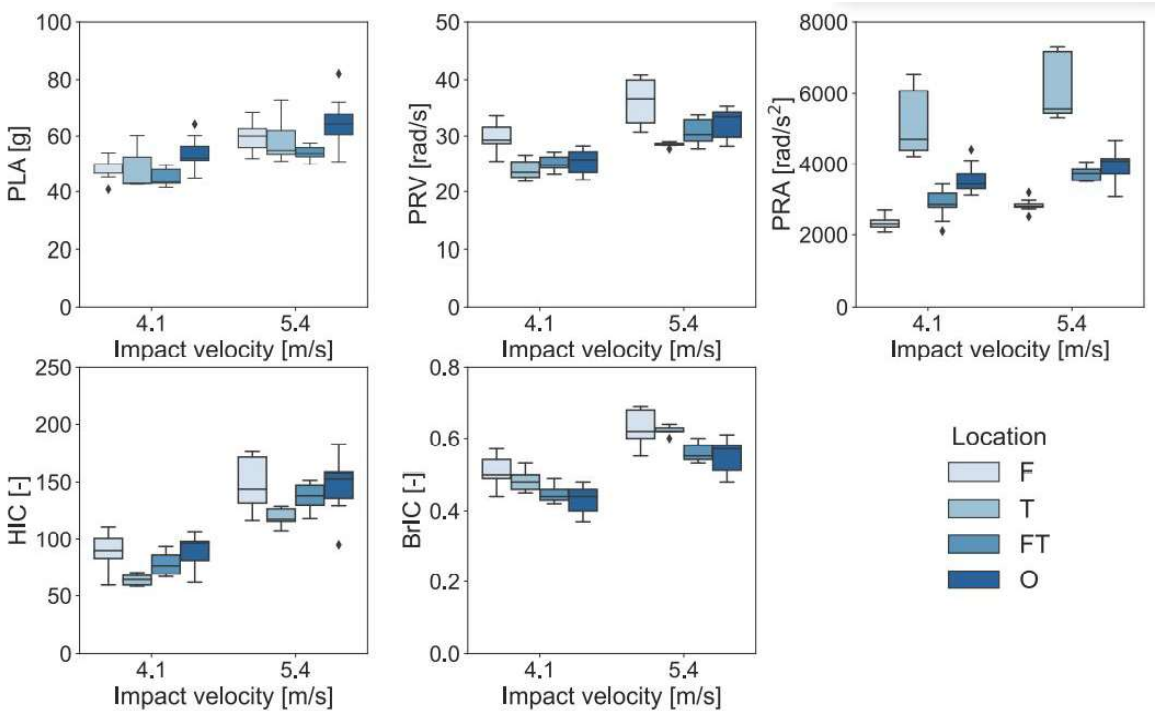

Figure 3.10: Impact location's effect on kinematics-based injury metrics. Boxplots representing impact data across all helmet types: F (Frontal), T (Temporal), FT (Frontotemporal), and O (Occipital) impacts.

occipital impacts resulted in the highest values. PLA values did not significantly differ between temporal and frontal impacts. However, frontal impacts resulted in significantly higher PRV values (30 ± 2 rad/s to 36 ± 4 rad/s) compared to other directions. On the other hand, temporal impacts produced the lowest PRV values (24 ± 2 rad/s for impacts at 4.1 m/s and 28 ± 0 rad/s for impacts at 5.4 m/s). PRA was significantly higher for temporal impacts (5092 ± 878 rad/s2 and 6076 ± 818 rad/s2) compared to other locations, while frontal impacts resulted in significantly lower values (2329 ± 170 rad/s2 and 2818 ± 170 rad/s2). Temporal impacts resulted in the lowest HIC values (64 ± 4 and 119 ± 7 for low and high velocity, respectively). In contrast, frontal and temporal impacts resulted in significantly higher BrIC values than frontotemporal and occipital impacts (on average 0.50 vs. 0.44 for low velocity tests and 0.63 vs. 0.56 for high velocity tests).

3.9.2 FE-based TBI metrics

We also compared helmets with and without rotation-damping technologies by evaluating TBI metrics based on brain tissue deformation through FE simulations of impacts

(Fig. 3.11). The MIPS system in helmets resulted in reduced tissue-level metrics compared to Conventional helmets in temporal and occipital impacts, with significantly lower MPS (-10% and -20%, respectively) and MPSR (-43% and -21%, respectively) in the whole brain at an impact speed of 4.1 m/s ($p < 0.05$). MIPS had higher mean values than Conventional helmets for MPS in the whole brain in high-velocity frontotemporal impacts (+10%). WaveCel helmets outperformed Conventional helmets in all four FE-based metrics in low-velocity temporal impacts, with reductions of -16% and -47% for MPS and MPSR in the whole brain, respectively. No significant differences were found for high-velocity temporal impacts. WaveCel and Conventional helmets showed similar results for FE-derived metrics in frontal, frontotemporal, and occipital impacts, except for high-velocity frontotemporal impacts, where WaveCel exhibited +8% MPSR.

In Fig. 3.12 FE-based injury metrics are grouped by impact location. Temporal impacts

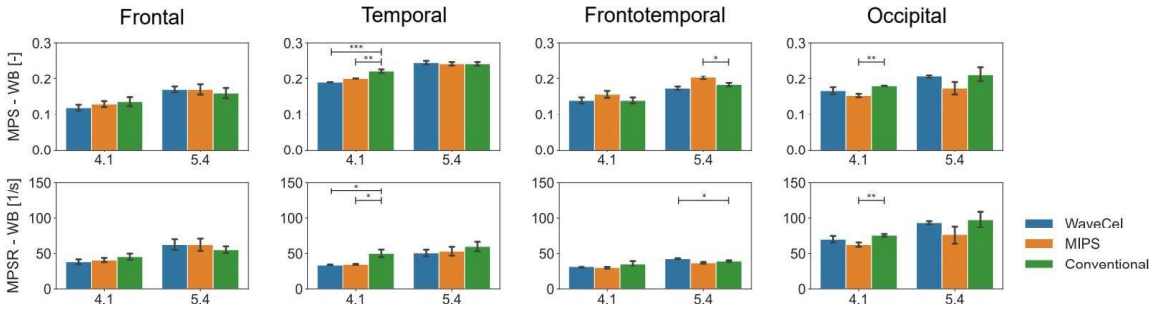

Figure 3.11: Helmet Performance Evaluation Using Tissue-Level TBI Metrics. Grouping of Impact Tests by Velocity and Location. FE-Based Metrics Calculated for Regions of Interest: Whole Brain (WB) and Bridging Veins (BV). Asterisks Denote Significance Levels Compared to Conventional Group: * = $p < 0.05$, ** = $p < 0.01$, **** = $p < 0.001$.

showed significantly higher MPS in the whole brain (0.20 ± 0.01 and 0.24 ± 0.00 for low and high velocity, respectively) compared to frontal impacts (0.13 ± 0.01 and 0.17 ± 0.01 for low and high velocity, respectively). Frontotemporal impacts had the lowest MPSR in the whole brain (31.7 ± 3.8/s and 39.9 ± 2.6/s for low and high velocity, respectively), while the highest MPSR was found in the occipital region. The pendulum device enabled repeatable and reproducible tests that considered the HIII neckform's effect on rotational head kinematics, emphasizing energy dissipation through rotational, not linear, kinematics.

3.10 Discussion

The pendulum device was chosen for its ability to conduct repeatable tests [61, 179] and incorporate the HIII neckform's effect on head rotational kinematics. Current pendulum tests focus on energy dissipation through rotational, not linear, kinematics. The study's head kinematics data falls within the ranges reported in a review article by Abderezaei et al. [50] for tests that included a neckform, while the PLA values were substantially lower. The study evaluated helmets' performance based on injury metrics that considered both global head kinematics and brain tissue deformations. The goal was to assess the effect of increased rotational impact conditions on helmets with different head rotational kinematics mitigation systems.

The helmet's performance is influenced by various factors, including the direction of

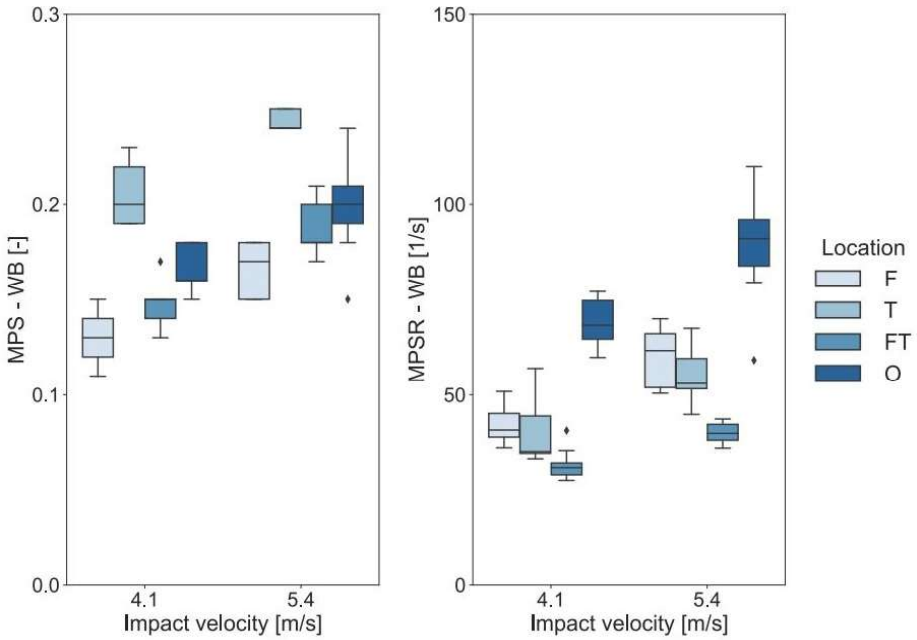

Figure 3.12: Impact Location's Effect on FE-Based Injury Metrics Boxplots Representing Impact Data Across All Helmet Types, with FE-Based Metrics Calculated for Regions of Interest: Whole Brain (WB) and Bridging Veins (BV).

the impact [57, 58], the moment of inertia of the headform [180–182], the stiffness response of the HIII neckform, and the design features [180, 181]. Helmets with mitigation systems for head rotational kinematics performed better than the standard EPS-only liner helmet in

terms of kinematics-based and FE-based injury metrics, especially at low impact velocity. MIPS helmet exhibited significantly lower PLA and HIC values, whereas WaveCel helmet performed very similarly to the Conventional helmet in frontal impacts. The design of the posterior part varied between the three helmet types, and the differences in geometrical shape and contact surface could explain the differences in kinematics-based injury metrics observed between the helmet types during occipital impacts.

The critical thresholds established in current helmet standards were well above the values obtained in the tests, indicating that the device is suboptimal for assessing helmet performance in terms of linear accelerations. However, some impact values exceeded tolerance levels for concussion risk and brain injury, particularly in low and high velocity temporal impacts. The rotation-damping systems in WaveCel and MIPS helmets were engaged in some loading scenarios. Tissue-level concussion thresholds ranged between 0.19 and 0.3 MPS [183–187], which were reached during the pendulum tests, especially in low and high velocity temporal, frontotemporal, and occipital impacts. The longitudinal engineering strains were well below the ASDH tolerance levels. Deformation-rate-based thresholds for 50% concussion risk ranged from MPSR = 48.5 to 60.0/s [9, 18, 166], and some impacts exceeded these thresholds, particularly in high velocity frontal and temporal impacts.

3.11 Conclusion

In this chapter, we reviewed the literature to collect and analyze various bicycle helmet technologies, investigating their resultant kinematic-based head injury data from drop test experiments. We observed that helmets utilizing new technologies like rotation damping systems, collapsible cellular structures, and expandable models outperformed conventional helmets in kinematics-based metrics at low impact velocities and angular momentum. The presence or absence of the neck surrogate in the experimental procedure was found to influence kinematics. These findings underscore the importance of rethinking conventional helmet designs, considering novel technologies for better prevention of cycling-related TBIs, and conducting more comprehensive impact testing. To further investigate the role of rotation mitigation systems, we performed pendulum tests on multiple impact locations, evaluating helmet performance using global head kinematics and tissue-level injury metrics. Our observations revealed a dependence on impact location, injury metric, and brain region,

potentially influenced by distinct helmet designs and contact surfaces. We propose that a thorough evaluation of bicycle helmet performance should encompass multi-directional impact tests targeting various locations and incorporate both global head kinematics and tissue-level injury metrics. Adopting such a comprehensive assessment approach will contribute to advancements in head rotation reduction technologies and the development of safer protective headgear designs.

The findings discussed in this chapter have been previously published in several papers, including references [50].

Chapter 4

TO INVESTIGATE THE EFFECT OF SPORTS HELMETS ON DYNAMICAL BEHAVIOR OF THE BRAIN SUBSTRUCTURES IN HELMETED IMPACTS

4.1 Introduction

mTBI, particularly those related to sports, pose a significant risk to the health of hundreds of thousands of athletes annually [74, 75], potentially resulting in long-term disability and neurocognitive deficits in certain cases [36]. Helmets have been used in several contact sports as a protection strategy to prevent or reduce the severity of mTBI. Although helmets have been shown to significantly reduce the risks of severe head injuries in football [76], bicycling [50, 77], skiing [78], and other sports, their effectiveness in mitigating the risks of milder forms of TBI is still being investigated [79–81].

Different contact sports require helmets with varying shapes, mechanical properties, and testing criteria [82–85]. Football and hockey helmets typically have hard shells and thicker but softer liners made of polyurethane (PU) and vinyl nitrate (VN) foams [76, 82, 83, 86], while bicycle and ski helmet liners usually consist of Expanded polystyrene (EPS) foam [84, 85]. The safety of these helmets is evaluated through laboratory impact setups [23, 25, 133] that measure head kinematics, such as rotational and linear accelerations. While hockey and football helmets are typically tested with setups that include rotational kinematics, such as an impact pendulum device [61] and a horizontal impactor [188], ski and bicycle helmets have been traditionally tested and evaluated with a vertical drop-test setup for linear kinematics. Testing procedures and criteria vary among different standards introduced for various sports helmets, such as the CPSC for bicycle helmets [23, 87] and National Operating Committee on Standards for Athletic Equipment (NOCSAE) [88] for football helmets. Traditionally, helmet design focuses on mitigating linear head kinematics during an impact [25, 26]. However, recent studies on dummy heads [7, 18–22, 89, 90] have highlighted the importance of rotational head kinematics in causing head injuries and

concussions. As a result, new helmet designs aim to reduce rotational head motion during impacts [21, 189]. Preliminary studies [23, 57] indicate that the latest helmet designs and mitigation systems can reduce rotational kinematics and brain strain [50]. However, despite these improvements, mTBI still occurs frequently in contact sports [89, 91], indicating the need for better helmet designs and testing criteria. Understanding brain injury mechanisms can help in designing more effective helmets.

Researchers have investigated the mechanics of mTBI by studying brain deformation during impacts through data collection [39–43] or simulation with brain-skull FE models [39–48]. Peak principal strain has been found to indicate injury severity in various contact sports [43, 49], and in addition to traditional helmet testing using head kinematics for evaluation purposes [24, 50–60], researchers have proposed investigating the mechanical behavior of the brain, which is closely linked to rotational kinematics during impacts. This approach can provide valuable insights into helmet effectiveness and improve understanding of how helmets can mitigate head injuries in different types of impacts [21, 60–62].Additionally, they have explored the mechanical behavior of the brain tissue [15, 16, 39, 68, 69] to understand the spatial and temporal variations in brain deformation characteristics that have injury-related implications. Brain FE models show nonlinear behavior during impacts, and investigating the biomechanics of substructures has revealed crucial frequency-dependent and localized phenomena associated with injury outcomes [16, 17]. In-vivo identification of the natural modes and frequencies of three-dimensional (3D) deformation of the human brain acquired by conducting tagged MRI during transient mild acceleration of the head and analyzing 3D strain fields using DMD[73]. Dynamic 3D brain deformation was analyzed and revealed fundamental oscillatory modes at frequencies near 7 Hz during neck rotation and 11 Hz during neck extension [73]. Finite element simulations using the DMD technique showed the existence of distinct modal frequencies in the corpus callosum and a strain concentration in deep white matter regions [16, 17]. The brain is particularly sensitive to displacement frequencies around 20-30 Hz, which can increase the observed deformation. Investigating the brain model's frequency response during an impact revealed that the corpus callosum experiences higher deformation at certain frequencies, which may have implications for mTBI [16].

To improve helmet design and reduce the severity of brain injuries, it is important to investigate the effect of different designs on the frequency response of vulnerable brain substructures like the CC. However, previous studies have mostly focused on the head's motion and kinematics [23, 24] rather than the substructural mechanics of the brain tissue due to its complexity. While some attempts have been made to analyze the efficacy of different helmet types by examining brain strain levels, a comprehensive design optimization has not been proposed. In order to gain a comprehensive understanding of the helmet's role in the brain injury mechanism, it is crucial to consider the substructural mechanics of the brain, since concussion diagnosis is correlated with maximum principal strain [11, 12]. in specific brain regions. This vulnerability has drawn attention to certain brain regions in sport-related concussion studies [13, 14].

In this chapter, the effect of different helmets on the frequency response of the brain FE model substructures was evaluated. Impact pendulum tests were performed on football, hockey, ski, and bicycle helmets, and the extracted kinematics from the helmeted dummy headforms were simulated in an FE brain-skull model. The frequency response of the substructures of the brain FE model across different helmet types was analyzed using the DMD technique. The final results provided insights into ways to improve sports helmet designs by considering the dynamical behavior of the brain in an FE model.

4.2 Methods

In this aim, we first conducted impact pendulum tests on headforms that were equipped with helmets. Then, we created a computational model of the brain-skull system by using the experimental head kinematics. Lastly, we utilized an advanced modal analysis technique to investigate the impact of various sports helmets on the frequency response of the brain substructures within the computational model.

4.2.1 Impact Pendulum Tests

We used an the same impact pendulum test setup explained in section 3.6, to apply impacts to a Hybrid III anthropomorphic head-neck system (Fig. 3.8). We released the impact pendulum at a 60° which corresponds to an impact velocity of 4.3 m/s. Four different commercially available helmets including a hockey helmet, a football helmet, a ski helmet, and a bike helmet were tested three times to compare their performance in

mitigating the head kinematics, and the resultant dynamic response of the brain FE model. Hockey and football helmets that were tested had VN liner foams [82, 86], and ski and bicycle helmet liners consisted of EPS foam [84, 85]. Head kinematics were measured as explained is section 3.6. We applied side impacts to induce coronal rotation since it has been reported that rotations in the coronal direction can cause large strains in certain vulnerable regions such as CC [68, 190]. We also performed front impact tests in order to understand the directional dependence of the brain FE model's frequency response.

4.2.2 Finite Element Simulations

To simulate head impacts in the LS-Dyna environment, the Global Human Body Models Consortium (GHBMC) 50th percentile male skull-brain FE model was used in this study [191]. GHBMC is a computational model that was developed for studying the biomechanics of human body movements and interactions with external forces, such as those that occur during automotive crashes [6, 192, 193]. The head model was developed based on CT and MRI scans of an adult male of average height and weight in the US [192]. The version used in this study had two primary parts: the brain and skull, each with several components, totaling 189,780 nodes and 244,485 elements. The CoG of the head model was subjected to linear acceleration and rotational velocity from impact pendulum tests. The goal of these tests and simulations was to observe the effect of different helmets on the dynamic response of the brain substructures in the computational model. Nodal coordinates of the brainstem, CC, cerebellum, and the whole brain in three directions were extracted, and the relative displacement of each node at each region with respect to the skull was calculated. These calculated relative displacements were then used as inputs for DMD analysis.

4.2.3 Modal Analysis

We used DMD, a multivariate method, to extract modal behavior of the brain tissue and analyze spatiotemporal differences within brain substructures as a function of modal frequency [16, 73, 194, 195]. The technique involves considering N equally spaced snapshots of a dynamic brain system with M nodes, and writing displacement fields at time t based on the temporal sequence of nodal displacement in x, y, and z directions, we can write down

the displacement fields at time t as:

$$\mathcal{U}(x, y, z, t) = \sum_{n=1}^{N} a_n exp(\lambda_n t)\phi_n(x, y, z) \tag{4.1}$$

where, a_n is the modal coefficient, λ_n is the complex modulus, and ϕ_n is the spatial distribution of each mode. As explained above, N is the number of spaced snapshots of M nodes, where each snapshot in DMD is assumed as a linear combination of the previous snapshots, $u_{j+1} = Au_j$ and can be written as:

$$\mathcal{U}_1^N = u_1, Au_1, ..., A^{N-1}u_1 \tag{4.2}$$

By calculating the eigenvalues and eigenvectors of matrix A, which defines the dynamical process, we can find the frequency $[\omega_j = \mathrm{Re}(\lambda_n)]$, decay rate $[\zeta_j = \mathrm{Im}(\lambda_n)]$, and amplitude $(|\Psi_j|)$ of the dynamic modes [16].

To get a more extensive understanding of how different helmet types can affect the amplitude pattern of the modes in the brain regions, we did a secondary analysis. We defined a term called *cumulative amplitude* as a summation of the amplitudes in a desired frequency range. Since it has been shown that the brain has a multimodal behavior [16, 17], the dominant frequency of the brain was considered as a reference frequency, ω_{ref}. We defined two frequency intervals and termed them as: low frequency range (ω_L), and high frequency range (ω_H) as (Eq. 4.3):

$$\omega = \begin{cases} \omega_{\mathrm{L}} & 0 \leq \omega \leq 2 \times \omega_{\mathrm{ref}} \\ \omega_{\mathrm{ref}} & \omega \text{ of the brain dominant harmonic} \\ \omega_{\mathrm{H}} & 2 \times \omega_{\mathrm{ref}} < \omega \end{cases} \tag{4.3}$$

In each case, we calculated the cumulative amplitude by summing up the amplitudes of the frequencies in low ω_L and high frequency range ω_H (Eq. 4.4), separately:

$$
\begin{aligned}
|\Psi_{\omega_{\mathrm{Sum}}}| &= \sum_{i=1}^{N} |\Psi_i|, \\
|\Psi_{\omega_{\mathrm{L}}}| = \sum_{i=1}^{N_L} |\Psi_i|, \quad |\Psi_{\omega_{\mathrm{H}}}| &= \sum_{i=1}^{N_H} |\Psi_i|
\end{aligned}
\tag{4.4}
$$

where $\Psi_{\omega_{Sum}}$ is the sum of the all mode amplitudes, and N_L and N_H are the indices of the frequencies which are in the range of ω_L, and ω_H, respectively. Our goal was to compare the performance of the helmets in reducing modal amplitudes, or in other words, dissipating energy in different frequency regimes. To compare low and high frequency ranges more accurately, we calculated the percentage of their cumulative amplitudes separately. This allowed us to see how different helmets affect the dominant bandwidths and shift the percentage of energy. This analysis helped to determine the amount of energy dissipated in high and low frequency regimes and how different helmets affect this behavior.

To verify the accuracy and reliability of our modal analysis results on relative displacements, we conducted an additional modal analysis on the maximum principal strain (MPS) values of individual elements in each brain region. The same procedures were followed, including applying DMD to the relative displacements. By adding MPS values to our modal analysis, we gained a more complete understanding of the brain FE model's dynamic behavior during helmet impacts. This approach also helped us establish a link between the modal characteristics of relative displacements and the corresponding MPS values, which increased the validity of our modal analysis technique.

4.2.4 Strain Analysis

MPS has been identified as a potential indicator of mTBI [68, 196, 197] and is an important parameter in understanding injury mechanisms [198]. We focused on analyzing the MPS values in the CC, brainstem, and cerebellum regions and calculated the ratio of the peak MPS in each region to that of the brain ($\frac{\mathrm{MPS}^{\mathrm{peak}}_{\mathrm{subregion}}}{\mathrm{MPS}^{\mathrm{peak}}_{\mathrm{Brain}}}$). Our purpose was to compare this metric with modal parameters and analyze them with respect to the helmet type.

4.3 Results

4.3.1 Frequency Response of the Brain Subregions with Helmeted Impacts

We used DMD analysis to examine the relative displacement between the brain and skull in four regions of the brain and the whole brain for different types of helmets in side

(Fig. 4.1A and Fig. 4.2A) and front (Fig. 4.1B and Fig. 4.2B) impacts. While most regions showed a primary harmonic around 7-15 Hz, there were some exceptions. The CC and cerebellum regions exhibited more variation from the whole brain dynamics, with high-frequency modes of oscillation observed in both impact directions. In the front impacts, the CC region showed a first harmonic at 23.1 Hz in the bicycle helmet, while the cerebellum region had a dominant second modal peak in the bicycle and ski helmets at around 37.5 Hz and 61.7 Hz, respectively (Fig. 4.1A). In front impacts, this dominant peak occurred at frequencies of 41.6, 31.3, and 38.0 Hz in the football, bicycle, and ski helmets (Fig. 4.1B).

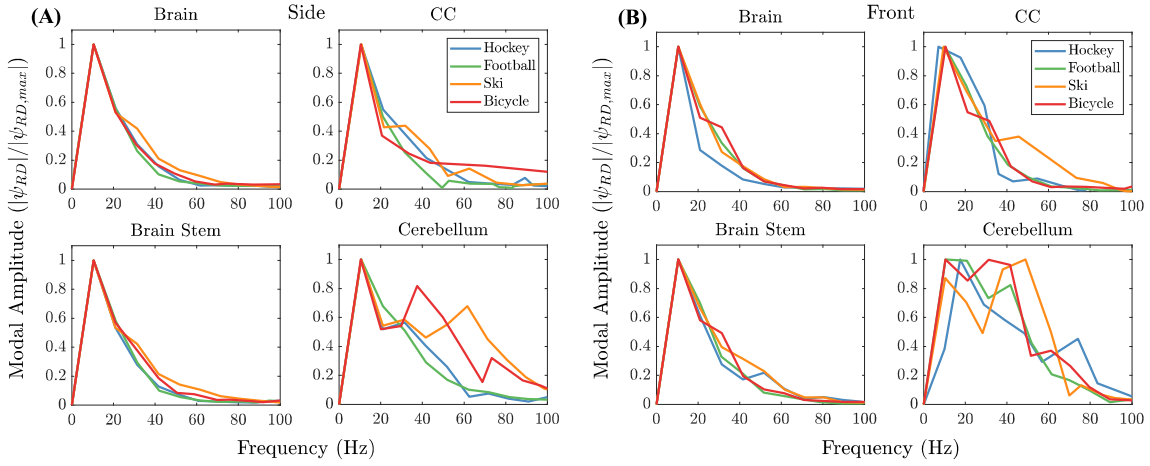

Figure 4.1: Comparison of DMD modes in the subregions across different impact directions and helmets using brain-skull relative displacements. Normalized modal amplitudes in the brain, and its substructures for different helmets in (A) side and (B) front impacts. The first harmonic in all regions was around 7.1-15.5 Hz for both directions. (B) Cerebellum demonstrated high-bandwidth modal response, with dominant high-frequency modes of oscillations observed in both directions.

We verified the accuracy and reliability of our modal analysis results by comparing the results obtained through modal analysis of maximum principal strain. The comparison revealed a high degree of similarity between the two sets of results, with identical frequencies observed for the main harmonic and a close frequency range for the secondary harmonic. Our findings were further supported by the observation of the second harmonic in specific cases. Moreover, our investigation of the bandwidth modal response across various helmet types for each region showed consistency and reliability between the two approaches.

We observed significant differences in the frequency distribution of modes among differ-

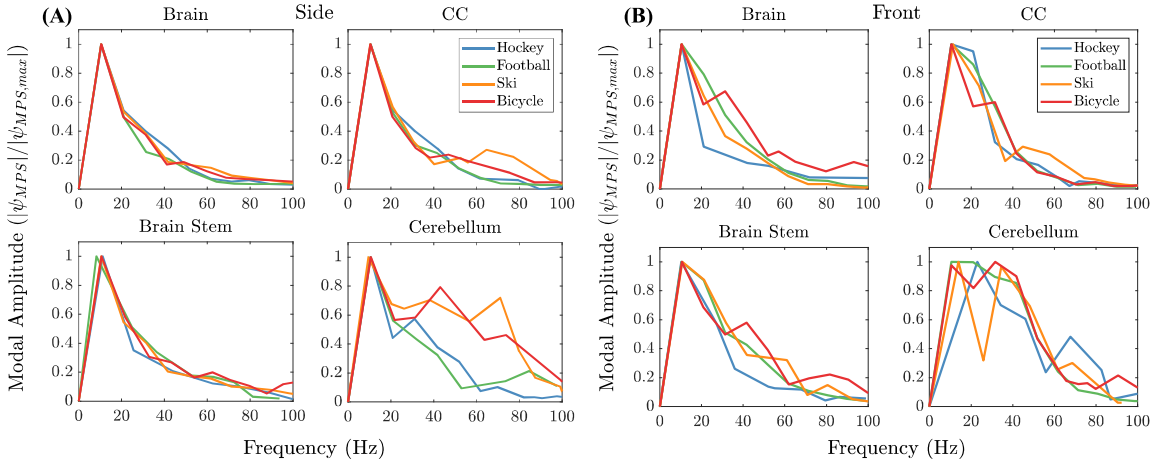

Figure 4.2: Comparison of DMD modes in brain's model subregions across different impact directions and helmets using MPS. Normalized modal amplitudes in the brain, and its substructures for different helmets in (A) side and (B) front impacts. The first harmonic in all regions was around 8.2-13.8 Hz for both directions. (B). Cerebellum showed a high-bandwidth modal response, with dominant high-frequency modes in both directions.

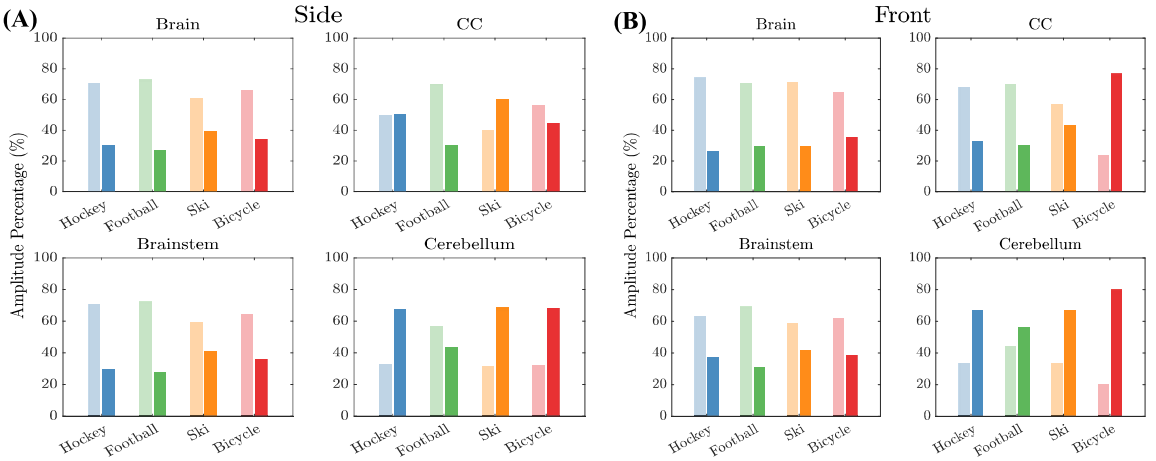

Figure 4.3: Distribution of the DMD modes in low and high frequencies. This figure compares cumulative modal amplitudes in ω_{L} and ω_{H} frequency ranges in (A) Side and (B) Front impacts. A) Ski and bicycle helmets had higher amplitudes in the high frequency range in brain and brainstem compared to hockey and football helmets. In CC and cerebellum, football helmet had the lowest amplitude percentage. B) Hockey and football helmets had the lowest percentage in high frequency range in brain, CC, and brainstem. In the cerebellum, football helmet had the lowest percentage.

ent helmets, particularly in various brain substructures (Fig. 4.1). To better understand these differences, we binned the modes into two main frequency intervals (ω_L and ω_H in

Eq. 4.3) and estimated their cumulative amplitude percentage distribution. This analysis allowed us to identify the dominant frequency regimes for brain modes in different helmets and impact conditions. Comparing the cumulative amplitudes in the side impacts in the brain and brainstem showed that for high-frequency regime (which were shown as a solid color in Fig. 4.3), hockey (26.9 %) and football (29.9 %) helmets had lower cumulative amplitudes than the bicycle (34.2 %) and ski helmets (40.9 %). In the CC, the high-frequency cumulative amplitude in the football helmet was the lowest in side impacts (29.9 %). In the cerebellum, the high-frequency cumulative amplitude of the football helmet was also the lowest (43.4 %). Similar cumulative amplitude behaviors were observed in the hockey, the bicycle, and ski helmets for side impacts in cerebellum (Fig. 4.3A).

In the front impact, the high-frequency cumulative amplitude in the brain was the lowest in the hockey helmet (26.0 %) and was the highest in the bicycle helmet (35.4 %). No significant differences were observed between the ski and football helmets (29.2 %). Also in the brainstem, the football helmet had the lowest (30.7 %) and the ski helmet had the highest value for high-frequency cumulative amplitude (41.5 %). In the CC, the high-frequency cumulative amplitudes were the lowest for football (30.3 %) and hockey helmets (32.4 %). In the cerebellum, which had more higher-amplitude modes in the higher frequency regimes compared to the other brain substructures, hockey helmet (66.8 %) and ski helmet (66.7 %) demonstrated the highest concentration of modes in the high-frequency regime (Fig. 4.3B).

4.3.2 Peak MPS pattern among Brain Subregions

We investigated the relationship between brain modal behavior and strain responses during helmeted impacts, based on previous studies that highlighted the importance of this relationship in understanding injury mechanisms [16, 17, 65, 73, 199]. Our hypothesis was that modal coupling and higher modal density could lead to energy localization in the brain, worsening the effects of strain and increasing injury risk.

We analyzed the peak MPS in CC, brainstem, and cerebellum, in a computer model and calculated the ratio of the peak MPS in these regions with respect to the peak MPS in the whole brain ($\frac{\mathrm{MPS}^{\mathrm{peak}}_{\mathrm{subregion}}}{\mathrm{MPS}^{\mathrm{peak}}_{\mathrm{Brain}}}$) to study strain localization patterns. In side impacts, CC had the highest ratio for all helmets except the ski helmet (Fig. 4.4 Side), while the brainstem had the highest ratio in front impacts (Fig. 4.4 Front). Previous studies also showed high

strain in these regions due to their stiff membranous structures [199–201]. The ski helmet had the highest MPS ratio in both brainstem and cerebellum in side impacts, while the football helmet had the lowest MPS ratio in cerebellum. In front impacts, the football helmet showed the highest MPS ratio in the cerebellum and the lowest in CC.

4.4 Discussion

We identified differences in modal behavior of the brain subregions in helmeted impacts. The main mode of oscillation was between 7-15 Hz, consistent with prior studies [65, 73], but in the cerebellum, higher harmonics were observed. However, in some cases the discrepancies are anticipated due to variations in the tested regions across different experiments, as well as inherent differences between in-vivo [73] and computer-simulated results [65]. Depending on the impact direction and helmet type, a second high-amplitude mode oscillated in the 38-62 Hz range, also previously reported. The cerebellum's multimodal dynamics [16] might cause higher harmonics due to longer vibration with lower dissipation. We also conducted modal analysis using MPS values to validate our relative displacement-based modal analysis. The similarity between the results suggests that our relative displacement-based method is a reliable way to investigate brain behavior during helmeted impacts.

We analyzed the modal behavior of various helmet types in a simulated human brain model to test our hypothesis about helmet types impact on brain substructure modal behavior. Results showed substantial differences in modal dynamics among brain substructures, especially after the ω_{ref}, revealed insight into the effect of the helmets in dissipating energy in higher frequency ranges. Ski and bicycle helmets were less effective in dissipating energy in higher frequencies than hockey and football helmets. This was particularly evident in the cerebellum, where high-frequency oscillations had higher amplitudes in ski and bicycle helmets. To compare the findings quantitatively, we analyzed cumulative amplitudes of frequencies higher than $2\times\omega_{\text{ref}}$ and found that ski and bicycle helmets had higher high-frequency cumulative amplitudes than football and hockey helmets in most cases. These differences may be due to variations in liner material properties. Hockey and football helmets with thicker and softer PU foam liners [76, 83, 86, 202] were more effective in absorbing impacts [202, 203] than bicycle and ski helmets with stiffer EPS liners [82–85] The difference in liner material properties can explain the observed variation in high-frequency cumulative

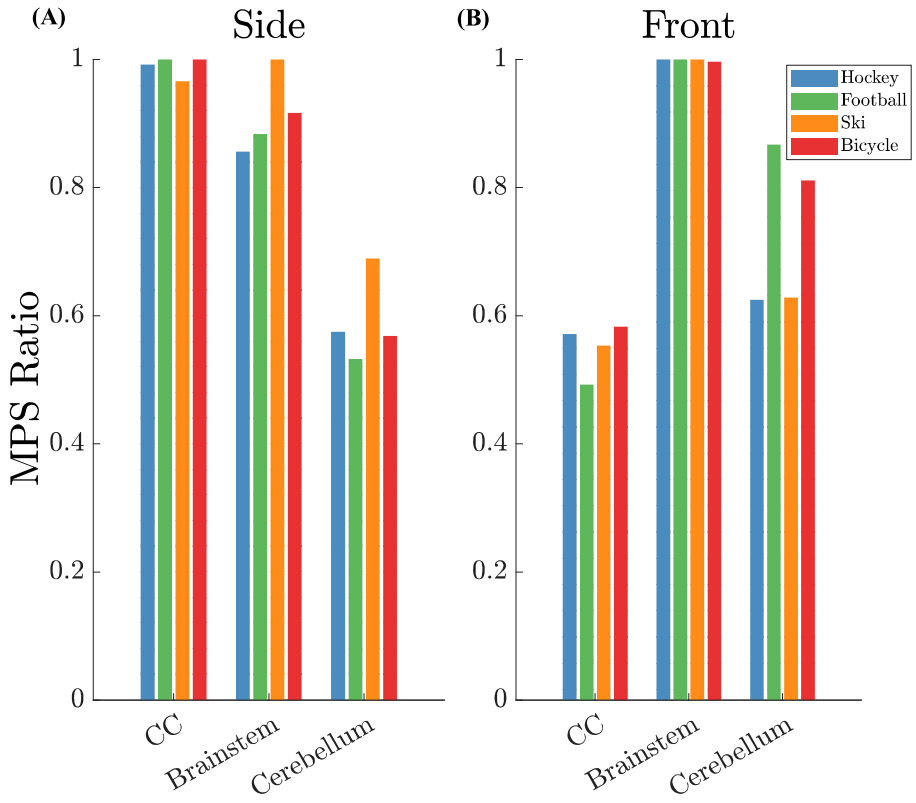

Figure 4.4: Regional pattern of the peak MPS with respect to the peak MPS in the brain. This figure shows the ratio of the peak MPS in the brain substructures with respect to the brain in (A) Side impact in which the peak MPS occurs in CC for all helmet types except ski helmet in which the peak MPS appears in the brainstem, but the difference between these two regions was negligible, and (B) Front impacts in which the brainstem and CC have the highest and lowest ratio in all helmet types, respectively.

amplitudes. The football helmet was found to be better at dissipating high-frequency modes than other helmets for side impacts [202, 203]. The geometry of the bicycle helmet with a lower radius of curvature at the front may also affect its ability to dissipate energy during front impacts (Fig. 4.3 A).

Since multimodal behavior of the brain, and the interaction of these modes were found to be associated with peak principal strains [16], we analyzed the relationship between modal amplitude distribution in the high and low frequency regimes and corresponding MPS values (Figs. 4.3 and 4.4). Our findings supported two hypotheses: 1) high-frequency cumulative amplitude is associated with high MPS, and 2) higher modal density and coupling leads to higher MPS (Figs. 4.3 and 4.4). We observed differences among helmet types in different

brain regions, with ski and bicycle helmets having higher high-frequency amplitudes and MPS in the brainstem and cerebellum (Fig. 4.4). Modal coupling and density also played a role in strain concentration, as observed in the football and hockey helmets in the cerebellum and CC (Fig. 4.1 and 4.2). This part of the study has limitations that affect the generalizability of our findings. We recommend using an impactor with an angled surface to better simulate real-world scenarios, particularly in terms of their protection ability in rotational kinematics [167, 204] and studying the impact of angled surfaces on different helmet types. Our testing method was limited to 100 milliseconds, but we used binned modes to obtain a broader understanding of mode frequency distribution. Our findings may only apply to the GHBMC model and a more accurate model may improve predictions of the brain's response to impacts. Using a more diverse set of helmet designs and impact conditions can provide a more comprehensive understanding of the modal behavior of helmeted impacts.

4.5 Conclusion

In many contact sports, athletes use protective headgear to minimize the risk of head injuries. Despite advancements in helmet technology and the increased use of helmets, the incidence of sports-related mild traumatic brain injuries (mTBI) remains high, highlighting the need for further improvements. Current helmet designs primarily focus on mitigating head kinematics, even though evidence suggests that the spatiotemporal mechanics of brain substructures play a significant role during mTBI events. The presence of localized modes and the multimodal behavior of various brain regions, along with the specific vulnerability of these regions to injury, indicate the need for a detailed analysis of brain substructure behavior in helmeted impacts. This study examined the differences in the modal behavior of brain subregions using finite element (FE) modeling in helmeted impacts, focusing on helmets associated with high injury rates. Across all brain regions, the primary mode of oscillation was observed between 7–15 Hz in both impact directions, consistent with previous findings that used tagged MRI and simulations. Discrepancies in frequency ranges could be due to differences in regions tested, experimental setups, and the inherent contrast between in vivo and computer-simulated results. The cerebellum displayed additional

higher harmonics between 38–62 Hz, attributed to its unique location and prolonged vibration with lower energy dissipation. To enhance the reliability of the modal analysis, maximum principal strain (MPS) values were also analyzed within each brain region. This dual approach allowed for a comprehensive assessment, correlating modal characteristics with strain patterns. Results from MPS-based analysis and relative displacement analysis showed significant similarity, validating the approach. However, some differences were noted, such as a higher amplitude of the second harmonic in the bicycle helmet's MPS results during front impacts. This could be related to the non-linear nature of MPS and its relationship with strain. Additionally, the brainstem exhibited higher frequency and amplitude in the second oscillation mode, particularly with the bicycle helmet, due to the high MPS ratio observed during front impacts. Consistency across helmet types and analysis methods supports the robustness of the relative-displacement-based modal analysis for evaluating brain dynamics in simulated impacts. Given our hypothesis on how helmet performance may influence the modal behavior of different brain regions in our model, we anticipated that distinct modal characteristics would emerge across helmet types. Our findings revealed notable differences in the brain substructures' modal dynamics. Specifically, ski and bicycle helmets exhibited less capability in dissipating energy at higher frequencies compared to hockey and football helmets within the same frequency range. This effect was particularly pronounced in the cerebellum, where ski and bicycle helmets generated higher amplitude oscillations at elevated frequencies. The simulated variations in modal behavior, especially after the reference frequency ω_{ref}, provided valuable insights into the energy dissipation characteristics of these helmets. To quantify these observations, we analyzed the cumulative amplitudes for frequencies exceeding $2\times\omega_{\text{ref}}$. Ski and bicycle helmets consistently demonstrated higher cumulative amplitudes at high frequencies than football and hockey helmets. This outcome likely results from the differences in liner materials. Football and hockey helmets utilized softer PU foam, which is more effective for shock absorption across a wider range of impacts, particularly high-velocity ones, compared to the stiffer EPS foam used in bicycle and ski helmets. Furthermore, the pronounced differences between the bicycle helmet and other helmets in the CC during frontal impacts might be attributable to the helmet's geometry, which reduces the contact area. Interestingly, the football helmet

was particularly effective at dissipating high-frequency modes for side impacts. Recognizing that multimodal brain behavior is linked to peak principal strains, we explored the relationship between modal amplitudes and maximum principal strain (MPS) values. Our analysis supported the hypothesis that higher modal amplitudes at elevated frequencies correspond with increased MPS values and that greater modal density and coupling exacerbate strain concentration. For example, in the brainstem, ski and bicycle helmets exhibited the highest high-frequency amplitudes, aligning with MPS analysis findings. Similarly, in side impacts, ski helmets produced the highest MPS ratio in the cerebellum, while football and hockey helmets resulted in lower MPS ratios in the CC for frontal impacts, consistent with their reduced high-frequency modal amplitudes. Modal coupling effects were evident, with certain helmets, like the football helmet in frontal impacts and the hockey helmet in side impacts, generating significant MPS ratios due to strong coupling near dominant modal frequencies. Our study has several limitations that may restrict the broader applicability of our findings. First, the current testing method, which uses a direct impact from a pendulum, does not incorporate the tangential components typical of real-world oblique impacts. Future studies could address this limitation by using an angled impactor to better simulate real-world conditions, particularly for assessing helmets' performance in managing rotational kinematics. Evaluating the impact of angled surfaces across various helmet types could provide new insights into their rotational energy absorption capabilities. However, it is unlikely that such tests would show substantially different results in the frequency domain. Additionally, our impact pendulum tests were conducted over a duration of 100 milliseconds. This limited the DMDtechnique's ability to resolve high-frequency modes accurately, potentially affecting the precision of the identified modal frequencies. To mitigate this limitation, we binned the modal frequencies into two ranges to gain a broader understanding of how frequency distribution influences brain response. Another important consideration is that prior modal analyses of the brain have either been performed in vivo or using different finite element (FE) brain models. Given the variability in geometry, material properties, and boundary conditions among these models, the specific frequencies observed in our study may only be relevant to the GHBMC model used. For instance, our model treats the brain's ventricles—filled with CSF—as incompressible solids with vis-

coelastic properties, rather than as true fluid structures. This simplification may alter the mechanical response and highlights the need for models that more accurately represent the brain's anatomical complexity. Furthermore, we used the isotropic version of the GHBMC head model with predefined material properties, which may limit the accuracy of our modal frequency predictions. A more comprehensive analysis could be achieved by employing a diverse set of helmet designs and impact conditions to better understand helmeted impact dynamics. Despite these limitations, our findings emphasize the need to consider the brain's substructure dynamics when designing helmets. Current helmets focus on mitigating head kinematics, but understanding the dynamics of brain substructures is crucial in addressing the mechanisms of concussion. The localized and multimodal behavior of the brain, with its hyperviscoelastic properties, necessitates further investigation into how helmets can be optimized to influence these modal characteristics. Our study lays the groundwork for future research, which could lead to improved helmet designs based on a deeper understanding of brain biomechanics, especially under more varied and complex impact scenarios. The findings discussed in this chapter have been previously published in several papers, including references [205, 206].

Chapter 5

TO INVESTIGATE *IN VIVO* BRAIN SUBSTRUCTURE DISPLACEMENT AS INDICATORS OF VENTRICULOPERITONEAL SHUNT OUTCOMES IN NPH USING AMRI

5.1 Introduction

With each heartbeat, periodic changes in arterial blood pressure propagate through the vasculature, causing localized deformations in both the arterial walls and surrounding tissues [1]. Measuring these motions could enhance our understanding of various cerebrovascular conditions, but it has remained a significant technical challenge. In this section, we present a novel image processing algorithm based on aMRI, termed aFlow, which facilitates the study of coupled brain-blood flow dynamics by integrating cine and 4D flow MRI amplification. To achieve this, we extended the use of aMRI to analyze transient dynamics. aFlow is a phase-based aMRI algorithm that employs DMDas a temporal filter, amplifying sub-voxel motions in both the brain parenchyma and vasculature for improved visualization. By incorporating DMD, aFlow captures characteristics of transient events, such as vascular motion observed in 4D flow MRI [102, 103]. This section also introduces neurodegenerative diseases that can be explored from a dynamic perspective using aMRI, with a particular focus on NPH, the central condition investigated in this thesis. Further details are provided on the image analysis conducted for these patients and the key parameters identified as significant contributors to successful surgical outcomes.

5.1.1 Amplified Magnetic Resonance Imaging (aMRI)

aMRI represents a significant advancement in the field of medical imaging, enabling highly detailed visualization of subtle brain motions and deformations caused by physiological dynamics such as blood vessel pulsation and CSF movement. These dynamics exert pressure on brain tissue, which in turn manifests in minuscule motions and deformations. aMRI uses a phase-based motion magnification algorithm applied to 2D multi-slice cardiac-gated (cine MRI) data, creating an amplified "movie" that dramatically enhances

the visibility of these subtle movements [31, 102].

This technique is particularly beneficial in the diagnosis and study of various neurological disorders where altered brain motion is a symptom, such as hydrocephalus, Chiari I malformation, idiopathic intracranial hypertension, and age-related diseases in small cerebral vessels. For instance, aMRI has been pivotal in differentiating abnormal from normal motion in Chiari I malformation patients, where affected individuals show increased caudal midbrain tissue displacement and downward displacement at the brainstem and craniocervical junction [32].

Furthermore, aMRI has expanded into other applications, including amplified flow imaging (aFlow) which captures transient events like blood flow interaction with arterial walls. This has been particularly useful in assessing evolving intracranial aneurysms and studying the biomechanical effects of head impacts, thereby contributing to our understanding of brain health post-impact and the region-specific vulnerability of brain structures to trauma [1].

Despite its effectiveness, the original aMRI approach had limitations, primarily due to its 2D nature that only amplified motion in the in-plane direction and ignored out-of-plane movements, leading to motion artifacts. Additionally, the use of multi-slice data, typically only supporting thick slices, exacerbated motion artifacts due to partial volume effects and asynchronized data acquisition across different heart rates. Ongoing improvements to the aMRI algorithm and acquisition techniques aim to address these issues, enhancing the capability of this promising technology in various clinical applications.

5.1.1.1 Cine Balanced Steady-state Free Precession (bSSFP) MRI (cine MRI)

Combining insights from recent advancements in MRI technology, Cine-bSSFP MRI (cine MRI) and aMRI have emerged as pivotal techniques in understanding and visualizing intrinsic brain motion caused by physiological dynamics such as blood vessel pulsation and CSF circulation. These imaging methods are particularly effective in highlighting subtle brain deformations and motions which are crucial for diagnosing and studying various neurological disorders like hydrocephalus and Chiari I malformation [102].

Cine MRI is valued for its ability to provide high-contrast images that can accurately track

significant deformations in lower brain regions such as the cerebellar tonsil and hindbrain. Despite its strengths, cine MRI traditionally suffers from limitations in spatial noise and resolution, which restrict its utility to capturing intrinsic brain motion primarily in the lower brain regions. This makes global characterization of brain motion challenging [1, 31]. aMRI, an advanced technique based on the phase-based motion magnification algorithm, enhances the visualization of minute, often subvoxel motions. It amplifies the biomechanical response of the brain to blood pulsation and CSF movement, thereby allowing for a more detailed examination of brain tissue dynamics. This method has proven effective in differentiating normal from abnormal motion, particularly in conditions like Chiari I malformation, where traditional methods might not reveal subtle yet clinically significant anomalies.

Further developments in aMRI technology have led to the introduction of a 3D aMRI post-processing algorithm applied to 3D cardiac-gated bSSFP cine data. This advancement captures motion in all three directions, significantly improving image quality and the visualization of amplified cardiac- and CSF-induced brain motion. The new 3D algorithm utilizes an extended version of 2D steerable pyramid filters to capture both in-plane and out-of-plane brain motion, thereby enhancing spatial resolution and overall performance [32, 102, 104].

The integration of DMDin aMRI's algorithm pipeline and the introduction of amplified flow imaging (aFlow) have broadened the applications of this technology. aFlow facilitates simultaneous visualization of brain and arterial deformations, showing promise in visualizing intracranial aneurysm wall deformation and potentially aiding in the assessment of rupture risk [103].

By combining these enhanced imaging capabilities with traditional approaches like PC-MRI and DENSE MRI, clinicians are equipped with a robust, non-invasive tool for assessing brain pathologies that alter biomechanical responses. This holistic approach not only assists in the clinical interpretation but also in the qualitative analysis through tools like optical flow vector maps, providing a comprehensive understanding of the brain's intrinsic dynamics and the mechanisms driving CSF circulation [1].

5.1.1.2 3D aMRI Algorithm [1]

The 3D aMRI technique enhances the existing 2D phase-based aMRI framework [1, 102, 104], enabling detailed visualization and measurement of voxel movements across three axes. The original 2D approach uses a linear steerable pyramid to split the data into various scales and orientations [102]. This pyramid approach incorporates scale-adjustable filtering ("pyramid") with orientation-specific adjustments ("steerability"), allowing filters at different scales to rotate and capture the entire domain effectively, breaking down the data into its components [207]. Temporal changes in these decomposed phases are then enhanced and temporally filtered to better illustrate the subtle 2D dynamics [102]. Expanding upon this, the 3D aMRI method evolves the linear steerable pyramid from two dimensions into three and modifies spatial filters from circular to spherical coordinates. Initially, the algorithm takes in 3D cine MRI data. A 3D steerable pyramid then deconstructs this volumetric data, organizing the local phase information of each time frame by scale and orientation. We modeled the 3D steerable pyramid based on guidelines in [207], utilizing steerable filters for a multi-scale decomposition that includes recurring low-pass filtering and down-sampling of each phase image [207, 208].

The 3D aMRI algorithm begins by processing the intensity data from each 3D cine MRI frame through both a low-pass filter L and a high-pass filter H. The low-pass phase L_0 is segmented into six oriented sub-bands $B_0, \ldots, B_5$, along with an additional lower-pass sub-band L_1. This lower-pass sub-band is subsequently down-sampled by a factor of two along the x, y, and z axes to further refine the analysis. This process is successively repeated to include further decomposition at the low-pass level. In this study, filters defined in [1, 208], which are formatted for the Fourier domain, are used as equations 5.1 and 5.2:

$$L(r) = \begin{cases} 2\cos\left(\frac{\pi}{2}\log_2\left(\frac{4r}{\pi}\right)\right), & \frac{\pi}{4} < r < \frac{\pi}{2} \\ 2, & r \leq \frac{\pi}{4} \\ 0, & r \geq \frac{\pi}{2} \end{cases} \tag{5.1}$$

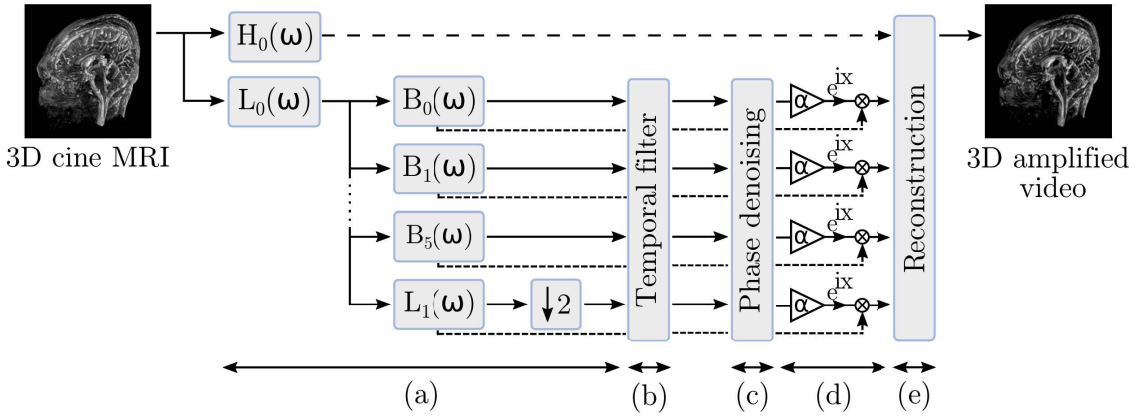

Figure 5.1: 3D aMRI decomposes the 3D cine MRI into different scales and orientations and amplifies the local phases over time to visualize small cardiac-induced brain motion. (a) A 3D complex steerable pyramid with 6 orientations (basis filters $B_j(k_x, k_y, k_z)$, $j = 0, 1, \ldots, 5$) is used to decompose each time point of the 3D cine MRI dataset into different spatial scales and orientations. (b) The decomposed phases at each scale and orientation are temporally filtered at the selected range of frequencies. (c) As an optional step, a Gaussian smoothing filter can be used to reduce noise and artifacts. (d) The processed signals in all the phases are amplified by an amplification factor α and are added back to the reference phase. (e) The amplified 3D cine MRI is reconstructed, allowing the visualization of the motion in three directions [1].

$$H(r) = \begin{cases} \cos\left(\frac{\pi}{2}\log_2\left(\frac{2r}{\pi}\right)\right), & \frac{\pi}{4} < r < \frac{\pi}{2} \\ 1, & r \geq \frac{\pi}{2} \\ 0, & r \leq \frac{\pi}{4} \end{cases} \tag{5.2}$$

To partition the low-passed phase across M orientations, we devised angular filters that uniformly segment the spherical coordinate system. In this context, M is set to 6, utilizing basis filters $B_j(k_x, k_y, k_z)$ in the Fourier domain. The orientations for these filters are derived from the vertices of a cuboctahedron, ensuring an equal division of the space [208]. The filters, which are conically shaped, are specified as follows:

$$B_j(\theta, \phi) = \cos^2(\Omega(\theta, \phi; \theta_j, \phi_j)), \quad j = 0, 1, \ldots, 5 \tag{5.3}$$

where Ω is the angle between $\vec{OM}$ and $\vec{OC}$, which can be determined by:

$$\cos\Omega = \frac{\vec{OM} \cdot \vec{OC}}{\|\vec{OM}\|\|\vec{OC}\|} \tag{5.4}$$

To analyze motion in various directions, we developed a set of six basis filters $B_j(k_x, k_y, k_z)$, which are defined using the directional properties derived from the vertices of a cuboctahedron. The filters are applied at multiple orientations and scales within a steerable pyramid framework to decompose the low-passed data into different phases. Each level of the decomposition is then processed to isolate and amplify the motion in desired frequency ranges. The processed data is then reassembled to enhance the visual representation of motion across three dimensions. For further details on the filter specifications and the decomposition process, see reference [1].

As mentioned above, several neurodegenerative diseases can be investigated using 3D aMRI. In this section, these diseases will be briefly introduced, followed by a detailed analysis of NPH cases, which is the focus of this thesis.

5.1.2 Chiari Malformation type 1 (CM-I)

Chiari Malformation Type I (CM-I) is a prevalent neurological disorder affecting the craniocervical junction, diagnosed in about 1% of adults and 3.6% of children undergoing MRI scans. It is characterized by a 3–5 mm downward herniation of the cerebellar tonsils through the foramen magnum [209]. Symptoms vary widely, including headaches, nausea, muscle weakness, sleep disorders, and in severe cases, paralysis. Notably, symptom manifestation can start in childhood or adulthood, with early diagnosis and surgical intervention often improving outcomes significantly [210].

However, the relationship between the radiographic presence of tonsillar herniation and symptom manifestation is inconsistent, with many patients showing no symptoms despite significant herniation [210]. This discrepancy highlights the complexity of CM-I, suggesting that factors beyond simple anatomical changes are involved in its pathogenesis. Recent studies have explored the role of intrinsic brain motion during the cardiac cycle in contributing to CM-I symptoms, facilitated by advanced imaging techniques like cine PC-MRI and aMRI [1].

aMRI, particularly, has been used to visualize and quantify brain motion anomalies in CM-I patients, identifying distinctive motion patterns at the craniocervical junction that differ from healthy controls. This technology has evolved from 2D to 3D, enhancing the ability to capture and analyze brain motion across three dimensions without invasive procedures.

These advancements suggest that 3D aMRI could integrate seamlessly into clinical protocols, offering detailed insights into the dynamics within the brain's structures in CM-I patients, potentially influencing diagnostic and treatment strategies [1].

5.1.3 Normal Pressure Hydrocephalus

NPH is a neurodegenerative disease commonly affecting the elderly population, and it is associated with a range of symptoms, such as difficulty walking, cognitive impairment, and urinary incontinence. NPH is characterized by an abnormal buildup of CSF in the brain's ventricles, despite normal intracranial pressure. One treatment method for NPH is shunt surgery, where a shunt is placed to drain excess fluid from the brain. However, the success rate of this procedure is inconsistent, and it is crucial to identify factors that contribute to its effectiveness. One potential approach is to use mechanical and engineering principles to better understand the factors that could help assess the success of shunt surgery [211]. The pathophysiology of NPH remains elusive, though studies have identified a distinctive "reversal" of CSF flow through the aqueduct of Sylvius, causing retrograde movement into the enlarged third and lateral ventricles [212–214]. Distinguishing the ventriculomegaly associated with NPH from cerebral atrophy poses significant diagnostic challenges, especially since NPH is notably prevalent, affecting approximately 5.9% of individuals aged 80 and older [215]. Radiologically, NPH is typically identified by disproportionately large ventricular dilation compared to cortical atrophy. Intracranial compliance (ICC), a measure of CSF pulsatility, usually decreases as hydrocephalus progresses, making conventional cine MR imaging techniques inadequate as they often capture only minimal changes in ventricular wall motion during the progression of hydrocephalus.

Currently, there lacks a robust, clinically validated non-invasive method to predict which NPH patients might benefit from surgical interventions, such as CSF shunt placement. Unfortunately, up to 30% of patients undergoing shunt surgery do not experience significant clinical improvement. This lack of efficacy, coupled with the potential need for multiple surgeries, poses considerable risks to patients and escalates healthcare costs [216].

aMRI emerges as a groundbreaking technique that leverages the Eulerian video magnification algorithm to enhance and analyze minute, often subvoxel motions like CSF pulsatility.

By utilizing the heartbeat as an endogenous mechanical driver, aMRI can effectively visualize the biomechanical response of brain tissues. This capability makes aMRI particularly valuable for assessing ventricular deformity and intracranial compliance, thereby offering a novel approach to evaluate brain motion in NPH patients [104]. This innovative imaging method holds promise not only in improving diagnostic accuracy but also in potentially refining patient selection for surgical interventions.

The aMRI technique applied in this research was first introduced by Holdsworth et al. [104] and later refined by Terem et al. [102]. The refined technique uses a phase-based method that better manages noise than its predecessor, the Eulerian Video Magnification (EVM) algorithm [1]. This newer approach processes motion-related local phase variations through complex steerable pyramids [217], enhancing these variations using a specific amplification factor. Such advancements allow for the detection and visualization of displacements that were once too subtle to see, employing advanced noise-filtering techniques [1]. This method effectively brings out fine brain motions, making it possible to visually and quantitatively assess the brain's inherent movements [1].

Building upon the 2D phase-based algorithm, the 3D aMRI method expands the capacity to detect and quantify voxel movements across three dimensions [102, 104]. It begins with processing a 3D cine MRI dataset through a 3D steerable pyramid, which breaks down the image into various scales and orientations. This includes splitting the initial image into low- and high-pass segments, and further dividing the low-pass segment into six oriented bandpass segments and an additional lower-pass segment, subsequently downsampled by two across all spatial dimensions [31, 103, 217, 218]. This layered breakdown aids in capturing intricate motion details.

For both the 2D and 3D models [31, 103, 218], the outputs are complex numbers reflecting the amplitude and phase at each scale and orientation, with phases indicating sub-voxel movements vital for enhancing motion visibility. These phases undergo filtering to focus on cardiac frequencies and eliminate static noise. Enhanced clarity and reduced noise are achieved by smoothing the filtered phases with an amplitude-weighted Gaussian filter, multiplying them by an amplification factor ($\alpha = 8$), and integrating them back with the original phase data. The final product is a synthesized 4D movie that magnifies motion during

the cardiac cycle, useful for both multi-slice and volumetric analyses [31, 103, 218]. This method utilizes a band-pass filter set to the heart rate and a Gaussian smoothing filter with a sigma value of 5, focusing on minimizing distractions from other temporal frequencies and ensuring targeted visualization of cardiac-induced brain movements. Our hypothesis in this study was that, due to the excess fluid in the brain, patients with NPH might experience restricted brain motion before surgery. After the shunt is placed, we hypothesized that the brain's displacement, particularly in specific regions, would increase, potentially offering insights into the success of the surgery. To investigate this, we used aMRI to measure brain displacement and motion before and after the surgery. This method allowed us to calculate the displacement of different brain regions across time during a cardiac cycle.

5.2 Methods

In this study, we adhered to HIPAA and IRB guidelines and institutional protocols to ethically recruit and scan Eight adults (5F, mean 75.6 years) were consented per IRB protocols and scanned up to 1 week before (n=8), and 3 months after (n=6) clinically indicated shunt surgery. Each participant provided informed consent prior to participation. We conducted imaging sessions both before and after the neurosurgical intervention, which involved the placement of a ventriculoperitoneal shunt. Pre-operative imaging was completed for all four participants, while post-operative imaging was successfully conducted for two of these individuals.

5.2.1 Human Subjects

In this study, we recruited eight subjects, all of whom underwent MRI scans both before and after surgical intervention. To maintain the integrity of a double-blind study, the subjects were initially classified as NPH patients. This blinding was essential to ensure unbiased analysis and to prevent any preconceptions from influencing the evaluators' interpretations of the imaging data. Pre- and post-operative scans were provided to the analysts without disclosure of the subjects' temporal status, reinforcing the reliability of the comparative assessments. All imaging sessions were conducted using a 3 Tesla Philips Elition X MRI system, ensuring high-resolution images for detailed analysis.

5.2.2 Imaging Protocols

In this study, we employed cardiac-gated whole-brain cine bSSFP MRI using a high-performance 3 Tesla Philips Elition X system (Best, Netherlands) to acquire detailed 3D volumetric data of the brain's intrinsic motion. The imaging sequence was synchronized with the subject's cardiac rhythm via a pulse oximeter, ensuring precise alignment of the MRI data with the heartbeat. Imaging parameters included an acquisition matrix of 240×173, a flip angle of $26°$, a field of view of $240 \times 240 \times 176\,\mathrm{mm}^3$, and a pixel bandwidth of $\pm 990\,\mathrm{kHz}$. Temporal resolution ranged from 40 to 60 ms, depending on the subject's heart rate, and data acquisition covered 80 slices with a spatial resolution of $1 \times 1 \times 1.25\,\mathrm{mm}^3$. Repetition time (TR) and echo time (TE) were set at 4.5 ms and 2.2 ms, respectively. Retrospective cardiac gating was performed using a pulse pressure unit (PPU) with a compression sensing (CS) factor of 3, capturing data over three cardiac cycles, each with 30 heart phases.
This sophisticated imaging protocol provided a comprehensive evaluation of the brain's mechanical behavior throughout the cardiac cycle, offering critical insights into neurological conditions and aiding the assessment of therapeutic interventions. All MRI acquisitions and data analyses were conducted blinded to the clinical and shunt status. Routine clinical evaluations of NPH, including timed gait tests, were performed both before and three months after shunt surgery.

5.2.3 3D aMRI Analysis of NPH in vivo Data

We analyzed displacement in all brain regions by measuring the displacement at each voxel over time, and then calculated the maximum displacement magnitude in three directions. For each region, we also extracted masks for the whole brain and specific substructures to compare the displacement magnitudes before and after surgery.
To ensure the reliability of our comparisons, we performed several types of analyses. First, we calculated the mean of the maximum displacement values, followed by the maximum of the maximum displacements. Additionally, we applied z-score normalization to standardize the data and ensure that the distribution of displacement magnitudes was approximately normal. To further reduce the impact of outliers, we performed an interquartile range (IQR) analysis. This step allowed us to remove extreme values and ensure that the displacement

data reflected the true distribution of the underlying measurements.

Once we had processed the data, we compared the pre- and post-surgery displacement patterns across all regions to determine whether any specific patterns of brain motion could be identified. Since this was a blind study, meaning the research team did not know whether each patient had undergone successful treatment, the analyses were conducted without prior knowledge of the outcomes. This allowed for an unbiased comparison of brain motion before and after surgery, helping to reveal any significant changes that might serve as indicators of surgical success. By identifying changes in brain displacement patterns, we hope to gain a better understanding of which factors contribute most to the success of shunt surgery in NPH patients. For all *in vivo* analyses, the 3D cine MRI data were amplified using an amplification factor $\alpha = 8$ and a frequency band f within the range [0, 4] Hz. This amplification factor was selected based on phantom simulations, which demonstrated a linear correlation between the amplified displacement and α when α was within [0, 10]. Both *in vivo* and phantom data remained free of artifacts within these settings. The frequency band was chosen based on observed peak displacements occurring within this range, corroborating previous studies that noted significant brain displacement within these frequencies. This frequency band correlates closely with the resting heart rate, typically around 1–2 Hz, and the dynamics of CSF circulation, which also falls within this selected frequency band.

For the processing and analysis of the acquired MRI data, we developed specialized scripts using MATLAB (versions R 2024a and R 2023a). These scripts were specifically designed to handle the large datasets typical of dynamic cine MRI, enabling the extraction and amplification of subtle physiological movements within the brain's structure. This in-house software facilitated a detailed examination of the biomechanical properties of brain tissue, essential for assessing the efficacy of ventriculoperitoneal shunting in our study participants. The *in vivo* analysis was conducted in three distinct phases:

1. Initially, 3D aMRI technique was applied to the 3D cine MRI data to assess and compare the image quality of the amplified results. For the 3D aMRI algorithm, the entire brain volume from the 3D cine MRI was amplified, and the temporal SNR map for the mid-sagittal slice was generated. For baseline 2D aMRI analysis, sagittal slices

from the 3D cine MRI data were individually amplified in two dimensions, and the temporal SNR for the mid-sagittal slice was subsequently calculated.

2. An image registration algorithm based on the Demons algorithm was then implemented on the amplified data to quantify the overall 3D brain displacements in subjects.

This analysis builds upon earlier validations conducted by our team, which included extensive testing using phantom models and assessments with healthy human subjects in prior studies.

In this study, the 3D cine MRI data from participants were processed using the 3D aMRI algorithm. Consistent with previous protocols, we set the amplification factor (α) to 8 and selected a frequency band from 0 to 4 Hz (see Section 5.1.4). Following amplification, we applied the Demons registration algorithm to quantify the 3D brain displacements of these individuals. We specifically focused on analyzing the displacement in ten critical brain regions: CC and its upper and lower intersections with the ventricle, brainstem, pons, cerebellum, central sulcus, precentral gyrus, postcentral gyrus, cerebral cortex, frontal gyrus, and the entire brain. These regions were selected based on prior research suggesting potential volume changes in NPH patients [219].

To accurately measure displacements in these regions, we utilized a semi-automated brain segmentation approach. Initially, T1-weighted MRIs of each subject were processed using FreeSurfer to extract the masks. For patients where the generated masks were inadequate—nearly all cases—manual segmentation was performed for each subject. These masks were subsequently refined manually to ensure greater precision.

Subsequently, an automatic intensity-based image registration method was employed in MATLAB (MathWorks, Natick, MA, version R2020b) to align the T1-weighted MRI of each participant with their corresponding 3D cine MRI data. The transformation matrix derived from this registration was applied to the masks, adapting them for use with the 3D cine MRI data. Each mask underwent manual inspection to verify its accuracy within the 3D cine MRI context. Finally, the anterior-posterior (AP), superior-inferior (SI), medial-lateral

(ML), and magnitude of displacement for these four brain structures were computed. To calculate the displacement magnitude $|U(x, y, z, t)|$, we employed the following formulation:

$$|U(x, y, z, t)| = \sqrt{U_{\mathrm{AP}}(x, y, z, t)^2 + U_{\mathrm{SI}}(x, y, z, t)^2 + U_{\mathrm{ML}}(x, y, z, t)^2} \tag{5.5}$$

where $U_{\mathrm{AP}}(x, y, z, t)$, $U_{\mathrm{SI}}(x, y, z, t)$, and $U_{\mathrm{ML}}(x, y, z, t)$ represent the anterior-posterior (AP), superior-inferior (SI), and medial-lateral (ML) displacements of the regions of interest, respectively.

Then, multiple preliminary analyses were performed on the MRI data, which included techniques such as IQR filtering, Min-Max normalization, and Z-score normalization. These methods were applied to effectively quantify brain displacement and deformation, thereby preparing the data for subsequent analysis stages. These methodologies and their implications will be briefly elaborated on in the following sections.

5.2.4 Interquartile Range Filtering

We also looked at other critical regions such as the pons and cerebellum. Here, we extracted the maximum displacement magnitude for all pixels within these regions. To ensure accuracy and reduce the impact of outliers, we applied an IQR analysis. This method helped us remove the highest and lowest values, focusing on the most consistent data.

5.2.5 MinMax Normalization

We did Min-Max normalization scales the data between the observed minimum ($U_{\min}$) and maximum ($U_{\max}$) values. Min-Max normalization is a data preprocessing technique that scales individual feature values to a specified range, typically between 0 and 1. This is achieved by subtracting the minimum value of the feature from each data point and then dividing by the range (the difference between the maximum and minimum values) using Eq.5.6. While we performed this analysis, it became clear that using normalized values is not an effective method for comparing images pre- and post-surgery for the same patient, as it obscures the actual changes in displacement that occurred. It is essential to know the real increase or decrease in measurements rather than relying solely on normalized values. After unblinding this study, normalized values may still be useful for comparisons among differ-

ent regions across all cases pre- and post-surgery, especially for analyses aimed at defining changes within a subject. For example, if researchers want to assess the maximum displacement of the CC in relation to the whole brain pre-surgery and compare it to the maximum displacement of the CC post-surgery, the results of this normalization can provide valuable insights.

$$U_{\text{norm}} = \frac{(U - U_{\text{min}})}{(U_{\text{max}} - U_{\text{min}})} \tag{5.6}$$

5.2.6 Z-Score Normalization

In my analysis, we employed Z-score normalization, also referred to as standard score normalization. This statistical technique was crucial for standardizing the data by recalculating each value to express its deviation from the mean in terms of standard deviations. The procedure began by determining the mean (μ) and standard deviation (σ) of the dataset. Subsequently, We adjusted each data point x_i to its normalized value z_i using the formula:

$$Z = \frac{(U - \mu)}{\sigma} \tag{5.7}$$

where μ is the mean of the dataset, and σ is the standard deviation. This transformation standardized the dataset to a mean of 0 and a standard deviation of 1, facilitating a uniform scale across different units or scales. This normalization not only helps in standardizing the data but also enables me to identify potential outliers, as any significant deviations from the mean will be evident in the normalized scores. The zero mean of the Z-scores suggests that the values we are averaging are either very close to each other, or there is a balanced distribution of positive and negative values, effectively neutralizing each other. This insight is crucial for confirming the homogeneity or identifying anomalies within the dataset.

5.2.7 Displacement Magnitude of the Amplified Data

After using FreeSurfer to extract masks (see Section 5.2.3), we noticed that the software did not capture the entire mask of the region. Because of this, we had to individually check each slice and manually extract the masks. After completing these preprocessing steps, we were able to extract the masks for the regions of interest and additional areas suggested by the neurosurgeon.

5.2.7.1 Displacement Magnitude in the Regions of Interest

For further analysis, we selected multiple regions, including the whole brain. These regions were chosen based on recommendations from neurosurgeons as well as findings from previous studies. Prior research has highlighted changes in ventricular volume following shunt placement, identifying potential areas for displacement analysis in pre- and post-shunt surgeries [219]. The regions of interest included the upper and lower intersections of the CC and ventricle, brainstem, pons, cerebellum, central sulcus, precentral gyrus, postcentral gyrus, cerebral cortex, frontal gyrus, and the entire brain.

5.2.7.2 Maximum Displacement Magnitude in the Mid-Sagittal Slice

As explained in Section 5.2.3, we initially extracted the maximum displacement magnitude of all voxels within the regions of interest across the cardiac cycle, as we defined in Eq. 5.5. Following this, we focused on the mid-sagittal slice, as it was recommended by the neurosurgeon for providing clearer insights. For this slice, we reported the maximum displacement magnitude. It is important to note that all these values were obtained after applying IQR analysis to ensure the accuracy and consistency of the results.

5.2.7.3 Mean Maximum Displacement Magnitude for the 10% of Slices Adjacent to the Mid-Sagittal Slice

Since the mid-sagittal slice may vary slightly between patients, relying solely on this slice could lead to inconsistent assessments of displacement. To address this, we included 10% of the slices adjacent to the mid-sagittal slice in the sagittal plane. For each slice in this selection, we identified the maximum displacement value and then calculated the mean of these maximum values across all slices. This approach provides a more robust and accurate determination of displacement.

5.2.8 Evaluation of Surgical Outcomes in NPH Patients Using ROC Curve and Correlation Analysis

In assessing the effectiveness of surgical interventions for patients with NPH, Receiver Operating Characteristic (ROC) curve analysis was utilized to measure the discriminative

power of clinical and aMRI-derived metrics. The Area Under the Curve (AUC) was specifically computed to evaluate the ability of these metrics to differentiate between improved and unimproved patient outcomes post-surgery. The ROC analysis incorporated both clinical outcomes and aMRI measurements from the frontal gyrus and whole brain across the mid-sagittal slice and adjacent slices. Additionally, Spearman's rank correlation was applied to ascertain the statistical significance of the findings, helping to confirm the reliability and importance of the results in predicting surgical benefits.

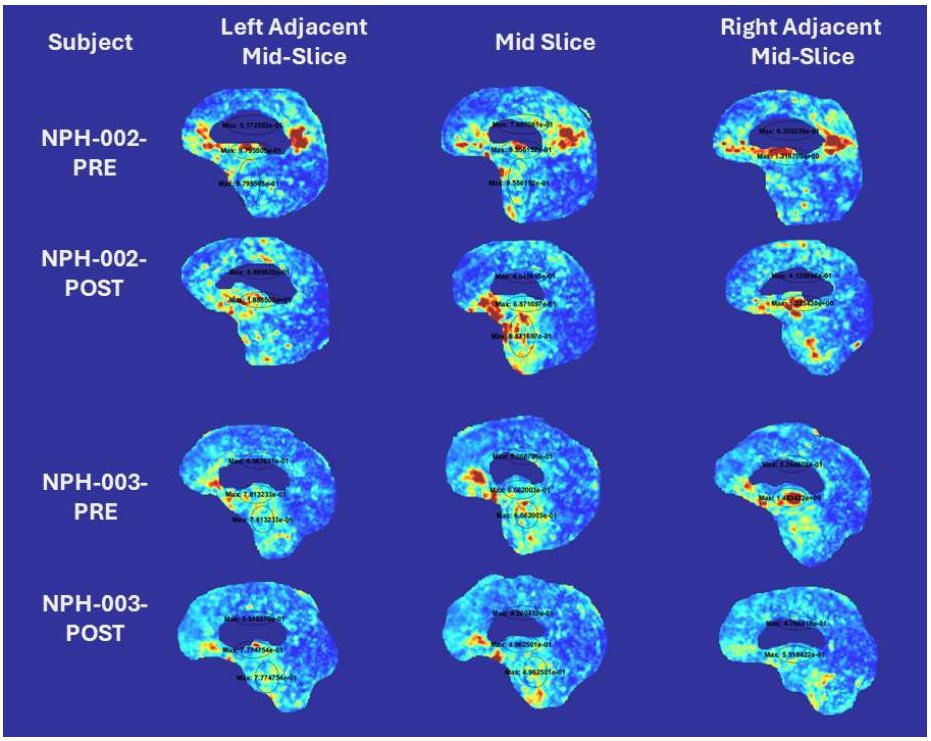

Figure 5.2: Maximum displacement of brain regions pre- and post shunt surgeries in subjects 2 and 3

5.3 Results

5.3.1 Displacement and In Vivo Motion Changes of NPH Patients Pre- and Post-Shunt Surgery

The initial hypothesis aimed to identify changes in brain displacement or specific subregions following shunt surgery. In some cases, increased displacement was observed in the upper section of the CC and ventricles, although this pattern was not consistent across subjects. In the majority of cases, the brainstem exhibited greater displacement post-surgery. However, as this was a blinded study, these observations could not definitively confirm or

refute the hypothesis. In patients 2 and 3 we saw slightly increase in the entire brain's displacement (Fig. 5.2). Notably, in patients 4 and 5 (Fig. 5.3, the displacement maps clearly revealed reduced displacement, even upon initial inspection. Conversely, patient 8 demonstrated a marked increase in displacement in the brainstem region following surgery, aligning partially with the initial hypothesis. In patients 6 and 8, there was not a significant change in the displacement pattern pre- and post-surgery (Fig. 5.4). These findings highlight the variability in displacement patterns and underscore the need for further investigation to interpret these changes in the context of clinical outcomes.

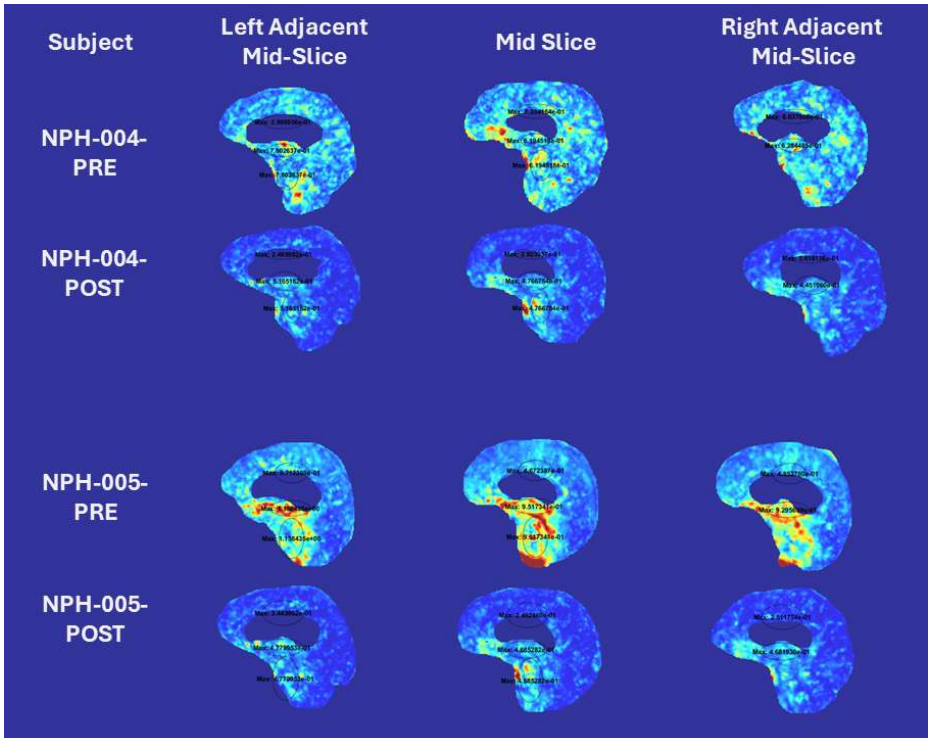

Figure 5.3: Maximum displacement of brain regions pre- and post shunt surgeries in subjects 4 and 5

5.3.2 Results of the Maximum Displacement Magnitude in the Mid-Sagittal Slice

The data in table 5.1 presents both increases and decreases in displacement magnitudes across different brain regions for each patient, represented by color gradients from red (indicating significant decreases) to green (indicating increases). The results are visualized in 2D (Fig. 5.5) and 3D (Fig. 5.6).

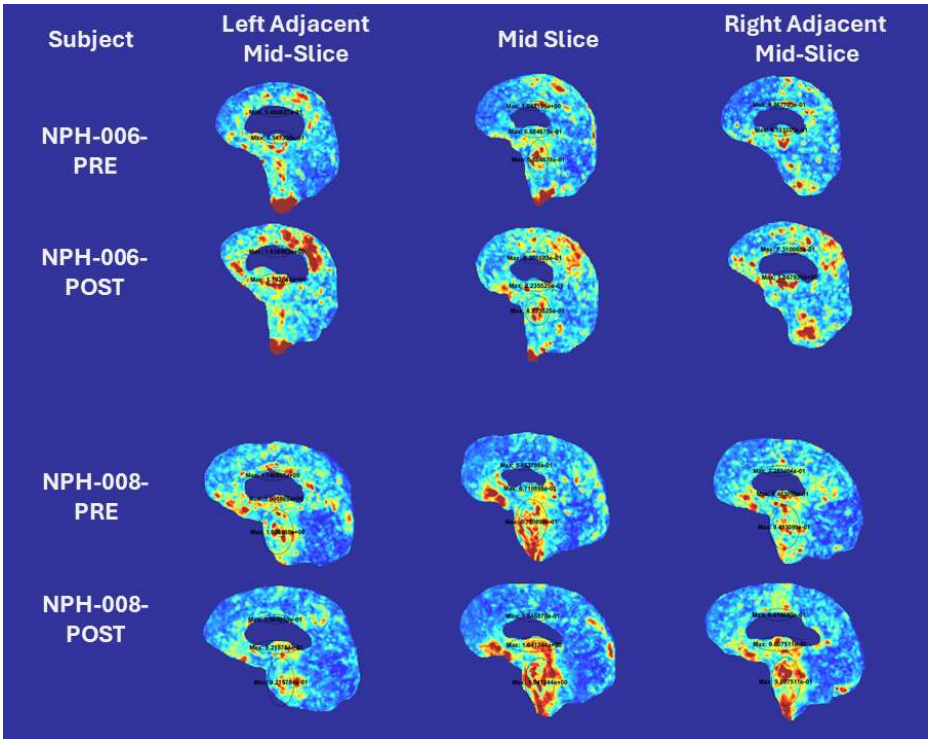

Figure 5.4: Maximum displacement of brain regions pre- and post shunt surgeries in subjects 6 and 8

5.3.2.1 Patient-Specific Trends

In subject NPH-2, significant reductions in displacement magnitude were observed in the upper and lower intersections of the CC, central sulcus, postcentral gyrus, and cortex (-75%, -39%, -45%, -34%, and -28% respectively). However, notable increases were present in regions such as the brainstem (32%), pons (33%), cerebellum (37%), and whole brain (25%) indicating differential regional responses to the shunt surgery. Subject NPH-3 displayed generally mild changes, with a maximum decrease of -35% in the lower CC intersection and slight increases in the pons (4%). The displacement changes here were less pronounced overall, suggesting a more stable or less variable response to treatment. Subject NPH-4 exhibited the most substantial negative shifts, with extreme reductions in regions like the upper CC intersection (-151%), cerebellum (-60%), and precentral gyrus (-114%). These huge decreases might suggest potential complications or a significant alteration in brain biomechanics post-surgery which also might be relevant to the blind nature of the study. In subject NPH-5 consistently large decreases were observed across almost all regions, with the

Table 5.1: Percentage change in maximum displacement magnitude pre- and post-shunt surgery across various regions for different patients, focusing on the mid-slice in the sagittal plane

	CC Upper Intersection	*CC Lower Intersection*	*Brainstem*	*Pons*	*Cerebellum*	*Central Sulcus*	*Precentral Gyrus*	*Postcentral Gyrus*	*Cortex*	*Frontal Gyrus*	*Whole Brain*
NPH-2	-75%	-39%	32%	33%	37%	-45%	-6%	-34%	-28%	-11%	25%
NPH-3	-23%	-35%	-1%	4%	-1%	-19%	-4%	-26%	-5%	-8%	11%
NPH-4	-151%	-24%	-17%	-45%	-60%	-151%	-114%	-107%	-70%	-83%	1%
NPH-5	-80%	-96%	-70%	-67%	-133%	-83%	-105%	-40%	-67%	-53%	-85%
NPH-6	-29%	6%	-1%	-12%	-15%	-17%	23%	13%	10%	0%	1%
NPH-8	11%	32%	21%	14%	35%	11%	19%	4%	6%	6%	-7%

cerebellum experiencing the highest reduction at -133%. The widespread nature of these reductions suggests a considerable shift in brain dynamics following the surgical intervention. Subject NPH-6 showed a mixed pattern, with moderate decreases in areas like the pons (-12%), cerebellum (-15%), central sulcus (-17%) but a notable increase in the precentral gyrus (23%). The combination of positive and negative changes may indicate a varied mechanical response throughout the brain. Subject NPH-8 showed a positive trend across most regions, with significant increases in the cerebellum (35%) and brainstem (32%). The overall increase in displacement suggests a potentially favorable biomechanical outcome from the shunt surgery.

5.3.2.2 Regional Observations

CC Intersections: Most patients, particularly NPH-4 and NPH-5, experienced substantial decreases in displacement magnitudes, implying that the CC region is heavily affected by the shunt surgery.

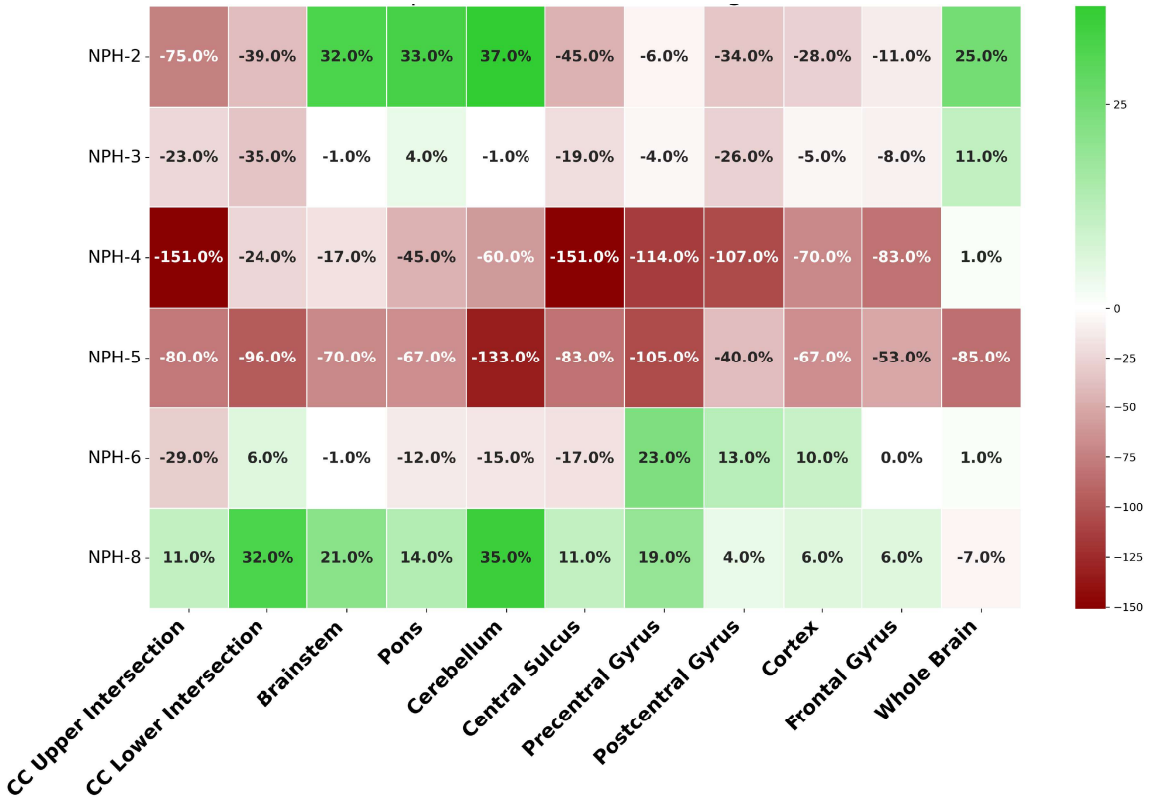

Figure 5.5: Percentage change in maximum displacement magnitude pre- and post-shunt surgery visualized using a 2D heatmap across various regions for different patients, focusing on the mid-slice in the sagittal plane.

Brainstem and Pons: Changes in these areas were less consistent, with some patients like NPH-8 showing considerable increases, while others, such as NPH-4 and NPH-5, displayed decreases. This variability might reflect differences in how cerebrospinal fluid dynamics influence brainstem regions.

Cerebellum: The cerebellum frequently showed large percentage changes, either positive or negative, across the patient cohort. The most extreme reductions were seen in NPH-4 and NPH-5, while NPH-8 showed notable increases.

Precentral and Postcentral Gyri: These regions displayed significant variability, with NPH-4 and NPH-5 exhibiting large decreases, whereas NPH-6 and NPH-8 had increases. This variability could reflect differences in cortical tissue responses post-surgery.

The results from different regions and across various patients demonstrate a highly individualized biomechanical response, which may be associated with shunt surgery in NPH

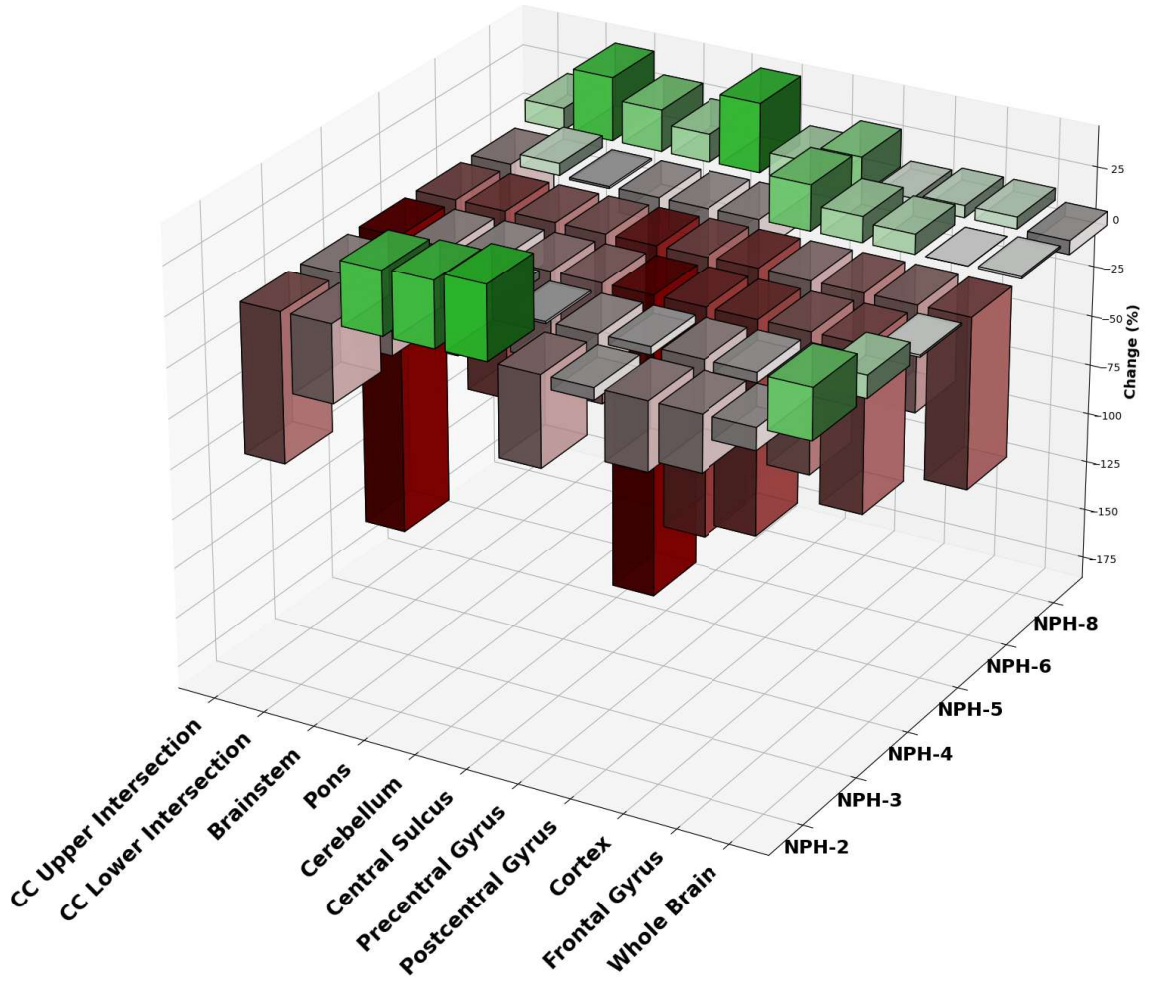

Figure 5.6: Percentage change in maximum displacement magnitude pre- and post-shunt surgery visualized using a 3D heatmap across various regions for different patients, focusing on the mid-slice in the sagittal plane. The height of the bars represents the magnitude of the change difference, while the color intensity indicates the significance or degree of these changes.

patients. However, given the blind nature of this study, there remains uncertainty about whether the presented cases represent true pre- and post-shunt conditions or if the shunt was activated in all instances. The observed variability in displacement magnitudes emphasized the need for region-specific analysis to better understand these changes.

Moreover, certain regions, such as the corpus callosum and cerebellum, seem more sensitive to these potential interventions, while others, like the pons and cortex, show greater variability. These findings point to the complex nature of brain biomechanics in NPH, high-

Table 5.2: Percentage change in maximum displacement magnitude pre- and post-shunt surgery across various regions for different patients, focusing on the mean of the maximum values from 10% of the slices adjacent to the mid-slice in the sagittal plane.

	CC Upper Intersection	*CC Lower Intersection*	*Brainstem*	*Pons*	*Cerebellum*	*Central Sulcus*	*Precentral Gyrus*	*Postcentral Gyrus*	*Cortex*	*Frontal Gyrus*	*Whole Brain*
NPH-2	-10%	-38%	32%	33%	33%	-12%	8%	-21%	-9%	8%	7%
NPH-3	-20%	-33%	3%	4%	-5%	-7%	1%	-15%	-8%	-15%	1%
NPH-4	-125%	-39%	-10%	-21%	-76%	-165%	-134%	-121%	-76%	-92%	-28%
NPH-5	-86%	-108%	-55%	-57%	-142%	-70%	-92%	-48%	-56%	-52%	-105%
NPH-6	-3%	8%	-4%	-7%	-6%	14%	19%	19%	13%	4%	1%
NPH-8	-22%	15%	12%	12%	26%	-2%	-1%	-20%	3%	0%	-3%

lighting the importance of personalized assessment approaches. Further, a more detailed statistical analysis, coupled with verification of clinical parameters and outcomes, could provide a clearer understanding of these biomechanical alterations.

5.3.3 Results of the Mean Maximum Displacement Magnitude for the 10% of Slices Adjacent to the Mid-Sagittal Slice

The results presented in table 5.2, and Fig. 5.7 and Fig. 5.8 summarize the percentage change in maximum displacement magnitude across various brain regions for different NPH patients. These results were calculated based on the mean of the maximum values from 10% of slices adjacent to the mid-sagittal slice, a method chosen to mitigate errors from inconsistencies in identifying the exact mid-slice across different patients. This approach provides a more reliable and consistent assessment of regional changes in brain displacement.

5.3.3.1 Patient-Specific Trends

Subject NPH-2 showed moderate displacement changes, with regions like the brainstem, pons, and cerebellum displaying increases (32%, 33%, and 33%, respectively), while areas such as the CC upper and lower intersections, central sulcus, and postcentral gyrus demonstrated significant negative changes (-10%, -38%, -12%, and -21% respectively). These findings suggest a mixed biomechanical response, with some areas potentially recovering or stabilizing post-surgery, while others exhibit considerable decreases. The trends for patient NPH-3 indicated relatively stable changes, with minimal positive and negative shifts. Regions like the brainstem and pons have negligible changes (3% and 4%, respectively), while the CC upper and lower intersection, cerebellum, postcentral gyrus and frontal gyrus show more notable decreases (-20%, -33%, -5%, -15% and -15%). This patient's data may reflect a more uniform biomechanical response with fewer extreme variations. Patient NPH-4 stood out for exhibiting the most pronounced negative changes across nearly all regions, with extreme reductions in the cerebellum (-165%), precentral gyrus (-134%), CC upper intersection (-125%), postcentral gyrus (-121%), frontal gyrus (-92%), and cortex (-76%). These substantial decreases may suggest severe alterations or potential complications post-surgery, warranting further investigation. Similar to NPH-4, patient NPH-5 also showed significant negative changes, in all regions including cerebellum (-142%), the CC lower intersection (-108%), whole brain (-105%), precentral gyrus (-92%), CC upper intersection (-86%), central sulcus (-70%) and pons, brainstem, cortex, frontal gyrus, and postcentral gyrus (-57%, -55%, -56%, -52%, and -48% respectively). The consistent downward trends across multiple regions highlight a more uniform decline in displacement magnitudes. The displacement changes for patient NPH-6 were more moderate, with small positive shifts observed in regions like the brainstem (8%), cortex (13%), central sulcus (14%), precentral gyrus (19%), and postcentral gyrus (19%). The relatively balanced nature of these changes may indicate a more stable biomechanical state post-surgery. Patient NPH-8 displayed mixed results, with increases in the cerebellum (26%), CC lower intersection (15%), brainstem (12%), and pons (12%), and slight decreases in regions like the cortex (-2%) and CC upper intersection (-22%). These variations suggested a differential biomechanical response depending on the

region.

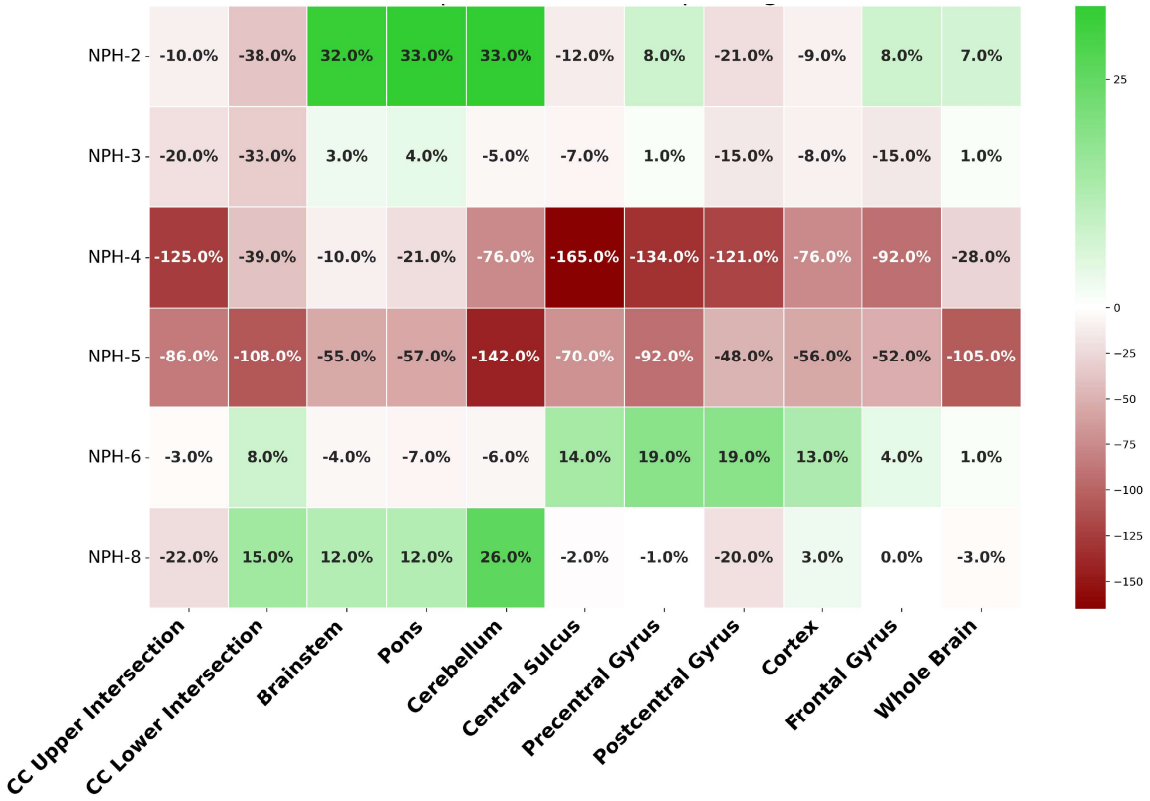

Figure 5.7: Percentage change in maximum displacement magnitude pre- and post-shunt surgery visualized using a 2D heatmap across various regions for different patients, focusing on the mean of the maximum values from 10% of the slices adjacent to the mid-slice in the sagittal plane.

5.3.3.2 Regional Observations

CC Intersections: Both the top and bottom CC intersections consistently show negative changes across most patients, with extreme reductions noted in NPH-4 and NPH-5. This trend indicates that the CC may be highly sensitive to shunt surgery or fluid dynamics alterations.

Brainstem and Pons: These regions generally display moderate increases or stable values, with NPH-2 and NPH-6 showing positive displacement changes. This suggests a potential recovery or normalization of movement in these areas for some patients.

Cerebellum: The cerebellum exhibits the most dramatic variations, with significant nega-

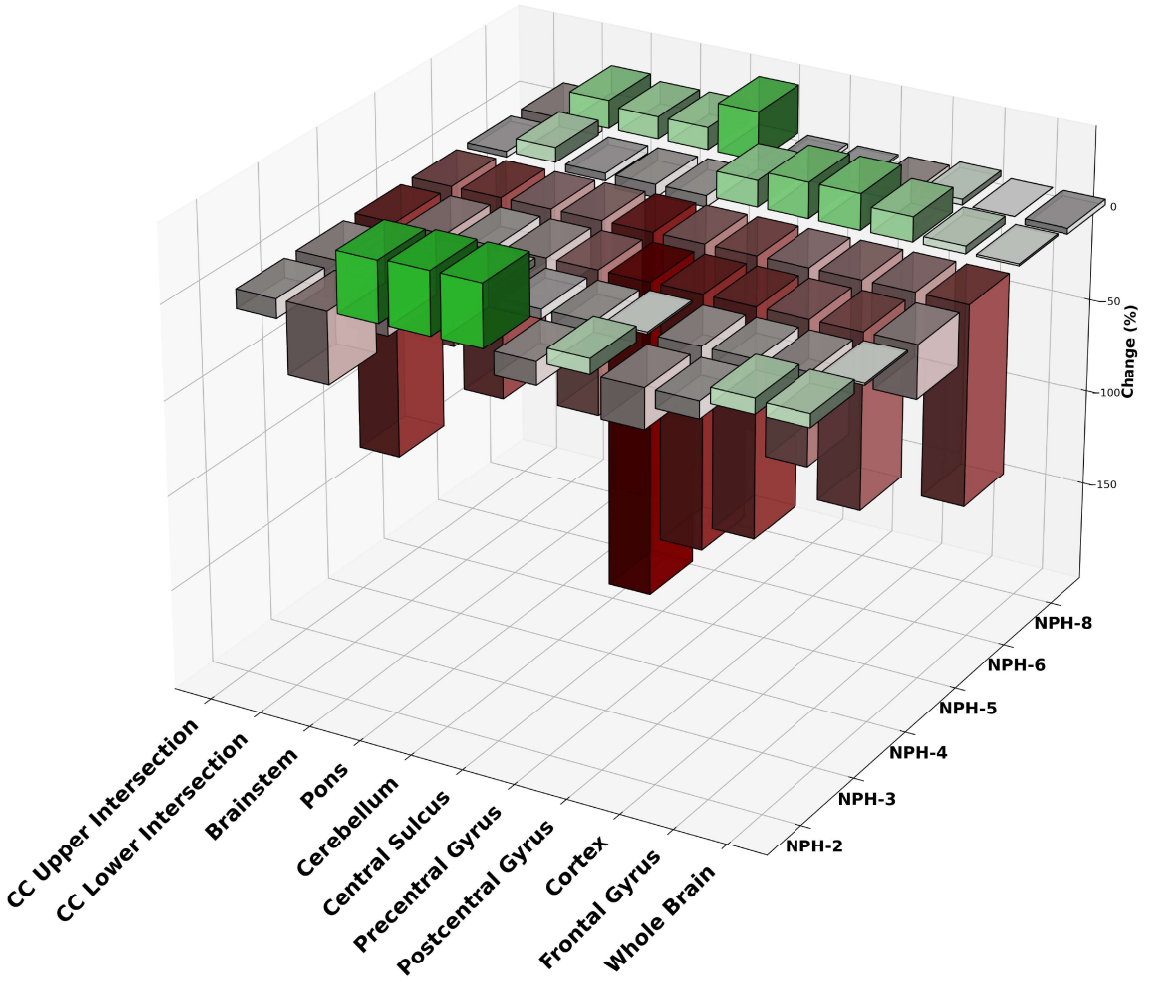

Figure 5.8: The percentage change in maximum displacement magnitude pre- and post-shunt surgery visualized using a 3D heatmap across various regions for different patients, focusing on the mean of the maximum values from 10% of the slices adjacent to the mid-slice in the sagittal plane. The height of the bars represents the magnitude of the change difference, while the color intensity indicates the significance or degree of these changes.

tive changes for NPH-4 and NPH-5, contrasting with positive shifts for NPH-2 and NPH-8. This variability underscores the cerebellum's complex response to shunt surgery.

Central Sulcus and Precentral Gyrus: These regions show more stable or positive trends, with notable increases in NPH-6 and NPH-8. These areas may be less affected by surgery or may reflect compensatory biomechanical changes.

Table 5.3: AUC and p-values for aMRI Metrics: This table shows the AUC and p-value for the percentage differences in maximum displacement magnitudes of the frontal gyrus and whole brain, identified as key indicators in both the mid-sagittal slice and 10% of the slices adjacent to the mid-sagittal slice. The percentage difference of the whole brain in the Mid-Sagittal slice exhibits the highest AUC, with a p-value that indicates a statistically significant difference.

aMRI Metric		**AUC**	**p-value**
Mid-Sagittal Slice	Percentage difference in Frontal Gyrus	0.5	0.54
	Percentage difference in Whole Brain	1	0.01
Multiple Slices adjacent to the Mid-Sagittal Slice	Percentage difference in Frontal Gyrus	0.75	0.62
	Percentage difference in Whole Brain	0.94	0.17

5.3.4 Analysis of Key Indicator Factors for Predicting Surgical Outcomes: Clinician's Insights and ROC Correlation

In a fully blinded way, three out of five subjects had their shunts deliberately set to the "off" position for the first three months following ventriculoperitoneal shunt (VPS) placement as part of a randomized clinical trial. All data analyses were conducted by analysts who were blinded to the shunt status. These three subjects exhibited impaired ventricular displacement on aMRI scans obtained three months post-VPS, corresponding with clinical metrics indicative of NPH. After the shunts were activated, all three subjects showed improvement in clinical measures of NPH at six months post-surgery, reflecting the impact of the shunt activation.

As shown in Table 5.3, the percentage difference in the whole brain for the mid-sagittal slice showed the highest AUC value with a statistically significant p-value of 0.01. Additional analyses demonstrated that the percentage difference in the whole brain across slices adjacent to the mid-sagittal slice had the second-highest AUC, though this result did not reach statistical significance.

Two subjects, NPH-1 and NPH-7, could not safely return for their post-shunt MRI scans due to complex medical conditions, leaving six subjects available for displacement analysis. Figure 1 visualizes displacement magnitude variations across brain regions for these six subjects. These variations are depicted across multiple slices, including and adjacent to the mid-sagittal slice, with a color gradient indicating the extent of changes—red for significant decreases and green for increases. Negative displacement changes were most notable at the upper and lower intersections of the corpus callosum, particularly in NPH-4 and NPH-5.
These analyses compared findings from aMRI with clinical notes provided by physicians and data obtained from objective clinical metrics (Table 5.3). Among the evaluated parameters, the percentage difference in maximal whole-brain displacement at the mid-sagittal slice demonstrated the highest discriminative power, reflected by a statistically significant AUC value ($p = 0.01$). This result underscores the potential of aMRI-derived displacement measures as reliable indicators of shunt efficacy, with increased whole-brain displacement serving as a marker of improved post-surgical functionality.
These findings highlight the capability of aMRI metrics to act as valuable non-invasive indicators of successful shunt surgery, offering an objective means to evaluate surgical outcomes. By providing insights into VPS functionality, aMRI measures have the potential to enhance patient management strategies, allowing for more effective clinical decision-making to optimize outcomes for individuals undergoing shunt placement.

5.3.5 Further Analysis: Extracting Motion Data that Represents the Physiological Dynamics of the Brain

Previous studies have demonstrated the effectiveness of Proper Orthogonal Decomposition (POD) analysis for assessing brain motion patterns, as seen in work by Abderezaei et al. [1, 103]. Given that 3D aMRI captures and enhances brain motion in three directions, we hypothesized that applying POD analysis to 3D aMRI displacement fields would reveal more comprehensive motion data, reflecting physiological dynamics and directional coupling more accurately than 2D aMRI. In a similar approach, we used modal analysis to examine the brain's intrinsic motion in response to cardiac pulsatility. Modal decomposition, frequently applied in structural dynamics for dynamic characterization and model

order reduction, has also been used to investigate brain dynamics following head impacts. To test this, we applied POD to the displacement fields from 3D aMRI. We extracted the primary modeshapes, $v_{1,3D}(x, y, z)$ and $v_{1,2D}(x, y)$, and calculated the energy contributions from these modeshapes. We applied this technique to characterize the brain's response to heartbeat-induced motion, isolating distinct patterns of motion and deformation. Through this method, we extracted key motion modes, enabling a reduction in data complexity while retaining critical insights into brain motion.

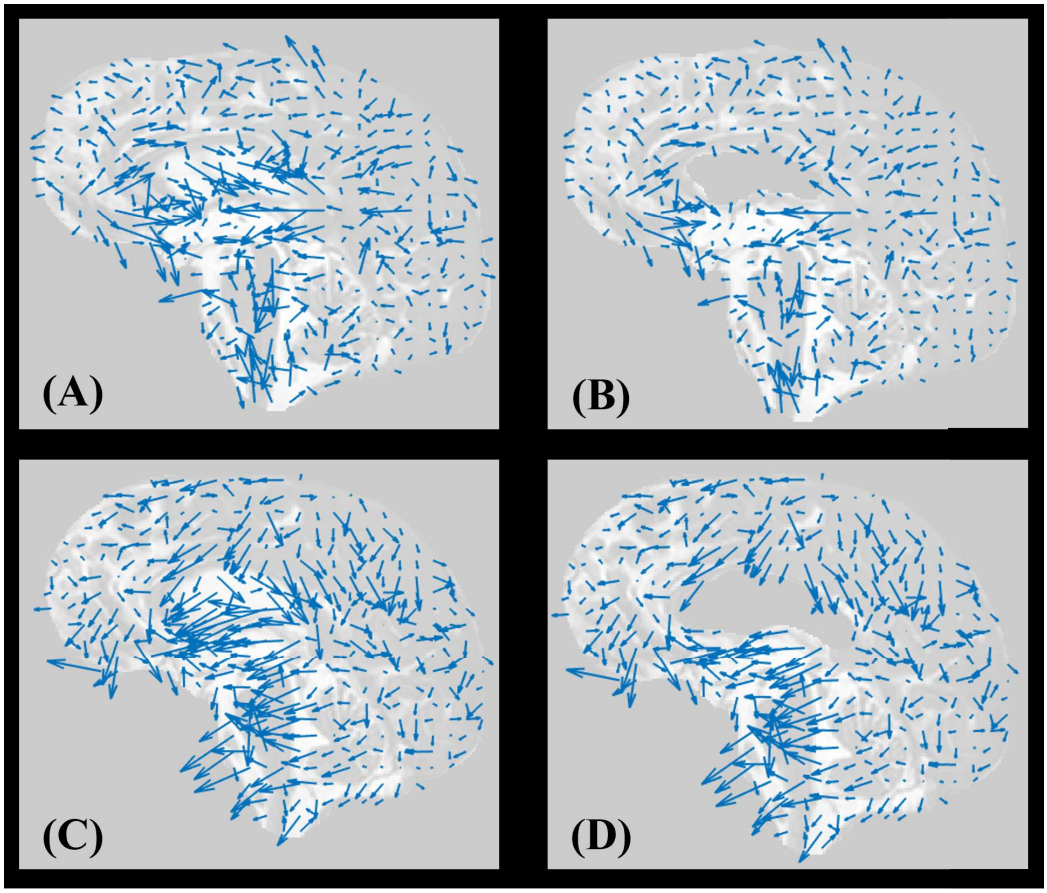

Figure 5.9: 1st modeshape of 3D amplified cine MRI for an NPH patient before and after shunt surgery. (A) 1st modeshape of 3D amplified cine MRI pre-shunt, with CC included. (B) 1st modeshape of 3D amplified cine MRI pre-shunt, with CC excluded. (C) 1st modeshape of 3D amplified cine MRI post-shunt, with CC included. (D) 1st modeshape of 3D amplified cine MRI post-shunt, with CC excluded.

Applying POD analysis on this dataset, including NPH patients, can help establish more

precise metrics for assessing shunt intervention success. This analysis was conducted on all available datasets at the time of writing; however, since the study remains in a blind state, we were unable to identify clear patterns or major takeaways from these results. The POD quiver plots are presented in Fig. 5.9. Our primary hypothesis for a successful surgery is that the quiver plots would resemble those of a healthy patient. However, this hypothesis requires further validation, and a more rigorous quantification of these quiver plots is recommended for future studies to determine their effectiveness as a reliable metric.

There were several

5.4 Discussion

In this pilot study, we explored the applicability of aMR as a marker of pulsatile ICP and ICC in the assessment of NPH, prior to and after VP shunt placement, and have demonstrated that obtaining MRIs in this patient population is feasible. In this part of the project, which primarily aimed to demonstrate the feasibility of MR imaging within this specific patient population, key aMRI metrics were identified that appear to correlate with functional VPS status. Notably, these metrics proved valuable in distinguishing shunts that were effectively in a virtual "off" position, thereby providing insights into the shunt's functional status post-surgery. Among the metrics evaluated, the percentage difference in maximal whole-brain displacement at the mid-sagittal slice showed the highest discriminative power, reflected by an Area Under the Curve (AUC) value that was statistically significant ($p = 0.01$). This finding highlights the potential of aMRI-derived displacement measures in assessing shunt efficacy, suggesting that increased whole-brain displacement may serve as an indicator of improved post-surgical functionality. Such insights offer promise for using aMRI as a non-invasive tool for monitoring VPS status in real time, helping to refine patient management and optimize clinical outcomes. Further studies with larger patient cohorts would be beneficial to validate these preliminary findings and potentially establish standardized aMRI metrics that could routinely assess shunt functionality in NPH patients. Future work will involve validation using advanced processing and computational fluid dynamics. During this part of my thesis, we faced several challenges and limitations. First, two participants were unable to safely undergo their post-shunt MR scans due to medical complications, likely impacting our ability to capture full longitudinal data for these cases. This highlights

a broader difficulty in performing follow-up imaging with neurodegenerative and medically vulnerable patient populations, where health conditions can prevent scheduled imaging sessions. Additionally, following shunt placement, several technical issues became apparent. The introduction of imaging artifacts and the often atypical morphology of the brain in these patients impeded the software's capability to automatically generate accurate masks for the brain and its subregions. So, masks had to be manually created, a labor-intensive and time-consuming process. This manual adjustment was critical to ensure accurate data for analysis but added significant effort to the workflow, underscoring the need for enhanced imaging techniques and software capable of accommodating such post-surgical alterations.

5.5 Conclusion

In this aim, we analyzed aMR images of NPH patients pre- and post-shunt surgery to identify indicators of surgical success and shunt activation status. Displacement was measured across brain regions by calculating the maximum displacement magnitude in three directions for each voxel over time. Masks for the whole brain and specific substructures were also extracted to compare displacement before and after surgery. Regions of interest, selected based on neurosurgeon input and prior studies, included areas like the corpus callosum, brainstem, pons, cerebellum, central sulcus, and frontal gyrus, with displacement calculated on the mid-sagittal slice and adjacent slices. This pilot study showed that key aMRI metrics correlated with functional VP shunt status, distinguishing shunts effectively in a virtual "off" position, with maximal whole-brain displacement showing the highest discriminative power (AUC, $p = 0.01$). These results support the potential of aMRI-derived displacement as a non-invasive tool for monitoring VPS efficacy in real-time. This work presented challenges, including two patients unable to complete post-shunt MR scans and imaging artifacts following surgery, which required time-consuming manual mask adjustments. Future work will validate these findings with larger patient cohorts and advanced computational techniques, like computational fluid dynamics, to refine aMRI metrics for assessing shunt functionality in NPH patients. We explored the applicability of aMR as a marker of pulsatile ICP and ICC in the assessment of NPH, prior to and after VP shunt placement, and have demonstrated that obtaining MRIs in this patient population is feasible. Future work will involve validation using advanced processing and computational fluid

dynamics. The findings discussed in this chapter have been previously published in several papers, including references [32, 220].

Chapter 6

TO IDENTIFY KEY BIOMARKERS AND SUBSTRUCTURAL MRI MORPHOMETRIC FEATURES FOR PREDICTING NEUROPSYCHOLOGICAL OUTCOMES IN CTE USING MACHINE LEARNING

6.1 Introduction

mTBI, also known as mild traumatic brain injury or concussion, is a prevalent condition with significant short- and long-term implications. When mTBI occurs repeatedly, referred to as repeated mTBI (RmTBI), it can result in cumulative and chronic neurological abnormalities which is particularly common among individuals engaged in contact sports like football, boxing, or ice hockey, as well as military veterans who have experienced multiple TBIs. Accurate assessment of mTBI severity and analysis of correlated factors, including biomarkers, are crucial for appropriate management and treatment decisions. Furthermore, repetitive head injuries, such as concussions or blows to the head, are closely associated with the development of a neurodegenerative condition called CTE. The hallmark of CTE is the accumulation of an abnormal protein called tau in the brain. Tau protein forms clumps or tangles, which disrupt normal brain function and result in the degeneration of brain tissue over an extended period. CTE is a neurodegenerative disease that, due to its inability to be diagnosed during a patient's lifetime, presents a significant challenge in both research and clinical settings. Identifying factors that may contribute to the presence of CTE during a patient's life is therefore of paramount importance. This portion of my PhD project focuses on addressing this challenge.

With recent advancements in ML algorithms, there is growing interest in leveraging these techniques to enhance the analysis of medical images [105] and improve the assessment of neurodegenrative conditions [109–113]. Deep learning algorithms, have transformed various fields by autonomously learning intricate patterns and features from extensive datasets. By analyzing diverse MRI features, these algorithms produce quantitative metrics that corre-

late with injury, offering an objective and consistent approach. These algorithms provide an objective and quantitative approach [108] to evaluate medical images and by analyzing a wide range of MRI features, these algorithms can generate quantitative metrics that correlate with injury, enabling more accurate and consistent assessments [105]. In the context of MRI analysis for mTBI, deep learning algorithms can be trained to extract meaningful information from MRI scans and aid in the identification of injury-related patterns.

Researchers have investigated different MRI-derived features to distinguish between normal brains and those affected by mTBI. These features encompass volumetric measurements of brain structures [114], texture analysis [115, 116], diffusion parameters for assessing white matter integrity [117], functional connectivity analysis to examine disruptions in brain networks, and the utilization of deep learning models to automatically extract relevant features. Ongoing research endeavors to refine these approaches, enhancing their accuracy, clinical utility, and ultimately improving mTBI diagnosis and patient management.

In this study, we utilized data from the DIAGNOSE CTE Research Project to predict selected neuropsychiatric and neurocognitive metrics using two categories of blood biomarkers, three categories of CSF biomarkers, and MRI morphometrics. By integrating these diverse data modalities, ML approaches enabled the prediction of neurocognitive and neuropsychiatric outcomes. These methods provided an objective framework for analyzing injury-related changes and contributed to the development of diagnostic and therapeutic strategies tailored to individual needs. Building upon prior research, this study leveraged ML models to evaluate the predictive potential of multimodal datasets from the DIAGNOSE CTE project, aiming to deepen the understanding of mTBI and its progression toward conditions such as CTE. The detailed characteristics of the features and metrics are outlined in Table A.1 to A.36, and the following sections provide a concise overview of the study's methodology and findings.

6.1.1 Selected Neuropsychiatric Measurements

The neuropsychiatric measures analyzed in this study, listed in table A.1, offer valuable insights into the emotional, behavioral, and psychological effects associated with CTE and concussion-related injuries. These metrics assess a range of neuropsychiatric symptoms,

including impulsivity, depression, anxiety, and overall emotional regulation, offering a comprehensive view of how traumatic brain injuries influence mental health and behavior.

Impulsivity and Behavioral Control metrics: The ABIS (Attentional, Motor, and Non-Planning Impulsiveness Factor Scores) and BIS-11 Total Score assess different dimensions of impulsivity, including attentional impulsivity (difficulty focusing or maintaining attention), motor impulsivity (acting without thinking), and non-planning impulsivity (lack of future-oriented thinking). These scores are particularly relevant in concussion and CTE studies, as impulsivity is often associated with frontal lobe dysfunction, a common consequence of head injuries. Increased impulsivity can lead to risky behaviors and impaired decision-making, which are critical factors in understanding the behavioral challenges faced by individuals with CTE.

Anxiety and Depression metrics: The BAI Total Score (Beck Anxiety Inventory) and BDI-II Total Score (Beck Depression Inventory) measure the severity of anxiety and depressive symptoms, respectively. These metrics are essential in assessing the emotional well-being of individuals with a history of traumatic brain injuries, as anxiety and depression are frequently reported in patients with CTE and concussions. High scores on these scales can indicate the need for targeted interventions to improve mental health outcomes in this population.

Hopelessness and Aggression metrics: The BHS Total Score (Beck Hopelessness Scale) evaluates feelings of hopelessness, often linked to depression and suicide risk. This measure is particularly significant in CTE studies, given the elevated suicide rates observed among individuals with the condition. Similarly, the BDHI Total Score (Buss-Durkee Hostility Inventory) assesses aggression and hostility levels, which may reflect irritability and emotional dysregulation caused by brain trauma.

Behavioral and Neurodevelopmental Challenges metrics: The BGLHA Scores (Childhood, Adolescence, and Adulthood Total Scores) capture a history of behavioral and emotional challenges across developmental stages. These measures help identify patterns of behavioral dysregulation that may predispose individuals to more severe neuropsychiatric symptoms following head trauma. The CNS-LS Total Score (Center for Neurologic Study-Lability Scale) specifically evaluates emotional lability, a common symptom in patients with frontal

lobe or limbic system damage.

Post-Traumatic Stress and Neurobehavioral Dysregulation metrics: The PCL-5 Total Symptom Severity Score (PTSD Checklist) quantifies the severity of post-traumatic stress disorder (PTSD) symptoms, which are common in individuals exposed to repetitive head trauma or other traumatic events. The NBD Total Score (Neurobehavioral Dysregulation Score) provides a comprehensive measure of behavioral and emotional dysregulation, encompassing impulsivity, aggression, and emotional instability, which are critical in understanding the neuropsychiatric burden of CTE.

These neuropsychiatric measures are invaluable for assessing the psychological and behavioral impact of repetitive head trauma. In the context of CTE and concussion-related studies, they help quantify the emotional and behavioral challenges faced by patients, including impulsivity, emotional instability, anxiety, and depression. These metrics also provide insights into the underlying neural disruptions caused by trauma, particularly in areas associated with emotional regulation, executive functioning, and social behavior. By systematically evaluating these measures, researchers can identify patterns of neuropsychiatric dysfunction, track changes over time, and develop targeted interventions to improve the quality of life for individuals affected by CTE and concussion.

6.1.2 Selected Neurocognitive Measurements

The neurocognitive measures listed in Table A.2 that were considered in this study play a critical role in understanding the cognitive and behavioral impacts associated with CTE and concussion-related injuries. These measures are designed to assess a broad range of cognitive and executive functions, emotional regulation, and behavioral control. Their relevance lies in their ability to provide insights into the functioning of key brain regions and their connections, which are often affected in individuals with a history of repetitive head trauma.

The Meta-Cognition Index (MI) and its T-score (tmi) assess an individual's ability to self-monitor, plan, and organize their thoughts and actions. These scores are particularly important in identifying deficits in higher-order cognitive processes, which are often impaired in individuals with CTE or other traumatic brain injuries. Similarly, the General Execu-

tive Composite (GEC) and its T-score (tgec) provide a comprehensive measure of executive functioning, encapsulating abilities such as problem-solving, decision-making, and adaptive thinking.

The Behavioral Regulation Index (BRI) and its T-score (tbri) evaluate the capacity for regulating emotions and behaviors in response to external stimuli. Measures like Inhibit Clinical Scale, Shift Clinical Scale, and Emotional Control Clinical Scale delve deeper into specific aspects of behavioral regulation, such as impulse control, cognitive flexibility, and emotional adjustment. These scores are vital in understanding how head injuries disrupt the neural networks responsible for maintaining appropriate emotional and behavioral responses.

CTE and concussions are known to affect both the prefrontal cortex and deeper brain structures involved in executive functioning, emotional regulation, and cognitive processing. Parameters such as Working Memory Clinical Scale, Plan/Organize Clinical Scale, and Task Monitor Clinical Scale offer detailed insights into the functional impairments resulting from these injuries. For example, deficits in working memory or planning and organization often correlate with structural and functional changes observed in neuroimaging studies of affected individuals.

Additionally, measures like the Organization of Materials Clinical Scale provide information about an individual's ability to manage physical and cognitive tasks effectively, which can reflect broader disruptions in neural coordination. Together, these metrics allow researchers and clinicians to quantify the extent of neurocognitive dysfunction and track changes over time, which is crucial for assessing the progression of neurodegenerative conditions like CTE or recovery from concussions.

These neurocognitive measures are important for understanding the functional consequences of head injuries. They not only help identify specific areas of impairment but also allow for the development of targeted interventions and therapies aimed at mitigating the cognitive and behavioral challenges associated with CTE and concussions. By comparing these metrics across different populations or over time, researchers can better elucidate the patterns of neurocognitive decline and resilience, ultimately advancing our understanding of brain health in individuals exposed to repetitive head trauma.

6.1.3 Features: Blood Biomarkers, CSF Biomarkers, MRI Morphometric Measures

A detailed list of blood biomarker, CSF biomarkers, and MRI morphometric features is presented in Table A.1 to A.34. Below, we highlight a few of the most significant biomarkers.

This study investigated a wide range of plasma and CSF biomarkers, offering valuable insights into the neurodegenerative, inflammatory, and vascular mechanisms underlying CTE and related traumatic brain injuries (TBIs). Among these, the following biomarkers demonstrated particular relevance: Amyloid-beta Peptides (Abeta40 and Abeta42): These peptides, fragments of amyloid precursor protein, are critical for understanding amyloid pathology. Altered levels of Abeta42, prone to forming plaques, are indicative of neurodegenerative changes linked to CTE and Alzheimer's disease.

Glial Fibrillary Acidic Protein (GFAP): As a marker of astrocyte activation, GFAP reflects neuroinflammation and brain injury. Elevated levels provide evidence of ongoing inflammatory responses and brain damage, crucial for assessing CTE progression.

Neurofilament Light Chain (NfL): Released during neuronal damage, NfL serves as a marker of neurodegeneration. Elevated levels correlate with the severity of neuronal injury, making it a valuable biomarker for monitoring TBI-related outcomes.

Phosphorylated and Total Tau Proteins: Tau proteins, particularly their phosphorylated forms (e.g., pT181, pT231), are associated with tauopathies like CTE. These biomarkers help assess microtubule destabilization and neuronal dysfunction, integral to evaluating neurodegenerative progression.

Vascular Biomarkers (PDGFRbeta, VEGF, and Qalb): PDGFRbeta levels provide insights into vascular health and blood-brain barrier (BBB) integrity. Similarly, VEGF-A, VEGF-C, and VEGF-D contribute to understanding angiogenesis and vascular changes. Qalb, the CSF/serum albumin ratio, directly measures BBB integrity, with elevated values signaling barrier dysfunction common in neuroinflammatory diseases.

Cytokines and Inflammatory Markers (e.g., IL-6, IL-17, CRP): Interleukins such as IL-6 and IL-17 play critical roles in immune modulation and neuroinflammation. C-reactive protein (CRP), a systemic inflammation marker, helps assess the inflammatory burden relevant to

CTE pathology.

Alpha-Synuclein (α-syn): This protein, linked to neurodegenerative diseases like Parkinson's, provides insight into synucleinopathy-related neuronal damage. Its plasma levels are pivotal in exploring CTE and related disorders.

Serum Albumin (s-alb): Changes in serum albumin concentration highlight systemic health and its interplay with neurological disorders, serving as a baseline health indicator in studying TBI outcomes.

In addition to blood and CSF biomarkers, our analysis also considered MRI morphometric measures. These measures include the subcortical volumes of various brain regions, volumes of distinct parts within both the right and left hemispheres, and the cortical thickness of these areas. Furthermore, the data encompassed the mean curvature of surfaces across both hemispheres, as well as detailed area measurements in square millimeters for various regions, including the APARC inferior parietal parcel on both the right and left sides. These MRI morphometric parameters provide crucial insights into the structural aspects of the brain, enhancing our understanding of its role in neurodegenerative conditions.

6.2 Methods

Our study involved acquiring both tabular and imaging data from CTE patients participated in the Diagnostics, Imaging, and Ge netics Network for the Objective Study and Evaluation of CTE (DIAGNOSE CTE) Research Project [221], to train a machine learning model aimed at predicting neurological and motor examinations, neurocognitive assessments, and neuropsychiatric measures. This dataset had previously been used to study CTE, develop detection methods, and establish diagnostic criteria in American football players with traumatic brain injuries [221, 222]. Participants for this study were recruited from the DIAGNOSE CTE Research Project, a comprehensive initiative aimed at understanding the clinical and biological characteristics of CTE. The cohort consisted of 120 former professional football players, 60 former college football players, and 60 asymptomatic men serving as control participants. The inclusion criteria for the former professional football players required a minimum of 12 years of organized football play, including at least three years at the college level and three seasons in the National Football League (NFL). Former college football players were required to have at least six years of organized football play, with a

minimum of three years at the college level. Control participants were asymptomatic men with no history of contact or collision sports, military combat, or TBIs. All participants were male, aged between 45 and 74 years. Further recruitment and enrollment details, including eligibility criteria and data collection protocols, have been previously documented in the DIAGNOSE CTE study protocol (reference). The study protocol was approved by the Institutional Review Boards of participating institutions, and written informed consent was obtained from all participants before enrollment.

In this study, we trained a machine learning model capable of using multiple algorithms to predict these neurological, cognitive, and psychiatric criteria. The model analyzed blood biomarkers, CSF biomarkers, and structural features extracted from different brain regions, including volumetric measurements and shape metrics of substructures. By comparing these features with those from a normal cohort, our objective was to identify and rank the features and markers most relevant to predicting clinical assessment outcomes (Fig 6.1).

The study on which this work was based was initiated by a collaborative group at Boston University, in partnership with several other institutions. Our goal was to analyze the comprehensive dataset gathered from this study, which includes demographic data, history of TBIs, various biomarkers, and imaging features for all subjects.

The primary objective was to determine whether these features could be used to predict neurocognitive, neurobehavioral, or neurological scores across different subject categories. Additionally, we aimed to identify which factors—such as biomarkers, morphometric characteristics, or imaging features—played a significant role in classifying patients. Through this analysis, we aimed to gain insights into the key contributors to these scores and investigate whether specific biomarkers or other factors were particularly predictive of CTE-related outcomes. This work may help differentiate patients from healthy controls and enhance our understanding of CTE risk factors and disease progression in the future.

By applying machine learning algorithms and statistical models to the dataset, we aimed to not only predict specific neurological outcomes but also to pinpoint the most influential features driving these predictions. The study considered a wide array of variables, including demographic information, historical data on TBI, blood biomarkers, CSF biomarkers, volumetric features, and imaging-derived biomarkers, allowing for a comprehensive examination

of factors contributing to the onset and progression of CTE.

The ability to accurately predict neurocognitive and neurobehavioral scores across different subject groups (former NFL players, college athletes, and healthy controls) could have revealed critical insights into how repetitive head trauma contributes to long-term neurological decline. Additionally, this analysis aimed to highlight whether certain biomarkers or structural brain features, as identified through imaging, serve as reliable indicators of CTE risk. The ultimate goal was to identify a set of biomarkers or imaging features that could serve as predictors or classifiers for CTE, with the potential to improve early intervention strategies and deepen our understanding of how CTE develops in athletes with a history of repetitive head trauma.

By investigating these factors, this project aimed to address key gaps in the literature regarding CTE, particularly in identifying preclinical signs that might be indicative of the disease. The outcomes of this work had the potential to inform future studies, guiding the development of diagnostic tools for the early identification of neurodegenerative diseases like CTE and, possibly, informing treatment options to mitigate the long-term effects of repetitive brain trauma.

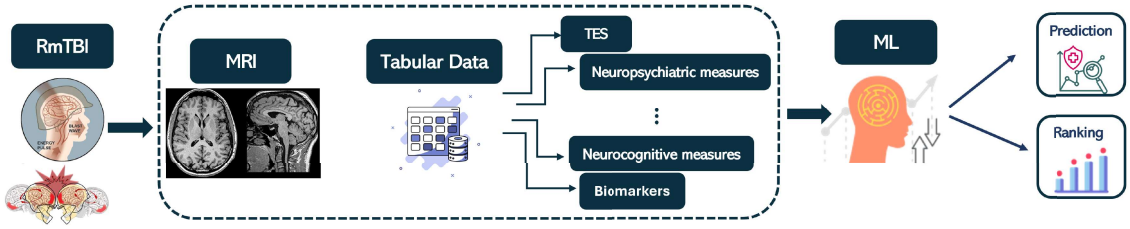

Figure 6.1: Overview of Aim 4's process flow for predicting neurocognitive, and neuropsychiatric measures in CTE patients. The flowchart shows the collection of tabular and imaging data, feature extraction, and training of a machine learning model on outcomes across neurological, neurocognitive, and neuropsychiatric domains. Key features include blood and CSF biomarkers, volumetric measurements, and shape metrics from brain substructures. Comparison with a control cohort supports identifying predictive features most relevant to these clinical assessments.

6.2.1 Preprocessing of Data

Based on the data dictionary, primary domain, and sub-domains of the available dataset, and following discussions with the neurosurgeon, we initially included only the total scores

for factors in neurocognitive and neuropsychiatric assessments. These factors include those specified in the table, derived from surveys and examinations. In some cases, sub-domain datasets contained subjects' individual responses to survey multiple questions, along with final scores for each questionnaire. In such cases, we excluded individual response features, retaining only the total scores for a more focused analysis.

The preprocessing of the data involved multiple steps, each of which will be explained in detail in the following sections.

6.2.1.1 Data Cleaning and Handling Missing Values

We checked each feature for null values and removed any with more than a certain threshold of nulls (e.g., 50%) [223]. Although we initially tried imputing missing values using the mean, median, or mode, this approach did not show meaningful results. Given the dataset's small size, imputing risked introducing inaccuracies and potentially misleading patterns, so we continued with feature removal. This decision was made by several factors: First, in a small dataset, filling missing values with the mean can add noise, especially if missing values are systematic rather than random [223]. This can limit the model's ability to detect meaningful patterns. Additionally, removing features with a high proportion of nulls helps reduce model complexity and avoid overfitting, as focusing on a smaller, more reliable set of predictors is advantageous when observations are limited. For crucial features with high null values, more advanced imputation techniques—such as k-nearest neighbors or predictive imputation—can be considered, as they leverage data relationships to fill missing values more accurately than mean imputation. [223].

In addition to automated data cleaning, which included handling null values and outliers, we manually removed features that lacked meaningful contributions to the analysis. Specifically, features with over 90% of the data containing identical values or those with descriptions deemed irrelevant to the study's objectives were excluded. Similarly, features that could directly influence the results without adding meaningful insights aligned with the project's aim were also eliminated.

6.2.1.2 Feature Scaling and Normalization

Feature selection was performed to identify the most significant biomarkers. Feature importance rankings were determined using ensemble-based methods, such as Random Forest, which provided feature importance scores by evaluating each feature's contribution to reducing model impurity. These scores were used to rank and select the top biomarkers and MRI morphometric features for further analysis. Standardization, which adjusts the data to have a mean of zero and a standard deviation of one, was specifically chosen. This scaling method is particularly important for distance-based models, such as Support Vector Regression (SVR) and K-Nearest Neighbors (KNN), as well as for neural networks, where varying feature scales could otherwise impede the model's learning process.

Feature selection was conducted to identify the most relevant biomarkers. Feature importance rankings were generated through methods like SelectKBest with univariate statistical testing, and feature importance scores from ensemble models, such as Random Forest, were used to identify the top contributing biomarkers and MRI morphometric features. These rankings provided insights into which biomarkers had the strongest associations with the neuropsychiatric outcomes. To further validate the robustness of selected features, models were trained using different numbers of top features, systematically reducing the dataset to only the most influential biomarkers.

These scaled and selected features were applied across multiple models, including Random Forest, Linear Regression, SVR, ANN, and ensemble methods. By evaluating the performance metrics, such as Mean Squared Error (MSE) and R-squared scores, for each model with varying feature sets, the analysis provided a clear assessment of the predictive power of each approach under different feature conditions. This comprehensive feature scaling and selection strategy aimed to maximize model accuracy while improving interpretability and computational efficiency.

Apart from the feature importance performed on each subset of features, such as both blood biomarkers, all three CSF biomarker groups, and all MRI morphometric groups, a two-stage feature importance approach was implemented. In this method, we first identified groups of features that showed better results in the initial analysis and then performed feature

importance again on these selected groups.

6.2.2 Utilized Machine Learning and Deep Learning algorithms

For this aim, several machine learning methods were employed to predict neuropsychiatric measurements based on a set of biomarkers. The approach included both traditional regression methods and advanced ensemble techniques to evaluate model performance across different feature sets.

First, Random Forest Regression was implemented due to its ability to handle non-linear relationships and provide feature importance scores. This method uses an ensemble of decision trees, reducing overfitting and capturing interactions between variables. Next, Multiple Linear Regression was applied as a baseline to capture simple linear relationships between the biomarkers and target neuropsychiatric measures, offering interpretable insights into direct associations between predictors and outcomes.

Other advanced models included Support Vector Regression (SVR), which utilizes a kernel trick to model non-linear relationships, and Artificial Neural Networks (ANN), allowing complex mappings through a multi-layer perceptron structure. K-Nearest Neighbors (KNN) was also used to assess the model's performance based on the proximity of similar data points.

Ensemble techniques, such as Stacking and Bagging, were utilized to enhance predictive accuracy. Stacking, involving multiple base models with a meta-learner, and Bagging, which averages predictions from multiple SVR estimators, were applied to capture model diversity. Regularization methods, including Lasso (L1) and Ridge (L2) Regression, were used to prevent overfitting and manage multicollinearity. Bayesian Linear Regression provided a probabilistic interpretation, while Gaussian Process Regression offered a flexible, non-parametric approach, particularly useful for smaller datasets.

Overall, these methods allowed for an extensive evaluation of predictive power across various modeling approaches, enabling a comparison of linear and non-linear algorithms as well as ensemble techniques for robust, accurate predictions.

6.3 Results

The primary goal of this aim was to predict neuropsychiatric and neurocognitive measurements using blood biomarkers, CSF biomarkers, and MRI morphometric measures. Several machine learning models as listed in the methods section, were evaluated for their performance. The performance of each model was evaluated using the metrics Mean Squared Error (MSE), Mean Absolute Error (MAE), and the Coefficient of Determination R^2. The results for selected metrics discussed in the following sections are presented in Fig. 6.2 to Fig. 6.10 in different colors nad shades.

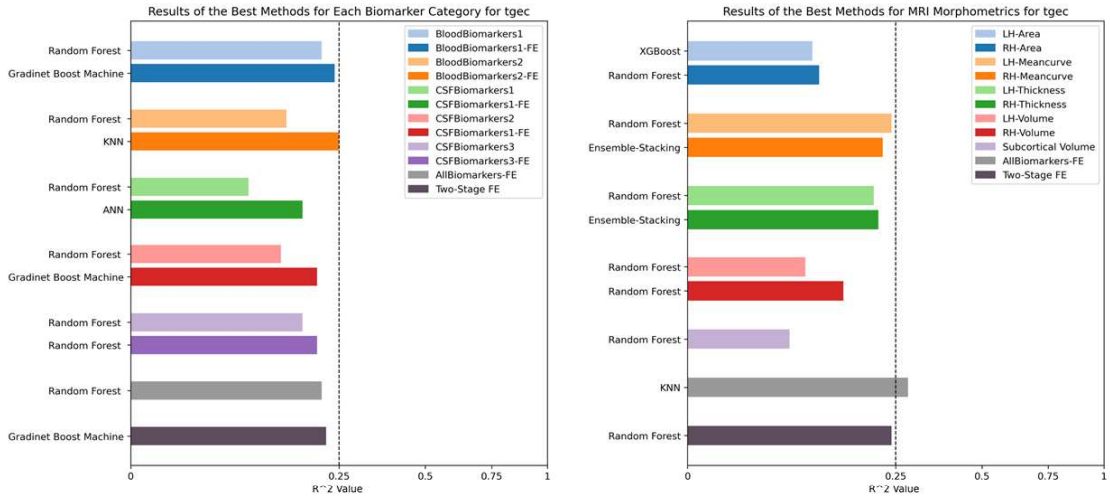

Figure 6.2: Comparative results of machine learning models predicting the TGEC metric using biomarkers (left) and MRI morphometric features (right). Both panels present the performance of models applied to the respective features, including feature engineering approaches (e.g., FE and two-stage FE), with MRI morphometrics showing higher predictive power overall. The dashed vertical line represents an R^2 threshold of 0.25 for reference.

6.3.1 Predicting neurocognitive Measures from blood biomarkers

All 15 neurocognitive metrics were predicted using Blood Biomarkers 1 and Blood Biomarkers 2 separately. In the feature importance analysis, only significant features from each category were considered, and the corresponding results are explained in the following section (Blue and orange bars in the left panel in Fig. 6.2 to Fig. 6.6).

Blood Biomarkers 1 performed best in predicting mi, using Random Forest Regression and XGBoost, with R^2 values of 0.27 and 0.29, respectively. The next metrics that were mod-

erately well-predicted by Blood Biomarkers 1 included TMI, GEC, and TGEC, with R^2 values of 0.27, 0.27, and 0.21, respectively, when using Random Forest. While these results indicate limited predictive accuracy, they provide valuable insights into potential biomarkers that could be explored in future studies.

Other metrics, such as PlanOrg ($R^2 = 0.22$) and inhibit ($R^2 = 0.18$), showed moderate prediction performance. However, for the remaining metrics, R^2 values were below 0.1, highlighting the challenges in predicting these outcomes solely from Blood Biomarkers 1.

Among the alternative methods, Multiple Linear Regression, Gradient Boosting Machines, Lasso Regression, and Ridge Regression performed as the second-best group, with R^2 values ranging from approximately 0.15 to 0.2. These results suggest that combining multiple machine learning approaches may improve the predictive accuracy of neurocognitive metrics in future work.

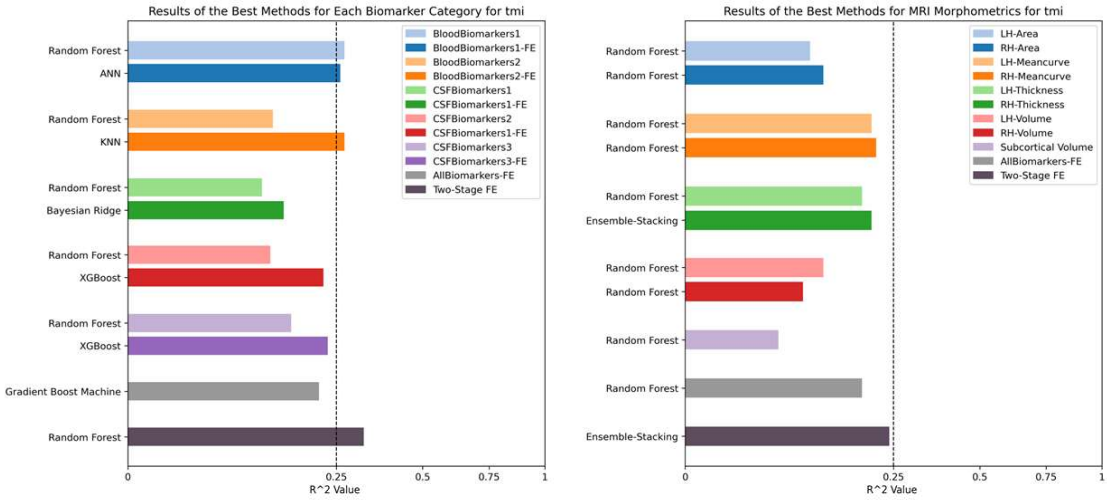

Figure 6.3: Comparative results of machine learning models predicting the TMI metric using biomarkers (left) and MRI morphometric features (right). Both panels present the performance of models applied to the respective features, including feature engineering approaches (e.g., FE and two-stage FE), with blood biomarkers showing higher predictive power overall. The dashed vertical line represents an R^2 threshold of 0.25 for reference.

Blood Biomarkers 2 were relatively less effective in predicting some of the neurocognitive metrics, including MI, TMI, GEC. TGEC, inhibit, shift, and initiate, compared to Blood

Biomarkers 1. On the other hand in other metrics such as taskmon, and WorkMem, blood biomarkers 2 performed better in predicting these metrics. Among the methods applied, Random Forest performed better than other approaches for most neurocognitive metrics, with the best R^2 observed for bri, tbri, and WorkMem, achieving R^2 values of 0.16, 0.14, and 0.16, respectively. The second best method was gradient boost machine, and XGBoost and multilinear regression were other good-performed methods in predicting these neurocognitive measures.

Interestingly, due to the high number of features and their potential irrelevance in predicting neurocognitive metrics, the use of Blood Biomarkers 2 sometimes resulted in negative R^2 values. These findings highlight the need for more refined feature selection and the importance of identifying biomarkers more closely associated with neurocognitive outcomes.

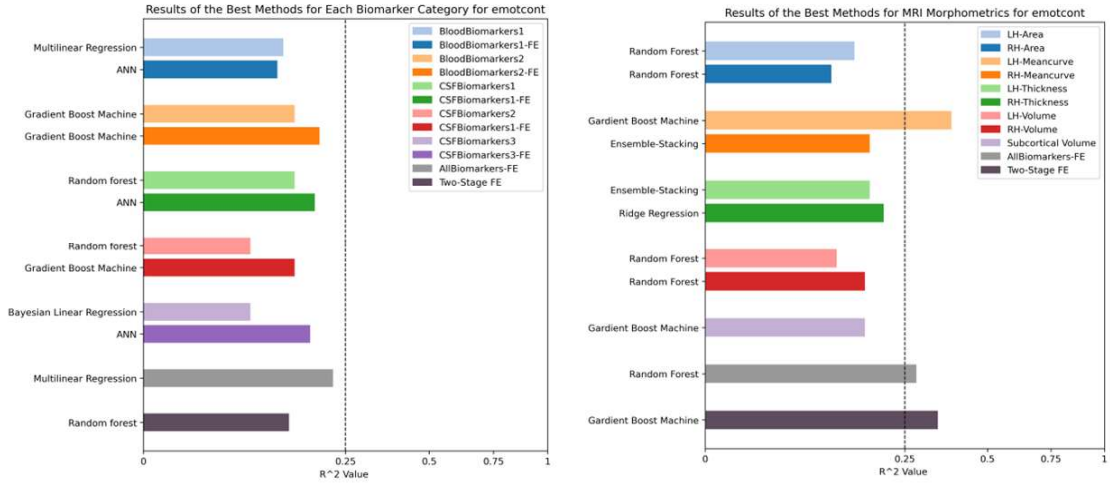

Figure 6.4: Comparative results of machine learning models predicting the EmotCont metric using biomarkers (left) and MRI morphometric features (right). Both panels present the performance of models applied to the respective features, including feature engineering approaches (e.g., FE and two-stage FE), with MRI morphometrics, and especially curvature features, showing higher predictive power overall. The dashed vertical line represents an R^2 threshold of 0.25 for reference.

6.3.1.1 Feature Importance Results for Predicting Neurocognitive Measures from Blood Biomarkers

In predicting *MI*, the top features identified from Blood Biomarkers 1 were p-GFAP and p-pT231 caused performance improvement for 10%, while key features from Biomarkers 2

included p-IL-1RA-cv, p-IL-10, age-decade, p-IL-8-2, p-MIP-1alpha, p-IL-10-cv, p-IL-17A-F, p-MCP-4-cv, chiiyrs-pf, p-IL-5-cv, and p-GM-CSF-cv that improved the performance from 0.09 to 0.26. For *TMI*, the top features from Blood Biomarkers 1 were p-PDGFRbeta, p-ttau, p-Ab42, and p-GFAP, whereas features from Biomarkers 2 included p-IL-1RA-cv, p-IL-10, p-IL-8-2, p-MIP-1alpha, p-IL-10-cv, p-IL-17A-F, chiiyrs-pf, age-decade, chiiseas-pl, p-MCP-4-cv, p-IL-5-cv, and p-IL-23.

Similarly, in predicting *GEC*, the most significant features from Blood Biomarkers 1 included p-PDGFRbeta, p-ttau, p-Ab42, and p-GFAP, while Biomarkers 2 featured p-IL-10-cv, chiiseas-pf, p-IL-13-cv, p-IL-17B, p-MIP-1alpha, p-ICAM-1-cv, p-MDC, p-TSLP-cv, p-IL-17B-cv, chiiyrs-pl, p-CRP-cv, and p-VEGF-D-cv as top predictors which improved the R^2 by 50%.

For *BRI* and the *Inhibit Clinical Scale*, the critical features from Blood Biomarkers 1 included p-GFAP, p-NFL, p-pT231, p-PDGFRbeta, p-ttau, and p-Ab40, while top-performing features from Biomarkers 2 were p-IL-23, p-MIP-1alpha, p-MIP-1-beta-cv, p-IL-13-cv, p-MDC, p-IL-10-cv, p-ICAM-1-cv, p-Tie-2-cv, p-Hb, p-IL-12-IL-23p40, p-IL-8-2, and p-asyn that improved the R^2 from 0.16 to 0.21. The results are shown as light blue and light orange bars in the left panel of Fig. 6.2 to Fig. 6.6.

In predicting the *Inhibit* Clinical Scale, the top features from Biomarkers 2 included p-IL-1RA-cv, p-IL-8-2, p-IL-10, p-IL-23, p-VEGF-A-cv, p-VEGF-A-2, p-VEGF-A, p-IP-10-cv, p-INF-gamma-cv, p-IL-1-beta, p-IL-17A-F, and p-MDC. For the *Shift* Clinical Scale, the most predictive features from Blood Biomarkers 1 were p-GFAP, p-PDGFRbeta, p-NFL, p-ttau, and p-pT231, while Biomarkers 2 featured p-IL-1RA-cv, p-IL-10, p-IL-8-2, p-MIP-1alpha, p-IL-23, p-MCP-4-cv, p-IL-9, p-IL-13-cv, p-MIP-1-beta-cv, p-Tie-2-cv, p-IL-10-cv, and p-CRP, that could improve the R^2 from 0.07 to 0.22.

For predicting *EmotCont*, the top-performing features from Blood Biomarkers 1 included p-GFAP, p-PDGFRbeta, p-NFL, p-ttau, and p-pT231. Biomarkers 2 added predictive strength with features such as p-IL-1RA-cv, p-IL-6, p-IL-8-2, p-IL-10, p-MIP-1alpha, p-IL-23, p-IL-13-cv, p-IL-17A-F, p-TNF-alpha-cv, p-IL-10-cv, p-IL-1-alpha, and p-IL-4. The performance while including top features improved from 0.14 to 0.19.

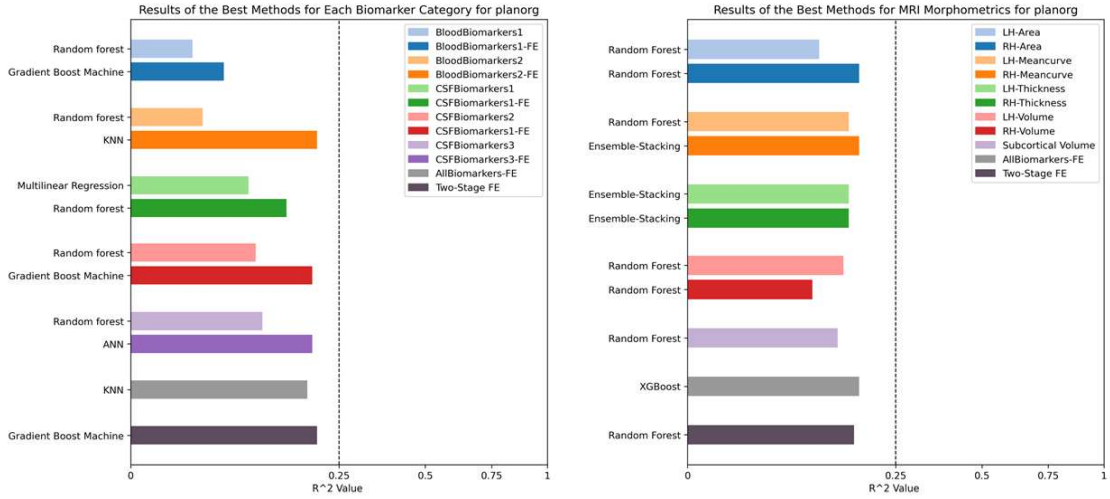

Figure 6.5: Comparative results of machine learning models predicting the PlanOrg metric using biomarkers (left) and MRI morphometric features (right). Both panels present the performance of models applied to the respective features, including feature engineering approaches (e.g., FE and two-stage FE), without any significant difference between the predictive power of MRI morphometrics, and biomarkers. The dashed vertical line represents an R^2 threshold of 0.25 for reference.

For other metrics such as *SelfMon*, *Initiate*, *WorkMem*, and *PlanOrg*, Blood Biomarkers 1 showed limited predictive utility. However, Biomarkers 2 performed significantly better. For *SelfMon*, the top features included p-IL-23, p-MIP-1-beta-cv, p-MIP-1alpha, p-TNF-beta-cv, p-Tie-2-cv, p-IL-6-cv, p-Eotaxin-3-cv, p-IL-12-IL-23p40, p-asyn, Qalb, p-IL-23-cv, and p-Hb.

In predicting *Initiate*, the top features from Biomarkers 2 were p-IL-23, p-IL-10-cv, p-IL-17B, p-IL-13-cv, p-IL-12-IL-23p40, p-PlGF, p-ICAM-1-cv, p-IL-21, p-VEGF-C-cv, p-VEGF-A-cv, p-IL-1-beta, and p-asyn. For *WorkMem*, the most predictive features were p-IL-23, p-IL-10-cv, p-TSLP-cv, p-MIP-1alpha, p-ICAM-1-cv, p-IL-17D-cv, p-IL-13-cv, p-Fit-1, p-MDC, p-IL-8-2, p-MDC-cv, and p-MCP-1-cv. For *PlanOrg*, the top features from Biomarkers 2 included p-IL-1RA-cv, p-MIP-1alpha, p-IL-10, p-IL-8-2, p-IL-17A-F, p-IL-10-cv, p-Eotaxin-3-cv, p-MCP-4-cv, p-GM-CSF-cv, p-IL-17B, p-VEGF-C-cv, and p-IL-5-cv, which improved the perfromance significantly from 0.03 to 0.2.

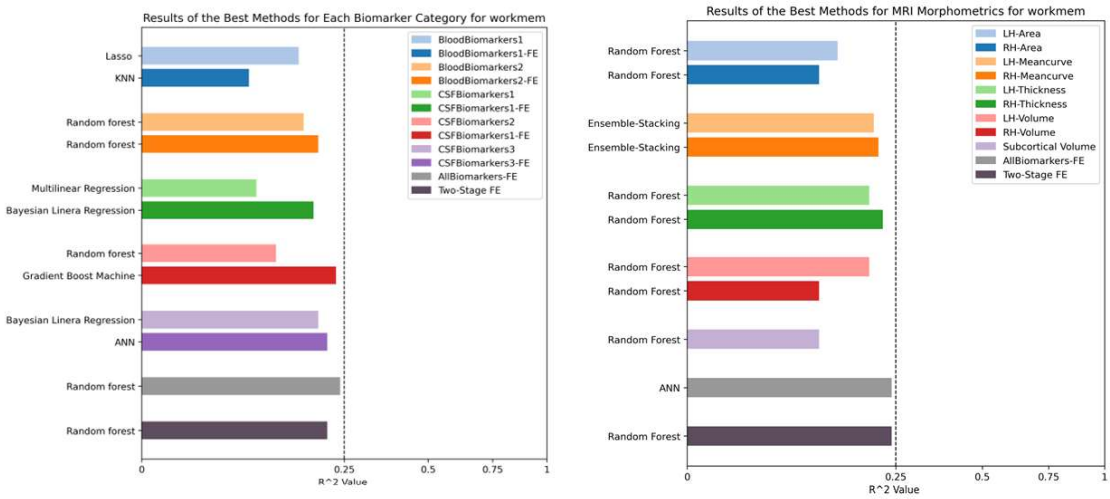

Figure 6.6: Comparative results of machine learning models predicting the WorkMem metric using biomarkers (left) and MRI morphometric features (right). Both panels present the performance of models applied to the respective features, including feature engineering approaches (e.g., FE and two-stage FE), with MRI morphometrics, and especially thickness and curvature features, showing higher predictive power overall. The dashed vertical line represents an R^2 threshold of 0.25 for reference.

6.3.2 Predicting neurocognitive Measures from CSF biomarkers

CSF biomarkers were overall less effective than blood biomarkers in predicting GEC, shift, and SelfMon measurements. Among the CSF categories, CSF Biomarkers 3 performed noticeably better compared to CSF Biomarkers 1 and CSF Biomarkers 2, in predicting mi, tgec, shift, SelfMon, and WorkMem particularly when using the Random Forest and XGBoost models. It was also noticed that these methods demonstrated relatively higher performance in predicting inhibit, tgec, WorkMem, and TMI metrics using various biomarkers. In contrast, other methods and the use of CSF Biomarkers 1 and CSF Biomarkers 2 showed poor results, likely due to similar issues observed with Blood Biomarkers 2, such as the inclusion of irrelevant or non-predictive features. Notably, incorporating feature importance methods led to significantly improved outcomes, emphasizing the necessity of targeted feature selection in such analyses. The results are shown as green, red, and purple bars in the left panel of Fig. 6.2 to Fig. 6.6.

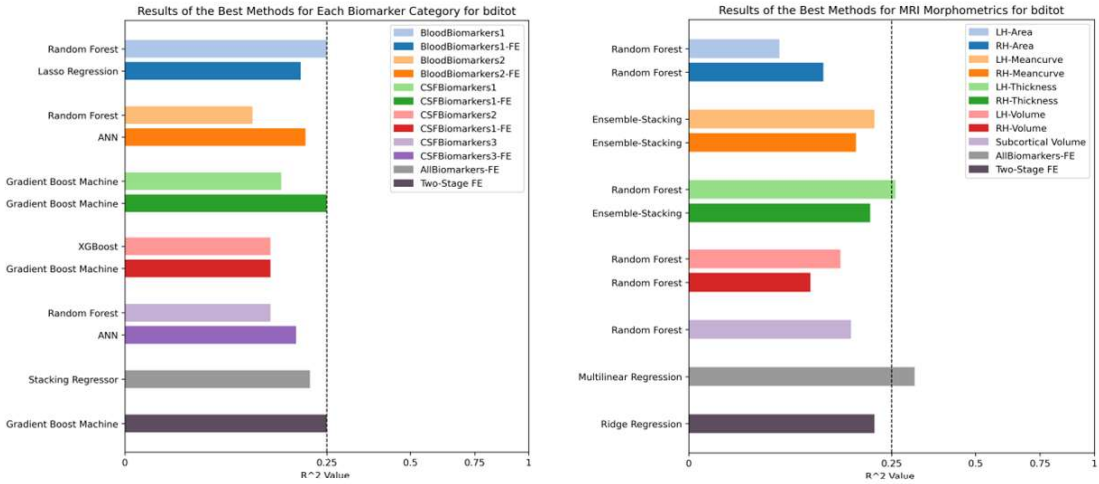

Figure 6.7: Comparative results of machine learning models predicting the BDITot metric using biomarkers (left) and MRI morphometric features (right). Both panels present the performance of models applied to the respective features, including feature engineering approaches (e.g., FE and two-stage FE), with MRI morphometrics, and especially thickness features, showing higher predictive power overall. The dashed vertical line represents an R^2 threshold of 0.25 for reference.

6.3.2.1 Feature Importance Results for Predicting Neurocognitive Measures from CSF biomarkers

In predicting MI from CSF biomarkers, the top features from CSF biomarkers 1 were c-PDGFRbeta, c-Ab40, and c-NfL. From CSF biomarkers 2, the significant contributors included c-IL-6, c-CRP, c-IL-12p70-cv, and c-IL-1RA-cv. Additionally, c-da from CSF biomarkers 3 substantially improved performance from 0.14 to 0.25. Similarly, for TMI, CSF biomarkers 1 highlighted c-PDGFRbeta and c-NfL as the most predictive features, while CSF biomarkers 2 added c-IL-12p70-cv, c-IL-6, c-CRP, c-IL-1RA-cv, c-TSLP, Qalb, c-IL-1-alpha, c-IL-27, and c-SAA. CSF biomarker 3's inclusion of c-da enhanced performance from 0.15 to 0.23.

For GEC, key features from CSF biomarkers 1 included c-strem2 and c-GFAP. CSF biomarkers 2 contributed additional predictive strength with c-IL-6, c-CRP, c-IL-1RA-cv, c-IL-12p70-cv, c-IL-31-cv, c-MIP-1-beta, and Qalb. Incorporating c-da from CSF biomarkers 3 improved performance from 0.14 to 0.23. In contrast, for BRI, Shift, and SelfMon, CSF biomarkers 1 failed to show significant results. However, for BRI, CSF biomarkers 2 pro-

vided impactful features such as c-IL-6, c-IL-31-cv, c-CRP, c-IL-1RA-cv, c-MIP-1-beta, and c-SAA, improving performance from 0.09 to 0.21. CSF biomarkers 3 did not contribute significantly to predicting Shift or SelfMon.

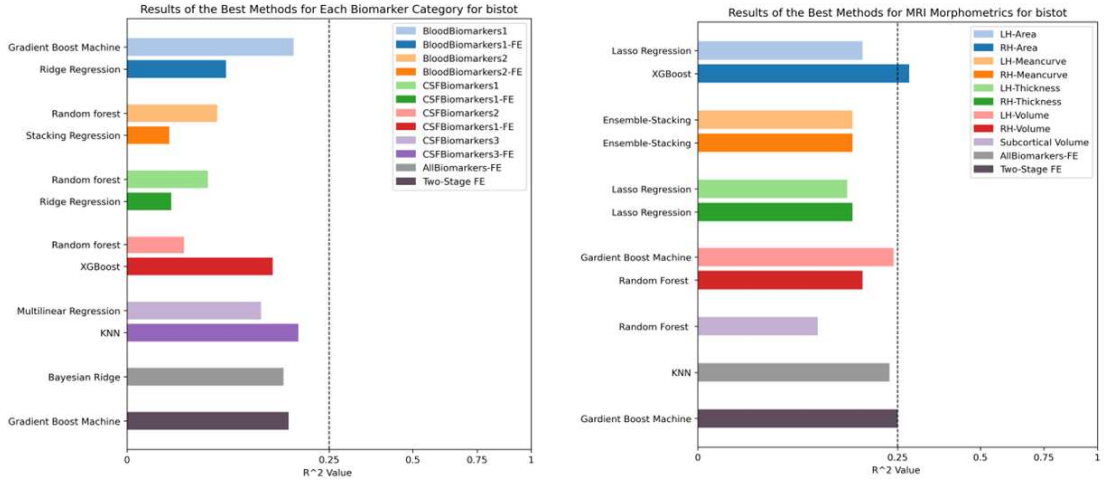

Figure 6.8: Comparative results of machine learning models predicting the BIS-Tot metric using biomarkers (left) and MRI morphometric features (right). Both panels present the performance of models applied to the respective features, including feature engineering approaches (e.g., FE and two-stage FE), with MRI morphometrics, and especially area and volume features, showing higher predictive power overall. The dashed vertical line represents an R^2 threshold of 0.25 for reference.

For Inhibit, predictive features from CSF biomarkers 1 were c-strem2 and c-ttau, while CSF biomarkers 2 included c-IL-6, c-MIP-1-beta, c-IL-7-cv, c-IL-12-IL-23p40-cv, and c-IL-31, resulting in an improved performance from 0.13 to 0.19. In predicting EmotCont, CSF biomarkers 1 identified c-GFAP, c-ttau, and c-strem2 as critical factors, while CSF biomarkers 2 featured c-bFGF-cv, c-IL-6, c-CRP, c-IL-13-cv, c-IL-1RA-cv, c-CRP-cv, c-IL-7, c-IL-17C, c-IL-8-cv, c-GM-CSF, c-MDC, c-IL-13, c-SAA, c-IL-1-alpha, c-IL-17B-cv, and c-VEGF-C-cv, improving performance from 0.07 to 0.14.

In predicting WorkMem, CSF biomarkers 1 highlighted c-ttau and c-PDGFRbeta as significant features, while CSF biomarkers 2 included c-IL-6, c-IL-1-alpha, and c-IL-12p70-cv. Similarly, for TaskMon and PlanOrg, CSF biomarkers 1 identified c-strem2, c-PDGFRbeta, c-GFAP, and c-NfL, while CSF biomarkers 2 added c-CRP, c-IL-12p70-cv, and c-IL-6, improving performance from 0.12 to 0.2.

Across metrics such as BRI, Shift, EmotCont, PlanOrg, and WorkMem, the inclusion of c-da from CSF biomarkers 3 consistently enhanced performance, with improvements ranging from 40% to 75%. The results are shown as light green, light red, and light purple bars in the left panel of Fig. 6.2 to Fig. 6.6.

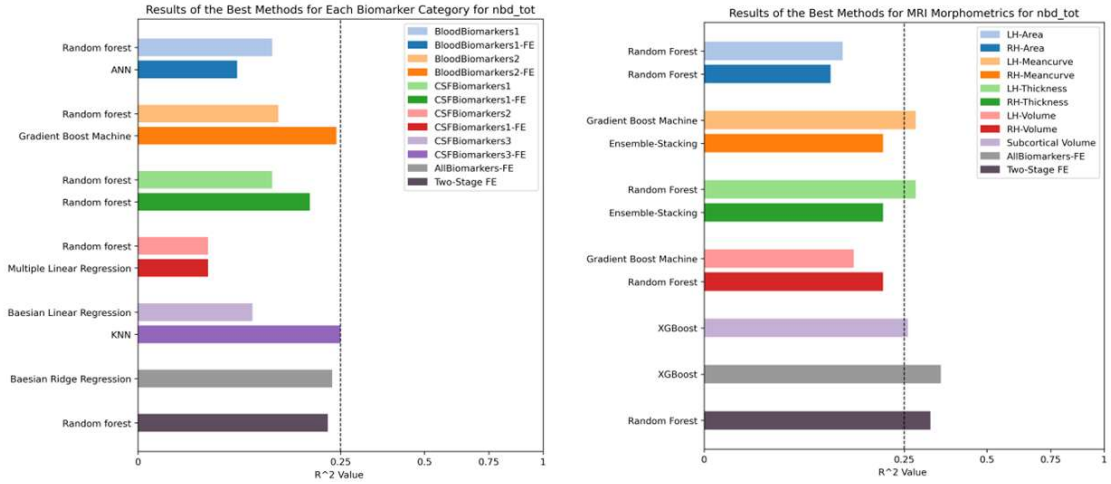

Figure 6.9: Comparative results of machine learning models predicting the NBD-Tot metric using biomarkers (left) and MRI morphometric features (right). Both panels present the performance of models applied to the respective features, including feature engineering approaches (e.g., FE and two-stage FE), with MRI morphometrics, and especially thickness and curvature features, showing higher predictive power overall. The dashed vertical line represents an R^2 threshold of 0.25 for reference.

6.3.3 Predicting neurocognitive Measures from MRI Morphometric Measures

In predicting mi, the mean curvature of different regions in the right hemisphere using random forest achieved the highest R^2, while parameters in the left hemisphere performed second best. Similarly, for predicting GEC, the mean curvature of the right and left hemispheres performed better using ensemble stacking and XGBoost, respectively. The second most important feature was the thickness of various substructures in the left and right hemispheres, predicted using XGBoost and random forest, respectively. For other neurocognitive measurements, the mean curvature of regions in the right and left hemispheres, followed by the thickness of these substructures, consistently delivered the second-best results in predictive models. The results are shown as blue, orange, green, red, and purple bars in the right panel of Fig. 6.2 to Fig. 6.6.

6.3.3.1 Feature Importance Results for Predicting neurocognitive Measures from MRI Morphometric Measures

Overall, in predicting all metrics, features within the curvature category—specifically the mean curvature of brain subregions—and regional thickness extracted from MRI played the most significant roles. In comparison, the contributions of area, volume, and subcortical volume were almost negligible relative to mean curvature and thickness.

The detailed feature importance demonstrated that incorporating these features improved predictive performance across various metrics. For MI, the inclusion of key morphometric features enhanced performance from a range of 0.07–0.21 across different categories to 0.25. Similarly, for GEC, the addition of regional thickness and mean curvature improved performance from 0.22 to 0.28. In other metrics, feature importance resulted in performance improvements: BRI (0.2 to 0.25), Inhibit (0.15 to 0.24), Shift (0.15 to 0.23), EmotCont (0.27 to 0.34), Initiate (0.14 to 0.18), WorkMem (0.2 to 0.24), PlanOrg (0.15 to 0.17), TaskMon (0.16 to 0.21), and OrgMat (0.1 to 0.16). These results show the pivotal role of mean curvature and thickness in predicting neurocognitive metrics based on MRI morphometric features. The results are shown as blue, orange, green, red, and purple bars in light in the right panel of Fig. 6.2 to Fig. 6.6.

6.3.4 Predicting Neuropsychiatric Measures from from Blood Biomarkerss

Given the significantly higher predictive performance of Neurocognitive measures derived from Blood Biomarkers 1 compared to other biomarker sets across multiple models, we decided to refine the analysis by selecting features from Blood Biomarkers 2, CSF Biomarkers 1, 2, and 3 that demonstrated comparable or equivalent importance to those from Blood Biomarkers 1. Feature selection was guided by feature importance rankings, focusing on the top contributors from each biomarker set. Subsequently, the models were retrained using these refined feature sets to optimize predictive accuracy. The results are shown as blue, and orange bars in the left panel of Fig. 6.7 to Fig. 6.10.

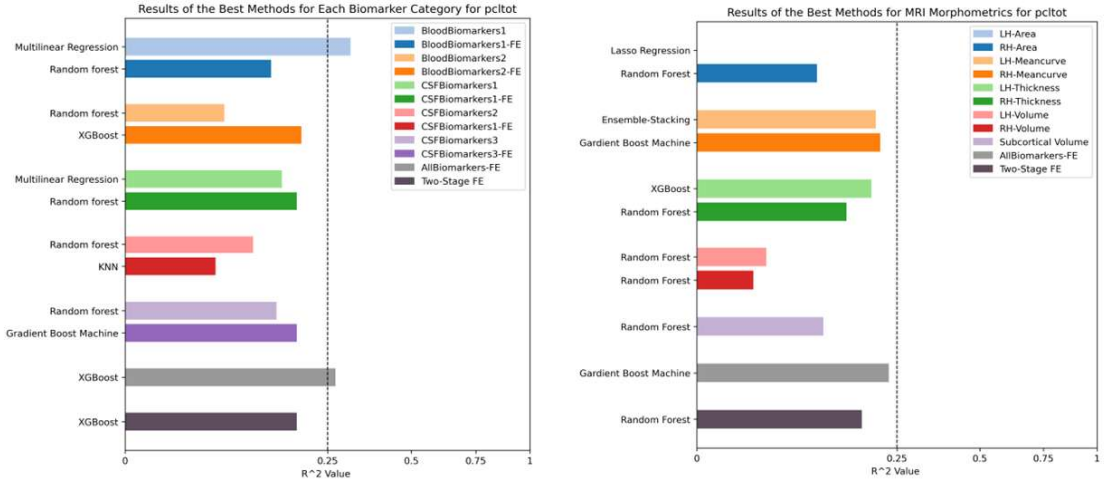

Figure 6.10: Comparative results of machine learning models predicting the pcltot metric using biomarkers (left) and MRI morphometric features (right). Both panels present the performance of models applied to the respective features, including feature engineering approaches (e.g., FE and two-stage FE), with biomarkers, and especially blood biomarkers 1 features, showing higher predictive power overall. The dashed vertical line represents an R^2 threshold of 0.25 for reference.

6.3.4.1 Feature Importance Results for Predicting Neuropsychiatric Measures from Blood Biomarkers

The results of the feature importance analysis demonstrated a significant improvement in predictive performance when using Blood Biomarkers 2. Notably, prior to feature importance, no model could predict ABIS-Attention. However, with key features from Blood Biomarkers 2, including p-IL-10-cv, p-CRP-cv, p-MCP-4-cv, p-MIP-1alpha, p-IL-17D-cv, p-IL-1RA-cv, p-IL-17B, p-MDC, Qalb, p-VEGF-D-cv, p-IL-10, and p-TSLP, the performance improved significantly.

In contrast, for metrics such as ABIS-Motor, ABIS-Nonplanning, BAITot, BDHI-Total, BIS-Tot, and CNSTot, the predictive models using both Blood Biomarkers 1 and 2 did not show improved R^2 with feature importance compared to models without feature selection. For predicting BDI-Tot, the inclusion of top features from Blood Biomarkers 2, such as p-IL-10, p-IL-8-2, p-IL-10-cv, p-IL-13-cv, p-IL-1RA-cv, p-MIP-1alpha, p-INF-gamma-cv, p-IL-5-cv, Qalb, p-MDC, p-IL-12-IL-23p40-cv, and p-ICAM-1-cv, improved performance from 0.1 to 0.2.

In predicting BGLHA-Adolescence-Total, the top features from Blood Biomarkers 2, including p-IL-12-IL-23p40, p-IL-23-cv, p-IL-10, p-VEGF-A, p-IL-21-cv, p-IL-21, p-VEGF-A-2, s-alb, p-IL-17AGenB, p-IL-17A, p-IL-22-cv, and p-TNF-beta, enhanced predictive performance from 0.04 to 0.2.

For NBD-Tot, the use of key features from Blood Biomarkers 2 significantly improved the results. In one case, features such as p-IL-1RA-cv, p-IL-10, p-IL-6, p-IL-17A-F, p-IL-8-2, p-IL-23, p-IL-12-IL-23p40, p-VEGF-A, p-asyn, p-VEGF-A-cv, p-VEGF-A-2, and p-IL-16 raised the performance from 0.12 to 0.24. In another instance, features including p-IL-8-2, p-asyn, p-IL-17B, p-IL-17A-F, p-IL-1RA-cv, p-VEGF-A-2, p-VEGF-A, p-IL-23, dxcte-asyn-p-flag-dv, p-IL-2-cv, p-IL-12-IL-23p40, and p-IL-12-IL-23p40-cv improved the performance from 0.06 to 0.19. The results are shown as light blue, and light orange bars in the left panel of Fig. 6.7 to Fig. 6.10.

6.3.5 Predicting Neuropsychiatric Measures from CSF Biomarkers

Overall, CSF biomarkers performed better with feature importance compared to blood biomarkers in predicting ABIS-Attention. They also outperformed in predicting metrics such as ABIS-Motor, ABIS-Nonplanning, BGLHA-Adolescence-Total, BGLHA-Childhood-Total, BHS-Tot, BIS-Tot, CNS-Tot, NBDH-Tot, and PCL-Tot. However, there were notable exceptions where CSF Biomarker 1 demonstrated strong predictive performance for BDHI-Total and BDI-Tot using Gradient Boosting, as well as for BGLHA-Adolescence-Total using KNN. Similarly, CSF Biomarkers 1 and 3 performed well in predicting BGLHA-Adulthood-Total through Random Forest Regression and KNN, respectively.

CSF biomarkers struggled in predicting BAITot. Among these, CSF Biomarker 3 performed better using the KNN method, and CSF Biomarker 1 showed improvement with Random Forest Regression. For BDHI-Total, CSF Biomarkers 2 and 3 performed poorly, while CSF Biomarker 1 achieved strong results using Gradient Boosting Machines. These findings highlight the varying strengths of different CSF biomarker sets and machine learning methods depending on the specific metric being predicted. The results are shown as green, red, and purple bars in the left panel of Fig. 6.7 to Fig. 6.10.

6.3.5.1 Feature Importance Results for Predicting Neuropsychiatric Measures from CSF Biomarkers

Using feature importance for CSF biomarkers significantly improved the predictive performance for ABIS-Attention. For CSF Biomarker 1, the R^2 increased from 0 to 0.17, while for CSF Biomarker 3, it improved from 0.09 to 0.15. Key features contributing to this improvement included c-bFGF-cv, c-IL-6, c-IL-1RA-cv, c-IL-1-alpha-cv, c-da, c-IL-17B-cv, c-IL-13-cv, and c-VEGF-A.

For ABIS-Motor, the results from CSF biomarkers were less promising, suggesting that this metric may not be effectively predicted using only one category of features. Feature importance proved useful with KNN applied to CSF Biomarker 3, where features like c-da and c-ne made significant contributions, improving the R^2 from 0.04 to 0.14. A similar pattern was observed for ABIS-Nonplanning, BDHI-Total, BGLHA-Adolescence-Total, BIS-Tot, CNS-Tot, and BHS-Tot, where performance gains were modest and consistent with the notion that a single category of features may not be sufficient.

In predicting BAITot and BDI-Tot, feature importance on CSF Biomarker 1 had a more substantial and positive impact. Features such as c-IL-6, c-IL-1RA-cv, c-VCAM-1, c-bFGF-cv, and c-IL-9 demonstrated higher contributions to prediction performance.

For PCLTot, CSF Biomarkers 1 and 3 had a greater impact compared to CSF Biomarker 2, with the R^2 improving by 30%. The results are shown as light green, light red, and light purple bars in the left panel of Fig. 6.7 to Fig. 6.10.

6.3.6 Predicting Neuropsychiatric Measures from MRI Morphometric Measures

Overall, MRI morphometrics demonstrated better capability in predicting neuropsychiatric metrics when considering feature importance results and the highest R^2 values achieved in this study. For ABIS-Attention, ABIS-Motor, and ABIS-Nonplanning, volumetric features, particularly those from the left hemisphere, showed better predictive performance. However, for other metrics, mean curvature and thickness-related features exhibited higher R^2 values. Different machine learning algorithms performed better depending on the metric, with Random Forest emerging as the most successful in most cases, followed by KNN and Gradient Boosting Machine. Interestingly, regularization models such as Ridge Regression

and Lasso also improved predictions in certain cases.

In predicting BAITot, BDHI-Total, BDITot, BIS-Tot, NBD-Tot, and PCLTot, mean curvature and thickness features from the left hemisphere, followed by the right hemisphere, showed better R^2 values. However, for other metrics such as BGLHA-Total across adulthood, childhood, and adolescence, MRI morphometrics did not produce satisfactory results. The results are shown as blue, orange, green, red, and purple bars in the right panel of Fig. 6.7 to Fig. 6.10.

6.3.6.1 Feature Importance Results for Predicting Neuropsychiatric Measures from MRI Morphometric Measures

Doing feature importance significantly improved results in some cases while having minimal impact in others. For certain metrics, volumetric-related features contributed more, but in most cases, curvature and thickness-related features had a notably higher impact. In predicting ABIS-related metrics, the results from the two-stage feature importance approach were similar to the R^2 values achieved using left hemisphere-related volumes or thicknesses. For BAITot, feature importance notably improved the results. When using specific groups of features, the R^2 values were significantly lower compared to using other groups. On average, feature importance methods improved R^2 from 0.13 to 0.18 for BAITot, from 0.26 to 0.31 for BDITot, and up to 0.22 for BGLHA-Adolescence and Adulthood. For NBD-Tot, the improvements were more pronounced, increasing from 0.2 to 0.35. The results are shown as blue, orange, green, red, and purple bars in the right panel of Fig. 6.7 to Fig. 6.10.

6.3.7 Two-Stage Feature Importance and Feature Importance on all Features

This approach proved was highly effective in many cases. For instance, in predicting BGLHA-Adulthood-Total, the results from MRI morphometrics using two-stage feature importance were significantly higher ($R^2 = 0.22$) compared to the single-stage feature importance applied to all MRI morphometrics ($R^2 = 0.05$). Similarly, in predicting BAITot from biomarkers, the two-stage feature importance improved the R^2 from 0.11 to 0.19. Another example was predicting TMI from biomarkers, where the R^2 increased from 0.21 using

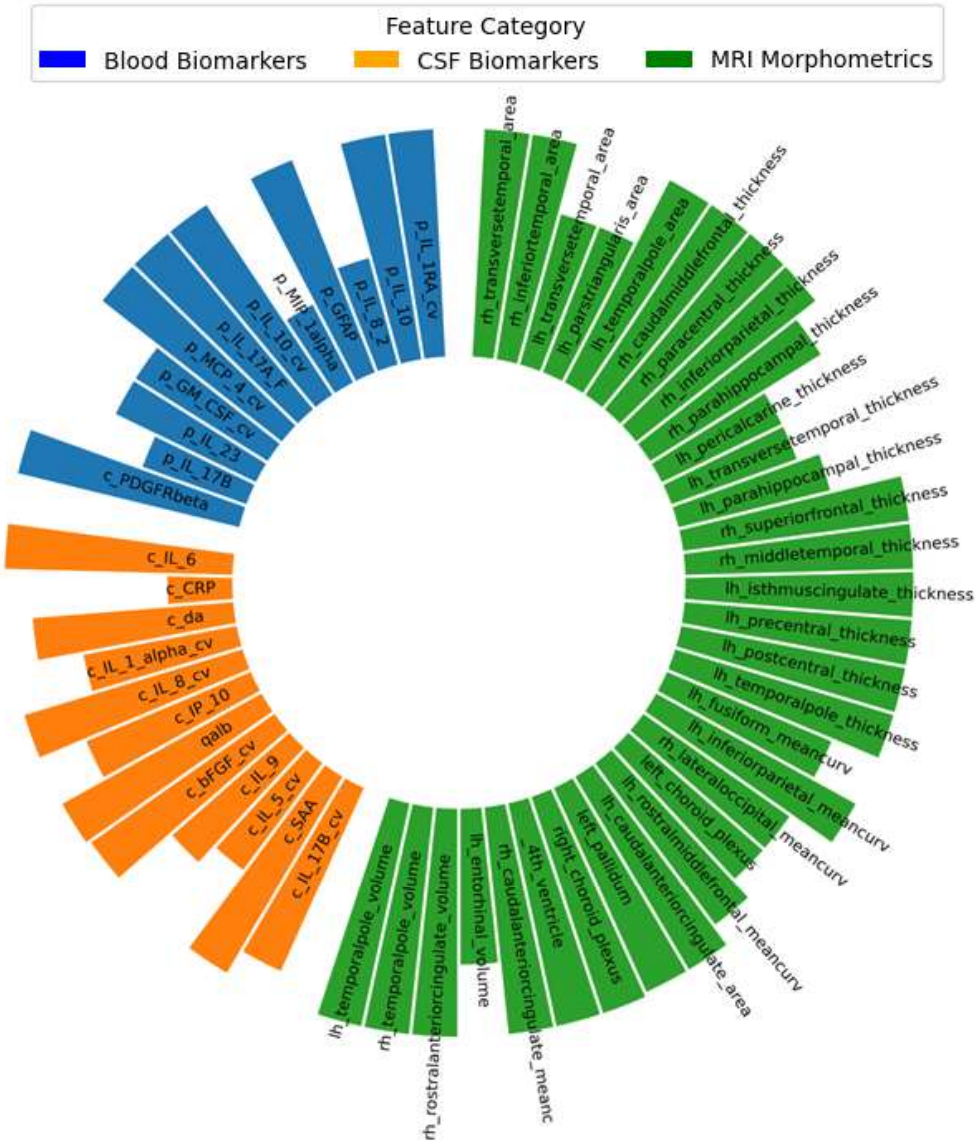

Figure 6.11: Cumulative contribution of features in predicting BRIEF-A metrics. The figure highlights the top features contributing to 80% of the cumulative importance for each metric, reflecting their substantial role in the predictive model. This approach ensures that the most influential features driving prediction are included for analysis and interpretation

a single-stage approach to 0.32 with the two-stage feature importance. This pattern was also observed in predicting MI from biomarkers (R^2 improved from 0.21 to 0.31), Emot-Cont from MRI morphometrics (R^2 increased from 0.28 to 0.34), ABIS-Attention from MRI morphometrics (R^2 improved from 0.21 to 0.26), and BGLHA-Adulthood-Total from 0.05

to 0.22.

However, the initial feature importance approach outperformed the two-stage approach in some cases. For example, in predicting BDITot from MRI morphometrics, the initial feature importance resulted in an R^2 of 0.31, compared to 0.21 achieved using the two-stage method. Similarly, for predicting BHSTot and PCLTot from biomarkers, the initial feature importance showed R^2 values of 0.25 and 0.27, respectively, compared to 0.08 and 0.18 with the two-stage approach.

These results highlight the importance of employing multiple strategies for feature importance and suggest that further categorization or more refined approaches in future studies could improve results even further. The observed variations underscore the complexity of this dataset and the study's nature, indicating that no single method is universally optimal, and adaptability in feature selection processes is essential. The results are shown as dark purple bars in bottom of the Fig. 6.2 to Fig. 6.10. To identify the most relevant features for predicting the BRIEF-A and neuropsychiatric metrics, we applied a feature selection strategy across three categories: blood biomarkers, CSF biomarkers, and MRI morphometrics. The selection process focused on the cumulative contribution of features, ensuring that the top contributors accounted for 80% of the cumulative predictive importance for each metric. This approach not only prioritized features with the highest impact but also maintained clarity and interpretability by narrowing the focus to the most biologically and clinically relevant predictors. By concentrating on a manageable number of key features, this method facilitated a deeper understanding of the relationships between the selected features and the target metrics while ensuring robust and interpretable results (Fig. 6.11 and 6.12.)

6.3.8 PCA and its Impact on the Results

We obtained the best results from Blood Biomarker Set 1 and decided to apply Principal Component Analysis (PCA) to evaluate whether transforming the most predictive features into principal components could further enhance performance. However, PCA did not lead to any improvement in the results, and this outcome could be explained by several factors related to the data and the nature of PCA.

One key reason is that PCA is an unsupervised technique that focuses on reducing di-

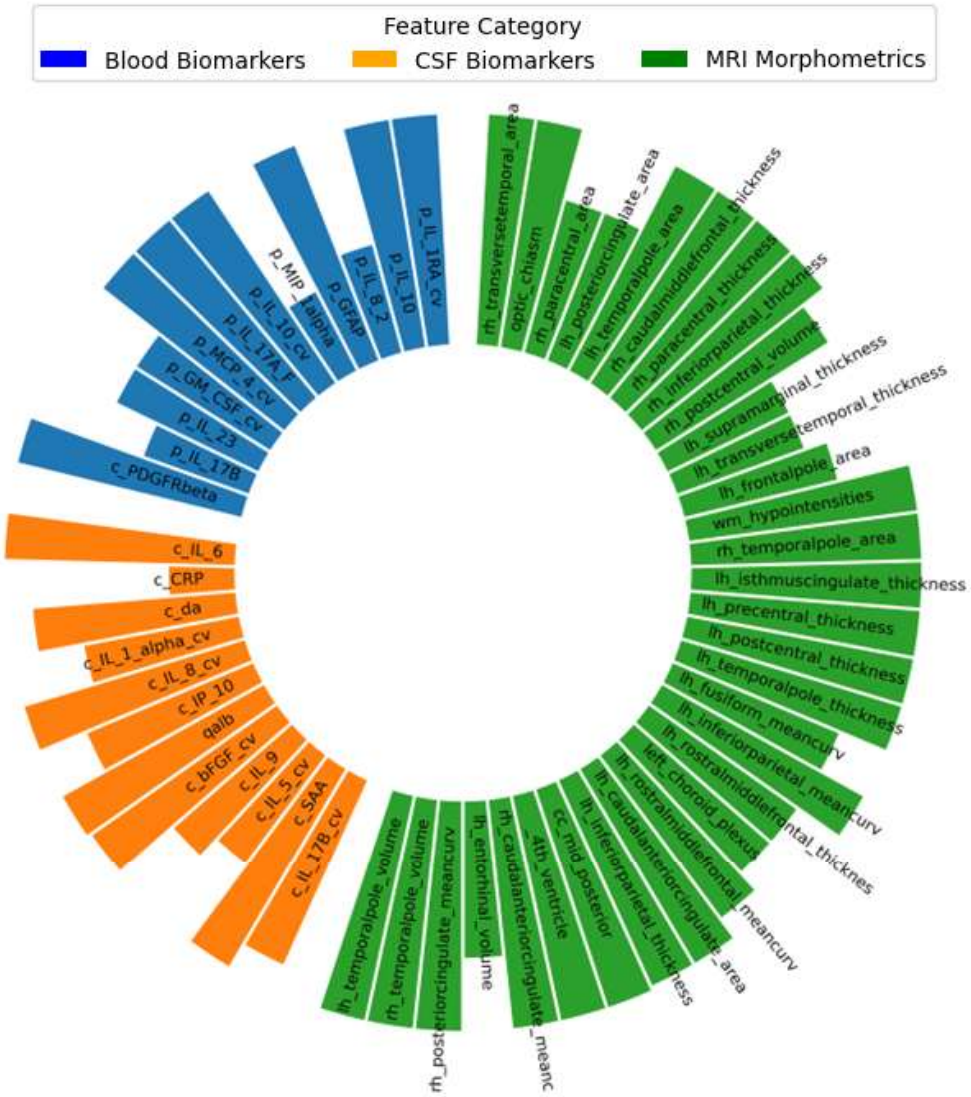

Figure 6.12: Cumulative contribution of features in predicting neuropsychiatric metrics. The figure highlights the top features contributing to 80% of the cumulative importance for each metric, reflecting their substantial role in the predictive model. This approach ensures that the most influential features driving prediction are included for analysis and interpretation

mensionality based on variance without considering the relevance of features to the target variable. If the variance in the data does not align with the predictive power of the features, PCA may remove important information, resulting in reduced performance. This highlights that supervised feature selection methods, such as model-derived feature importance scores,

may be more effective in this context.

Additionally, PCA is limited to capturing linear relationships. If the dataset contains complex non-linear patterns that contribute to the target variable, PCA may fail to capture these dynamics. Non-linear techniques, such as kernel PCA or tree-based approaches, might be better suited to address such cases. Furthermore, the quality and structure of the original data play an essential role. If the dataset includes noise or features with weak relevance to the target variable, PCA cannot enhance the predictive signal.

We also examined the explained variance of the PCA components and found that they did not capture enough relevant information for the predictions. This suggests that variance alone may not always correspond to predictive value. In the future, alternative approaches, such as advanced feature engineering informed by domain knowledge or trying other dimensionality reduction methods, may be more effective. These findings underscore the importance of aligning the analysis methods with the specific nature of the data and prediction objectives.

6.4 Discussion

This aim investigated the capability of ML algorithms to predict neurocognitive and neuropsychiatric metrics using data derived from blood biomarkers, CSF biomarkers, and MRI morphometrics, utilizing the DIAGNOSE CTE dataset. While the predictive accuracy of the models varied, the findings provide valuable insights into the potential of using advanced computational methods to enhance the understanding and management of conditions such as mTBI and CTE.

The findings of this aim provide valuable insights into the predictive power of blood biomarkers, CSF biomarkers, and MRI morphometric features in relation to neurocognitive and neuropsychiatric measures in individuals at risk of or experiencing mTBI. While the predictive performance varied across metrics and feature categories, the results emphasize the potential of MRI morphometrics and biomarkers to enhance the assessment and management of conditions like mTBI and its long-term sequelae, such as CTE (Fig. 6.11 and 6.12.).

The integration of deep learning algorithms in MRI analysis holds immense potential for advancing the assessment of injury severity in mTBI patients. By leveraging these al-

gorithms, clinicians can obtain more objective, sensitive, and specific measures of mTBI severity, leading to improved diagnosis, prognosis, and personalized treatment planning. Further research and collaborations between clinicians, neuroscientists, and data scientists are essential to refine and validate these algorithms, ultimately improving patient outcomes in the management of mTBI.

MRI morphometrics demonstrated notable predictive capability, particularly for neuropsychiatric metrics such as BDI-II (BDITot), BIS-11 total (BIS-Tot), Behavioral Regulation Index (BRI), Emotional Control (EmotCont), and Total Neurobehavioral Dysregulation Score (NBD-Tot), with R^2 values ranging between 0.3 and 0.38. These findings align with prior research highlighting the utility of MRI-derived features, such as volumetric and structural measures, in distinguishing between normal brains and those affected by neurodegenerative conditions. The performance of MRI morphometrics, though not perfect, is promising, particularly given the heterogeneity and complexity of mTBI and CTE-related pathologies. Notably, the predictive power achieved here compares favorably to other studies, such as those predicting cognitive metrics like MoCA (Montreal Cognitive Assessment) in Alzheimer's disease populations ($R^2 = 0.41$) [224], despite the inherent challenges of working with a broader and more diverse mTBI population. Moreover, other studies have demonstrated similar findings, highlighting the correlations between cognitive and neuropsychiatric abilities and various factors such as blood biomarkers, CSF biomarkers, and MRI morphometrics [225–228].

Blood and CSF biomarkers also demonstrated promise, particularly in predicting neurocognitive metrics such as GEC, Initiate, MI, PCL-5, and TMI, with R^2 values ranging from 0.30 to 0.47. These results highlighted the potential of integrating fluid biomarkers with ML algorithms to capture underlying biological processes that contributed to cognitive and psychiatric outcomes. Notably, while MRI morphometrics excelled in predicting certain metrics, blood and CSF biomarkers provided complementary value, reflecting the multifaceted nature of neuropsychiatric and neurocognitive disorders. This demonstrated the importance of leveraging a multimodal approach that combined structural, functional, and molecular data to achieve a comprehensive understanding of these conditions. Importantly, the integration of feature importance and machine learning approaches identified specific

biomarkers with high predictive relevance, which guided future investigations into their mechanistic roles in mTBI and CTE.

The predictive performance of MRI morphometric features performed better than biomarkers in predicting neurocognitive metrics. Specifically, for MI, left hemisphere curvature metrics emerged as the most significant predictors, particularly when analyzed using ensemble methods. The combination of left and right hemisphere mean curvature metrics, evaluated through XGBoost and ensemble stacking approaches, showed the most robust results. Subcortical regions were excluded from the analysis due to their predictive performance being non-comparable to other regions and morphometric measurements.

Some biomarker metrics, including Ab42 and GFAP, demonstrated higher importance or, in other words, were significant contributors to the predictive results. These biomarkers aligned with findings from previous studies, where they were identified as key players in the context of CTE research. Their prominence in this study further showed their relevance in understanding and predicting neurodegenerative conditions associated with repeated traumatic brain injuries.

When predicting metrics from MRI morphometrics, features related to thickness and mean curvature consistently outperformed those related to volume and area across various metrics. Notably, features from the left hemisphere were often more significant predictors and emerged as better indicators of neuropsychiatric measures, particularly for predicting BDI-Tot and NBD-Tot scores.

In this study, predictive models were initially run using all features from each category, followed by models incorporating feature selection based on feature importance. Given the dataset size of 240 subjects and the high dimensionality of the features (50 in total), this approach aimed to evaluate the impact of feature selection on model performance and interpretability. Feature selection plays a pivotal role in refining predictive models, particularly in datasets with limited sample sizes, by helping identify key predictors, enhancing model interpretability, mitigating overfitting, and providing insights into feature utility. By comparing models with and without feature selection, it became evident which predictors contributed most significantly to the outcome metric, as models with fewer, high-importance features often performed comparably to those using all features, reinforcing the value of fea-

ture selection in optimizing performance without sacrificing interpretability. This process highlighted the importance of removing less impactful features to reduce noise, improve model efficiency, and facilitate a clearer understanding of the factors driving outcomes. Moreover, using fewer features reduced the risk of overfitting, ensuring the model generalized better to unseen data, particularly in a dataset with a high feature-to-sample ratio. Performance comparisons, such as accuracy and R^2 scores, revealed that many features contributed little to no value, and their removal not only streamlined the modeling process but also simplified data collection and preprocessing. In cases where performance dropped after feature selection, it underscored the importance of certain features even if their individual importance scores were low, providing further insights into the complex interplay of predictors in the model. This comparative approach provided a clearer understanding of indispensable features while identifying sources of noise, reinforcing the importance of balancing complexity and interpretability in predictive modeling. Ultimately, the findings highlight that feature selection is a critical step for designing robust, interpretable models, particularly when working with datasets of limited size but high dimensionality, allowing for streamlined analyses and the development of more effective predictive tools in future studies.

Also, two feature importance procedures were performed in this study. The first approach involved applying feature importance to all biomarkers and MRI morphometric features separately for each neuropsychiatric and neurocognitive measure. The second, a two-stage process, first applied feature importance to each category of features to predict each metric. Subsequently, only the top-performing categories were selected for another round of feature importance to refine the selection of contributing features within these categories. This two-stage feature importance method proved more effective in certain cases. Given the complexity of the data, the minor correlations between some features, and the nature of the metrics being predicted, implementing such feature selection processes was highly recommended to enhance the reliability of the results.

In terms of machine learning methods, no single algorithm consistently outperformed others. However, random forest, XGBoost, gradient boosting machines, and KNN generally showed better results. In instances where performance was particularly poor, regularization

methods like ridge regression and lasso showed promise in improving outcomes.

Although these results were quite promising, there are several limitations that need to be addressed. First, the overall R^2 values, while encouraging, remained moderate and indicated room for improvement in predictive accuracy. This was likely attributable to the inherent complexity of mTBI and CTE, as well as the variability in patient presentations and disease progression. Additionally, the reliance on machine learning methods introduced challenges related to overfitting, particularly in datasets with limited sample sizes relative to the number of features. Careful feature selection, as well as techniques like two-stage feature importance applied in this study, mitigated some of these issues, but further methodological refinements could enhance future studies.

Another limitation was the reliance on cross-sectional data from the DIAGNOSE CTE project. Longitudinal data could have provided a more comprehensive understanding of how predictive features evolved over time and related to neurocognitive and neuropsychiatric outcomes. Furthermore, while machine learning models captured complex relationships, the interpretability of these models remained a challenge, especially for clinical translation. Combining machine learning insights with domain knowledge and simpler, more interpretable models can bridge this gap.

Another limitation of this study was the challenge of identifying correlations among features without domain expertise. For an engineer, determining feature interrelationships solely through literature was difficult. Future research could benefit from the involvement of a neurologist to assess whether specific features were correlated and, if so, to what extent. This was critical as machine learning models could be misled by multicollinearity (correlated features), resulting in less reliable predictions. Interestingly, in some cases, CSF biomarkers from the third category demonstrated stronger predictive power compared to those from the first and second categories.

In conclusion, this study underscored the utility of advanced machine learning approaches in leveraging biomarkers and MRI morphometric features for predicting neurocognitive and neuropsychiatric outcomes in mTBI populations. While the predictive accuracy was not yet optimal, the findings highlighted promising avenues for future research, particularly through integrating multi-modal data and exploring longitudinal designs. These advancements could

ultimately aid in improving diagnostic precision, monitoring, and personalized management of mTBI and its long-term consequences, including CTE.

6.5 Conclusion

This study explored the application of machine learning algorithms to predict neurocognitive and neuropsychiatric outcomes using multimodal data, including blood biomarkers, CSF biomarkers, and MRI morphometrics, from the DIAGNOSE CTE dataset. The findings highlight the potential of ML techniques in analyzing complex data to better understand and manage conditions associated with mild TBI and CTE. While the predictive accuracy of the models varied, the results emphasize the utility of combining computational methods with diverse biological and structural data.

MRI morphometric features demonstrated significant predictive power, particularly for neuropsychiatric metrics, underscoring their value in assessing brain injury and associated conditions. Biomarkers from blood and CSF provided complementary insights, further enriching the predictive models and reflecting the multifaceted nature of neurocognitive and neuropsychiatric disorders. The implementation of a two-stage feature selection process proved effective in refining models, enhancing their reliability, and identifying high-impact features, which improved overall interpretability and performance.

While the results were encouraging, challenges such as moderate predictive accuracy, data complexity, and variability in model performance highlight areas for future improvement. The reliance on cross-sectional data limited the ability to examine changes over time, underscoring the need for longitudinal studies to capture dynamic patterns in mTBI and CTE progression. Additionally, the interpretability of ML models remains a challenge for clinical translation, suggesting a need for methods that combine advanced algorithms with domain knowledge for greater clarity and application.

In conclusion, this aim demonstrates the potential of ML algorithms in leveraging multimodal data for understanding and predicting outcomes in mTBI populations. Future efforts should focus on addressing current limitations by incorporating longitudinal data, refining feature selection methods, and fostering interdisciplinary collaboration. These advancements could significantly enhance the development of personalized diagnostic and thera-

peutic strategies for mTBI and related neurodegenerative conditions.

Chapter 7

CONCLUSIONS AND FUTURE WORK

7.1 Conclusions

This thesis investigated the biomechanics of brain injury and explored the utility of advanced imaging and computational approaches for understanding and managing TBI, NPH, and CTE. By integrating experimental methods, finite element modeling, advanced MRI techniques, and machine learning algorithms, the study offered novel insights into brain injury mechanisms, and neurodegenerative diseases and highlighted potential tools for diagnosis and patient management.

In Chapter 3, a comprehensive review of helmet technologies revealed the critical role of design innovations, such as rotational damping systems, in reducing kinematics-based injury metrics during impacts. Experimental findings underscored the need for multi-directional testing and incorporating tissue-level metrics to evaluate helmet performance more comprehensively. Limitations included the use of simplified test conditions, which may not fully replicate real-world impacts, and a reliance on specific helmet designs. Future research should explore more diverse testing scenarios to improve helmet safety standards.

Chapter 4 extended this analysis by investigating the modal behavior of brain substructures during helmeted impacts. Using finite element models, distinct oscillatory behaviors were identified in different helmets, with frequency and amplitude patterns correlating with injury metrics. The findings highlighted the importance of understanding substructural brain dynamics, particularly in regions like the brainstem and corpus callosum. However, testing limitations, such as the exclusion of tangential impact components and simplified ventricle modeling, suggest the need for more advanced simulations and in vivo validation.

In Chapter 5, the feasibility of using aMRI to assess NPH and VPS efficacy was demonstrated. Key displacement metrics correlated with functional shunt status, showing potential as non-invasive markers for surgical success. Notably, the percentage difference in

whole-brain displacement at the mid-sagittal slice exhibited significant discriminative power. Challenges included imaging artifacts, manual segmentation, and the inability to collect longitudinal data from all patients due to medical complications. Future work should focus on validating these metrics with larger cohorts and incorporating computational fluid dynamics to improve precisions.

Chapter 6 explored the predictive power of machine learning algorithms applied to multimodal data, including blood biomarkers, CSF biomarkers, and MRI morphometrics, from the DIAGNOSE CTE dataset. The study demonstrated that MRI morphometrics offered significant predictive capability for neuropsychiatric metrics, while biomarkers provided complementary value, enriching the understanding of complex neurodegenerative conditions. Despite promising results, limitations included moderate predictive accuracy, data complexity, and challenges in clinical interpretability. Addressing these limitations requires longitudinal studies and interdisciplinary collaboration to enhance model reliability and applicability.

Overall, this work underscored the importance of combining experimental, computational, and clinical approaches to advance our understanding of TBI, NPH, and CTE. While the findings provided valuable insights, the identified limitations highlight areas for future exploration, including improved helmet design, advanced imaging techniques, and the integration of machine learning with domain expertise. By addressing these challenges, this research lays the groundwork for more effective diagnostic and therapeutic strategies, ultimately improving outcomes for patients affected by neurodegenerative conditions and brain injuries.

7.2 Future Directions for the Entrepreneurial Journey

7.2.1 Entrepreneurial Direction and Practical Applications

Throughout my journey, I have always been driven by the desire to translate scientific discoveries and research into practical applications that can make a real-world impact. It excites me to work in the intersection of mechanics and biology, contributing to the development of solutions that can aid patients and address diseases. With this motivation, my team and I have embarked on a project that originated from our lab, focused on creating a platform for the segmentation of neurodegenerative conditions in medical imaging. Initially, our work was centered on brain tumor segmentation, but we later expanded the

scope to include stroke. Moving forward, we aim to integrate explainability features into our platform, which can be beneficial in other areas such as medical billing. For example, by incorporating explainability, we can contribute to solving issues related to CPT coding, where many cases are either overbilled or underbilled. This addition could not only improve transparency in medical imaging but also provide significant value in ensuring accuracy in healthcare documentation and billing processes.
These ideas and future directions will be elaborated more in the following paragraphs.

7.2.1.1 Background

The research has shown that brain cancer is the 10th leading cause of cancer deaths, with glioblastoma multiforme (GBM) accounting for over 50% of cases. Annually, about 15,000 Americans are diagnosed with GBM [229], and over 10,000 die from it. The healthcare costs for these patients are approximately $201,749 per patient within the first year of diagnosis [230], totaling around $3 billion in the US. Neurosurgeons face limited visibility of tumor boundaries during surgeries, crucial for complete tumor removal. Limited visibility prolongs surgeries and affects patient survival. Current machine learning algorithms can assess tumor severity, but they often struggle to explain their results and are mainly useful before surgery. This highlights the need for more advanced algorithms that can predict tissue changes during and after surgery accurately. Also, Taking into account the markets for 3D medical and surgical imaging platforms [231], surgical navigation systems [232], surgical equipment for neurosurgery [233], and stroke diagnostics [234], we project that the total market size will surpass $6 billion by 2030, which is a promising market to enter.

7.2.1.2 Overview

Our generative AI-driven platform is a novel image analysis algorithm that segments various brain malformations to enhance diagnostic accuracy in medical imaging. The platform also features explainability, which helps physicians understand the algorithm's suggestions better. Explainability enhances decision-making and builds trust in the system. The improvement supports early detection, diagnosis, triage prioritization, and treatment plan-

ning, particularly for surgeries. This improvement helps in early detection, diagnosis, triage prioritization, and treatments, especially surgeries. Our broader scope is to expand the application of our platform's explainability feature for other purposes, such as improving the precision of treatment-related billing to help healthcare systems avoid financial losses due to inaccurate coding. The error rate in medical billing is so high that it results in billions of dollars in erroneous charges.

Our technology leverages the power of advanced, trustworthy neural network models designed for high-precision brain tumor segmentation, alongside developing a cutting-edge deep-learning tool for stroke lesion identification and classification. This approach significantly improves the accuracy of tumor segmentation beyond the state-of-the-art. Moving beyond earlier algorithms that focused narrowly on precise stroke lesion boundary prediction, we are pioneering the development of an end-to-end object detection model. This model incorporates a vision transformer as its backbone model to not only identify but also segment the stroke lesions area effectively. We aim to enhance our platform with explainability features, as this increases adoption rates and builds physician trust. We will extend explainability's use to post-treatment billing processes.This expansion shows how versatile our technology is and helps fix major problems in medical billing, where errors often lead to big financial losses. By improving billing accuracy, our platform helps healthcare systems cut down on incorrect charges, demonstrating its practical usefulness and value. Originating from extensive research, our tool employs adaptive learning techniques that continuously refine its performance, adeptly handling the complex variations in tumor shapes and sizes. This innovative approach ensures our technology adapts and evolves, providing consistently reliable and enhanced diagnostic capabilities. Our technology is strategically designed to enhance medical practices in imaging centers and hospitals. Focusing on brain tumors, it significantly sharpens the precision of surgeries, thereby reducing operation times and fostering quicker patient recovery. This leads to lower healthcare costs and a reduced need for repeat surgeries, ultimately boosting the overall quality of patient care. For stroke management, our technology plays a crucial role in emergency rooms by swiftly differentiating between ischemic and hemorrhagic strokes—conditions that require distinctly different treatments. Utilizing explainable AI (XAI), our system not only identifies potential ischemic strokes but

also promptly alerts medical staff. This alert system includes explanations from the AI, and provides the clinicians with transparent results together with its decision process. helping to accelerate the diagnostic and treatment processes. By improving the speed and accuracy of stroke diagnosis, our technology ensures that patients receive the optimal treatment within a limited time, enhancing outcomes in critical care situations. This algorithm can be used for analyzing tumors at the detection and diagnosis stages, detecting strokes in a timely manner, and helping in performing precise surgeries. It can also be utilized in surgical navigation systems. By applying this technology to reduce medical billing errors, we enhance its market potential, making it more appealing to healthcare facilities interested in purchasing it. Considering the relevant markets for 3D medical and surgical imaging platforms, surgical navigation systems, surgical equipment for neurosurgery, and stroke diagnostics, we estimate a market size bigger than $6 billion by 2030.

7.2.1.3 Potential Commercial Impact

We have identified several customer segments and stakeholders that could benefit from this innovation in different ways, including healthcare improvement and financial benefits. These include neurosurgeons, neuroradiologists, hospitals, and medical imaging centers. Although patients are neither users nor the paying customers, they are categorized as one of the main stakeholders as they benefit from this platform the most. Additionally, insurance companies and preoperative planning companies are other targeted customers.

The customer need that would be met by this innovation is addressing the challenges of limited visibility of tumor boundaries during brain tumor surgeries, which is crucial for complete removal. This issue is especially highlighted in cranial surgeries, where full visibility relies on preoperative neuroimaging data. Limited visibility can prolong surgeries and impact patient survival. Additionally, the subtle nature of certain tumors can make detection and analysis difficult for neuroradiologists, leading to treatment delays and complications. Accurately identifying and segmenting gliomas before surgery is challenging, even for experienced clinicians. This highlights the need for advanced algorithms that can predict tissue changes during and after surgery. Our platform addresses these challenges by

helping neuroradiologists improve the accuracy and speed of their diagnoses and analyses. It also provides explanations for the final findings and decisions, ensuring that the choices made are valid and understandable to physicians. This helps neurosurgeons in performing tumor resection surgeries with greater precision and less damage to healthy tissue, resulting in higher survival rates and reduced chances of functional loss in patients. Based on market research and previous interviews with customers across various segments, we estimate that hospitals and medical centers might pay between $20,000 and 50,000$ annually for a license to our technology. This estimate aligns with the pricing models of competitors and similar companies in the field.

Currently, neuroradiologists identify and detect tumors based solely on their observations and manually define tumor boundaries for analysis. This process is time-consuming and can be challenging, especially when detecting subtle tumors. Neurosurgeons also perform manual segmentation before surgery, which is time-consuming and less accurate compared to AI algorithms.

7.2.1.4 Innovation

Our innovation aims to develop an advanced algorithm to enhance tumor detection, improve stroke diagnostics, and potentially expand to other neurodegenerative diseases in neuroimaging. The proposed innovation leverages deep learning techniques on medical images to improve the accuracy and speed of detection, diagnosis, and precision in brain tumor resection surgeries by performing tumor and stroke segmentation from MRI scans. To this end, we have built a framework that achieves segmentation in MRI scans of the mentioned diseases with higher accuracy. This innovation originates from the team's participation in a global research challenge, called BraTS challenge. The model was trained on the BraTS Challenge 2023 dataset. This dataset includes multi-institutional, clinically acquired preoperative multimodal MRI scans of glioblastoma and low-grade glioma including native (T1), post-contrast T1-weighted (T1Gd), T2-weighted (T2), and Fluid Attenuated Inversion Recovery (FLAIR) volumes. The model was trained using a compound loss function to predict the tumor core, enhancing tumor, and whole tumor. We achieved an average Dice score

of 92.15% on the validation dataset. Our work shows the potential of further improving tumor segmentation by combining diffusion models and discrepancy modeling. Our original NSF LEAP-HI award (CMMI #2227232) titled "LEAP-HI: Tackling Brain Diseases with Mechanics: A Data-Driven Approach to Merge Advanced Neuroimaging and Multi-Physics Modeling", proposed to develop methodologies to study neurological disorders. As part of this study, we have developed novel machine learning methods for accurate analysis and segmentation of brain tumors and substructures in MR images. As such, the fundamental research conducted as part of this NSF award led to the innovative project proposed here.

7.2.1.5 Progress Steps and Commercialization Plan

As part of my postdoctoral journey, I will be joining the Postdoctoral Entrepreneurship Program with CoMotion, where I will focus on advancing *NeuroSeg*. Our team has already taken significant steps towards commercialization. We participated in the regional I-Corps program, conducting 16 customer interviews, and successfully secured the Gap Fund Award through our participation in the Gap Fund Program. Following this, our application to the NSF I-Corps program was accepted, resulting in an interview and an invitation to submit a full proposal. We are set to participate in the third winter cohort. Additionally, we applied to the Female Founded Conference and were accepted for the first phase, where we were asked to submit a video. If we advance in this round, we will move on to a pitch session in November. Throughout this program, we aim to achieve the following objectives:

- Establish a clear commercialization path for *NeuroSeg*.
- Develop a robust business model with backup plans for risk mitigation.
- Conduct a thorough competitive analysis to consider critical market dynamics.
- Secure intellectual property protection to safeguard against potential challenges.
- Identify primary customers and target beachhead customers for the NSF I-Corps interviews.

- Gain familiarity with regulatory affairs to set up an effective future plan.
- Prepare for potential market retaliation.
- Perform a comprehensive SWOT analysis to address critical factors.
- Conduct detailed cost and financial analysis to refine our business and revenue models.
- Establish clear margin expectations.
- Submit the SBIR/STTR grant application and aim to secure funding.
- Identify and prioritize the best potential investment sectors for funding.

These activities are designed to enhance the commercial readiness and value of our technology, ensuring we are positioned for a successful market entry. Furthermore, it is crucial to examine reimbursement systems and potential coverage based on our business model and market analysis findings. Like any startup, we anticipate multiple barriers before entering the market. Identifying these barriers and actively engaging with early adopters and key opinion leaders in the field will be essential to overcoming challenges related to market adoption.

7.2.2 Commercialization Strategy

In outlining the commercialization path for *NeuroSeg*, we are integrating customer discovery, market analysis, product analysis, and financial planning. Initially, we conducted customer interviews to understand their needs and gather feedback on potential applications of our technology. This feedback is pivotal in refining our business model, taking into account competitor products, market dynamics, and essential distribution channels. We thoroughly analyze our product's unique selling points, including cost, performance, and regulatory considerations, ensuring it stands out in the marketplace. Financially, we assess the production and delivery costs, explore funding opportunities such as private investments or grants, and calculate potential revenue and margins to ensure project sustainability. This comprehensive approach forms a well-rounded strategy, addressing customer preferences,

market needs, and financial viability, thereby maximizing the chances of successful commercialization for *NeuroSeg*.

The findings discussed in this chapter have been previously published in several papers, including references [**?** **?**]

BIBLIOGRAPHY

[1] Javid Abderezaei. *Spatio-Temporal Characteristics of Human Brain and Cerebrovasculature Biomechanics Through in Vivo Imaging and Computational Analysis*. PhD thesis, Stevens Institute of Technology, 2021.

[2] Yujun Hou, Xiuli Dan, Mansi Babbar, Yong Wei, Steen G Hasselbalch, Deborah L Croteau, and Vilhelm A Bohr. Ageing as a risk factor for neurodegenerative disease. *Nature Reviews Neurology*, 15(10):565–581, 2019.

[3] G Bellomo, P Piscopo, M Corbo, E Pupillo, G Stipa, E Beghi, N Vanacore, and E Lacorte. A systematic review on the risk of neurodegenerative diseases and neurocognitive disorders in professional and varsity athletes. *Neurological Sciences*, 43(12):6667–6691, 2022.

[4] Javier S Morales, Pedro L Valenzuela, Gonzalo Saco-Ledo, Adrián Castillo-García, Cristina S Carabias, Paul McCrory, Alejandro Santos-Lozano, and Alejandro Lucia. Mortality risk from neurodegenerative disease in sports associated with repetitive head impacts: preliminary findings from a systematic review and meta-analysis. *Sports Medicine*, pages 1–12, 2022.

[5] Christopher A Taylor, Jeneita M Bell, Matthew J Breiding, and Likang Xu. Traumatic brain injury–related emergency department visits, hospitalizations, and deaths—united states, 2007 and 2013. *MMWR Surveillance Summaries*, 66(9):1, 2017.

[6] Erik G Takhounts, Matthew J Craig, Kevin Moorhouse, Joe McFadden, and Vikas Hasija. Development of brain injury criteria (bric). Technical report, SAE Technical Paper, 2013.

[7] Erik G Takhounts, Vikas Hasija, Stephen A Ridella, Steve Rowson, and Stefan M

Duma. Kinematic rotational brain injury criterion (bric). In *Proceedings of the 22nd enhanced safety of vehicles conference. Paper*, number 11-0263, pages 1–10, 2011.

[8] Steven Rowson, Stefan M Duma, Jonathan G Beckwith, Jeffrey J Chu, Richard M Greenwald, Joseph J Crisco, P Gunnar Brolinson, Ann-Christine Duhaime, Thomas W McAllister, and Arthur C Maerlender. Rotational head kinematics in football impacts: an injury risk function for concussion. *Annals of biomedical engineering*, 40:1–13, 2012.

[9] Albert I King, King H Yang, Liying Zhang, Warren Hardy, and David C Viano. Is head injury caused by linear or angular acceleration. In *IRCOBI conference*, volume 12. Lisbon, Portugal, 2003.

[10] Jamshid Ghajar. Traumatic brain injury. *The Lancet*, 356(9233):923–929, 2000.

[11] Xianghao Zhan, Yiheng Li, Yuzhe Liu, August G Domel, Hossein Vahid Alizadeh, Samuel J Raymond, Jesse Ruan, Saeed Barbat, Stephen Tiernan, Olivier Gevaert, et al. The relationship between brain injury criteria and brain strain across different types of head impacts can be different. *Journal of the Royal Society Interface*, 18(179):20210260, 2021.

[12] Hideyuki Kimpara and Masami Iwamoto. Mild traumatic brain injury predictors based on angular accelerations during impacts. *Annals of biomedical engineering*, 40(1):114–126, 2012.

[13] Thomas W McAllister, James C Ford, Songbai Ji, Jonathan G Beckwith, Laura A Flashman, Keith Paulsen, and Richard M Greenwald. Maximum principal strain and strain rate associated with concussion diagnosis correlates with changes in corpus callosum white matter indices. *Annals of biomedical engineering*, 40(1):127–140, 2012.

[14] Songbai Ji, Wei Zhao, James C Ford, Jonathan G Beckwith, Richard P Bolander, Richard M Greenwald, Laura A Flashman, Keith D Paulsen, and Thomas W McAllister. Group-wise evaluation and comparison of white matter fiber strain and maximum principal strain in sports-related concussion. *Journal of neurotrauma*, 32(7):441–454, 2015.

[15] Panagiotis G Massouros, Philip V Bayly, and Guy M Genin. Strain localization in an oscillating maxwell viscoelastic cylinder. *International journal of solids and structures*, 51(2):305–313, 2014.

[16] Kaveh Laksari, Mehmet Kurt, Hessam Babaee, Svein Kleiven, and David Camarillo. Mechanistic insights into human brain impact dynamics through modal analysis. *Physical review letters*, 120(13):138101, 2018.

[17] Javid Abderezaei, Wei Zhao, Carissa L Grijalva, Gloria Fabris, Songbai Ji, Kaveh Laksari, and Mehmet Kurt. Nonlinear dynamical behavior of the deep white matter during head impact. *Physical Review Applied*, 12(1):014058, 2019.

[18] Steven Rowson and Stefan M Duma. Brain injury prediction: assessing the combined probability of concussion using linear and rotational head acceleration. *Annals of biomedical engineering*, 41(5):873–882, 2013.

[19] Kewei Bian and Haojie Mao. Mechanisms and variances of rotation-induced brain injury: a parametric investigation between head kinematics and brain strain. *Biomechanics and modeling in mechanobiology*, 19(6):2323–2341, 2020.

[20] Lee F Gabler, Jeff R Crandall, and Matthew B Panzer. Development of a second-order system for rapid estimation of maximum brain strain. *Annals of biomedical engineering*, 47(9):1971–1981, 2019.

[21] Kianoosh Ghazi, Mark Begonia, Steven Rowson, and Songbai Ji. American football helmet effectiveness against a strain-based concussion mechanism. *Annals of biomedical engineering*, pages 1–12, 2022.

[22] Logan E Miller, Jillian E Urban, Mark A Espeland, Michael P Walkup, James M Holcomb, Elizabeth M Davenport, Alexander K Powers, Christopher T Whitlow, Joseph A Maldjian, and Joel D Stitzel. Cumulative strain-based metrics for predicting subconcussive head impact exposure–related imaging changes in a cohort of american youth football players. *Journal of Neurosurgery: Pediatrics*, 29(4):387–396, 2022.

[23] Emily Bliven, Alexandra Rouhier, Stanley Tsai, Rémy Willinger, Nicolas Bourdet, Caroline Deck, Steven M Madey, and Michael Bottlang. Evaluation of a novel bicycle helmet concept in oblique impact testing. *Accident Analysis & Prevention*, 124:58–65, 2019.

[24] Megan L Bland, Craig McNally, and Steven Rowson. Differences in impact performance of bicycle helmets during oblique impacts. *Journal of biomechanical engineering*, 140(9), 2018.

[25] T Blaine Hoshizaki and Susan E Brien. The science and design of head protection in sport. *Neurosurgery*, 55(4):956–967, 2004.

[26] Mari Angelica Allison. The performance of helmet-based kinematic measurement systems: Importance for mild traumatic brain injury prevention. 2015.

[27] Alireza Mojahed, Javid Abderezaei, Mehmet Kurt, Lawrence A. Bergman, and Alexander F. Vakakis. A nonlinear reduced-order model of the corpus callosum under planar coronal excitation. *Journal of Biomechanical Engineering*, 142(9), 2020.

[28] Noam Alperin, Eric M. Vikingstad, Beatriz Gomez-Anson, and David N. Levin. Hemodynamically independent analysis of cerebrospinal fluid and brain motion observed with dynamic phase contrast mri. *Magnetic Resonance in Medicine*, 35(5):741–754, 1996.

[29] Soroush Heidari Pahlavian, Francis Loth, Mark Luciano, John Oshinski, and Bryn A. Martin. Neural tissue motion impacts cerebrospinal fluid dynamics at the cervical medullary junction: A patient-specific moving-boundary computational model. *Annals of Biomedical Engineering*, 43(12):2911–2923, 2015.

[30] Philippe Moireau, Nan Xiao, Matteo Astorino, C. Alberto Figueroa, Dominique Chapelle, C.A. Taylor, and J-F. Gerbeau. External tissue support and fluid-structure simulation in blood flows. *Biomechanics and Modeling in Mechanobiology*, 11(1-2):1–18, 2012.

[31] Javid Abderezaei, John Martinez, Itamar Terem, Gloria Fabris, Aymeric Pionteck, Yang Yang, Samantha J Holdsworth, Kambiz Nael, and Mehmet Kurt. Amplified flow imaging (aflow): A novel mri-based tool to unravel the coupled dynamics between the human brain and cerebrovasculature. *IEEE Transactions on Medical Imaging*, 39(12):4113–4123, 2020.

[32] Javid Abderezaei, Fargol Rezayaraghi, Aymeric Pionteck, Ya-Chen Chuang, Alejandro Carrasquilla, Gizem Bilgili, Tianyi Ren, Tyson Lam, Tse-An Lu, Miriam Scadeng, et al. Increased hindbrain motion in chiari i malformation patients measured through 3d amplified mri (3d amri). *Brain Multiphysics*, page 100100, 2024.

[33] Marcia Louis, Michael Alosco, Benjamin Rowland, Huijin Liao, Joseph Wang, Ajay Joshi, Robert Stern, and Alexander Lin. Biomarkers for cte diagnosis in retired nfl player using machine learning. *Biomarkers*, 11:8, 2017.

[34] Christian Oldenburg, Anders Lundin, Gunnar Edman, Catharina Nygren-de Boussard, and Aniko Bartfai. Cognitive reserve and persistent post-concussion symptoms—a prospective mild traumatic brain injury (mtbi) cohort study. *Brain injury*, 30(2):146–155, 2016.

[35] Trevor C Wu, Elisabeth A Wilde, Erin D Bigler, Xiaoqi Li, Tricia L Merkley, Ragini Yallampalli, Stephen R McCauley, Kathleen P Schnelle, Ana C Vasquez, Zili Chu, et al. Longitudinal changes in the corpus callosum following pediatric traumatic brain injury. *Developmental neuroscience*, 32(5-6):361–373, 2010.

[36] James F Malec, Allen W Brown, Cynthia L Leibson, Julie Testa Flaada, Jayawant N Mandrekar, Nancy N Diehl, and Patricia K Perkins. The mayo classification system for traumatic brain injury severity. *Journal of neurotrauma*, 24(9):1417–1424, 2007.

[37] Michael P Alexander. Mild traumatic brain injury: pathophysiology, natural history, and clinical management. *Neurology*, 1995.

[38] Pieter E Vos, Y Alekseenko, Leontino Battistin, Edvard Ehler, Franz Gerstenbrand,

Dafin Fior Muresanu, A Potapov, Christoph A Stepan, Pavel Traubner, László Vécsei, et al. Mild traumatic brain injury. *European journal of neurology*, 19(2):191–198, 2012.

[39] Fidel Hernandez, Lyndia C Wu, Michael C Yip, Kaveh Laksari, Andrew R Hoffman, Jaime R Lopez, Gerald A Grant, Svein Kleiven, and David B Camarillo. Six degree-of-freedom measurements of human mild traumatic brain injury. *Annals of biomedical engineering*, 43(8):1918–1934, 2015.

[40] Calvin Kuo, Lyndia C Wu, Patrick P Ye, Kaveh Laksari, David B Camarillo, and Ellen Kuhl. Pilot findings of brain displacements and deformations during roller coaster rides. *Journal of neurotrauma*, 34(22):3198–3205, 2017.

[41] Xianghao Zhan, Yuzhe Liu, Samuel J Raymond, Hossein Vahid Alizadeh, August G Domel, Olivier Gevaert, Michael Zeineh, Gerald Grant, and David B Camarillo. Deep learning head model for real-time estimation of entire brain deformation in concussion. *arXiv preprint arXiv:2010.08527*, 2020.

[42] Wei Zhao, Yunliang Cai, Zhigang Li, and Songbai Ji. Injury prediction and vulnerability assessment using strain and susceptibility measures of the deep white matter. *Biomechanics and modeling in mechanobiology*, 16(5):1709–1727, 2017.

[43] Logan E Miller, Jillian E Urban, Elizabeth M Davenport, Alexander K Powers, Christopher T Whitlow, Joseph A Maldjian, and Joel D Stitzel. Brain strain: computational model-based metrics for head impact exposure and injury correlation. *Annals of biomedical engineering*, 49(3):1083–1096, 2021.

[44] Erik G Takhounts, Stephen A Ridella, Vikas Hasija, Rabih E Tannous, J Quinn Campbell, Dan Malone, Kerry Danelson, Joel Stitzel, Steve Rowson, and Stefan Duma. Investigation of traumatic brain injuries using the next generation of simulated injury monitor (simon) finite element head model. *Stapp car crash journal*, 52:1, 2008.

[45] Logan E Miller, Jillian E Urban, and Joel D Stitzel. Validation performance comparison for finite element models of the human brain. *Computer methods in biomechanics and biomedical engineering*, 20(12):1273–1288, 2017.

[46] Svein Kleiven. *Finite element modeling of the human head*. PhD thesis, KTH, 2002.

[47] Songbai Ji, Hamidreza Ghadyani, Richard P Bolander, Jonathan G Beckwith, James C Ford, Thomas W McAllister, Laura A Flashman, Keith D Paulsen, Karin Ernstrom, Sonia Jain, et al. Parametric comparisons of intracranial mechanical responses from three validated finite element models of the human head. *Annals of biomedical engineering*, 42(1):11–24, 2014.

[48] Logan E Miller, Jillian E Urban, and Joel D Stitzel. Development and validation of an atlas-based finite element brain model. *Biomechanics and modeling in mechanobiology*, 15(5):1201–1214, 2016.

[49] Songbai Ji, Mazdak Ghajari, Haojie Mao, Reuben H Kraft, Marzieh Hajiaghamemar, Matthew B Panzer, Remy Willinger, Michael D Gilchrist, Svein Kleiven, and Joel D Stitzel. Use of brain biomechanical models for monitoring impact exposure in contact sports. *Annals of Biomedical Engineering*, pages 1–20, 2022.

[50] Javid Abderezaei, Fargol Rezayaraghi, Brigit Kain, Andrea Menichetti, and Mehmet Kurt. An overview of the effectiveness of bicycle helmet designs in impact testing. *Frontiers in bioengineering and biotechnology*, 9, 2021.

[51] NJ Mills and A Gilchrist. Oblique impact testing of bicycle helmets. *International Journal of Impact Engineering*, 35(9):1075–1086, 2008.

[52] Kirk Hansen, Nathan Dau, Florian Feist, Caroline Deck, Rémy Willinger, Steven M Madey, and Michael Bottlang. Angular impact mitigation system for bicycle helmets to reduce head acceleration and risk of traumatic brain injury. *Accident Analysis & Prevention*, 59:109–117, 2013.

[53] Peter A Cripton, Daniel M Dressler, Cameron A Stuart, Christopher R Dennison, and Darrin Richards. Bicycle helmets are highly effective at preventing head injury during head impact: head-form accelerations and injury criteria for helmeted and unhelmeted impacts. *Accident Analysis & Prevention*, 70:1–7, 2014.

[54] Helena Stigson, Matteo Rizzi, Anders Ydenius, Emma Engström, and Anders Kullgren. Consumer testing of bicycle helmets. In *International Research Council on the Biomechanics of Injury Conference (IRCOBI Conference), Antwerp, Belgium, Sept*, pages 13–15, 2017.

[55] Philip G Petersen, Lloyd V Smith, and Derek Nevins. The effect of surface roughness on oblique bicycle helmet impact tests. *Proceedings of the Institution of Mechanical Engineers, Part P: Journal of Sports Engineering and Technology*, 234(4):320–327, 2020.

[56] Mehmet Kurt, Kaveh Laksari, Calvin Kuo, Gerald A Grant, and David B Camarillo. Modeling and optimization of airbag helmets for preventing head injuries in bicycling. *Annals of biomedical engineering*, 45(4):1148–1160, 2017.

[57] Fady Abayazid, Ke Ding, Karl Zimmerman, Helena Stigson, and Mazdak Ghajari. A new assessment of bicycle helmets: the brain injury mitigation effects of new technologies in oblique impacts. *Annals of biomedical engineering*, pages 1–18, 2021.

[58] Megan L Bland, David S Zuby, Becky C Mueller, and Steven Rowson. Differences in the protective capabilities of bicycle helmets in real-world and standard-specified impact scenarios. *Traffic injury prevention*, 19(sup1):S158–S163, 2018.

[59] Megan L Bland, Craig McNally, and Steven Rowson. Headform and neck effects on dynamic response in bicycle helmet oblique impact testing. In *Proceedings of the IRCOBI Conference. Athens, Greece*, pages 413–423, 2018.

[60] Megan L Bland, Craig McNally, David S Zuby, Becky C Mueller, and Steven Rowson. Development of the star evaluation system for assessing bicycle helmet protective performance. *Annals of biomedical engineering*, 48(1):47–57, 2020.

[61] Bethany Rowson, Steven Rowson, and Stefan M Duma. Hockey star: a methodology for assessing the biomechanical performance of hockey helmets. *Annals of biomedical engineering*, 43(10):2429–2443, 2015.

[62] Mark Begonia, Abigail M Tyson, Bethany Rowson, and Steven Rowson. Hockey star methodology. 2020.

[63] Susan Sheps Margulies, Lawrence E Thibault, and Thomas A Gennarelli. Physical model simulations of brain injury in the primate. *Journal of biomechanics*, 23(8):823–836, 1990.

[64] Narayan Yoganandan, Jianrong Li, Jiangyue Zhang, Frank A Pintar, and Thomas A Gennarelli. Influence of angular acceleration–deceleration pulse shapes on regional brain strains. *Journal of biomechanics*, 41(10):2253–2262, 2008.

[65] Kaveh Laksari, Lyndia C Wu, Mehmet Kurt, Calvin Kuo, and David C Camarillo. Resonance of human brain under head acceleration. *Journal of The Royal Society Interface*, 12(108):20150331, 2015.

[66] Teresa M Abney, Y Aaron Feng, Robert Pless, Ruth J Okamoto, Guy M Genin, and Philip V Bayly. Principal components of brain deformation in response to skull acceleration: the roles of sliding and tethering between the brain and skull. In *26th Southern Biomedical Engineering Conference SBEC 2010, April 30-May 2, 2010, College Park, Maryland, USA*, pages 9–12. Springer, 2010.

[67] Erik H Clayton, Guy M Genin, and Philip V Bayly. Transmission, attenuation and reflection of shear waves in the human brain. *Journal of The Royal Society Interface*, 9(76):2899–2910, 2012.

[68] Svein Kleiven. Evaluation of head injury criteria using a finite element model validated against experiments on localized brain motion, intracerebral acceleration, and intracranial pressure. *International Journal of Crashworthiness*, 11(1):65–79, 2006.

[69] Wei Zhao and Songbai Ji. White matter anisotropy for impact simulation and response sampling in traumatic brain injury. *Journal of neurotrauma*, 36(2):250–263, 2019.

[70] ES Gurdjian, VR Hodgson, LM Thomas, and LM Patrick. Significance of relative movements of scalp, skull, and intracranial contents during impact injury of the head. *Journal of neurosurgery*, 29(1):70–72, 1968.

[71] Wei Zhao, Adam Bartsch, Edward Benzel, Vincent Miele, Brian D Stemper, and Songbai Ji. Regional brain injury vulnerability in football from two finite element models of the human head. *IRCOBI. Florence, Italy*, pages 619–621, 2019.

[72] Bruno Giammarinaro, David Espíndola, François Coulouvrat, and Gianmarco Pinton. Focusing of shear shock waves. *Physical Review Applied*, 9(1):014011, 2018.

[73] JD Escarcega, AK Knutsen, RJ Okamoto, DL Pham, and PV Bayly. Natural oscillatory modes of 3d deformation of the human brain in vivo. *Journal of biomechanics*, 119:110259, 2021.

[74] Michael McCrea, Thomas Hammeke, Gary Olsen, Peter Leo, and Kevin Guskiewicz. Unreported concussion in high school football players: implications for prevention. *Clinical journal of sport medicine*, 14(1):13–17, 2004.

[75] Jean A Langlois, Wesley Rutland-Brown, and Marlena M Wald. The epidemiology and impact of traumatic brain injury: a brief overview. *The Journal of head trauma rehabilitation*, 21(5):375–378, 2006.

[76] Michael L Levy, Burak M Ozgur, Cherisse Berry, Henry E Aryan, and Michael LJ Apuzzo. Birth and evolution of the football helmet. *Neurosurgery*, 55(3):656–662, 2004.

[77] Robyn G Attewell, Kathryn Glase, and Michael McFadden. Bicycle helmet efficacy: a meta-analysis. *Accident Analysis & Prevention*, 33(3):345–352, 2001.

[78] Michael D Cusimano and Judith Kwok. The effectiveness of helmet wear in skiers and snowboarders: a systematic review. *British Journal of Sports Medicine*, 44(11):781–786, 2010.

[79] Lagina R Scott, Shahrzad Bazargan-Hejazi, Anaheed Shirazi, Deyu Pan, Steven Lee, Stacey A Teruya, and Magda Shaheen. Helmet use and bicycle-related trauma injury outcomes. *Brain injury*, 33(13-14):1597–1601, 2019.

[80] Je Yeong Sone, Douglas Kondziolka, Jason H Huang, and Uzma Samadani. Helmet efficacy against concussion and traumatic brain injury: a review. *Journal of neurosurgery*, 126(3):768–781, 2017.

[81] Christopher M Bonfield, Samuel S Shin, and Adam S Kanter. Helmets, head injury and concussion in sport. *The Physician and Sportsmedicine*, 43(3):236–246, 2015.

[82] P Rousseau, A Post, and TB Hoshizaki. The effects of impact management materials in ice hockey helmets on head injury criteria. *Proceedings of the Institution of Mechanical Engineers, Part P: Journal of Sports Engineering and Technology*, 223(4):159–165, 2009.

[83] Andrew Post, Anna Oeur, Blaine Hoshizaki, and Michael D Gilchrist. An examination of american football helmets using brain deformation metrics associated with concussion. *Materials & Design*, 45:653–662, 2013.

[84] NJ Mills and Adam Gilchrist. Bicycle helmet design. *Proceedings of the Institution of Mechanical Engineers, Part L: Journal of materials: Design and applications*, 220(4):167–180, 2006.

[85] D Stewart, Laurence R Young, Rahul Goel, et al. Evaluating the performance of helmet linings incorporating fluid channels. *Journal of ASTM International*, 7(10), 2010.

[86] David C Viano and David Halstead. Change in size and impact performance of football helmets from the 1970s to 2010. *Annals of biomedical engineering*, 40(1):175–184, 2012.

[87] Consumer Product Safety Commission et al. Safety standard for bicycle helmets; final rule, 16 cfr part 1203. *Consumer Product Safety Commission, Bethesda, Maryland*, 1998.

[88] NOCSAE. Standard test method and equipment used in evaluating the performance characteristics of protective headgear/equipment. *NOCSAE*, 2013.

[89] Michael Goutnik, Joel Goeckeritz, Zackary Sabetta, Tala Curry, Matthew Willman, Jonathan Willman, Theresa Currier Thomas, and Brandon Lucke-Wold. Neurotrauma prevention review: improving helmet design and implementation. *Biomechanics*, 2(4):500–512, 2022.

[90] Kabir Singh Lota, Nikos Malliaropoulos, Wiesław Blach, Takeshi Kamitani, Akira Ikumi, Vasileios Korakakis, and Nicola Maffulli. Rotational head acceleration and traumatic brain injury in combat sports: a systematic review. *British medical bulletin*, 141(1):33–46, 2022.

[91] T Blaine Hoshizaki, Andrew Post, R Anna Oeur, and Susan E Brien. Current and future concepts in helmet and sports injury prevention. *Neurosurgery*, 75(suppl_4):S136–S148, 2014.

[92] Niall C Colgan, Michael D Gilchrist, and Kathleen M Curran. Applying dti white matter orientations to finite element head models to examine diffuse tbi under high rotational accelerations. *Progress in biophysics and molecular biology*, 103(2-3):304–309, 2010.

[93] Matthew D Bockman, Akash P Kansagra, Shawn C Shadden, Eric C Wong, and Alison L Marsden. Fluid mechanics of mixing in the vertebrobasilar system: comparison of simulation and mri. *Cardiovascular Engineering and Technology*, 3:450–461, 2012.

[94] Philip V Bayly, Ahmed Alshareef, Andrew K Knutsen, Kshitiz Upadhyay, Ruth J Okamoto, Aaron Carass, John A Butman, Dzung L Pham, Jerry L Prince, KT Ramesh, et al. Mr imaging of human brain mechanics in vivo: new measurements to facilitate the development of computational models of brain injury. *Annals of biomedical engineering*, 49:2677–2692, 2021.

[95] Efe Ozkaya, Gloria Fabris, Fabiola Macruzb, Zeynep M. Suar, Javid Abderezaei, Bochao Su, Kaveh Laksari, Lyndia Wu, David B. Camarillo, Kim B. Pauly, Max Wintermarkb, and Mehmet Kurt. Viscoelasticity of children and adolescent brains

through mr elastography. *Journal of the Mechanical Behavior of Biomedical Materials*, 2020.

[96] Curtis L Johnson, Matthew DJ McGarry, Armen A Gharibans, John B Weaver, Keith D Paulsen, Huan Wang, William C Olivero, Bradley P Sutton, and John G Georgiadis. Local mechanical properties of white matter structures in the human brain. *Neuroimage*, 79:145–152, 2013.

[97] E Ozkaya, ER Triolo, F Rezayaraghi, J Abderezaei, W Meinhold, K Hong, A Alipour, P Kennedy, L Fleysher, J Ueda, et al. Brain-mimicking phantom for biomechanical validation of motion sensitive mr imaging techniques. *Journal of the Mechanical Behavior of Biomedical Materials*, 122:104680, 2021.

[98] Waiman Meinhold, Efe Ozkaya, Derek Petti, Vaughn Rice, Emily Triolo, Fargol Rezayaraghi, Paul Kennedy, Lazar Fleysher, Ai-Ping Hu, Jun Ueda, et al. Towards image guided magnetic resonance elastography via active driver positioning robot. *IEEE Transactions on Biomedical Engineering*, 69(11):3345–3355, 2022.

[99] Andreas A Linninger, Michalis Xenos, David C Zhu, MahadevaBharath R Somayaji, Srinivasa Kondapalli, and Richard D Penn. Cerebrospinal fluid flow in the normal and hydrocephalic human brain. *IEEE Transactions on Biomedical Engineering*, 54(2):291–302, 2007.

[100] Alexander I Veress, Grant T Gullberg, and Jeffrey A Weiss. Measurement of strain in the left ventricle during diastole with cine-mri and deformable image registration. 2005.

[101] Vannessa Leung, John S. Magnussen, Marcus A. Stoodley, and Lynne E. Bilston. Cerebellar and hindbrain motion in chiari malformation with and without syringomyelia. *Journal of Neurosurgery: Spine*, 24(4):546–555, 2016.

[102] Itamar Terem, Wendy W. Ni, Maged Goubran, Mahdi Salmani Rahimi, Greg Zaharchuk, Kristen W. Yeom, Michael E. Moseley, Mehmet Kurt, and Samantha J.

Holdsworth. Revealing sub-voxel motions of brain tissue using phase-based amplified mri (amri). *Magnetic Resonance in Medicine*, 80(6):2549–2559, 2018.

[103] Javid Abderezaei, Aymeric Pionteck, Itamar Terem, Leo Dang, Miriam Scadeng, Peter Morgenstern, Raj Shrivastava, Samantha J Holdsworth, Yang Yang, and Mehmet Kurt. Development, calibration, and testing of 3d amplified mri (amri) for the quantification of intrinsic brain motion. *Brain Multiphysics*, 2:100022, 2021.

[104] Samantha J. Holdsworth, Mahdi Salmani Rahimi, Wendy W. Ni, Greg Zaharchuk, and Michael E. Moseley. Amplified magnetic resonance imaging (amri). *Magnetic Resonance in Medicine*, 75(6):2245–2254, 2016.

[105] Xiaoqing Liu, Kunlun Gao, Bo Liu, Chengwei Pan, Kongming Liang, Lifeng Yan, Jiechao Ma, Fujin He, Shu Zhang, Siyuan Pan, et al. Advances in deep learning-based medical image analysis. *Health Data Science*, 2021, 2021.

[106] Muhannad Faleh Alanazi, Muhammad Umair Ali, Shaik Javeed Hussain, Amad Zafar, Mohammed Mohatram, Muhammad Irfan, Raed AlRuwaili, Mubarak Alruwaili, Naif H Ali, and Anas Mohammad Albarrak. Brain tumor/mass classification framework using magnetic-resonance-imaging-based isolated and developed transfer deep-learning model. *Sensors*, 22(1):372, 2022.

[107] Priyansh Saxena, Akshat Maheshwari, and Saumil Maheshwari. Predictive modeling of brain tumor: a deep learning approach. In *Innovations in Computational Intelligence and Computer Vision: Proceedings of ICICV 2020*, pages 275–285. Springer, 2020.

[108] Ye Shen, Zhijun Fang, Yongbin Gao, Naixue Xiong, Cengsi Zhong, and Xianhua Tang. Coronary arteries segmentation based on 3d fcn with attention gate and level set function. *Ieee Access*, 7:42826–42835, 2019.

[109] Jhimli Mitra, Kai-kai Shen, Soumya Ghose, Pierrick Bourgeat, Jurgen Fripp, Olivier Salvado, Kerstin Pannek, D Jamie Taylor, Jane L Mathias, and Stephen Rose. Sta-

tistical machine learning to identify traumatic brain injury (tbi) from structural disconnections of white matter networks. *NeuroImage*, 129:247–259, 2016.

[110] Bin Zhang, Zhouyang Lian, Liming Zhong, Xiao Zhang, Yuhao Dong, Qiuying Chen, Lu Zhang, Xiaokai Mo, Wenhui Huang, Wei Yang, et al. Machine-learning based mri radiomics models for early detection of radiation-induced brain injury in nasopharyngeal carcinoma. *BMC cancer*, 20:1–9, 2020.

[111] Anna Schroder, Tim Lawrence, Natalie Voets, Daniel Garcia-Gonzalez, Mike Jones, Jose-Maria Peña, and Antoine Jerusalem. A machine learning enhanced mechanistic simulation framework for functional deficit prediction in tbi. *Frontiers in bioengineering and biotechnology*, 9:587082, 2021.

[112] M VergaraVictor, R MayerAndrew, A KiehlKent, et al. Detection of mild traumatic brain injury by machine learning classification using resting state functional network connectivity and fractional anisotropy. *Journal of neurotrauma*, 2017.

[113] Moumin Mohamed, A Alamri, M Mohamed, N Khalid, Pj O'Halloran, Ve Staartjes, and C Uff. Prognosticating outcome using magnetic resonance imaging in patients with moderate to severe traumatic brain injury: a machine learning approach. *Brain Injury*, 36(3):353–358, 2022.

[114] Peter Ferrazzano, Benjamin Yeske, Jeanette Mumford, Gregory Kirk, Erin D Bigler, Katherine Bowen, Nicole O'Brien, Bedda Rosario, Sue R Beers, Paul Rathouz, et al. Brain magnetic resonance imaging volumetric measures of functional outcome after severe traumatic brain injury in adolescents. *Journal of Neurotrauma*, 38(13):1799–1808, 2021.

[115] Anthony Bianchi, Bir Bhanu, Virginia Donovan, and Andre Obenaus. Visual and contextual modeling for the detection of repeated mild traumatic brain injury. *IEEE transactions on medical imaging*, 33(1):11–22, 2013.

[116] Debanjali Bhattacharya, Neelam Sinha, Shweta Prasad, Pramod Kumar Pal, Jitender Saini, and Sandhya Mangalore. A new statistical framework for corpus callosum sub-

region characterization based on lbp texture in patients with parkinsonian disorders: a pilot study. *Frontiers in Neuroscience*, 14:477, 2020.

[117] Martha Elizabeth Shenton, HM Hamoda, JS Schneiderman, Sylvain Bouix, Ofer Pasternak, Yogesh Rathi, M-A Vu, Maulik Prafull Purohit, K Helmer, I Koerte, et al. A review of magnetic resonance imaging and diffusion tensor imaging findings in mild traumatic brain injury. *Brain imaging and behavior*, 6:137–192, 2012.

[118] Ethan A Winkler, John K Yue, John F Burke, Andrew K Chan, Sanjay S Dhall, Mitchel S Berger, Geoffrey T Manley, and Phiroz E Tarapore. Adult sports-related traumatic brain injury in united states trauma centers. *Neurosurgical focus*, 40(4):E4, 2016.

[119] Victor G Coronado, Tadesse Haileyesus, Tabitha A Cheng, Jeneita M Bell, Juliet Haarbauer-Krupa, Michael R Lionbarger, Javier Flores-Herrera, Lisa C McGuire, and Julie Gilchrist. Trends in sports-and recreation-related traumatic brain injuries treated in us emergency departments: the national electronic injury surveillance system-all injury program (neiss-aip) 2001-2012. *The Journal of head trauma rehabilitation*, 30(3):185, 2015.

[120] Thomas Sanford, Charles E McCulloch, Rachael A Callcut, Peter R Carroll, and Benjamin N Breyer. Bicycle trauma injuries and hospital admissions in the united states, 1998-2013. *Jama*, 314(9):947–949, 2015.

[121] Pam Fischer. A right to the road: Understanding & addressing bicyclist safety. 2017.

[122] Daniel G Healy. Head injuries in sport. *ABC of Sports and Exercise Medicine*, page 10, 2015.

[123] Sports-related head injury, american association of neurological surgeons (aans), https://www.aans.org/patients/neurosurgical-conditions-and-treatments/sports-related-head-injury, 2018.

[124] Bellal Joseph, Asad Azim, Ansab A Haider, Narong Kulvatunyou, Terence O'Keeffe, Ahmed Hassan, Lynn Gries, Emily Tran, Rifat Latifi, and Peter Rhee. Bicycle helmets

work when it matters the most. *The American Journal of Surgery*, 213(2):413–417, 2017.

[125] Jake Olivier and Prudence Creighton. Bicycle injuries and helmet use: a systematic review and meta-analysis. *International journal of epidemiology*, 46(1):278–292, 2017.

[126] Alena Høye. Bicycle helmets–to wear or not to wear? a meta-analyses of the effects of bicycle helmets on injuries. *Accident Analysis & Prevention*, 117:85–97, 2018.

[127] National highway traffic safety administration, fatality analysis reporting system (fars), national highway traffic safety administration, https://www-fars.nhtsa.dot.gov/main/index.aspx, 2019.

[128] Jeffrey J Sacks, Patricia Holmgreen, Suzanne M Smith, and Daniel M Sosin. Bicycle-associated head injuries and deaths in the united states from 1984 through 1988: how many are preventable? *Jama*, 266(21):3016–3018, 1991.

[129] Mohammad Karkhaneh, Jean-Claude Kalenga, Brent Edward Hagel, and BH Rowe. Effectiveness of bicycle helmet legislation to increase helmet use: a systematic review. *Injury Prevention*, 12(2):76–82, 2006.

[130] David W Sproule, Eamon T Campolettano, and Steven Rowson. Football helmet impact standards in relation to on-field impacts. *Proceedings of the Institution of Mechanical Engineers, Part P: Journal of Sports Engineering and Technology*, 231(4):317–323, 2017.

[131] Consumer Product Safety Commision. Cpsc 16 cfr part 1203-safety standard for bicycle helmets. *Federal Registry*, 63(46):11711–11747, 1998.

[132] Andrew S McIntosh, Adrian Lai, and Edgar Schilter. Bicycle helmets: head impact dynamics in helmeted and unhelmeted oblique impact tests. *Traffic injury prevention*, 14(5):501–508, 2013.

[133] Megan Lindsay Bland. *Assessing the Efficacy of Bicycle Helmets in Reducing Risk of Head Injury*. PhD thesis, Virginia Tech, 2019.

[134] Safety standard for bicycle helmets final rule (16 CFR Part 1203). Standard, United States Consumer Product Safety Commission, 1998.

[135] Definitions and headforms. in: Methods of testing protective helmets. Standard, Sydney, New Zealand: Standards Australia/Standards New Zealand, 2009.

[136] Nicolas Bourdet, Caroline Deck, Rui P Carreira, and Remy Willinger. Head impact conditions in the case of cyclist falls. *Proceedings of the Institution of Mechanical Engineers, Part P: Journal of Sports Engineering and Technology*, 226(3-4):282–289, 2012.

[137] Nicolas Bourdet, Caroline Deck, Thierry Serre, Christophe Perrin, Maxime Llari, and Rémy Willinger. In-depth real-world bicycle accident reconstructions. *International journal of crashworthiness*, 19(3):222–232, 2014.

[138] R Willinger, C Deck, P Halldin, and D Otte. Towards advanced bicycle helmet test methods. In *International Cycling Safety Conference*, pages 18–19, 2014.

[139] AHS Holbourn. The mechanics of trauma with special reference to herniation of cerebral tissue. *Journal of Neurosurgery*, 1(3):190–200, 1944.

[140] A.H.S. Holbourn. Mechanics of head injuries. *The Lancet*, 242(6267):438 – 441, 1943. Originally published as Volume 2, Issue 6267.

[141] Andrew Post and T Blaine Hoshizaki. Rotational acceleration, brain tissue strain, and the relationship to concussion. *Journal of biomechanical engineering*, 137(3), 2015.

[142] Warren N Hardy, Matthew J Mason, Craig D Foster, Chirag S Shah, James M Kopacz, King H Yang, Albert I King, Jennifer Bishop, Michael Bey, William Anderst, et al. A study of the response of the human cadaver head to impact. *Stapp car crash journal*, 51:17, 2007.

[143] Caroline Deck, Nicolas Bourdet, Frank Meyer, and Rémy Willinger. Protection performance of bicycle helmets. *Journal of safety research*, 71:67–77, 2019.

[144] Michael Bottlang, Alexandra Rouhier, Stanley Tsai, Jordan Gregoire, and Steven M Madey. Impact performance comparison of advanced bicycle helmets with dedicated rotation-damping systems. *Annals of biomedical engineering*, 48(1):68–78, 2020.

[145] Vaibhav V Gokhale. *Design of a helmet with an advanced layered composite for energy dissipation using a multi-material compliant mechanism synthesis.* PhD thesis, 2016.

[146] F. Pedregosa, G. Varoquaux, A. Gramfort, V. Michel, B. Thirion, O. Grisel, M. Blondel, P. Prettenhofer, R. Weiss, V. Dubourg, J. Vanderplas, A. Passos, D. Cournapeau, M. Brucher, M. Perrot, and E. Duchesnay. Scikit-learn: Machine learning in Python. *Journal of Machine Learning Research*, 12:2825–2830, 2011.

[147] James A Newman. A generalized acceleration model for brain injury threshold (gambit). In *Proceedings of International IRCOBI Conference, 1986*, 1986.

[148] James A Newman and Nicholas Shewchenko. A proposed new biomechanical head injury assessment function-the maximum power index. Technical report, SAE Technical Paper, 2000.

[149] Corina Klug, Florian Feist, and Ernst Tomasch. Testing of bicycle helmets for preadolescents. *International Research Council on the Biomechanics of Injury (IRCOBI), Lyon, France*, pages 136–155, 2015.

[150] Peter Halldin, Magnus Aare, Svein Kleiven, and Hans von Holst. Improved helmet design and test methods to reduce rotational induced brain injuries. In *RTO Specialist Meeting, the NATO's Research and Technology Organization (RTO)*, 2003.

[151] Marjolein H Woering, Bart Depreitere, and Jos Vander Sloten. Estimated and underreported parameters in report based vehicle-bicycle accident reconstructions have a significant influence. *Accident Analysis & Prevention*, 150:105903, 2021.

[152] S Brand, D Otte, M Petri, C Müller, T Stübig, C Krettek, and C Haasper. Bicyclist-bicyclist crashes-a medical and technical crash analysis. *Traffic Injury Prevention*, 14(1):56–60, 2013.

[153] JC Park, IB Chang, JH Ahn, JH Kim, JK Oh, and JH Song. Epidemiology and risk factors for bicycle-related severe head injury: A single center experience. *Korean Journal of Neurotrauma*, 13(2):90, 2017.

[154] WS Chen, RY Dunn, AJ Chen, and JG Linakis. Epidemiology of nonfatal bicycle injuries presenting to united states emergency departments, 2001-2008. *Academic Emergency Medicine*, 20(6):570–575, 2013.

[155] Kelly Sarmiento, Tadesse Haileyesus, Dana Waltzman, and Jill Daugherty. Emergency department visits for bicycle-related traumatic brain injuries among children and adults—united states, 2009–2018. *Morbidity and Mortality Weekly Report*, 70(19):693, 2021.

[156] Annemieke C Scholten, Suzanne Polinder, Martien J Panneman, Ed F Van Beeck, and Juanita A Haagsma. Incidence and costs of bicycle-related traumatic brain injuries in the netherlands. *Accident Analysis & Prevention*, 81:51–60, 2015.

[157] Bart Depreitere, Christophe Van Lierde, Stefan Maene, Cindy Plets, Jos Vander Sloten, Remy Van Audekercke, Georges Van der Perre, and Jan Goffin. Bicycle-related head injury: a study of 86 cases. *Accident Analysis & Prevention*, 36(4):561–567, 2004.

[158] N Dodds, R Johnson, B Walton, O Bouamra, D Yates, F E Lecky, and J Thompson. Evaluating the impact of cycle helmet use on severe traumatic brain injury and death in a national cohort of over 11000 pedal cyclists: A retrospective study from the nhs england trauma audit and research network dataset. *BMJ Open*, 9(9), 2019.

[159] Madelen Fahlstedt, Peter Halldin, and Svein Kleiven. The protective effect of a helmet in three bicycle accidents—a finite element study. *Accident Analysis & Prevention*, 91:135–143, 2016.

[160] Xinzhe Zhan, Yu Liu, Scott J Raymond, H Vahid Alizadeh, Augustin Domel, Olivier Gevaert, Michael Zeineh, Gerald Grant, and David B Camarillo. Rapid estimation

of entire brain strain using deep learning models. *IEEE Transactions on Biomedical Engineering*, 68(11):3424–3434, 2021.

[161] N Bourdet, C Deck, F Meyer, and R Willinger. Experimental and numerical considerations of helmet evaluation under oblique impact. *Journal of Transportation Safety Security*, 12(1):52–65, 2020.

[162] Madelen Fahlstedt, Fady Abayazid, Matthew B Panzer, Antonia Trotta, Wei Zhao, Mazdak Ghajari, Michael D Gilchrist, Songbai Ji, Svein Kleiven, Xiaogai Li, et al. Ranking and rating bicycle helmet safety performance in oblique impacts using eight different brain injury models. *Annals of biomedical engineering*, 49(3):1097–1109, 2021.

[163] Andrew Stuart McIntosh, Kate Curtis, Tiffany Rankin, Megan Cox, Toh Yen Pang, P McCrory, and Caroline Frances Finch. Associations between helmet use and brain injuries amongst injured pedal-and motor-cyclists: A case series analysis of trauma centre presentations. *Journal of the Australasian College of Road Safety*, 24(2):11–20, 2013.

[164] Caroline Deck and Rémy Willinger. Improved head injury criteria based on head fe model. *International Journal of Crashworthiness*, 13(6):667–678, 2008.

[165] Mazdak Ghajari, Peter J Hellyer, and David J Sharp. Computational modelling of traumatic brain injury predicts the location of chronic traumatic encephalopathy pathology. *Brain*, 140(2):333–343, 2017.

[166] Svein Kleiven. Predictors for traumatic brain injuries evaluated through accident reconstructions. *Stapp Car Crash Journal*, 51, 2007.

[167] Peter Halldin and Svein Kleiven. The development of next generation test standards for helmets. In *1st International Conference on Helmet Performance and Design*, volume 1, 2013.

[168] Alexander Trotta, John M Clark, Andrew McGoldrick, Michael D Gilchrist, and Aisling Ní Annaidh. Biofidelic finite element modelling of brain trauma: Importance of

the scalp in simulating head impact. *International Journal of Mechanical Sciences*, 173:105448, 2020.

[169] Wei Zhao and Songbai Ji. Displacement-and strain-based discrimination of head injury models across a wide range of blunt conditions. *Annals of biomedical engineering*, 48:1661–1677, 2020.

[170] J. M. Clark, K. Taylor, A. Post, T. B. Hoshizaki, and M. D. Gilchrist. Comparison of ice hockey goaltender helmets for concussion type impacts. *Annals of Biomedical Engineering*, 46(7):986–1000, 2018.

[171] B. S. Elkin, L. F. Gabler, M. B. Panzer, and G. P. Siegmund. Brain tissue strains vary with head impact location: A possible explanation for increased concussion risk in struck versus striking football players. *Clinical Biomechanics*, 64:49–57, 2019.

[172] Madelen Fahlstedt, Fatemah Abayazid, Matthew B Panzer, Andrew Trotta, Wenqing Zhao, Masoud Ghajari, Michael D Gilchrist, Songbai Ji, Svein Kleiven, Xiaogai Li, Aonghus Ni'annaidh, Niamh Ni'annaidh, and Peter Halldin. Ranking and rating bicycle helmet safety performance in oblique impacts using eight different brain injury models. *Annals of Biomedical Engineering*, 2020.

[173] Helena Stigson. Bicycle helmets 2020 tested by folksam. Technical report, Folksam, 2020.

[174] R. A. Oeur, M. D. Gilchrist, and T. B. Hoshizaki. Parametric study of impact parameters on peak head acceleration and strain for collision impacts in sport. *International Journal of Crashworthiness*, 26(1):16–25, 2021.

[175] Virginia Tech. Bicycle helmet ratings, 2020. Accessed on May 3, 2023.

[176] Florian Groder, Ebru Ozkaya, Linda Conetta, and Mehmet Kurt. Designing an impact pendulum to test different concussion prevention helmet accessories. In *Summer Biomechanics, Bioengineering and Biotransport Conference SB3C*, Seven Springs, PA, USA, 2019.

[177] BR Cobb, A Macalister, TJ Young, AR Kemper, S Rowson, and SM Duma. Quantitative comparison of hybrid iii and national operating committee on standards for athletic equipment headform shape characteristics and implications on football helmet fit. *Proceedings of the Institution of Mechanical Engineers, Part P: Journal of Sports Engineering and Technology*, 229(1):39–46, 2015.

[178] John Versace. A review of the severity index. 1971.

[179] E. J. Pellman, D. C. Viano, C. Withnall, N. Shewchenko, C. A. Bir, and P. D. Halstead. Concussion in professional football: Helmet testing to assess impact performance - part 11. *Neurosurgery*, 58(1):78–95, 2006.

[180] J.R. Funk, R.E. Quesada, A.M. Miles, and J.R. Crandall. Inertial properties of football helmets. *Journal of Biomechanical Engineering*, 140(6):011007, 2018.

[181] J.S. Giudice, W. Zeng, T. Wu, A. Alshareef, D.F. Shedd, and M.B. Panzer. An analytical review of the numerical methods used for finite element modeling of traumatic brain injury. *Annals of Biomedical Engineering*, 47(9):1882–1902, 2019.

[182] N. Yoganandan, F.A. Pintar, J. Zhang, and J.L. Baisden. Physical properties of the human head: Mass, center of gravity and moment of inertia. *Journal of Biomechanics*, 42(9):1177–1192, 2009.

[183] Haojie Mao, Liying Zhang, King H Yang, and Albert I King. Application of a finite element model of the brain to study traumatic brain injury mechanisms in the rat. Technical report, SAE Technical Paper, 2006.

[184] Hong Mao and King H Yang. Investigation of brain contusion mechanism and threshold by combining finite element analysis with in vivo histology data. *International Journal for Numerical Methods in Biomedical Engineering*, 27(3):357–366, 2011.

[185] Alessandra Menichetti, Laura Bartsoen, Bart Depreitere, and Jos Vander Sloten. A machine learning approach to investigate the uncertainty of tissue-level injury metrics for cerebral contusion. *Frontiers in Bioengineering and Biotechnology*, 9:1–17, 2021.

[186] David I Shreiber, Alistair C Bain, and David F Meaney. In vivo thresholds for mechanical injury to the blood-brain barrier. In *Stapp Car Crash Conference Proceedings*, volume 41, pages 277–291, 1997.

[187] David C Viano and Per Lövsund. Biomechanics of brain and spinal-cord injury: Analysis of neuropathologic and neurophysiology experiments. *Journal of Crash Prevention and Injury Control*, 1(1):35–43, 1999.

[188] Andrew Post, Lauren Dawson, T Blaine Hoshizaki, Michael D Gilchrist, and Michael D Cusimano. Development of a test method for adult ice hockey helmet evaluation. *Computer methods in biomechanics and biomedical engineering*, 23(11):690–702, 2020.

[189] NOCSAE. National operating committee on standards for athletic equipment. standard performance specification for newly manufactured football helmets. *NOCSAE DOC (ND)*, pages 002–17m21, 2021.

[190] Zhou Zhou, Xiaogai Li, and Svein Kleiven. Biomechanics of periventricular injury. *Journal of neurotrauma*, 2020.

[191] Stephen Tiernan, Aidan Meagher, David O'Sullivan, and Eoin O'Kelly. Finite element simulation of head impacts in mixed martial arts. *Computer methods in biomechanics and biomedical engineering*, pages 1–11, 2020.

[192] Haojie Mao, Liying Zhang, Binhui Jiang, Vinay V Genthikatti, Xin Jin, Feng Zhu, Rahul Makwana, Amandeep Gill, Gurdeep Jandir, Amrinder Singh, et al. Development of a finite element human head model partially validated with thirty five experimental cases. *Journal of biomechanical engineering*, 135(11):111002, 2013.

[193] Ahmed Alshareef, Taotao Wu, J Sebastian Giudice, and Matthew B Panzer. Toward subject-specific evaluation: methods of evaluating finite element brain models using experimental high-rate rotational brain motion. *Biomechanics and Modeling in Mechanobiology*, 20(6):2301–2317, 2021.

[194] Peter J Schmid. Dynamic mode decomposition of numerical and experimental data. *Journal of fluid mechanics*, 656:5–28, 2010.

[195] Muzio Grilli, Peter J Schmid, Stefan Hickel, and Nikolaus A Adams. Analysis of unsteady behaviour in shockwave turbulent boundary layer interaction. *Journal of Fluid Mechanics*, 700:16–28, 2012.

[196] Lee F Gabler, Hamed Joodaki, Jeff R Crandall, and Matthew B Panzer. Development of a single-degree-of-freedom mechanical model for predicting strain-based brain injury responses. *Journal of biomechanical engineering*, 140(3):031002, 2018.

[197] Yuzhe Liu, Xianghao Zhan, August G Domel, Michael Fanton, Zhou Zhou, Samuel J Raymond, Hossein Vahid Alizadeh, Nicholas J Cecchi, Michael Zeineh, and Gerald Grant. Theoretical and numerical analysis for angular acceleration being determinant of brain strain in mtbi. *arXiv preprint arXiv:2012.13507*, 2020.

[198] Marzieh Hajiaghamemar and Susan S Margulies. Multi-scale white matter tract embedded brain finite element model predicts the location of traumatic diffuse axonal injury. *Journal of neurotrauma*, 38(1):144–157, 2021.

[199] Andrew K Knutsen, Arnold D Gomez, Mihika Gangolli, Wen-Tung Wang, Deva Chan, Yuan-Chiao Lu, Eftychios Christoforou, Jerry L Prince, Philip V Bayly, John A Butman, et al. In vivo estimates of axonal stretch and 3d brain deformation during mild head impact. *Brain Multiphysics*, page 100015, 2020.

[200] DRS Bradshaw, Johan Ivarsson, CL Morfey, and David C Viano. Simulation of acute subdural hematoma and diffuse axonal injury in coronal head impact. *Journal of biomechanics*, 34(1):85–94, 2001.

[201] Liying Zhang, King H Yang, and Albert I King. Comparison of brain responses between frontal and lateral impacts by finite element modeling. *Journal of neurotrauma*, 18(1):21–30, 2001.

[202] Aleksandar Subic. *Materials in sports equipment*. Woodhead Publishing, 2019.

[203] William C Moss, Michael J King, and Eric G Blackman. Towards reducing impact-induced brain injury: lessons from a computational study of army and football helmet

pads. *Computer methods in biomechanics and biomedical engineering*, 17(11):1173–1184, 2014.

[204] Magnus Aare and Peter Halldin. A new laboratory rig for evaluating helmets subject to oblique impacts. *Traffic injury prevention*, 4(3):240–248, 2003.

[205] Fargol Rezayaraghi, Javid Abderezaei, Efe Ozkaya, Aymeric Pionteck, Devlin Stein, and M Kurt. Frequency response of the human brain substructures during helmeted side impacts. In *9th US National Congress on Theoretical and Applied Mathematics, USNC/TAM2022*, 2022.

[206] Fargol Rezayaraghi, Javid Abderezaei, Efe Ozkaya, Devlin Stein, Aymeric Pionteck, and Mehmet Kurt. Modal analysis of computational human brain dynamics during helmeted impacts. *Brain Multiphysics*, 5:100082, 2023.

[207] William T Freeman, Edward H Adelson, et al. The design and use of steerable filters. *IEEE Transactions on Pattern analysis and machine intelligence*, 13(9):891–906, 1991.

[208] John Mathewson and Dave Hale. Detection of channels in seismic images using the steerable pyramid. In *SEG International Exposition and Annual Meeting*, pages SEG–2008. SEG, 2008.

[209] Jeffery Meadows, Michael Kraut, Michael Guarnieri, Raymond I Haroun, and Benjamin S Carson. Asymptomatic chiari type i malformations identified on magnetic resonance imaging. *Journal of neurosurgery*, 92(6):920–926, 2000.

[210] Frederick R Taylor and Mark V Larkins. Headache and chiari i malformation: clinical presentation, diagnosis, and controversies in management. *Current pain and headache reports*, 6(4):331–337, 2002.

[211] David Shprecher, Jason Schwalb, and Roger Kurlan. Normal pressure hydrocephalus: diagnosis and treatment. *Current neurology and neuroscience reports*, 8(5):371–376, 2008.

[212] R.D. Penn, S. Basati, B. Sweetman, X. Guo, and A. Linninger. Ventricle wall movements and cerebrospinal fluid flow in hydrocephalus. *Journal of Neurosurgery*, 115(1):159–164, 2011.

[213] D. Greitz, A. Franck, and B. Nordell. On the pulsatile nature of intracranial and spinal csf-circulation demonstrated by mr imaging. *Acta Radiol*, 34(4):321–328, 1993.

[214] T.Y. Huang, H.W. Chung, M.Y. Chen, et al. Supratentorial cerebrospinal fluid production rate in healthy adults: quantification with two-dimensional cine phase-contrast mr imaging with high temporal and spatial resolution. *Radiology*, 233(2):603–608, 2004.

[215] D. Jaraj, K. Rabiei, T. Marlow, C. Jensen, I. Skoog, and C. Wikkelso. Prevalence of idiopathic normal-pressure hydrocephalus. *Neurology*, 82(16):1449–1454, 2014.

[216] M.A. Williams, J.P. McAllister, M.L. Walker, D.A. Kranz, M. Bergsneider, M.R. Del Bigio, L. Fleming, D.M. Frim, K. Gwinn, J.R.W. Kestle, M.G. Luciano, J.R. Madsen, S. Molchan, M.L. Oster-Granite, and G. Spinella. Priorities for hydrocephalus research: Report from an nih-sponsored workshop. *Journal of Neurosurgery (Pediatrics)*, 107:345–357, 2007.

[217] E. P. Simoncelli and W. T. Freeman. The steerable pyramid: A flexible architecture for multi-scale derivative computation. In *Proc. Int. Conf. Image Process.*, volume 3, pages 444–447, 1995.

[218] Itamar Terem, Leo Dang, Allen Champagne, Javid Abderezaei, Aymeric Pionteck, Zainab Almadan, Anna-Maria Lydon, Mehmet Kurt, Miriam Scadeng, and Samantha J Holdsworth. 3d amplified mri (amri). *Magnetic resonance in medicine*, 86(3):1674–1686, 2021.

[219] Petrice M Cogswell, MC Murphy, ML Senjem, H Botha, JL Gunter, BD Elder, J Graff-Radford, DT Jones, JK Cutsforth-Gregory, CG Schwarz, et al. Changes in ventricular and cortical volumes following shunt placement in patients with idiopathic normal pressure hydrocephalus. *American Journal of Neuroradiology*, 42(12):2165–2171, 2021.

[220] Fargol Rezayaraghi, M. A. Williams, Mehmet Kurt, M. Levitt, E. McGee, S. Holdsworth, I. Terem, D. Turley, A. Wilson, S. Rane, and J. B. Andre. Amplified mr assessment of idiopathic normal pressure hydrocephalus pre-/post shunt surgery. In *International Society for Magnetic Resonance in Medicine (ISMRM)*, HW, USA, 2025.

[221] Michael L Alosco, Megan L Mariani, Charles H Adler, Laura J Balcer, Charles Bernick, Rhoda Au, Sarah J Banks, William B Barr, Sylvain Bouix, Robert C Cantu, et al. Developing methods to detect and diagnose chronic traumatic encephalopathy during life: rationale, design, and methodology for the diagnose cte research project. *Alzheimer's research & therapy*, 13(1):1–23, 2021.

[222] Michael L Alosco, Yi Su, Thor D Stein, Hillary Protas, Jonathan D Cherry, Charles H Adler, Laura J Balcer, Charles Bernick, Surya Vamsi Pulukuri, Bobak Abdolmohammadi, et al. Associations between near end-of-life flortaucipir pet and postmortem cte-related tau neuropathology in six former american football players. *European Journal of Nuclear Medicine and Molecular Imaging*, 50(2):435–452, 2023.

[223] Chia-Hui Liu, Chih-Fong Tsai, Kuen-Liang Sue, and Min-Wei Huang. The feature selection effect on missing value imputation of medical datasets. *applied sciences*, 10(7):2344, 2020.

[224] Aaron Ritter, Nanako Hawley, Sarah J Banks, and Justin B Miller. The association between montreal cognitive assessment memory scores and hippocampal volume in a neurodegenerative disease sample. *Journal of Alzheimer's Disease*, 58(3):695–699, 2017.

[225] Daniel J King and Amanda G Wood. Clinically feasible brain morphometric similarity network construction approaches with restricted magnetic resonance imaging acquisitions. *Network Neuroscience*, 4(1):274–291, 2020.

[226] Cong Chu, Tales Santini, Jr-Jiun Liou, Ann D Cohen, Pauline M Maki, Anna Louise Marsland, Rebecca C Thurston, Peter J Gianaros, and Tamer S Ibrahim. Brain

morphometrics correlations with age among 352 participants imaged with both 3t and 7t mri: 7t improves statistical power and reduces required sample size. *medRxiv*, pages 2024–10, 2024.

[227] Ziyi Zhang, William Robert Kwapong, Le Cao, Zijuan Feng, Peng Liu, Ruilin Wang, Bo Wu, and Shuting Zhang. Correlation between serum biomarkers, brain volume, and retinal neuronal loss in early-onset alzheimer's disease. *Neurological Sciences*, 45(6):2615–2623, 2024.

[228] Zhenxu Xiao, Xue Wu, Wanqing Wu, Jingwei Yi, Xiaoniu Liang, Saineng Ding, Li Zheng, Jianfeng Luo, Hongchen Gu, Qianhua Zhao, et al. Plasma biomarker profiles and the correlation with cognitive function across the clinical spectrum of alzheimer's disease. *Alzheimer's Research & Therapy*, 13:1–12, 2021.

[229] P Bongioanni, R Del Carratore, S Corbianco, A Diana, G Cavallini, SM Masciandaro, and R Buizza. Climate change and neurodegenerative diseases. *Environmental research*, 201:111511, 2021.

[230] D M Wilson, M R Cookson, L Van Den Bosch, H Zetterberg, D M Holtzman, and I Dewachter. Hallmarks of neurodegenerative diseases. *Cell*, 186(4):693–714, 2023.

[231] BCC Research. Global 3d medical and surgical imaging platform market, 2024. Available at https://academic.bccresearch.com/market-research/healthcare/global-3d-medical-and-surgical-imaging-platform-market.html.

[232] BCC Research. Surgical navigation systems: Technologies and global markets, 2024. Available at https://academic.bccresearch.com/market-research/healthcare/surgical-navigation-systems-market-report.html.

[233] BCC Research. Surgical equipment: Technologies and global markets, 2024. Available at https://academic.bccresearch.com/market-research/healthcare/surgical-equipment-markets.html.

[234] Coherent Market Insights. Stroke diagnostics market size and share analysis – growth trends and forecasts (2024–2031), 2024. Retrieved from

https://www.coherentmarketinsights.com/industry-reports/stroke-diagnostics-market: :text=Stroke

Appendix A

COMPREHENSIVE OVERVIEW OF PARAMETERS INCLUDED IN CHAPTER 6

A.0.1 MRI Morphometric Measures

MRI morphometrics were included in four main categories for each hemishpere, including meancurve, area, thickness, and volume for various regions and each of these groups included multiple features. also another category was considered among these metrics which was subcortical volume.

Table A.1: Neuropsychiatric Metrics

Variable Name	Label	Important Notes
BIS-Tot	BIS-11 Total Score	Represents overall impulsiveness score from the Barratt Impulsiveness Scale-11, assessing impulsivity traits.
ABIS-Attention	ABIS Attentional Impulsiveness Factor Score	Measures impulsiveness related to attentional focus, part of the ABIS.
ABIS-Motor	ABIS Motor Impulsiveness Factor Score	Assesses impulsive actions or motor responses, derived from the ABIS scale.
ABIS-Nonplanning	ABIS Non-planning Impulsiveness Factor Score	Evaluates impulsivity related to future planning and foresight, part of ABIS.
BAITot	BAI Total Score	Total score from the Beck Anxiety Inventory (BAI), assessing the severity of anxiety symptoms.
BDITot	BDI-II Total Score	Total score from the Beck Depression Inventory-II, used for measuring depression severity.
bhstot	BHS Total Score	Total score from the Beck Hopelessness Scale (BHS), evaluating negative outlook and hopelessness.
BDHI-Total	BDHI Total Score	Total score from the Buss-Durkee Hostility Inventory, assessing levels of hostility.
CNSTot	CNS-LS Total Score	Overall score on the CNS-Lability Scale (CNS-LS), evaluating emotional lability.
pcltot	PCL-5 Total Symptom Severity Score	Total symptom severity score from the PTSD Checklist for DSM-5 (PCL-5), indicating PTSD symptoms.
BGLHA_Childhood_Total	BGLHA Childhood Total Score	Childhood score from the Behavioral Health and Lifestyle Assessment (BGLHA), capturing early behavioral health indicators.
BGLHA_Adolescence_Total	BGLHA Adolescence Total Score	Adolescence score from the BGLHA, assessing behavioral health during adolescence.
BGLHA_Adulthood_Total	BGLHA Adulthood Total Score	Adulthood score from the BGLHA, reflecting behavioral health and lifestyle in adulthood.
NBD-Tot	Total Neurobehavioral Dysregulation Score	Comprehensive score assessing neurobehavioral dysregulation, indicating behavioral irregularities.

Table A.2: neurocognitive/Neuropsychiatric Measures Metrics (BRIEF-A Metacognition)

Variable Name	Label	Important Notes
MI	Meta-Cognition Index (MI): Total score	Represents the overall score for metacognitive abilities, assessing self-awareness and control over one's own cognitive processes.
TMI	Meta-Cognition Index (MI): T-score	Standardized T-score for the Meta-Cognition Index, useful for comparisons across populations.
GEC	General Executive Composite (GEC): Total score	Total score of executive functioning, measuring abilities like planning, organizing, and goal-setting.
TGEC	General Executive Composite (GEC): T-score	Standardized T-score for the General Executive Composite, facilitating cross-sectional analysis.
BRI	Behavioral Regulation Index (BRI): Total score	Summative score indicating behavioral regulation capabilities, including impulse control and self-monitoring.
TBRI	Behavioral Regulation Index (BRI): T-score	T-score version of the BRI, providing normative data comparison for behavioral regulation.
inhibit	Inhibit Clinical Scale	Assesses an individual's ability to control impulses and refrain from inappropriate responses.
shift	Shift Clinical Scale	Measures cognitive flexibility, or the ability to transition between tasks or mental states.
EmotCont	Emotional Control Clinical Scale	Evaluates the ability to manage emotional responses appropriately in various situations.
SelfMon	Self-Monitor Clinical Scale	Indicates the ability to observe and regulate one's own behavior in social settings.
initiate	Initiate Clinical Scale	Assesses the ability to begin tasks independently and generate ideas.
WorkMem	Working Memory Clinical Scale	Measures capacity to hold and manipulate information over short periods.
PlanOrg	Plan/Organize Clinical Scale	Evaluates skills in planning, organizing, and managing current and future-oriented tasks.
taskmon	Task Monitor Clinical Scale	Assesses an individual's ability to track task progress and adjust performance as needed.
orgmat	Organization of Materials Clinical Scale	Measures ability to keep track of personal items and belongings in an organized manner.

Table A.3: Blood biomarkers 1.

Variable Name	Label	Important Notes
p_Ab40	Plasma Abeta40 Concentration (pg/dL)	Abeta40 is a form of amyloid-beta protein; abnormal levels are linked to Alzheimer's and other neurodegenerative diseases.
p_Ab42	Plasma Abeta42 Concentration (pg/dL)	Abeta42, like Abeta40, is an amyloid-beta protein variant. Abnormal ratios of Abeta42 to Abeta40 can be significant in diagnosing Alzheimer's.
p_GFAP	Plasma GFAP Concentration (pg/dL)	GFAP (Glial Fibrillary Acidic Protein) is a marker for astrocytic damage; elevated levels are associated with brain injury and neurodegeneration.
p_NfL	Plasma NfL Concentration (pg/dL)	NfL (Neurofilament Light Chain) is a marker of neuronal injury, useful for monitoring neurodegenerative disease progression.
p_Ab40_FLAG_below_ref_range	Below Reference Range for Abeta40	Indicates if Abeta40 levels are below the established reference range. Useful for tracking abnormal levels in context.
p_Ab42_FLAG_below_ref_range	Below Reference Range for Abeta42	Indicates if Abeta42 levels are below the reference range, providing context for evaluating amyloid-beta concentration.
p_GFAP_FLAG_below_ref_range	Below Reference Range for GFAP	Identifies if GFAP is below the reference range, indicating a lack of astrocytic response if flagged.
p_NfL_FLAG_below_ref_range	Below Reference Range for NfL	Highlights if NfL is below the reference range; low levels may be relevant in monitoring baseline values in neurodegeneration studies.
p_PDGFRbeta	Plasma PDGFRbeta Concentration (pg/mL)	PDGFRbeta is involved in cellular growth and repair mechanisms. Changes in levels may indicate disruptions in neurovascular function.
p_PDGFRbeta_FLAG_other	Other PDGFRbeta Flags	Flags additional abnormalities related to PDGFRbeta; context-dependent for analyzing irregular concentrations.
p_pT181	Plasma pT181 Concentration (pg/mL)	pT181 is a phosphorylated form of tau protein. Elevated levels are implicated in tauopathies like Alzheimer's disease.

Table A.4: Blood biomarkers 1.

Variable Name	**Label**	**Important Notes**
p_pT231	Plasma pT231 Concentration (pg/mL)	Another phosphorylated tau form; pT231 levels can indicate tau pathology, relevant in Alzheimer's and related neurodegenerative conditions.
p_ttau	Plasma Total Tau Concentration (pg/mL)	Total tau is a marker for overall tau pathology. Elevated tau levels can indicate neural cell damage and neurodegeneration.

Table A.5: Blood biomarkers 2.

Variable Name	Label	Important Notes
Qalb	Qalb (mg/g) - (CSF conc/serum conc)	The Qalb ratio indicates the blood-brain barrier integrity, with abnormal levels suggesting permeability issues linked to neuroinflammation or neurodegeneration.
s_alb	Serum Albumin Concentration (g/dL)	Serum albumin is a primary protein in blood; its levels reflect overall health, with deviations potentially indicating liver dysfunction or systemic inflammation.
p_IL_17A_F_cv	Plasma interleukin-17A/F CV	Coefficient of variation for IL-17A/F concentrations; monitors consistency and reliability of IL-17A/F measurements in plasma.
p_IL_17A_F	Plasma interleukin-17A/F Concentration (pg/mL)	IL-17A/F are pro-inflammatory cytokines involved in immune responses; elevated levels may indicate inflammatory conditions, including autoimmune disorders.
p_IL_17B_cv	Plasma interleukin-17B CV	Coefficient of variation for IL-17B concentrations; ensures measurement reliability of IL-17B levels in plasma.
p_IL_17B	Plasma interleukin-17B Concentration (pg/mL)	IL-17B is part of the IL-17 family involved in inflammatory responses; higher levels may be associated with autoimmune or inflammatory diseases.
p_IL_17C_cv	Plasma interleukin-17C CV	Coefficient of variation for IL-17C concentrations, which helps assess the consistency of IL-17C plasma measurements.
p_IL_17C	Plasma interleukin-17C Concentration (pg/mL)	IL-17C plays a role in innate immunity and inflammation; its expression can be elevated in response to infection or autoimmune diseases.
p_IL_17D_cv	Plasma interleukin-17D CV	Coefficient of variation for IL-17D measurements, reflecting data consistency for this cytokine's concentration.

Table A.6: Blood biomarkers 2.

Variable Name	Label	Important Notes
p_IL_17D	Plasma interleukin-17D Concentration (pg/mL)	IL-17D is another member of the IL-17 family, involved in regulating inflammatory processes; elevated levels may indicate chronic inflammatory conditions.
p_IL_1RA_cv	Plasma interleukin-1RA CV	Coefficient of variation for IL-1RA concentrations; indicates reliability in measuring IL-1RA, an anti-inflammatory cytokine.
p_IL_1RA	Plasma interleukin-1RA Concentration (pg/mL)	IL-1RA is an anti-inflammatory cytokine that blocks IL-1 signaling; elevated levels may help mitigate inflammatory responses.
p_IL_3_cv	Plasma interleukin-3 CV	Coefficient of variation for IL-3 concentrations; ensures consistency in IL-3 plasma measurement data.
p_IL_3	Plasma interleukin-3 Concentration (pg/mL)	IL-3 is involved in hematopoiesis and immune regulation; high levels may indicate immune activation or inflammatory responses.
p_IL_9_cv	Plasma interleukin-9 CV	Coefficient of variation for IL-9 concentrations; provides data consistency for IL-9 measurements.
p_IL_9	Plasma interleukin-9 Concentration (pg/mL)	IL-9 is associated with T-helper cell responses and can play a role in asthma and other allergic responses.
p_TSLP_cv	Plasma thymic stromal lymphopoietin CV	Coefficient of variation for TSLP measurements; provides consistency data for TSLP concentrations in plasma.

Table A.7: Blood biomarkers 2.

Variable Name	Label	Important Notes
p_TSLP	Plasma thymic stromal lymphopoietin Concentration (pg/mL)	TSLP is involved in the regulation of immune responses and is linked to allergic inflammation and immune system dysregulation.
p_IL_17AGenB_cv	Plasma interleukin-17A Generation B CV	Coefficient of variation for IL-17A Generation B; provides consistency data for IL-17A measurements in Generation B plasma samples.
p_IL_17AGenB	Plasma interleukin-17A Generation B Concentration (pg/mL)	IL-17A is a pro-inflammatory cytokine that plays a critical role in autoimmune conditions and inflammatory responses.
p_IL_21_cv	Plasma interleukin-21 CV	Coefficient of variation for IL-21 concentrations, which ensures reliable and consistent IL-21 data.
p_IL_21	Plasma interleukin-21 Concentration (pg/mL)	IL-21 is a cytokine involved in regulating immune cells, contributing to immune responses and inflammation.
p_IL_22_cv	Plasma interleukin-22 CV	Coefficient of variation for IL-22 concentrations, confirming data consistency for IL-22 measurements.
p_IL_22	Plasma interleukin-22 Concentration (pg/mL)	IL-22 is important in immune defense and tissue repair, especially in mucosal tissues and epithelial cell health.
p_IL_23_cv	Plasma interleukin-23 CV	Coefficient of variation for IL-23, confirming consistency in IL-23 measurements for reliability in inflammatory response assessment.
p_IL_23	Plasma interleukin-23 Concentration (pg/mL)	IL-23 is involved in inflammatory responses and plays a key role in autoimmune conditions.
p_IL_27_cv	Plasma interleukin-27 CV	Coefficient of variation for IL-27 concentrations, ensuring reliability of IL-27 measurements.

Table A.8: Blood biomarkers 2.

Variable Name	Label	Important Notes
p_IL_27	Plasma interleukin-27 Concentration (pg/mL)	IL-27 regulates immune responses, with implications in inflammatory conditions and infection defense.
p_IL_31_cv	Plasma interleukin-31 CV	Coefficient of variation for IL-31, aiding in measurement consistency for studies on skin and chronic inflammatory diseases.
p_IL_31	Plasma interleukin-31 Concentration (pg/mL)	IL-31 is primarily associated with inflammatory and allergic responses, playing a significant role in itch and dermatitis.
p_MIP_3alpha_cv	Plasma macrophage inflammatory protein-3 alpha CV	Coefficient of variation for MIP-3, essential for verifying the consistency of inflammatory response data.
p_MIP_3alpha	Plasma macrophage inflammatory protein-3 alpha Concentration (pg/mL)	MIP-3 plays a role in immune cell recruitment to inflammation sites, relevant in immune response studies.
p_CRP_cv	Plasma C-reactive protein CV	Coefficient of variation for CRP measurements, crucial for consistent data on inflammatory markers.
p_CRP	Plasma C-reactive protein Concentration (pg/mL)	CRP is a marker of inflammation, with elevated levels indicating systemic inflammation or infection.
p_ICAM_1_cv	Plasma intercellular adhesion molecule-1 CV	Coefficient of variation for ICAM-1, useful for ensuring reliable adhesion molecule measurements related to immune response.

Table A.9: Blood biomarkers 2.

Variable Name	Label	Important Notes
p_ICAM_1	Plasma intercellular adhesion molecule-1 Concentration (pg/mL)	ICAM-1 plays a crucial role in immune cell recruitment and adhesion, relevant in inflammation studies.
p_SAA_cv	Plasma serum amyloid A CV	Coefficient of variation for SAA levels, ensuring measurement consistency in inflammation and acute-phase response studies.
p_SAA	Plasma serum amyloid A Concentration (pg/mL)	SAA is an acute-phase protein linked to inflammation, used as a biomarker for systemic inflammatory responses.
p_VCAM_1_cv	Plasma vascular cell adhesion molecule-1 CV	Coefficient of variation for VCAM-1 levels, which ensures reliable measurement for inflammation and endothelial function studies.
p_VCAM_1	Plasma vascular cell adhesion molecule-1 Concentration (pg/mL)	VCAM-1 aids in immune cell adhesion and movement across endothelium, relevant in vascular inflammation.
p_Fit_1_cv	Plasma Fms-like tyrosine kinase-1 CV	Coefficient of variation for Fit-1, ensuring reliable measurements in vascular growth and development studies.
p_Fit_1	Plasma Fms-like tyrosine kinase-1 Concentration (pg/mL)	Fit-1 is essential in angiogenesis and vascular function, involved in endothelial growth and repair.
p_PlGF_cv	Plasma placental growth factor CV	Coefficient of variation for PlGF, confirming consistent measurements relevant to angiogenesis and placental function.
p_PlGF	Plasma placental growth factor Concentration (pg/mL)	PlGF is a key factor in angiogenesis, with roles in placental development and vascular health.
p_Tie_2_cv	Plasma tyrosine kinase-2 CV	Coefficient of variation for Tie-2, ensuring consistent measurement for studies on vascular integrity and endothelial function.
p_Tie_2	Plasma tyrosine kinase-2 Concentration (pg/mL)	Tie-2 plays a role in vascular stability and integrity, especially in endothelial cell signaling.

Table A.10: Blood biomarkers 2.

Variable Name	Label	Important Notes
p_VEGF_A_2_cv	Plasma vascular endothelial growth factor-A (VEGF-A) CV from Angiogenesis Panel 1	CV for VEGF-A, ensuring measurement accuracy in studies focused on vascular growth and repair.
p_VEGF_A_2	Plasma vascular endothelial growth factor-A (VEGF-A) Concentration (pg/mL) from Angiogenesis Panel 1	VEGF-A is critical for blood vessel formation, playing roles in angiogenesis and wound healing.
p_VEGF_C_cv	Plasma vascular endothelial growth factor-C (VEGF-C) CV	Coefficient of variation for VEGF-C, ensuring reliable data in lymphangiogenesis studies.
p_VEGF_C	Plasma vascular endothelial growth factor-C (VEGF-C) Concentration (pg/mL)	VEGF-C supports lymphangiogenesis and vascular function, relevant in cancer and immune studies.
p_VEGF_D_cv	Plasma vascular endothelial growth factor-D (VEGF-D) CV	CV for VEGF-D, ensuring consistent data for vascular and lymphatic health research.
p_VEGF_D	Plasma vascular endothelial growth factor-D (VEGF-D) Concentration (pg/mL)	VEGF-D is associated with lymphatic vessel growth and remodeling, relevant in cancer and tissue repair.
p_bFGF_cv	Plasma basic fibroblast growth factor CV	Coefficient of variation for bFGF, ensuring measurement consistency, crucial in studies of cell growth and wound healing.
p_bFGF	Plasma basic fibroblast growth factor Concentration (pg/mL)	bFGF is a key growth factor involved in tissue repair and regeneration, playing roles in angiogenesis and cell proliferation.
p_INF_gamma_cv	Plasma interferon gamma CV	Coefficient of variation for interferon gamma, crucial for reliable data in immune response studies.
p_INF_gamma	Plasma interferon gamma Concentration (pg/mL)	Interferon gamma is essential in immune defense, especially against infections, and is used to assess immune activation.

Table A.11: Blood biomarkers 2.

Variable Name	Label	Important Notes
p_IL_10_cv	Plasma interleukin-10 CV	Coefficient of variation for IL-10, ensuring reliable readings for immune modulation and anti-inflammatory response.
p_IL_10	Plasma interleukin-10 Concentration (pg/mL)	IL-10 is an anti-inflammatory cytokine, relevant in regulating immune responses and inflammation.
p_IL_12p70_cv	Plasma interleukin-12p70 CV	Coefficient of variation for IL-12p70, ensuring data consistency in studies on immune function and inflammation.
p_IL_12p70	Plasma interleukin-12p70 Concentration (pg/mL)	IL-12p70 is involved in activating immune responses, important in inflammation and infection response studies.
p_IL_13_cv	Plasma interleukin-13 CV	Coefficient of variation for IL-13, providing consistent measurements for studies on allergy and immune regulation.
p_IL_13	Plasma interleukin-13 Concentration (pg/mL)	IL-13 is associated with allergic responses and immune regulation, playing a role in inflammatory processes.
p_IL_1_alpha_cv	Plasma interleukin-1alpha CV	Coefficient of variation for IL-1alpha, ensuring consistent measurement in inflammatory response studies.
p_IL_1_alpha	Plasma interleukin-1alpha Concentration (pg/mL)	IL-1alpha is a pro-inflammatory cytokine, crucial in the body's inflammatory response.
p_IL_2_cv	Plasma interleukin-2 CV	Coefficient of variation for IL-2, confirming consistent data in immune system activation studies.
p_IL_2	Plasma interleukin-2 Concentration (pg/mL)	IL-2 promotes T-cell growth and is vital for immune regulation and response.
p_IL_4_cv	Plasma interleukin-4 CV	Coefficient of variation for IL-4, ensuring reliable measurement for studies related to allergy and immune function.

Table A.12: Blood biomarkers 2.

Variable Name	Label	Important Notes
p_IL_4	Plasma interleukin-4 Concentration (pg/mL)	IL-4 is involved in immune response modulation, influencing B-cell proliferation and allergy response.
p_IL_6_cv	Plasma interleukin-6 CV	Coefficient of variation for IL-6, essential for consistent measurement in inflammation studies.
p_IL_6	Plasma interleukin-6 Concentration (pg/mL)	IL-6 is a key inflammatory cytokine; its levels are associated with chronic inflammation and autoimmune diseases.
p_IL_8_cv	Plasma interleukin-8 using IL-8 ab CV	Coefficient of variation for IL-8, ensuring data reliability in studies involving immune cell recruitment.
p_IL_8	Plasma interleukin-8 using IL-8 ab Concentration (pg/mL)	IL-8 is a chemokine involved in attracting immune cells to inflammation sites, playing a role in immune defense.
p_TNF_alpha_cv	Plasma tumor necrosis factor alpha CV	Coefficient of variation for TNF-alpha, providing measurement consistency for inflammation studies.
p_TNF_alpha	Plasma tumor necrosis factor alpha Concentration (pg/mL)	TNF-alpha is a major pro-inflammatory cytokine, crucial for studying inflammation and immune response.
p_Eotaxin_cv	Plasma exotaxin CV	Coefficient of variation for Eotaxin, ensuring reliable data in chemokine studies linked to allergies.
p_Eotaxin	Plasma exotaxin Concentration (pg/mL)	Eotaxin is a chemokine involved in the recruitment of eosinophils, associated with allergic responses.
p_Eotaxin_3_cv	Plasma exotaxin-3 CV	Coefficient of variation for Eotaxin-3, for reliable data in inflammation and allergic reaction studies.

Table A.13: Blood biomarkers 2.

Variable Name	Label	Important Notes
p_Eotaxin_3	Plasma exotaxin-3 Concentration (pg/mL)	Eotaxin-3 plays a role in immune response and is linked to inflammation and allergy.
p_IL_8_2_cv	Plasma interleukin-8 using HA ab CV	Coefficient of variation for IL-8 (HA ab), crucial for consistent immune response measurements.
p_IL_8_2	Plasma interleukin-8 using HA ab Concentration (pg/mL)	IL-8 (HA ab) is involved in immune cell recruitment and inflammation regulation.
p_IP_10_cv	Plasma IP-10 CV	Coefficient of variation for IP-10, supporting reliable data on immune response under various conditions.
p_IP_10	Plasma IP-10 Concentration (pg/mL)	IP-10 is a chemokine involved in immune response and inflammation, linked to chronic disease states.
p_MCP_1_cv	Plasma monocyte chemotactic protein-1 CV	Coefficient of variation for MCP-1, critical for consistent data on immune cell migration.
p_MCP_1	Plasma monocyte chemotactic protein-1 Concentration (pg/mL)	MCP-1 is essential for immune cell recruitment, associated with inflammation and chronic disease.
p_MCP_4_cv	Plasma monocyte chemotactic protein-4 CV	Coefficient of variation for MCP-4, providing reliable measurements in chemokine and immune studies.
p_MCP_4	Plasma monocyte chemotactic protein-4 Concentration (pg/mL)	MCP-4 is a chemokine linked to immune cell migration, relevant to inflammatory responses.
p_MDC_cv	Plasma MDC CV	Coefficient of variation for MDC, ensuring data consistency for chemokine studies and immune research.

Table A.14: Blood biomarkers 2.

Variable Name	Label	Important Notes
p_MDC	Plasma MDC Concentration (pg/mL)	MDC (Macrophage-Derived Chemokine) is involved in immune cell recruitment, relevant to inflammatory responses.
p_MIP_1alpha_cv	Plasma MIP-1alpha CV	Coefficient of variation for MIP-1alpha, essential for data reliability in inflammation research.
p_MIP_1alpha	Plasma MIP-1alpha Concentration (pg/mL)	MIP-1alpha is a chemokine involved in immune response, particularly in inflammation and tissue injury.
p_MIP_1_beta_cv	Plasma MIP-1beta CV	Coefficient of variation for MIP-1beta, ensuring data consistency in chemokine-related studies.
p_MIP_1_beta	Plasma MIP-1beta Concentration (pg/mL)	MIP-1beta is a chemokine linked to immune cell activation and inflammation.
p_TARC_cv	Plasma TARC CV	Coefficient of variation for TARC, supporting reliable measurements in immune response studies.
p_TARC	Plasma TARC Concentration (pg/mL)	TARC is a chemokine involved in immune cell recruitment, important in inflammatory processes.
p_GM_CSF_cv	Plasma granulocyte-macrophage colony stimulating factor CV	Coefficient of variation for GM-CSF, critical for consistent immune response data.
p_GM_CSF	Plasma granulocyte-macrophage colony stimulating factor Concentration (pg/mL)	GM-CSF supports white blood cell production, particularly in inflammation and immune response.
p_IL_12_IL_23p40_cv	Plasma interleukin-12/interleukin-23p40 CV	Coefficient of variation for IL-12/IL-23p40, ensuring reliable cytokine measurements.
p_IL_12_IL_23p40	Plasma interleukin-12/interleukin-23p40 Concentration (pg/mL)	IL-12/IL-23p40 is a subunit shared by IL-12 and IL-23, involved in immune response modulation.

Table A.15: Blood biomarkers 2.

Variable Name	Label	Important Notes
p_IL_15_cv	Plasma interleukin-15 CV	Coefficient of variation for IL-15, necessary for consistent immune study measurements.
p_IL_15	Plasma interleukin-15 Concentration (pg/mL)	IL-15 is crucial for T-cell proliferation and immune function, relevant in autoimmune studies.
p_IL_16_cv	Plasma interleukin-16 CV	Coefficient of variation for IL-16, ensuring data consistency in cytokine research.
p_IL_16	Plasma interleukin-16 Concentration (pg/mL)	IL-16 acts as a chemoattractant for immune cells, implicated in inflammatory responses.
p_IL_17A_cv	Plasma interleukin-17A CV	Coefficient of variation for IL-17A, supporting reliable inflammatory marker measurements.
p_IL_17A	Plasma interleukin-17A Concentration (pg/mL)	IL-17A is a pro-inflammatory cytokine, often elevated in autoimmune diseases.
p_IL_1_beta_cv	Plasma interleukin-1 beta CV	Coefficient of variation for IL-1 beta, ensuring data consistency in inflammation studies.
p_IL_1_beta	Plasma interleukin-1 beta Concentration (pg/mL)	IL-1 beta is a pro-inflammatory cytokine involved in immune responses and chronic inflammation.
p_IL_5_cv	Plasma interleukin-5 CV	Coefficient of variation for IL-5, essential for reliable data in studies of allergic inflammation.
p_IL_5	Plasma interleukin-5 Concentration (pg/mL)	IL-5 is involved in the activation and growth of eosinophils, commonly associated with allergic inflammation.
p_IL_7_cv	Plasma interleukin-7 CV	Coefficient of variation for IL-7, ensuring consistency in cytokine data.
p_IL_7	Plasma interleukin-7 Concentration (pg/mL)	IL-7 supports T-cell development and homeostasis, relevant for immune function.

Table A.16: Blood biomarkers 2.

Variable Name	Label	Important Notes
p_TNF_beta_cv	Plasma tumor necrosis factor beta CV	Coefficient of variation for TNF-beta, providing data reliability in inflammatory studies.
p_TNF_beta	Plasma tumor necrosis factor beta Concentration (pg/mL)	TNF-beta is a cytokine involved in systemic inflammation, linked to autoimmune diseases.
p_VEGF_A_cv	Plasma vascular endothelial growth factor (VEGF-A) CV	Coefficient of variation for VEGF-A, critical for maintaining accurate angiogenesis-related measurements.
p_VEGF_A	Plasma vascular endothelial growth factor (VEGF-A) Concentration (pg/mL)	VEGF-A promotes blood vessel growth; it is significant in cancer, wound healing, and cardiovascular health.
p_asyn_cv	Plasma alpha-synuclein CV	Coefficient of variation for alpha-synuclein, ensuring consistency in measurements associated with neurodegenerative conditions.
p_asyn	Plasma alpha-synuclein Concentration (pg/mL)	Alpha-synuclein is a protein associated with neurodegenerative diseases like Parkinson's; abnormal levels are relevant in neurological studies.
p_Hb	Hemoglobin Concentration (ng/mL)	Hemoglobin is a marker for oxygen transport in the blood, crucial for evaluating overall health and anemia.
dxcte_asyn_p_flag_dv	Dilution Flag - Samples were re-run at a higher dilution	Quality assurance flag indicating samples required higher dilution for accurate alpha-synuclein measurement.

Table A.17: CSF biomarkers 1.

Variable Name	Label	Important Notes
c_strem2_FLAG_insufficient	Flag for Insufficient Strem2	Quality assurance indicator noting insufficient sample quantity for Strem2 measurement.
c_PDGFRbeta_FLAG_insufficient	Flag for Insufficient PDGFR-beta	Indicates insufficient sample amount for accurate PDGFRbeta concentration measurement.
c_strem2	CSF Strem2 Concentration (pg/mL)	Strem2 is associated with immune response in the brain; abnormal levels may be linked to neuroinflammation.
c_PDGFRbeta	CSF PDGFRbeta Concentration (pg/mL)	PDGFRbeta is involved in cell growth; its presence in CSF may indicate neurovascular function changes.
c_Ab40	CSF Abeta40 Concentration (pg/mL)	Abeta40 is a form of amyloid-beta, with abnormal levels potentially linked to Alzheimer's disease.
c_Ab42	CSF Abeta42 Concentration (pg/mL)	Abeta42 is another amyloid-beta variant; its ratio to Abeta40 is crucial for Alzheimer's diagnosis.
c_pT181	CSF pT181 Concentration (pg/mL)	pT181 is a phosphorylated tau protein variant, commonly elevated in Alzheimer's disease.
c_tTau_FLAG_below_ref_range	Flag - Below Reference Range for Total Tau	Indicates if CSF total tau is below the reference range, affecting interpretation in neurodegenerative studies.
c_FLAG_hemolysis	Hemolysis Flag	Quality flag indicating sample hemolysis, which can impact the accuracy of biomarker levels.
c_tTau_FLAG_insufficient	Insufficient Flag for Total Tau	Notes insufficient sample quantity for reliable total tau measurement.
c_ttau	CSF Total Tau Concentration (pg/mL)	Total tau is an indicator of neurodegeneration; elevated levels suggest neural cell damage.
c_NfL	CSF NfL Concentration (pg/mL)	Neurofilament light chain (NfL) is a marker for neuronal injury, often used in neurodegenerative disease monitoring.
c_GFAP	CSF GFAP Concentration (pg/mL)	Glial fibrillary acidic protein (GFAP) is linked to astrocyte activation and damage, relevant in brain injury.
c_pT231	CSF pT231 Concentration (pg/mL)	Another tau phosphorylation site; pT231 is studied in tauopathies like Alzheimer's.
c_pT217	CSF pT217 Concentration (pg/mL)	pT217 is a phosphorylated tau marker, relevant in diagnosing Alzheimer's and related conditions.
dxcte_ptau217_csf_flag_dv	Quality Flag for CSF pTau 217	Ensures accuracy for pTau 217 measurements by flagging quality issues.

Table A.18: CSF biomarkers 2.

Variable Name	Label	Important Notes
Qalb	Qalb (mg/g) - (CSF conc/serum conc)	Qalb ratio helps in assessing the blood-brain barrier integrity by comparing albumin levels in CSF and serum.
dxcte_albumin_csf_flag_dv	Quality Flag - Sample had pink CSF	Indicates sample quality; pink coloration in CSF may affect measurements, signaling potential contamination or bleeding.
c_alb	CSF Albumin Concentration (mg/dL)	CSF albumin levels are used to evaluate blood-brain barrier function, with high levels often indicating barrier breakdown.
c_IL_17A_F_cv	CSF interleukin-17A/F CV	Reflects the coefficient of variation for IL-17A/F, important for assessing inflammatory response accuracy.
c_IL_17A_F	CSF interleukin-17A/F Concentration (pg/mL)	IL-17A/F is linked to immune response and inflammation, with elevated levels indicating neuroinflammatory conditions.
c_IL_17B_cv	CSF interleukin-17B CV	Coefficient of variation for IL-17B, providing insight into data consistency for inflammatory markers.
c_IL_17B	CSF interleukin-17B Concentration (pg/mL)	IL-17B plays a role in neuroinflammation, with abnormal levels indicating immune response variations.
c_IL_17C_cv	CSF interleukin-17C CV	Variation metric for IL-17C, ensuring reliable measurement for neuroinflammatory response analysis.
c_IL_17C	CSF interleukin-17C Concentration (pg/mL)	IL-17C is associated with immune cell recruitment; higher levels suggest increased inflammatory activity in the CNS.
c_IL_17D_cv	CSF interleukin-17D CV	Represents the consistency of IL-17D values, useful for determining inflammatory response reliability.
c_IL_17D	CSF interleukin-17D Concentration (pg/mL)	IL-17D is involved in immune signaling; elevated levels may correlate with neuroinflammatory conditions.
c_IL_1RA_cv	CSF interleukin-1RA CV	Coefficient of variation for IL-1RA, providing measurement consistency information.

Table A.19: CSF biomarkers 2.

Variable Name	Label	Important Notes
c_IL_1RA	CSF interleukin-1RA Concentration (pg/mL)	IL-1RA is an anti-inflammatory cytokine; changes in concentration indicate shifts in inflammatory status.
c_IL_3_cv	CSF interleukin-3 CV	CV for IL-3, ensuring accuracy in measuring this cytokine related to growth and repair functions in the brain.
c_IL_3	CSF interleukin-3 Concentration (pg/mL)	IL-3 promotes survival and function of certain neural cells; fluctuations indicate potential neuroimmune changes.
c_IL_9_cv	CSF interleukin-9 CV	Variation measure for IL-9, assessing measurement reliability for inflammation-related studies.
c_IL_9	CSF interleukin-9 Concentration (pg/mL)	IL-9 is associated with immune cell activation, with high levels suggesting inflammatory responses in neurodegenerative conditions.
c_TSLP_cv	CSF thymic stromal lymphopoietin CV	CV for TSLP concentration, indicating measurement consistency for this cytokine involved in immune response.
c_TSLP	CSF thymic stromal lymphopoietin Concentration (pg/mL)	TSLP plays a role in immune system regulation, and changes may reflect immune dysregulation in neurological disorders.
c_IL_17AGenB_cv	CSF interleukin-17A Generation B CV	Coefficient of variation for IL-17A Gen B, important for assessing inflammatory response consistency.
c_IL_17AGenB	CSF interleukin-17A Generation B Concentration (pg/mL)	IL-17A Generation B is linked to immune and inflammatory responses, particularly relevant in neuroinflammation.
c_IL_21_cv	CSF interleukin-21 CV	Variation in IL-21 levels, ensuring consistency in measuring this cytokine associated with immune regulation.
c_IL_21	CSF interleukin-21 Concentration (pg/mL)	IL-21 is implicated in autoimmune conditions; elevated levels may indicate immune response activation in the CNS.

Table A.20: CSF biomarkers 2.

Variable Name	Label	Important Notes
c_IL_22_cv	CSF interleukin-22 CV	CV for IL-22 measurements, useful for consistency in immune response data.
c_IL_22	CSF interleukin-22 Concentration (pg/mL)	IL-22 is involved in inflammation; abnormal levels are associated with neuroinflammatory diseases.
c_IL_23_cv	CSF interleukin-23 CV	Coefficient of variation for IL-23, ensuring reliability in inflammatory marker data.
c_IL_23	CSF interleukin-23 Concentration (pg/mL)	IL-23 is linked to autoimmune inflammation, and higher levels could indicate neuroinflammatory activity.
c_IL_27_cv	CSF interleukin-27 CV	Variation measure for IL-27 levels, assessing immune response reliability.
c_IL_27	CSF interleukin-27 Concentration (pg/mL)	IL-27 regulates immune activity; elevated levels are associated with chronic inflammation in the CNS.
c_IL_31_cv	CSF interleukin-31 CV	Variation in IL-31 levels, ensuring consistency for immune response-related studies.
c_IL_31	CSF interleukin-31 Concentration (pg/mL)	IL-31 is involved in immune cell recruitment, with implications in inflammatory diseases.
c_MIP_3alpha_cv	CSF macrophage inflammatory protein-3 alpha CV	Coefficient of variation for MIP-3 alpha, used to verify data consistency for inflammation markers.
c_MIP_3alpha	CSF macrophage inflammatory protein-3 alpha Concentration (pg/mL)	MIP-3 alpha is associated with immune cell movement to inflammation sites, elevated in CNS inflammation.
c_CRP_cv	CSF C-reactive protein CV	Consistency metric for CRP, ensuring measurement reliability.
c_CRP	CSF C-reactive protein Concentration (pg/mL)	CRP is a general marker of inflammation; elevated in various neuroinflammatory conditions.
c_ICAM_1_cv	CSF intercellular adhesion molecule-1 CV	CV for ICAM-1, ensuring reliability in inflammation-related data.

Table A.21: CSF biomarkers 2.

Variable Name	Label	Important Notes
c_ICAM_1	CSF intercellular adhesion molecule-1 Concentration (pg/mL)	ICAM-1 plays a role in immune cell adhesion and migration; higher levels may indicate neuroinflammation.
c_SAA_cv	CSF serum amyloid A CV	Coefficient of variation for SAA, indicating data reliability for inflammatory marker measurements.
c_SAA	CSF serum amyloid A Concentration (pg/mL)	SAA is linked to acute inflammation; elevated in neurodegenerative and neuroinflammatory conditions.
c_VCAM_1_cv	CSF vascular cell adhesion molecule-1 CV	CV for VCAM-1, used to assess consistency in immune response data.
c_VCAM_1	CSF vascular cell adhesion molecule-1 Concentration (pg/mL)	VCAM-1 aids immune cell attachment and migration; elevated in CNS inflammatory responses.
c_Fit_1_cv	CSF Fms-like-tyrosine kinase-1 CV	Variation measure for Flt-1, assessing vascular function in the CNS.
c_Fit_1	CSF Fms-like-tyrosine kinase-1 Concentration (pg/mL)	Flt-1, a marker of vascular health, changes in concentration indicate potential neurovascular issues.
c_PlGF_cv	CSF placental growth factor CV	Consistency metric for PlGF, assessing measurement reliability in neurovascular studies.
c_PlGF	CSF placental growth factor Concentration (pg/mL)	PlGF is involved in angiogenesis; alterations may reflect neurovascular dysfunction.
c_Tie_2_cv	CSF tyrosine kinase-2 CV	Variation metric for Tie-2 levels, used to ensure accuracy in vascular growth-related data.
c_Tie_2	CSF tyrosine kinase-2 Concentration (pg/mL)	Tie-2 regulates blood vessel development; abnormalities in levels indicate vascular issues.
c_VEGF_A_2_cv	CSF vascular endothelial growth factor-A CV	Consistency of VEGF-A, ensuring reliable vascular data.
c_VEGF_A_2	CSF vascular endothelial growth factor-A Concentration (pg/mL)	VEGF-A promotes blood vessel growth; abnormal levels may signal neurovascular complications.

Table A.22: CSF biomarkers 2.

Variable Name	Label	Important Notes
c_VEGF_C_cv	CSF vascular endothelial growth factor-C CV	CV for VEGF-C, assessing measurement reliability for this growth factor.
c_VEGF_C	CSF vascular endothelial growth factor-C Concentration (pg/mL)	VEGF-C is involved in lymphatic and vascular health, with changes indicating neurovascular dysfunction.
c_VEGF_D_cv	CSF vascular endothelial growth factor-D CV	Variation in VEGF-D levels, ensuring consistency for vascular health assessments.
c_VEGF_D	CSF vascular endothelial growth factor-D Concentration (pg/mL)	VEGF-D plays a role in angiogenesis and lymphatic development; abnormal levels can indicate vascular abnormalities.
c_bFGF_cv	CSF basic fibroblast growth factor CV	CV for bFGF, verifying consistency in growth factor data.
c_bFGF	CSF basic fibroblast growth factor Concentration (pg/mL)	bFGF is critical for cell growth and repair; elevated levels may suggest neuroinflammation or repair processes.
c_INF_gamma_cv	CSF interferon gamma CV	CV for INF-gamma, ensuring reliability for immune response data.
c_INF_gamma	CSF interferon gamma Concentration (pg/mL)	INF-gamma is crucial in immune responses and can indicate CNS inflammation or infection.
c_IL_10_cv	CSF interleukin-10 CV	Coefficient of variation for IL-10, ensuring consistency in measuring this anti-inflammatory cytokine.
c_IL_10	CSF interleukin-10 Concentration (pg/mL)	IL-10 is known for its anti-inflammatory properties; elevated levels may suggest regulatory immune responses.
c_IL_12p70_cv	CSF interleukin-12p70 CV	CV for IL-12p70, ensuring measurement reliability for this pro-inflammatory cytokine.
c_IL_12p70	CSF interleukin-12p70 Concentration (pg/mL)	IL-12p70 plays a role in T-cell differentiation; linked to autoimmune conditions and inflammation.
c_IL_13_cv	CSF interleukin-13 CV	Variation in IL-13 levels, supporting measurement reliability in immune response studies.
c_IL_13	CSF interleukin-13 Concentration (pg/mL)	IL-13 is involved in allergic responses and inflammation; elevated in various immune-related diseases.

Table A.23: CSF biomarkers 2.

Variable Name	Label	Important Notes
c_IL_1_alpha_cv	CSF interleukin-1alpha CV	Coefficient of variation for IL-1alpha, ensuring consistency in inflammation data.
c_IL_1_alpha	CSF interleukin-1alpha Concentration (pg/mL)	IL-1alpha is a pro-inflammatory cytokine; elevated levels can indicate immune activation.
c_IL_2_cv	CSF interleukin-2 CV	CV for IL-2, assessing consistency for this immune-regulatory cytokine.
c_IL_2	CSF interleukin-2 Concentration (pg/mL)	IL-2 is essential in immune system regulation; abnormal levels may signal immune dysregulation.
c_IL_4_cv	CSF interleukin-4 CV	Coefficient of variation for IL-4, ensuring measurement reliability.
c_IL_4	CSF interleukin-4 Concentration (pg/mL)	IL-4 is involved in allergic and inflammatory responses; significant in neuroinflammation.
c_IL_6_cv	CSF interleukin-6 CV	CV for IL-6, ensuring consistency in this inflammatory marker measurement.
c_IL_6	CSF interleukin-6 Concentration (pg/mL)	IL-6 is associated with inflammation and can be elevated in neurodegenerative diseases.
c_IL_8_cv	CSF interleukin-8 using IL-8 ab CV	Variation in IL-8 levels, assessing consistency in inflammatory data.
c_IL_8	CSF interleukin-8 using IL-8 ab Concentration (pg/mL)	IL-8 is a chemokine involved in immune cell recruitment; elevated in CNS inflammation.
c_TNF_alpha_cv	CSF tumor necrosis factor alpha CV	Coefficient of variation for TNF-alpha, ensuring consistency in measurement of this pro-inflammatory cytokine.
c_TNF_alpha	CSF tumor necrosis factor alpha Concentration (pg/mL)	TNF-alpha is linked to neuroinflammation and is commonly elevated in neurodegenerative diseases.
c_Eotaxin_cv	CSF exotaxin CV	Variation in Eotaxin levels, ensuring measurement reliability for inflammatory data.
c_Eotaxin	CSF exotaxin Concentration (pg/mL)	Eotaxin is associated with immune cell migration; elevated levels may indicate an immune response in CNS.

Table A.24: CSF biomarkers 2.

Variable Name	Label	Important Notes
c_Eotaxin_3_cv	CSF exotaxin-3 CV	Coefficient of variation for exotaxin-3, indicating measurement consistency for this chemokine.
c_Eotaxin_3	CSF exotaxin-3 Concentration (pg/mL)	Exotaxin-3 is involved in eosinophil recruitment and inflammation; may be elevated in CNS inflammatory conditions.
c_IL_8_2_cv	CSF interleukin-8 using HA ab CV	CV for IL-8 using HA antibody, ensuring reliability in IL-8 measurements.
c_IL_8_2	CSF interleukin-8 using HA ab Concentration (pg/mL)	IL-8 with HA antibody provides insights into inflammation; elevated levels are linked to CNS inflammatory responses.
c_IP_10_cv	CSF IP-10 CV	Coefficient of variation for IP-10, supporting consistency in measurements for this chemokine.
c_IP_10	CSF IP-10 Concentration (pg/mL)	IP-10 attracts immune cells to sites of inflammation, relevant in studying neuroinflammatory conditions.
c_MCP_1_cv	CSF monocyte chemotactic protein-1 CV	Variation coefficient for MCP-1, confirming measurement reliability.
c_MCP_1	CSF monocyte chemotactic protein-1 Concentration (pg/mL)	MCP-1 is a chemokine involved in monocyte recruitment; elevated in various CNS diseases.
c_MCP_4_cv	CSF monocyte chemotactic protein-4 CV	CV for MCP-4, supporting consistency in chemokine measurement data.
c_MCP_4	CSF monocyte chemotactic protein-4 Concentration (pg/mL)	MCP-4 contributes to monocyte and eosinophil recruitment; relevant in studying neuroinflammation.
c_MDC_cv	CSF MDC CV	CV for MDC, ensuring reliable measurements of this chemokine involved in immune responses.
c_MDC	CSF MDC Concentration (pg/mL)	MDC (Macrophage-Derived Chemokine) plays a role in immune signaling; elevated in inflammatory conditions.

Table A.25: CSF biomarkers 2.

Variable Name	Label	Important Notes
c_MIP_1alpha_cv	c_MIP-1alpha CV	Variation for MIP-1alpha, a chemokine involved in immune cell recruitment.
c_MIP_1alpha	c_MIP-1alpha (pg/mL)	MIP-1alpha is a chemokine significant in inflammation; its levels can indicate immune response status.
c_MIP_1_beta_cv	CSF MIP-1beta CV	CV for MIP-1beta, maintaining measurement accuracy in inflammation studies.
c_MIP_1_beta	CSF MIP-1beta Concentration (pg/mL)	MIP-1beta is another chemokine involved in immune response, relevant in CNS inflammation.
c_TARC_cv	CSF TARC CV	Coefficient of variation for TARC, providing reliable data on this chemokine.
c_TARC	CSF TARC Concentration (pg/mL)	TARC (Thymus and Activation-Regulated Chemokine) is associated with T-cell trafficking and immune response.
c_GM_CSF_cv	CSF granulocyte-macrophage colony stimulating factor CV	CV for GM-CSF, maintaining consistency for this cytokine measurement.
c_GM_CSF	CSF granulocyte-macrophage colony stimulating factor Concentration (pg/mL)	GM-CSF plays a role in immune cell proliferation and is involved in CNS inflammation responses.
c_IL_12_IL_23p40_cv	CSF interleukin-12/interleukin-23p40 CV	Variation in IL-12/IL-23p40, supporting data reliability for these cytokines.
c_IL_12_IL_23p40	CSF interleukin-12/interleukin-23p40 Concentration (pg/mL)	IL-12/IL-23p40 are pro-inflammatory cytokines; important in immune responses and inflammation.
c_IL_15_cv	CSF interleukin-15 CV	CV for IL-15, confirming measurement accuracy in immune studies.
c_IL_15	CSF interleukin-15 Concentration (pg/mL)	IL-15 is involved in T-cell proliferation and immune responses, relevant in CNS studies.
c_IL_16_cv	CSF interleukin-16 CV	Coefficient of variation for IL-16, ensuring consistency in measurement for inflammatory markers.

Table A.26: CSF biomarkers 2.

Variable Name	Label	Important Notes
c_IL_16	CSF interleukin-16 Concentration (pg/mL)	IL-16 is involved in T-cell recruitment and immune modulation; elevated levels may indicate inflammatory processes in the CNS.
c_IL_17A_cv	CSF interleukin-17A CV	Coefficient of variation for IL-17A, maintaining measurement reliability for this pro-inflammatory cytokine.
c_IL_17A	CSF interleukin-17A Concentration (pg/mL)	IL-17A is a key cytokine in inflammatory pathways, associated with autoimmune and inflammatory diseases.
c_IL_1_beta_cv	CSF interleukin-1 beta CV	Variation coefficient for IL-1 beta, ensuring accurate measurements of this important inflammatory mediator.
c_IL_1_beta	CSF interleukin-1 beta Concentration (pg/mL)	IL-1 beta is a major inflammatory cytokine, elevated levels may be linked to neuroinflammation and CNS injury.
c_IL_5_cv	CSF interleukin-5 CV	CV for IL-5, supporting consistency in measurement data for this immune-regulating cytokine.
c_IL_5	CSF interleukin-5 Concentration (pg/mL)	IL-5 plays a role in eosinophil activation, relevant in allergic and inflammatory responses.
c_IL_7_cv	CSF interleukin-7 CV	Coefficient of variation for IL-7, ensuring reliability in measurement for immune function studies.
c_IL_7	CSF interleukin-7 Concentration (pg/mL)	IL-7 is involved in T-cell development and survival, relevant in immunological studies of the CNS.
c_TNF_beta_cv	CSF tumor necrosis factor beta CV	CV for TNF-beta, maintaining accuracy in measurements of this cytokine involved in inflammation.
c_TNF_beta	CSF tumor necrosis factor beta Concentration (pg/mL)	TNF-beta is associated with inflammatory responses, with potential relevance in neurodegenerative disease.

Table A.27: CSF biomarkers 2.

Variable Name	Label	Important Notes
c_VEGF_A_cv	CSF vascular endothelial growth factor (VEGF-A) from Cytokine Panel 1 CV	CV for VEGF-A, ensuring reliable measurements in studies of vascular integrity.
c_VEGF_A	CSF vascular endothelial growth factor (VEGF-A) from Cytokine Panel 1 Concentration (pg/mL)	VEGF-A promotes blood vessel growth, relevant in studies of blood-brain barrier integrity and repair.
c_asyn_cv	CSF alpha-synuclein CV	Coefficient of variation for alpha-synuclein, supporting data accuracy for this protein associated with neurodegenerative diseases.
c_asyn	CSF alpha-synuclein Concentration (pg/mL)	Alpha-synuclein is linked to neurodegenerative disorders like Parkinson's; elevated levels may indicate neuronal damage.
dxcte_asyn_c_flag_dv	Missing Data Flag - samples contained too much Hb (above 200 ng/mL), data removed due to quality control	Quality control flag for alpha-synuclein, indicating samples with excess hemoglobin that may affect data reliability.

Table A.28: CSF biomarkers 3.

Variable Name	Label	Important Notes
c_dhpg	CSF 3,4-dihydroxyphenylglycol (pg/mL)	DHPG is a metabolite of norepinephrine, often used as a marker for sympathetic nervous system activity.
c_ne	CSF Norepinephrine (pg/mL)	Norepinephrine is a neurotransmitter involved in stress response; its levels can reflect sympathetic activity in the CNS.
c_dopa	CSF 3,4-dihydroxyphenylalanine (pg/mL)	DOPA is a precursor to dopamine, relevant in studying catecholaminergic pathways in neurological disorders.
c_da	CSF Dopamine (pg/mL)	Dopamine is a key neurotransmitter associated with motor control, cognition, and reward pathways; altered levels can be indicative of neurodegenerative conditions.
c_dopac	CSF 3,4-dihydroxyphenylacetic acid (pg/mL)	DOPAC is a dopamine metabolite, useful in assessing dopamine turnover in the brain.
c_catecholamine_flag_blood_dv	Quality Flag - Sample had visible blood contamination	Indicates potential blood contamination in CSF sample, which may affect catecholamine measurements.
c_catecholamine_flag_diluted_dv	Quality Flag - Sample had to be diluted	Notes that the sample was diluted to meet assay requirements, which may impact concentration accuracy.

Table A.29: MRI Morphometric Measures ; Cortical Area

Variable Name	Label	Important Notes
lh_bankssts_area	Left Hemisphere Bankssts Area (mm^2)	Surface area of the APARC bankssts parcel in the left hemisphere.
lh_caudalanteriorcingulate_area	Left Hemisphere Caudal Anterior Cingulate Area (mm^2)	Surface area of the APARC caudalanteriorcingulate parcel in the left hemisphere.
lh_caudalmiddlefrontal_area	Left Hemisphere Caudal Middle Frontal Area (mm^2)	Surface area of the APARC caudalmiddlefrontal parcel in the left hemisphere.
lh_cuneus_area	Left Hemisphere Cuneus Area (mm^2)	Surface area of the APARC cuneus parcel in the left hemisphere.
lh_entorhinal_area	Left Hemisphere Entorhinal Area (mm^2)	Surface area of the APARC entorhinal parcel in the left hemisphere.
lh_fusiform_area	Left Hemisphere Fusiform Area (mm^2)	Surface area of the APARC fusiform parcel in the left hemisphere.
lh_inferiorparietal_area	Left Hemisphere Inferior Parietal Area (mm^2)	Surface area of the APARC inferiorparietal parcel in the left hemisphere.
lh_inferiortemporal_area	Left Hemisphere Inferior Temporal Area (mm^2)	Surface area of the APARC inferiortemporal parcel in the left hemisphere.
lh_isthmuscingulate_area	Left Hemisphere Isthmus Cingulate Area (mm^2)	Surface area of the APARC isthmuscingulate parcel in the left hemisphere.
lh_lateraloccipital_area	Left Hemisphere Lateral Occipital Area (mm^2)	Surface area of the APARC lateraloccipital parcel in the left hemisphere.
lh_lateralorbitofrontal_area	Left Hemisphere Lateral Orbitofrontal Area (mm^2)	Surface area of the APARC lateralorbitofrontal parcel in the left hemisphere.
lh_lingual_area	Left Hemisphere Lingual Area (mm^2)	Surface area of the APARC lingual parcel in the left hemisphere.
lh_medialorbitofrontal_area	Left Hemisphere Medial Orbitofrontal Area (mm^2)	Surface area of the APARC medialorbitofrontal parcel in the left hemisphere.
lh_middletemporal_area	Left Hemisphere Middle Temporal Area (mm^2)	Surface area of the APARC middletemporal parcel in the left hemisphere.
lh_parahippocampal_area	Left Hemisphere Parahippocampal Area (mm^2)	Surface area of the APARC parahippocampal parcel in the left hemisphere.
lh_paracentral_area	Left Hemisphere Paracentral Area (mm^2)	Surface area of the APARC paracentral parcel in the left hemisphere.
lh_parsopercularis_area	Left Hemisphere Pars Opercularis Area (mm^2)	Surface area of the APARC parsopercularis parcel in the left hemisphere.
lh_parsorbitalis_area	Left Hemisphere Pars Orbitalis Area (mm^2)	Surface area of the APARC parsorbitalis parcel in the left hemisphere.

Table A.30: MRI Morphometric Measures ; Cortical Area

Variable Name	Label	Important Notes
lh_parstriangularis_area	Left Hemisphere Pars Triangularis Area (mm^2)	Surface area of the APARC parstriangularis parcel in the left hemisphere.
lh_pericalcarine_area	Left Hemisphere Pericalcarine Area (mm^2)	Surface area of the APARC pericalcarine parcel in the left hemisphere.
lh_postcentral_area	Left Hemisphere Postcentral Area (mm^2)	Surface area of the APARC postcentral parcel in the left hemisphere.
lh_posteriorcingulate_area	Left Hemisphere Posterior Cingulate Area (mm^2)	Surface area of the APARC posteriorcingulate parcel in the left hemisphere.
lh_precentral_area	Left Hemisphere Precentral Area (mm^2)	Surface area of the APARC precentral parcel in the left hemisphere.
lh_precuneus_area	Left Hemisphere Precuneus Area (mm^2)	Surface area of the APARC precuneus parcel in the left hemisphere.
lh_rostralanteriorcingulate_area	Left Hemisphere Rostral Anterior Cingulate Area (mm^2)	Surface area of the APARC rostralanteriorcingulate parcel in the left hemisphere.
lh_rostralmiddlefrontal_area	Left Hemisphere Rostral Middle Frontal Area (mm^2)	Surface area of the APARC rostralmiddlefrontal parcel in the left hemisphere.
lh_superiorfrontal_area	Left Hemisphere Superior Frontal Area (mm^2)	Surface area of the APARC superiorfrontal parcel in the left hemisphere.
lh_superiorparietal_area	Left Hemisphere Superior Parietal Area (mm^2)	Surface area of the APARC superiorparietal parcel in the left hemisphere.
lh_superiortemporal_area	Left Hemisphere Superior Temporal Area (mm^2)	Surface area of the APARC superiortemporal parcel in the left hemisphere.
lh_supramarginal_area	Left Hemisphere Supramarginal Area (mm^2)	Surface area of the APARC supramarginal parcel in the left hemisphere.
lh_frontalpole_area	Left Hemisphere Frontal Pole Area (mm^2)	Surface area of the APARC frontalpole parcel in the left hemisphere.
lh_temporalpole_area	Left Hemisphere Temporal Pole Area (mm^2)	Surface area of the APARC temporalpole parcel in the left hemisphere.
lh_transversetemporal_area	Left Hemisphere Transverse Temporal Area (mm^2)	Surface area of the APARC transversetemporal parcel in the left hemisphere.
lh_insula_area	Left Hemisphere Insula Area (mm^2)	Surface area of the APARC insula parcel in the left hemisphere.
lh_WhiteSurfArea_area	Left Hemisphere White Surface Area (mm^2)	Total white matter surface area in the left hemisphere.

Table A.31: MRI Morphometric Measures; Cortical Thickness

Variable Name	Label	Important Notes
lh_bankssts_thickness	Left Hemisphere Bankssts Thickness (mm)	Thickness of the APARC bankssts parcel in the left hemisphere pial surface.
lh_caudalanteriorcingulate_thick	Left Hemisphere Caudal Anterior Cingulate Thickness (mm)	Thickness of the APARC caudalanteriorcingulate parcel in the left hemisphere.
lh_caudalmiddlefrontal_thickness	Left Hemisphere Caudal Middle Frontal Thickness (mm)	Thickness of the APARC caudalmiddlefrontal parcel in the left hemisphere.
lh_cuneus_thickness	Left Hemisphere Cuneus Thickness (mm)	Thickness of the APARC cuneus parcel in the left hemisphere.
lh_entorhinal_thickness	Left Hemisphere Entorhinal Thickness (mm)	Thickness of the APARC entorhinal parcel in the left hemisphere.
lh_fusiform_thickness	Left Hemisphere Fusiform Thickness (mm)	Thickness of the APARC fusiform parcel in the left hemisphere.
lh_inferiorparietal_thickness	Left Hemisphere Inferior Parietal Thickness (mm)	Thickness of the APARC inferiorparietal parcel in the left hemisphere.
lh_inferiortemporal_thickness	Left Hemisphere Inferior Temporal Thickness (mm)	Thickness of the APARC inferiortemporal parcel in the left hemisphere.
lh_isthmuscingulate_thickness	Left Hemisphere Isthmus Cingulate Thickness (mm)	Thickness of the APARC isthmuscingulate parcel in the left hemisphere.
lh_lateraloccipital_thickness	Left Hemisphere Lateral Occipital Thickness (mm)	Thickness of the APARC lateraloccipital parcel in the left hemisphere.
lh_lateralorbitofrontal_thickness	Left Hemisphere Lateral Orbitofrontal Thickness (mm)	Thickness of the APARC lateralorbitofrontal parcel in the left hemisphere.
lh_lingual_thickness	Left Hemisphere Lingual Thickness (mm)	Thickness of the APARC lingual parcel in the left hemisphere.
lh_medialorbitofrontal_thickness	Left Hemisphere Medial Orbitofrontal Thickness (mm)	Thickness of the APARC medialorbitofrontal parcel in the left hemisphere.
lh_middletemporal_thickness	Left Hemisphere Middle Temporal Thickness (mm)	Thickness of the APARC middletemporal parcel in the left hemisphere.
lh_parahippocampal_thickness	Left Hemisphere Parahippocampal Thickness (mm)	Thickness of the APARC parahippocampal parcel in the left hemisphere.
lh_paracentral_thickness	Left Hemisphere Paracentral Thickness (mm)	Thickness of the APARC paracentral parcel in the left hemisphere.
lh_parsopercularis_thickness	Left Hemisphere Pars Opercularis Thickness (mm)	Thickness of the APARC parsopercularis parcel in the left hemisphere.

Table A.32: MRI Morphometric Measures; Cortical Thickness

Variable Name	Label	Important Notes
lh_parsorbitalis_thickness	Left Hemisphere Pars Orbitalis Thickness (mm)	Thickness of the APARC parsorbitalis parcel in the left hemisphere.
lh_parstriangularis_thickness	Left Hemisphere Pars Triangularis Thickness (mm)	Thickness of the APARC parstriangularis parcel in the left hemisphere.
lh_pericalcarine_thickness	Left Hemisphere Pericalcarine Thickness (mm)	Thickness of the APARC pericalcarine parcel in the left hemisphere.
lh_postcentral_thickness	Left Hemisphere Postcentral Thickness (mm)	Thickness of the APARC postcentral parcel in the left hemisphere.
lh_posteriorcingulate_thickness	Left Hemisphere Posterior Cingulate Thickness (mm)	Thickness of the APARC posteriorcingulate parcel in the left hemisphere.
lh_precentral_thickness	Left Hemisphere Precentral Thickness (mm)	Thickness of the APARC precentral parcel in the left hemisphere.
lh_precuneus_thickness	Left Hemisphere Precuneus Thickness (mm)	Thickness of the APARC precuneus parcel in the left hemisphere.
lh_rostralanteriorcingulate_thickness	Left Hemisphere Rostral Anterior Cingulate Thickness (mm)	Thickness of the APARC rostralanteriorcingulate parcel in the left hemisphere.
lh_rostralmiddlefrontal_thickness	Left Hemisphere Rostral Middle Frontal Thickness (mm)	Thickness of the APARC rostralmiddlefrontal parcel in the left hemisphere.
lh_superiorfrontal_thickness	Left Hemisphere Superior Frontal Thickness (mm)	Thickness of the APARC superiorfrontal parcel in the left hemisphere.
lh_superiorparietal_thickness	Left Hemisphere Superior Parietal Thickness (mm)	Thickness of the APARC superiorparietal parcel in the left hemisphere.
lh_superiortemporal_thickness	Left Hemisphere Superior Temporal Thickness (mm)	Thickness of the APARC superiortemporal parcel in the left hemisphere.
lh_supramarginal_thickness	Left Hemisphere Supramarginal Thickness (mm)	Thickness of the APARC supramarginal parcel in the left hemisphere.
lh_frontalpole_thickness	Left Hemisphere Frontal Pole Thickness (mm)	Thickness of the APARC frontalpole parcel in the left hemisphere.
lh_temporalpole_thickness	Left Hemisphere Temporal Pole Thickness (mm)	Thickness of the APARC temporalpole parcel in the left hemisphere.
lh_transversetemporal_thickness	Left Hemisphere Transverse Temporal Thickness (mm)	Thickness of the APARC transversetemporal parcel in the left hemisphere.
lh_insula_thickness	Left Hemisphere Insula Thickness (mm)	Thickness of the APARC insula parcel in the left hemisphere.
lh_MeanThickness_thickness	Left Hemisphere Mean Thickness (mm)	Mean thickness across all APARC parcels in the left hemisphere.

Table A.33: MRI Morphometric Measures; Cortical Curvature

Variable Name	Label	Important Notes
lh_bankssts_meancurv	Left Hemisphere Bankssts Mean Curvature	Mean curvature of the APARC bankssts parcel in the left hemisphere pial surface.
lh_caudalanteriorcingulate_meanc	Left Hemisphere Caudal Anterior Cingulate Mean Curvature	Mean curvature of the APARC caudalanteriorcingulate parcel in the left hemisphere.
lh_caudalmiddlefrontal_meancurv	Left Hemisphere Caudal Middle Frontal Mean Curvature	Mean curvature of the APARC caudalmiddlefrontal parcel in the left hemisphere.
lh_cuneus_meancurv	Left Hemisphere Cuneus Mean Curvature	Mean curvature of the APARC cuneus parcel in the left hemisphere.
lh_entorhinal_meancurv	Left Hemisphere Entorhinal Mean Curvature	Mean curvature of the APARC entorhinal parcel in the left hemisphere.
lh_fusiform_meancurv	Left Hemisphere Fusiform Mean Curvature	Mean curvature of the APARC fusiform parcel in the left hemisphere.
lh_inferiorparietal_meancurv	Left Hemisphere Inferior Parietal Mean Curvature	Mean curvature of the APARC inferiorparietal parcel in the left hemisphere.
lh_inferiortemporal_meancurv	Left Hemisphere Inferior Temporal Mean Curvature	Mean curvature of the APARC inferiortemporal parcel in the left hemisphere.
lh_isthmuscingulate_meancurv	Left Hemisphere Isthmus Cingulate Mean Curvature	Mean curvature of the APARC isthmuscingulate parcel in the left hemisphere.
lh_lateraloccipital_meancurv	Left Hemisphere Lateral Occipital Mean Curvature	Mean curvature of the APARC lateraloccipital parcel in the left hemisphere.
lh_lateralorbitofrontal_meancurv	Left Hemisphere Lateral Orbitofrontal Mean Curvature	Mean curvature of the APARC lateralorbitofrontal parcel in the left hemisphere.
lh_lingual_meancurv	Left Hemisphere Lingual Mean Curvature	Mean curvature of the APARC lingual parcel in the left hemisphere.
lh_medialorbitofrontal_meancurv	Left Hemisphere Medial Orbitofrontal Mean Curvature	Mean curvature of the APARC medialorbitofrontal parcel in the left hemisphere.
lh_middletemporal_meancurv	Left Hemisphere Middle Temporal Mean Curvature	Mean curvature of the APARC middletemporal parcel in the left hemisphere.
lh_parahippocampal_meancurv	Left Hemisphere Parahippocampal Mean Curvature	Mean curvature of the APARC parahippocampal parcel in the left hemisphere.
lh_paracentral_meancurv	Left Hemisphere Paracentral Mean Curvature	Mean curvature of the APARC paracentral parcel in the left hemisphere.

Table A.34: MRI Morphometric Measures; Cortical Curvature

Variable Name	Label	Important Notes
lh_parsopercularis_meancurv	Left Hemisphere Pars Opercularis Mean Curvature	Mean curvature of the APARC parsopercularis parcel in the left hemisphere.
lh_parsorbitalis_meancurv	Left Hemisphere Pars Orbitalis Mean Curvature	Mean curvature of the APARC parsorbitalis parcel in the left hemisphere.
lh_parstriangularis_meancurv	Left Hemisphere Pars Triangularis Mean Curvature	Mean curvature of the APARC parstriangularis parcel in the left hemisphere.
lh_pericalcarine_meancurv	Left Hemisphere Pericalcarine Mean Curvature	Mean curvature of the APARC pericalcarine parcel in the left hemisphere.
lh_postcentral_meancurv	Left Hemisphere Postcentral Mean Curvature	Mean curvature of the APARC postcentral parcel in the left hemisphere.
lh_posteriorcingulate_meancurv	Left Hemisphere Posterior Cingulate Mean Curvature	Mean curvature of the APARC posteriorcingulate parcel in the left hemisphere.
lh_precentral_meancurv	Left Hemisphere Precentral Mean Curvature	Mean curvature of the APARC precentral parcel in the left hemisphere.
lh_precuneus_meancurv	Left Hemisphere Precuneus Mean Curvature	Mean curvature of the APARC precuneus parcel in the left hemisphere.
lh_rostralanteriorcingulate_meanc	Left Hemisphere Rostral Anterior Cingulate Mean Curvature	Mean curvature of the APARC rostralanteriorcingulate parcel in the left hemisphere.
lh_rostralmiddlefrontal_meancurv	Left Hemisphere Rostral Middle Frontal Mean Curvature	Mean curvature of the APARC rostralmiddlefrontal parcel in the left hemisphere.
lh_superiorfrontal_meancurv	Left Hemisphere Superior Frontal Mean Curvature	Mean curvature of the APARC superiorfrontal parcel in the left hemisphere.
lh_superiorparietal_meancurv	Left Hemisphere Superior Parietal Mean Curvature	Mean curvature of the APARC superiorparietal parcel in the left hemisphere.
lh_superiortemporal_meancurv	Left Hemisphere Superior Temporal Mean Curvature	Mean curvature of the APARC superiortemporal parcel in the left hemisphere.
lh_supramarginal_meancurv	Left Hemisphere Supramarginal Mean Curvature	Mean curvature of the APARC supramarginal parcel in the left hemisphere.
lh_frontalpole_meancurv	Left Hemisphere Frontal Pole Mean Curvature	Mean curvature of the APARC frontalpole parcel in the left hemisphere.
lh_temporalpole_meancurv	Left Hemisphere Temporal Pole Mean Curvature	Mean curvature of the APARC temporalpole parcel in the left hemisphere.
lh_transversetemporal_meancurv	Left Hemisphere Transverse Temporal Mean Curvature	Mean curvature of the APARC transversetemporal parcel in the left hemisphere.
lh_insula_meancurv	Left Hemisphere Insula Mean Curvature	Mean curvature of the APARC insula parcel in the left hemisphere.

Table A.35: MRI Morphometric Measures; Cortical Volumetrics

Variable Name	Label	Important Notes
lh_bankssts_volume	Left Hemisphere Bankssts Volume	Volume of the APARC bankssts parcel in the left hemisphere pial surface.
lh_caudalanteriorcingulate_volume	Left Hemisphere Caudal Anterior Cingulate Volume	Volume of the APARC caudalanteriorcingulate parcel in the left hemisphere.
lh_caudalmiddlefrontal_volume	Left Hemisphere Caudal Middle Frontal Volume	Volume of the APARC caudalmiddlefrontal parcel in the left hemisphere.
lh_cuneus_volume	Left Hemisphere Cuneus Volume	Volume of the APARC cuneus parcel in the left hemisphere.
lh_entorhinal_volume	Left Hemisphere Entorhinal Volume	Volume of the APARC entorhinal parcel in the left hemisphere.
lh_fusiform_volume	Left Hemisphere Fusiform Volume	Volume of the APARC fusiform parcel in the left hemisphere.
lh_inferiorparietal_volume	Left Hemisphere Inferior Parietal Volume	Volume of the APARC inferiorparietal parcel in the left hemisphere.
lh_inferiortemporal_volume	Left Hemisphere Inferior Temporal Volume	Volume of the APARC inferiortemporal parcel in the left hemisphere.
lh_isthmuscingulate_volume	Left Hemisphere Isthmus Cingulate Volume	Volume of the APARC isthmuscingulate parcel in the left hemisphere.
lh_lateraloccipital_volume	Left Hemisphere Lateral Occipital Volume	Volume of the APARC lateraloccipital parcel in the left hemisphere.
lh_lateralorbitofrontal_volume	Left Hemisphere Lateral Orbitofrontal Volume	Volume of the APARC lateralorbitofrontal parcel in the left hemisphere.
lh_lingual_volume	Left Hemisphere Lingual Volume	Volume of the APARC lingual parcel in the left hemisphere.
lh_medialorbitofrontal_volume	Left Hemisphere Medial Orbitofrontal Volume	Volume of the APARC medialorbitofrontal parcel in the left hemisphere.
lh_middletemporal_volume	Left Hemisphere Middle Temporal Volume	Volume of the APARC middletemporal parcel in the left hemisphere.
lh_parahippocampal_volume	Left Hemisphere Parahippocampal Volume	Volume of the APARC parahippocampal parcel in the left hemisphere.
lh_paracentral_volume	Left Hemisphere Paracentral Volume	Volume of the APARC paracentral parcel in the left hemisphere.
lh_parsopercularis_volume	Left Hemisphere Pars Opercularis Volume	Volume of the APARC parsopercularis parcel in the left hemisphere.

Table A.36: MRI Morphometric Measures; Cortical Volumetrics

Variable Name	Label	Important Notes
lh_parsorbitalis_volume	Left Hemisphere Pars Orbitalis Volume	Volume of the APARC parsorbitalis parcel in the left hemisphere.
lh_parstriangularis_volume	Left Hemisphere Pars Triangularis Volume	Volume of the APARC parstriangularis parcel in the left hemisphere.
lh_pericalcarine_volume	Left Hemisphere Pericalcarine Volume	Volume of the APARC pericalcarine parcel in the left hemisphere.
lh_postcentral_volume	Left Hemisphere Postcentral Volume	Volume of the APARC postcentral parcel in the left hemisphere.